

**Development of coupled processes numerical models  
of tracer, colloid and radionuclide transport in field  
migration experiments**

by

BENJAMIN EDWARD HARVEY

A thesis submitted to The University of Birmingham for the degree of  
DOCTOR OF PHILOSOPHY

Hydrogeology Research Group, Earth Sciences  
School of Geography, Earth and Environmental Sciences,  
College of Life and Environmental Sciences,  
University of Birmingham,

July 2018

UNIVERSITY OF  
BIRMINGHAM

**University of Birmingham Research Archive**

**e-theses repository**

This unpublished thesis/dissertation is copyright of the author and/or third parties. The intellectual property rights of the author or third parties in respect of this work are as defined by The Copyright Designs and Patents Act 1988 or as modified by any successor legislation.

Any use made of information contained in this thesis/dissertation must be in accordance with that legislation and must be properly acknowledged. Further distribution or reproduction in any format is prohibited without the permission of the copyright holder.

## **ABSTRACT**

Deep geological disposal is widely recognised as the best method for disposing of higher-activity radioactive wastes. There is a need to increase understanding of processes that can lead to radionuclide migration from a geological disposal facility (GDF). Colloids are sub-microscopic particles that are ubiquitous in groundwater. If radionuclides become associated with colloids they can potentially be transported by different processes than would be predicted by traditional solute transport modelling.

Colloid-facilitated radionuclide transport is being investigated as part of the Colloid Formation and Migration (CFM) project at the Grimsel Test Site in Switzerland, where migration experiments investigating the transport of conservative tracers, bentonite colloids and radionuclides have been carried out in a well characterised shear zone within fractured granodiorite. This study produced a new modelling approach that describes colloid-facilitated radionuclide transport, which is applied to two migration experiments, modelling the migration of conservative tracers, bentonite colloids and radionuclides.

For the first time, a model that includes a detailed distribution of transmissivity generated by inverse modelling has been combined with a colloid-facilitated radionuclide transport model to describe these field experiments. The model was able to replicate successfully the transport of tracers, colloids and radionuclides in both experiments, using consistent parameters and processes to describe transport for most species, identifying important radionuclide transport processes in the different experiments. Certain radionuclides showed different transport behaviour in the two migration experiments due to their redox or sorption chemistry, and this study was able to model and highlight this as a further area for

investigation. The colloids at least partially facilitated the transport of all of the radionuclides modelled. However, the sorption of the radionuclides to the colloids was shown to be reversible, with the rate of desorption forming a key control on their migration in these field experiments.

The methods and tools developed here can be applied to future migration experiments as part of CFM, and to assess the colloid-facilitated radionuclide migration at other sites, including a future GDF site.

## **DEDICATION**

This thesis is dedicated to everyone who has helped me get here, thank you.

## **ACKNOWLEDGEMENTS**

Thank you to the Natural Environment Research Council (NERC), Radioactive Waste Management Ltd. (RWM) and the Environment Agency (EA) for providing the funding for this project under the HydroFrame consortium with Imperial College and the University of Leeds under the wider Radioactivity and the Environment (RATE) programme. Thank you to ESI Ltd. (now Stantec) for providing CASE sponsorship to the project.

Special thanks need to go to Nagra for access to the CFM experimental data, and to all of the CFM Partner organisations for funding the project. Particular thanks need to go to Ingo Blechschmidt and Bill Lanyon for answering many questions about the experiment and the data, and for providing guidance on the modelling.

Thank you to my supervisors, Alan Herbert, John Tellam and Mick Riley for the support and guidance, for the constructive comments improving this thesis and for allowing me to go to Japan. Special thanks go to the other members of this work package, Lindsay McMillan for developing the Inverse Model and resulting transmissivity distribution, as well as for supporting the development of the transport model; and to Janice Kenney for helping with the geochemical modelling and for providing insight into radionuclide geochemistry.

Thanks to my other Hydrogeology colleagues for their helpful input and support through some difficult periods, including: Christopher Barry, Simiao Sun, Gary Clarke, Ban To, Omar Al-Azzo, Rohazaini Muhammad Jamil, Mahmoud Jaweesh and Mark Cuthbert.

For their help navigating university bureaucracy, thanks go to Aruna Mistry and Gretchel Coldicott. Thanks go to PhD and staff members of the Earth Sciences department, but

particular thanks go to Emma Dunne, David Cavell, Daniel Cox, Alan Hastie, Gäel Lymer, Andrew Rees, Derren Cresswell, Alastair Hodgetts and Jonathan Hall for enlightening conversation and for generally making the department a friendly and interesting place to work.

Thanks to friends and family for their supporting and for pretending to be interested by my waffling describing the months of writing, and last but certainly not least thank you to Millie, my partner in crime, for your support and understanding during this entire project, it would not have been possible without you.

# Table of Contents

<b>1. INTRODUCTION</b> .....	1
1.1. Background.....	1
1.2. Geological Disposal of Radioactive Wastes.....	1
1.3. Colloid-Facilitated Radionuclide Transport.....	4
1.4. The Grimsel Test Site, and the Colloid Formation and Migration Project (CFM).....	9
1.5. Aim and Objectives .....	11
1.6. Thesis Structure.....	12
1.7. List of References .....	13
<b>2. LITERATURE REVIEW</b> .....	16
2.1. Introduction .....	16
2.2. Colloid transport processes.....	17
2.2.1. Colloid interaction .....	17
2.2.2. Colloid formation .....	19
2.2.3. Colloid attachment and straining.....	21
2.2.4. Colloid size.....	24
2.3. Radionuclide interaction with colloids.....	26
2.4. Models of colloid-facilitated radionuclide transport .....	30
2.5. Summary .....	33
2.6. List of References .....	34
<b>3. FIELD MIGRATION EXPERIMENTS AT THE GRIMSEL TEST SITE</b> .....	39
3.1. Introduction .....	39
3.2. Grimsel Test Site.....	40
3.2.1. Geological Setting.....	40
3.2.2. Hydrogeology .....	43
3.3. Colloid Formation and Migration (CFM) Project.....	49
3.3.1. Background and Objectives.....	49
3.3.2. Previous Experiments in the MI Shear Zone .....	49
3.3.3. CFM Project .....	51
3.4. Experimental Procedures .....	52
3.4.1. Introduction.....	52
3.4.2. Injection Process .....	53
3.4.3. Monitoring Process .....	56

3.5.	Previous Modelling.....	60
3.6.	Inverse Model.....	67
3.6.1.	Model overview.....	67
3.6.2.	Data included in model .....	71
3.6.3.	Model setup .....	72
3.6.4.	Model results.....	74
3.7.	Summary .....	77
3.8.	List of References .....	79
<b>4.</b>	<b>DEVELOPMENT OF COLLOID-FACILITATED RADIONUCLIDE TRANSPORT MODEL.....</b>	<b>83</b>
4.1.	Introduction .....	83
4.2.	Conceptual Model .....	84
4.2.1.	Geology/ Hydrogeology.....	84
4.2.2.	Experimental Processes.....	85
4.3.	Governing Equations .....	89
4.4.	Model Verification.....	94
4.4.1.	Advection-dispersion, retardation and radioactive decay.....	94
4.4.2.	Colloid transport and attachment.....	97
4.4.3.	Colloid-facilitated radionuclide transport.....	100
4.5.	Numerical Model.....	102
4.6.	Transport Model Application .....	111
4.7.	Summary .....	113
4.8.	List of References .....	114
<b>5.</b>	<b>MODELLING CONSERVATIVE TRACER AND COLLOID TRANSPORT IN CFM RUN 13-05 AND CRR RUN 32 .....</b>	<b>117</b>
5.1.	Introduction .....	117
5.2.	Numerical model setup.....	118
5.3.	Conservative tracer model calibration.....	120
5.3.1.	CFM Run 13-05.....	122
5.3.2.	CRR Run 32 .....	125
5.3.3.	Discussion of the calibration parameters.....	128
5.4.	Bentonite colloid model calibration.....	130
5.4.1.	CFM Run 13-05.....	133
5.4.2.	CRR Run 32 .....	136

5.4.3.	Discussion on calibration parameters .....	138
5.5.	1D 'channel' model .....	141
5.5.1.	Background.....	141
5.5.2.	Model development.....	141
5.5.3.	Model Results.....	144
5.5.4.	Discussion and Conclusions.....	147
5.6.	Blind predictions for the REMO-2 experiment.....	149
5.6.1.	Background.....	149
5.6.2.	Alterations to Model .....	150
5.6.3.	Model Predictions .....	154
5.6.4.	Discussion and Conclusions.....	157
5.7.	Summary .....	158
5.8.	List of References .....	159
<b>6.</b>	<b>MODELLING THE MIGRATION OF AMERICIUM AND PLUTONIUM IN CFM 13-05 AND CRR 32</b>	<b>161</b>
6.1.	Introduction .....	161
6.2.	Americium model calibration.....	162
6.2.1.	Conceptual Model .....	163
6.2.2.	Transport Model setup.....	170
6.2.3.	Model Results.....	171
6.2.4.	Discussion and Conclusions.....	176
6.3.	Plutonium model calibration.....	180
6.3.1.	Conceptual Model .....	180
6.3.2.	Transport Model setup.....	186
6.3.3.	Model Results.....	186
6.3.4.	Discussion and Conclusions.....	191
6.4.	Summary .....	194
6.5.	List of References .....	196
<b>7.</b>	<b>MODELLING THE TRANSPORT OF CAESIUM, URANIUM AND NEPTUNIUM IN CFM RUN 13-05 AND CRR RUN 32</b>	<b>198</b>
7.1.	Introduction .....	198
7.2.	Caesium model calibration.....	199
7.2.1.	Conceptual Model .....	199
7.2.2.	Transport Model setup.....	205

7.2.3.	Model Results.....	209
7.2.4.	Discussion and Conclusions.....	215
7.3.	Uranium model calibration .....	224
7.3.1.	Geochemical conceptual model.....	224
7.3.2.	Transport Model setup.....	233
7.3.3.	Model Results.....	234
7.3.4.	Discussion and Conclusions.....	239
7.4.	Neptunium model calibration .....	242
7.4.1.	Geochemical conceptual model.....	242
7.4.2.	Transport Model setup.....	250
7.4.3.	Model Results.....	251
7.4.4.	Discussion and Conclusions.....	255
7.5.	Summary .....	260
7.6.	List of References .....	261
<b>8.</b>	<b>CONCLUSIONS</b> .....	<b>266</b>
8.1.	Introduction .....	266
8.2.	Objectives 1 and 2: Development of the model for Colloid-Facilitated Radionuclide Transport.....	267
8.3.	Objective 3: Application of the transport model to two in-situ field experiments.....	268
8.4.	Objective 4: Identifying important radionuclide transport processes.....	274
8.4.1.	Americium and plutonium .....	275
8.4.2.	Caesium .....	277
8.4.3.	Uranium and neptunium.....	278
8.5.	Modelling implications.....	280
8.6.	Areas for future work.....	284
8.7.	List of References .....	286
	<b>APPENDICES</b> .....	<b>289</b>

## List of Figures

Figure 1.1 Artist’s impression of a geological disposal facility (Department of Energy and Climate Change, 2014) .....	2
Figure 1.2 Examples of the multiple engineered barriers for a geological disposal facility (Department of Energy and Climate Change, 2014).....	3
Figure 1.3 Diagram of different processes involved in colloid-facilitated radionuclide transport within a fracture. Processes: colloid transport (1); colloid attachment (2); radionuclide (RN) transport (3); RN sorption to rock surfaces (4); RN matrix diffusion (5); RN sorption to mobile colloids (6); attachment of colloids with RN sorbed (7); desorption of RN from colloid (8); colloid aggregation (9). Processes not shown include colloid sedimentation and straining. ....	6
Figure 2.1 The ‘colloid ladder’ of conditions that if met will result in colloid-facilitated radionuclide transport being significant in an environmental safety case for a geological disposal facility (From: Möri et al. 2004).....	17
Figure 2.2 Component forces that make up DLVO energy profiles (Black = double layer repulsion, Red = van der Waals attraction, Green = Total forces) (From: Hahn and O’Melia, 2004) .....	18
Figure 2.3 Calculated DLVO energy profiles showing attractive/ favourable (red line) and repulsive/ unfavourable (black line) conditions for deposition of silver colloids onto quartz and iron oxide (From: Molnar et al. 2015).....	19
Figure 3.1 Aerial view at the surface of the Grimsel Test Site looking west. 1: Grimsel Test Site, 2: Räterichsbodensee, 3: Grimselsee, 4: Juchlistock. (From: Schlickenrieder et al. 2017) .....	41
Figure 3.2 Schematic diagram of the different tunnels and boreholes drilled at the Grimsel Test Site (Altered from Schlickenrieder et al. 2017).....	41
Figure 3.3 Map of the MI shear zone, showing the intersection with the AU tunnel (highlighted by the CFM megapacker), the VE Tunnel and the main KWO access tunnel (From: Schlickenrieder et al. 2017) .....	42
Figure 3.4 Map of the structure of the MI shear zone, as taken from the outcrop at the intersecting AU tunnel (From: Gaus and Smith 2008) .....	43
Figure 3.5 Schematic of the mega-packer system installed during the CFM project. Full details found in Schlickenrieder et al. (2017).....	45
Figure 3.6 Map of the MI shear zone, with the transmissivity field generated by inverse modelling using a geostatistical approach during the CRR project, detailed in Jódar et al. (2002). Boreholes drilled from different locations in the AU tunnel, shown where they intersect with MI shear zone. BOCR 99.002 and BOCR 00.003 refer to boreholes CRR 99.002 and CRR 00.003. Red arrow shows CFM dipole between CFM 06.002 and Pinkel (used in CFM 12-02) and blue arrow shows CRR Dipole 1 between CRR 99.002 and BOMI 87.010 (used in CRR 31, 32 and CFM 13-05). Altered from: Schlickenrieder et al. (2017).....	46
Figure 3.7 Positive saturation indices for mineral phases in Grimsel groundwater as a function of pH (Eh -220mV), as calculated using PHREEQC, using the PSI/ Nagra TDB. Blue line = pH 9.6, the average value for Grimsel groundwater. ....	48
Figure 3.8 Positive saturation indices for mineral phases in Grimsel groundwater as a function of Eh (pH 9.6), as calculated using PHREEQC and PSI/Nagra TDB. Blue line = Eh -220mV, the average value measured in Grimsel groundwater. ....	48

Figure 3.9 Conceptual diagram showing the injection used in CFM Run 13-05. Natural cross flow estimated by measuring the slope of the tracer concentration decline in the injection interval. ....	56
Figure 3.10 Summary of inverse model domain .....	73
Figure 3.11 The resulting transmissivity distribution from the inverse model, with head contours representing CRR experimental conditions (McMillan et al., in prep.).....	75
Figure 3.12 (a) Observed versus simulated steady-state heads; and (b) Observed versus simulated transient drawdowns .....	75
Figure 3.13 Best fit tracer breakthrough across adjacent dipoles D1 and D2 using MT3D. ....	77
Figure 4.1 Diagram of different processes involved in colloid-facilitated radionuclide transport within a fracture. Processes: colloid transport (1); colloid attachment (2); radionuclide (RN) transport (3); RN sorption to rock surfaces (4); RN matrix diffusion (5); RN sorption to mobile colloids (6); attachment of colloids with RN sorbed (7); desorption of RN from colloid (8); colloid aggregation (9). Processes not shown include colloid sedimentation and straining.....	85
Figure 4.2 Different phases solved in transport model (includes matrix diffusion, excludes kinetic sorption to rock surfaces) .....	92
Figure 4.3 Comparison between analytical solution using Ogata-Banks solution for advection dispersion equation with 1D Model in COMSOL Multiphysics .....	95
Figure 4.4 Initial 2D model for verification of ADE. Source term applied to left hand boundary, advective only flux applied to right hand boundary. Model domain 0.1 x 1 metre. ....	96
Figure 4.5 Comparison between 1D and 2D numerical models solving the advection-dispersion equation within COMSOL.....	96
Figure 4.6 Comparison between colloid attachment modelling in Burns (2013), (blue line) and this model (red squares) using parameters in tables above. Time is in seconds, concentration in $C/C_0$ ....	97
Figure 4.7 Sensitivity analysis of $k_{iat}$ on COMSOL model using parameters in Table 4.3 .....	99
Figure 4.8 Result of calibrated model for Experiment B in Walkden (2014), using the parameters in Table 4.3. Full details of the model found in Appendix C. ....	99
Figure 4.9 Model domain used for verification of CFRT attachment/ detachment equations. Inlet is on left hand side, right hand side is outlet. The centre line is the concentration measurement point. .	100
Figure 4.10 Sensitivity analysis for test case, values represent sorption rate $k_{amc}$ ( $m^3/kg.s$ ), with 10 hour pulse injection. ....	101
Figure 4.11 Sensitivity analysis for test case, values represent desorption rate $k_{mca}$ (1/s), with 10 hour pulse injection. ....	102
Figure 4.12 Geometry of 2D Transport Model (co-ordinate system centred on the centre of the tunnel, model domain represents plane view of shear zone dipping $\sim 75^\circ$ to the south) .....	104
Figure 4.13 Close up of model domain (highlighted in blue, co-ordinate system centred on the centre of the tunnel). Explanation of low T square given in text below. ....	104
Figure 4.14 Transmissivity of part of model area ( $m^2/s$ in log scale), including low transmissivity block highlighted. ....	106
Figure 4.15 Mesh used in transport model, plane view of shear zone (co-ordinate system centred on tunnel in metres).....	110
Figure 5.1 Mesh used in transport model, plane view of shear zone (co-ordinate system centred on tunnel in metres).....	119

Figure 5.2 Model calibration for conservative tracer for CFM 13-05 (blue), CRR 32 (red) and CRR 29 (green). Concentrations normalised in this and all subsequent figures with normalised concentration against $M_0$ (mass injected) .....	122
Figure 5.3 Calibrated model results for amino-G acid in CFM 13-05 .....	123
Figure 5.4 Comparison of cumulative recovery for observed and modelled data for CFM Run 13-05 conservative tracer.....	123
Figure 5.5 Concentration in $\mu\text{g/l}$ of conservative tracer remaining in CFM Run 13-05 model after 1200 hours. ....	124
Figure 5.6 Calibrated model results for $^{131}\text{I}$ in CRR 32.....	125
Figure 5.7 Comparison of cumulative recovery for observed and modelled data for CRR Run 32 conservative tracer.....	126
Figure 5.8 Predicted model results for uranine breakthrough in CRR 29 .....	127
Figure 5.9 Comparison of cumulative recovery for observed and modelled data for CRR Run 32 conservative tracer.....	127
Figure 5.10 Effect of heterogeneity on the number of parallel plates required to scale between transport and hydraulic aperture. From Forbes (2016).....	130
Figure 5.11 Example of a colloid recovery map for CFM Run 13-05, $k_{\text{iat}} = 1\text{e-}6$ 1/s, colours show the predicted colloid recovery. Arrows show where model values obtained. This map is a slice through a 3D parameter space due to the irreversible colloid attachment parameter.....	132
Figure 5.12 Model calibration for bentonite colloid breakthrough in CFM Run 13-05 (blue) and CRR Run 32 (red).....	133
Figure 5.13 Model calibration result for bentonite colloids in CFM Run 13-05.....	134
Figure 5.14 Comparison of observed and modelled cumulative recovery for CFM Run 13-05 bentonite colloids .....	134
Figure 5.15 Model calibration for bentonite colloids in CRR Run 32 .....	137
Figure 5.16 Comparison of observed and modelled cumulative recovery for CRR Run 32 bentonite colloids .....	137
Figure 5.17 Layout and input of analytical spreadsheet model (showing results from CRR Run 32 calibration) .....	142
Figure 5.18 Approximate source term used in analytical model for CFM Run 13-05.....	143
Figure 5.19 Model calibration from 1D analytical and COMSOL models for CFM Run 13-05 conservative tracer.....	145
Figure 5.20 Model calibration from 1D Analytical and COMSOL models for CRR Run 32 conservative tracer .....	145
Figure 5.21 Model calibration for 1D bentonite colloid model in CFM Run 13-05.....	146
Figure 5.22 Model calibration for 1D bentonite colloid model in CRR Run 32 .....	146
Figure 5.23 Groundwater head colour flood (with contours) during injection of colloids for REMO-2. Co-ordinate system centred on tunnel in metres.....	151
Figure 5.24 Groundwater head colour flood (with contours) during rest period for REMO-2. Co-ordinate system centred on tunnel in metres. ....	152
Figure 5.25 Groundwater head colour flood (with contours) during extraction of colloids for REMO-2. Co-ordinate system centred on tunnel in metres.....	152
Figure 5.26 Predicted breakthrough for bentonite colloids in REMO-2 (for CRR 99.002 and Pinkel) .....	154

Figure 5.27 Predicted breakthrough curves for bentonite colloids in REMO-2 (for CRR 99.002 and Pinkel).....	155
Figure 5.28 Predicted colloid concentration at 2hr in REMO-2 (end of injection of freshwater).....	155
Figure 5.29 Predicted colloid concentration at 26 hr in REMO-2 (end of 24hr rest period) .....	156
Figure 5.30 Predicted colloid concentration at 36 hours in REMO-2 (end of 10 hr extraction) in REMO-2.....	156
Figure 6.1 Speciation of americium in the CFM Run 13-05 injection cocktail as predicted by PHREEQC. Blue line = Grimsel groundwater (pH 9.6).....	165
Figure 6.2 Speciation of americium in the CRR Run 32 injection cocktail as predicted by PHREEQC. Blue line = Grimsel groundwater (pH 9.6).....	165
Figure 6.3 Predicted saturation indexes of americium precipitates in CFM Run 13-05 injection cocktail from PHREEQC. Blue line = pH (9.6) of the reference Grimsel groundwater .....	166
Figure 6.4 Predicted saturation indexes of americium precipitates in the CRR Run 32 injection cocktail from PHREEQC. Blue line = pH (9.6) of reference Grimsel groundwater. ....	166
Figure 6.5 Calibrated breakthrough curves for americium in CFM Run 13-05 and CRR Run 32.....	172
Figure 6.6 Calibrated breakthrough curve for <sup>243</sup> Am in CFM Run 13-05. Includes the modelled colloid breakthrough for comparison, dotted black line. ....	173
Figure 6.7 Comparison of cumulative recovery for observed and modelled data for <sup>243</sup> Am in CFM Run 13-05 .....	174
Figure 6.8 Calibrated breakthrough curve for <sup>241</sup> Am in CRR Run 32. Includes the modelled colloid breakthrough for comparison, dotted black line. ....	175
Figure 6.9 Comparison of cumulative recovery for observed and modelled data for <sup>241</sup> Am in CRR Run 32. Note that the modelled data was compared to the ICP-MS data, but the observed recovery used the $\alpha$ -spectroscopy data, analysed in a pair with <sup>238</sup> Pu due to issues calculating recovery with ICP-MS. ....	175
Figure 6.10 Breakthrough of aqueous and colloid bound americium in CFM Run 13-05 and CRR Run 32 (Solid = total; Dotted = aqueous phase; Dashed = colloid bound).....	179
Figure 6.11 Speciation of plutonium in the CFM Run 13-05 injection cocktail as predicted by PHREEQC. Blue line = Grimsel groundwater pH (pH 9.6).....	181
Figure 6.12 Speciation of plutonium in the CRR Run 32 injection cocktail as predicted by PHREEQC. Blue line = Grimsel groundwater pH (pH 9.6) .....	182
Figure 6.13 Predicted saturation indexes of plutonium precipitates in the injection cocktail of CFM Run 13-05 from PHREEQC. Blue line = pH 9.6 of reference Grimsel groundwater.....	182
Figure 6.14 Predicted saturation indexes of plutonium precipitates in the injection cocktail of CRR Run 32 from PHREEQC. Blue line = pH 9.6 of reference Grimsel groundwater. ....	183
Figure 6.15 Calibrated breakthrough curves for plutonium in CFM Run 13-05 and CRR Run 32 .....	187
Figure 6.16 Calibrated breakthrough curve for <sup>242</sup> Pu in CFM Run 13-05. Includes the modelled colloid breakthrough for comparison, dotted black line. ....	189
Figure 6.17 Comparison of cumulative recovery between observed and modelled data for <sup>242</sup> Pu in CFM Run 13-05.....	189
Figure 6.18 Calibrated breakthrough curve for <sup>244</sup> Pu in CRR Run 32. Includes the modelled colloid breakthrough for comparison, dotted black line. ....	190

Figure 6.19 Comparison of cumulative recovery between observed and modelled data for <sup>244</sup> Pu (measured by ICP-MS) in CRR Run 32 .....	191
Figure 6.20 Contribution of aqueous and colloid bound plutonium in CFM Run 13-05 and CRR Run 32 (Solid = total concentration; Dotted = aqueous phase; Dashed = colloid bound) .....	194
Figure 7.1 Predicted caesium speciation in CFM Run 13-05 from PHREEQC. Red line = Grimsel groundwater average pH (9.6) .....	200
Figure 7.2 Predicted caesium speciation in CRR Run 32 from PHREEQC. Red line = Grimsel groundwater average pH (9.6) .....	201
Figure 7.3 Caesium sorption isotherm to FEBEX bentonite colloids in Grimsel groundwater, contact time two weeks. $C_{s_{ads}}$ represents sorbed concentration of Cs, $C_{s_{fin}}$ represents final aqueous Cs concentration (From: Missana and Geckeis, 2006).....	202
Figure 7.4 Conceptual diagram for the two sorption sites on FEBEX bentonite clay colloids (not to scale). .....	203
Figure 7.5 Caesium $K_d$ values to FEBEX bentonite colloids with varying Cs concentration. Blue = CFM Run 13-05 Cs concentration ( $8.8 \times 10^{-10}$ mol/l), Green = CRR Run 32 Cs Concentration ( $1.38 \times 10^{-8}$ mol/l). Altered from Missana et al. (2004) .....	204
Figure 7.6 Calibrated breakthrough curve for one-site caesium model in CFM Run 13-05 and CRR Run 32. The dotted red line represents a modelled breakthrough for Cs in CRR Run 32 which used the parameters obtained from the CFM Run 13-05 one-site calibrated model. ....	210
Figure 7.7 Calibrated breakthrough curve for two-site caesium model for CFM Run 13-05 and CRR Run 32 .....	212
Figure 7.8 Calibrated breakthrough curve for two-site caesium model in CFM Run 13-05 .....	213
Figure 7.9 Comparison of cumulative recovery for observed and modelled data for <sup>137</sup> Cs in CFM Run 13-05 (two site model) .....	213
Figure 7.10 Calibrated breakthrough curve for two-site caesium model for CRR Run 32.....	214
Figure 7.11 Comparison of cumulative recovery for observed and modelled data for <sup>137</sup> Cs in CRR Run 32 (two-site model) .....	215
Figure 7.12 Contribution of different caesium phases to modelled breakthrough curves. (Solid = total concentration, dotted = aqueous caesium, dashed = colloid Site 1, dash/dot = colloid Site 2, red lines represents CRR Run 32 components, blue lines represent CFM Run 13-05).....	217
Figure 7.13 Calculated caesium $K_d$ values to colloids (blue line) with changes in caesium concentration using sorption rates in Table 7.5, compared to results from Missana et al. (2004) .....	218
Figure 7.14 Results of one-site FFM model for CFM Run 13-05. Dashed and dotted lines are model results with two sorption sites on colloid and one sorption site on FFM.....	222
Figure 7.15 Results of one-site FFM model for CRR Run 32. Dashed and dotted lines are model results with two sorption sites on colloid and one sorption site on FFM.....	223
Figure 7.16 Predicted uranium speciation in CFM Run 13-05 from PHREEQC. Blue line = Grimsel groundwater pH (9.6). This modelling assumes an $E_h(SHE) = -220mV$ .....	226
Figure 7.17 Predicted uranium speciation in CRR Run 32 from PHREEQC. Blue line = Grimsel groundwater pH (9.6). This modelling assumes an $E_h(SHE) = -220mV$ .....	226
Figure 7.18 Predicted saturation indexes in CFM Run 13-05 for uranium precipitates. Blue line = Grimsel groundwater pH (9.6). This modelling assumes an $E_h(SHE) = -220mV$ .....	227

Figure 7.19 Predicted saturation indexes in CRR Run 32 for uranium precipitates. Blue line = Grimsel groundwater pH (9.6). This modelling assumes an $E_h(SHE) = -220mV$ .....	227
Figure 7.20 Calibrated model results for uranium breakthrough in CFM Run 13-05 and CRR Run 32234	
Figure 7.21 Calibrated model breakthrough for uranium-233 in CFM Run 13-05 (Blue line = CFM Run 13-05 model; Green line = Model run using CRR Run 32 parameter values) .....	236
Figure 7.22 Comparison of cumulative recovery for observed and modelled data for $^{233}U$ in CFM Run 13-05 .....	236
Figure 7.23 Calibrated model breakthrough for uranium-233 in CRR Run 32. Green line = CFM Run 13-05 model parameter values. ....	238
Figure 7.24 Comparison of cumulative recovery for observed and modelled data for $^{233}U$ in CRR Run 32.....	238
Figure 7.25 Contribution of different uranium phases to modelled breakthrough curves in CFM Run 13-05 and CRR Run 32. Total = Solid line; Colloid-bound = Dashed line; Aqueous = Dotted line.....	239
Figure 7.26 Predicted neptunium speciation in CFM Run 13-05 from PHREEQC. Blue line = Grimsel groundwater pH (9.6).....	243
Figure 7.27 Predicted neptunium speciation in CRR Run 32 from PHREEQC. Blue line = Grimsel groundwater pH (9.6).....	244
Figure 7.28 Predicted saturation indexes in CFM Run 13-05 for neptunium precipitates. Blue line = Grimsel groundwater pH (9.6) .....	244
Figure 7.29 Predicted saturation indexes in CRR Run 32 for neptunium precipitates. Blue line = Grimsel groundwater pH (9.6) .....	245
Figure 7.30 Calibrated model results for neptunium transport in CFM Run 13-05 and CRR Run 32 .	252
Figure 7.31 Calibrated model breakthrough for neptunium-237 in CFM Run 13-05. Blue line = CFM model, Green line = CRR model parameter values. ....	253
Figure 7.32 Comparison of cumulative recovery for observed and modelled data for $^{237}Np$ in CFM Run 13-05 .....	253
Figure 7.33 Calibrated model breakthrough for neptunium-237 in CRR Run 32. Green line = model run with CFM Run 13-05 parameter values.....	254
Figure 7.34 Comparison of cumulative recovery for observed and modelled data for $^{237}Np$ in CRR Run 32.....	255
Figure 7.35 Contribution of different neptunium phases to modelled breakthroughs (Dashed = colloid bound; Dotted = aqueous) .....	256
Figure 8.1 Calibrated model results for breakthrough of conservative tracer and bentonite colloids in CFM Run 13-05 and CRR Run 32. ....	270
Figure 8.2 Calibrated model results for breakthrough of americium and plutonium in CFM Run 13-05 and CRR Run 32. ....	270
Figure 8.3 Calibrated model results for breakthrough of caesium (two-site model), uranium and neptunium in CFM Run 13-05 and CRR Run 32.....	271
Figure C.1 Pictures from visual fluorescein migration test. Images taken at (from left to right): Top - 1, 5 and 10 minutes; Middle - 15, 20 and 25 minutes; Bottom - 30, 32 and 50 minutes .....	310
Figure C.2 Zones of lower permeability (highlighted in blue).....	311
Figure C.3 Colour Plots of Concentration ( $kg/m^3$ ), with experimental results to the right. Images taken at 15 and 20 minutes after tracer injection .....	311

Figure C.4 Calibrated Breakthrough for Experiment B (blue line), with conservative breakthrough (yellow line).....	314
Figure D.1 Colloid recovery plot with no irreversible colloid attachment.....	319
Figure D.2 Colloid recovery plot with an irreversible attachment rate $k_{iat} = 1 \times 10^{-7}$ 1/s .....	319
Figure D.3 Colloid recovery plot with an irreversible attachment rate $k_{iat} = 1 \times 10^{-6}$ 1/s .....	320
Figure D.4 Colloid recovery plot with an irreversible attachment rate $k_{iat} = 3 \times 10^{-6}$ 1/s .....	320
Figure D.5 Colloid recovery with an irreversible attachment rate $k_{iat} = 5 \times 10^{-6}$ 1/s. Red points indicate areas where parameters gave good match to CRR 32 breakthrough.....	321
Figure D.6 Colloid recovery with an irreversible attachment rate $k_{iat} = 6 \times 10^{-6}$ 1/s. Red points indicate areas where parameters gave good match to CRR 32 breakthrough.....	321

## List of Tables

Table 1.1 Summary of the migration experiments investigating bentonite colloids and radionuclide migration carried out at the Grimsel Test Site.....	10
Table 2.1 Summary of different laboratory investigations of radionuclide sorption to bentonite derived colloids, full details found in Chapters 6 and 7.....	29
Table 3.1 Composition of Grimsel groundwater, as used in Bennett (2014).....	47
Table 3.2 Summary of background and hydraulic parameters for radionuclide-colloid field migration experiments. ....	53
Table 3.3 Concentrations in the injection cocktails used in the two migration experiments. ....	54
Table 3.4 Analytical methods used to measure concentration of species in abstraction borehole (unless indicated) in CFM Run 13-05 and CRR Run 32. ....	59
Table 3.4 Summary of model assumptions and processes in the CRR models. Information from Smith et al. (2006). ....	61
Table 3.5 Summary of model assumptions and processes in documented models used in the CFM project. Information from Noseck et al. (2016), Reiche et al. (2015), Pudewills (2008), and Huber et al. (2014). ....	62
Table 3.6 Final value of calibration parameters used in inverse model .....	76
Table 3.7 Inverse modelling transport metrics results .....	77
Table 4.1 Parameters used in 1D COMSOL model to verify advection-dispersion, retardation and radioactive decay processes .....	94
Table 4.2 Parameters used in 1D COMSOL model to verify colloid transport and attachment equations.....	97
Table 4.3 Parameters used in 2D COMSOL model for modelling experiments carried out by Walkden (2014). Parameters in italics are calibration parameters.....	98
Table 4.4 Parameters used in initial verification testing of radionuclide sorption and desorption ...	101
Table 5.1 Transport model non-calibration parameters.....	118
Table 5.2 Transport model boundary conditions.....	120
Table 5.3 Mass and concentration of conservative tracers used in CFM Run 13-05 and CRR Run 32	121
Table 5.4 Calibrated parameters from Conservative tracer breakthrough .....	121
Table 5.5 Mass and concentration of Bentonite colloids used in CFM Run 13-05 and CRR Run 32...	131
Table 5.6 Calibrated parameters from bentonite colloid breakthrough .....	132
Table 5.7 Parameters derived from analytical model calibration for conservative tracer breakthrough .....	144
Table 5.8 Parameters used in COMSOL 1D model of colloid breakthrough .....	144
Table 5.9 Stress period setup for REMO-2 MODFLOW model. Pinkel flow = -25ml/min throughout experiment.....	151
Table 5.10 Recovery of bentonite colloids as calculated after 100 hours. ....	154
Table 6.1 Mass and concentration of americium isotopes used in CFM Run 13-05 and CRR Run 32	162
Table 6.2 Concentration of elements used in PHREEQC calculations, Grimsel groundwater concentrations taken from Bennett (2014) .....	164
Table 6.3 Non-calibration parameters for americium model .....	170
Table 6.4 Calibration parameters resulting from model calibration to americium transport.....	172

Table 6.5 Mass and concentration of plutonium isotopes in CFM Run 13-05 and CRR Run 32 .....	180
Table 6.6 Non-calibration parameters for plutonium model.....	186
Table 6.7 Calibration parameters resulting from model calibration to plutonium transport .....	187
Table 7.1 Mass and concentration of caesium used in CFM Run 13-05 and CRR Run 32.....	199
Table 7.2 Non-calibration parameters for one-site caesium model.....	206
Table 7.3 Calibration parameters for two-site caesium model, with methodology of setting initial parameter values .....	209
Table 7.4 Calibrated parameter values for one-site caesium model.....	210
Table 7.5 Calibrated parameter values for two-site caesium model.....	211
Table 7.6 Concentrations and percentages of caesium sorbed to different sites on colloids.....	217
Table 7.7 Mass and concentration of uranium used in CFM Run 13-05 and CRR Run 32 .....	224
Table 7.8 Non-calibration parameters for uranium model.....	233
Table 7.9 Calibrated parameter values for uranium model.....	234
Table 7.10 Mass and concentration of neptunium used in CFM Run 13-05 and CRR Run 32 .....	242
Table 7.11 Non-calibration parameters for neptunium model.....	251
Table 7.12 Calibrated parameter values for neptunium model.....	251
Table 8.1 Experimental recovery values for the different species modelled in both experiments. Values in brackets represent modelled recovery values. ....	269
Table 8.2 Summary of the calibrated parameter values for conservative tracer breakthrough in both experiments. Red = sensitive parameter. ....	272
Table 8.3 Summary of the calibrated parameter values for bentonite colloid breakthrough in both experiments. Red = sensitive parameter. ....	272
Table 8.4 Summary of the calibrated parameter values for radionuclide breakthrough in both experiments. Red = sensitive parameter. *Indicates parameters for the second sorption site on either the colloid or FFM as used in the caesium model (see Chapter 7). In addition, the capacity of the individual sites on the colloids are not shown for Cs model.....	273

## List of Equations

Equation 3.1 Cubic law derived fracture aperture.....	69
Equation 3.2 The geometric mean of transmissivity.....	69
Equation 3.3 The arithmetic mean of transmissivity .....	69
Equation 3.4 The harmonic mean of transmissivity.....	69
Equation 3.5 Effective fracture aperture .....	70
Equation 3.6 Porosity scaling factor.....	70
Equation 3.7 Specific storage from fracture aperture .....	70
Equation 4.1 Groundwater flow.....	89
Equation 4.2 Average linear velocity.....	89
Equation 4.3 Colloid transport .....	90
Equation 4.4 Reversible colloid attachment .....	90
Equation 4.5 Irreversible colloid attachment.....	90
Equation 4.6 Aqueous phase radionuclide transport with one site sorption to colloids and equilibrium sorption to rock surfaces.....	91
Equation 4.7 Radionuclides sorbed to mobile colloids .....	92
Equation 4.8 Radionuclides sorbed to reversibly attached colloids .....	92
Equation 4.9 Radionuclides sorbed to irreversibly attached colloids.....	92
Equation 4.10 Radionuclide matrix diffusion .....	93
Equation 4.11 Radionuclide kinetic sorption to rock surfaces.....	93
Equation 4.12 Dilution Factor used to set CFM Run 13-05 boundary conditions.....	108
Equation 4.13 Exponential source term factor .....	108
Equation 4.14 Equation to load transmissivity field into COMSOL model.....	110
Equation 5.1 Fracture aperture calculation .....	129
Equation 7.1 Transport of colloid-bound caesium sorbed to the second edge site.....	206
Equation 7.2 Second radionuclide sorption site on FFM .....	207

## List of Abbreviations

AGA	Amino-G Acid
AMS	Accelerator Mass Spectroscopy
BELBaR	Bentonite erosion: effects on the long term performance of the engineered barrier and radionuclide transport project
CFM	Colloid Formation and Migration project
CFRT	Colloid-facilitated radionuclide transport
CRR	Colloid and Radionuclide Retardation project
EC	European Commission
EP	Excavation Project
FFM	Fracture Fill Material
FZK-INE	Forschungszentrum Karlsruhe (predecessor to KIT-INE), Germany
GDF	Geological Disposal Facility
GGW	Grimsel Groundwater
GRS	Gesellschaft für Anlagen- und Reaktorsicherheit gGmbH, Germany
GTS	Grimsel Test Site
IAEA	International Atomic Energy Authority
ICP-MS	Inductively coupled plasma mass spectroscopy
JNC	Japan Nuclear Cycle Development Institute, Japan
KAERI	Korea Atomic Energy Research Institute, Korea
KIT-INE	Karlsruhe Institute of Technology – Institute for Nuclear Waste Disposal, Germany
KTH	Royal Institute of Technology, Sweden
LANL	Los Alamos National Laboratory, USA
LIBD	Laser Induced Breakdown Detection
LIT	Long term in-situ Experiment

MI	Migration Experiment
NAGRA	National Co-operative for the Disposal of Radioactive Waste, Switzerland
NUMO	Nuclear Waste Management Organisation of Japan, Japan.
PCS	Photon Correlation Spectroscopy
PSI	Paul Scherrer Institute, Switzerland
REMO	Colloid remobilisation Experiment
RWM	Radioactive Waste Management Ltd., UK
SHE	Standard hydrogen electrode
SKB	Svensk Kärnbränslehantering Aktiebolag, Sweden
SPC	Single Particle Counting
TBM	Tunnel Boring Machine
TDB	Thermodynamic database
WCF	Water Conducting Feature
WMO	Waste Management Organisation
URL	Underground Research Laboratory

# 1. INTRODUCTION

## 1.1. Background

This thesis details the development of new numerical models that describe the transport of conservative tracers, bentonite colloids and radionuclides. This model is applied to model two *in situ* field migration experiments that have been carried out at the Grimsel Test Site during the Colloid Formation and Migration (CFM) project, with the aim of providing greater understanding of colloid, radionuclide and colloid-facilitated radionuclide transport to provide insight into relevant radionuclide transport processes for an environmental safety case for the deep geological disposal of radioactive waste.

## 1.2. Geological Disposal of Radioactive Wastes

A range of radioactive wastes has been generated by a variety of activities in the nuclear industry, including power generation, medicine, research and defence (Nuclear Decommissioning Authority, 2015). In the UK, radioactive waste is classified into four categories by the level of heat and radioactivity generation (Department of Business Energy and Industrial Strategy and Nuclear Decommissioning Authority, 2017).

Higher activity wastes are wastes that contain a high level of radioactivity that cannot be disposed of in current surface facilities, and potentially generate significant heat (Department of Energy and Climate Change, 2014). Internationally, it is widely considered that the best method for disposing of higher activity radioactive wastes is through deep geological disposal (Department of Energy and Climate Change, 2014). This involves placing the waste in a specially engineered Geological Disposal Facility (GDF) at a depth between 200 and 1000 metres (Nuclear Decommissioning Authority, 2010a). Waste will be contained in

a GDF by multiple barriers, which work together to ensure that the waste is prevented from harming the environment or humans over hundreds of thousands of years. A schematic of a geological disposal facility is shown in Figure 1.1.

A number of different disposal concepts exist for the construction of a geological disposal facility, which depend on the geology and waste to be disposed (Alexander et al., 2011). Examples of two disposal concepts are shown in Figure 1.2, which also shows the different engineered barriers for a GDF, such as the form of the waste, its packaging and buffer material (Department of Energy and Climate Change, 2014). One such concept is the KBS-3 concept that has been designed by Posiva in Finland and SKB in Sweden to dispose high level waste in fractured hard rock (Nuclear Decommissioning Authority, 2014).

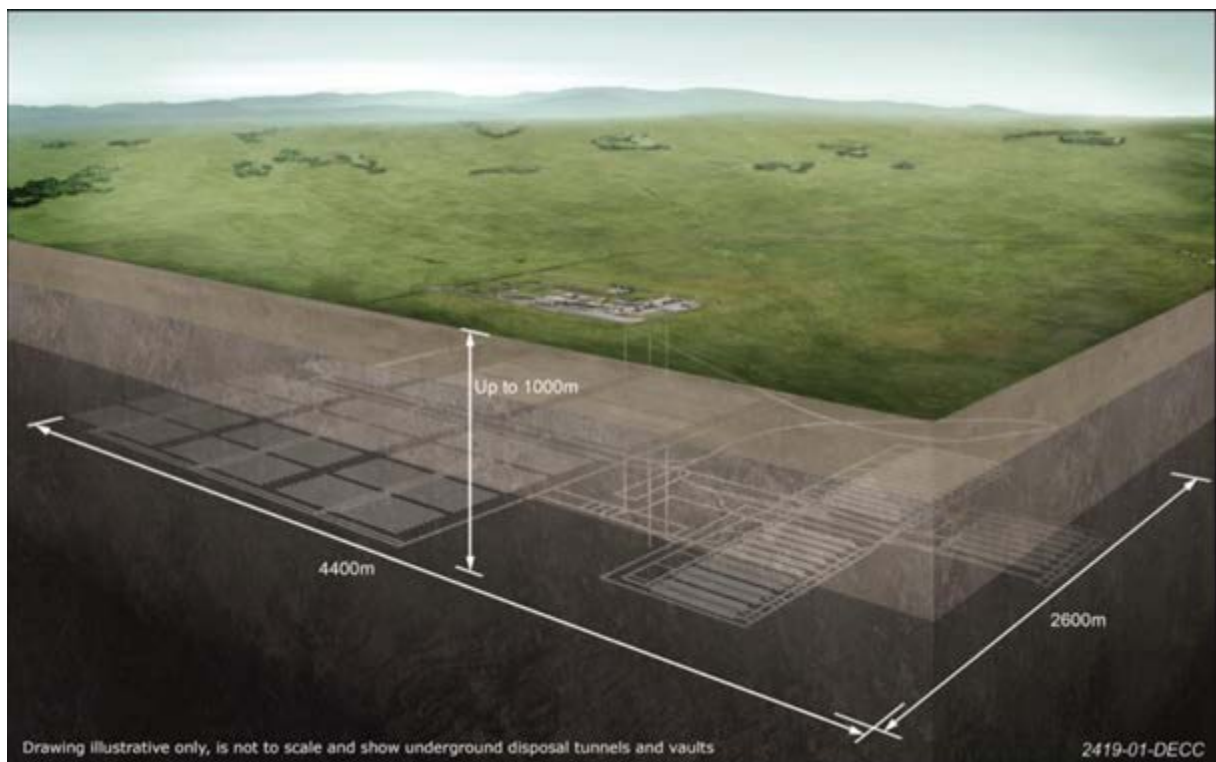


Figure 1.1 Artist's impression of a geological disposal facility (Department of Energy and Climate Change, 2014)

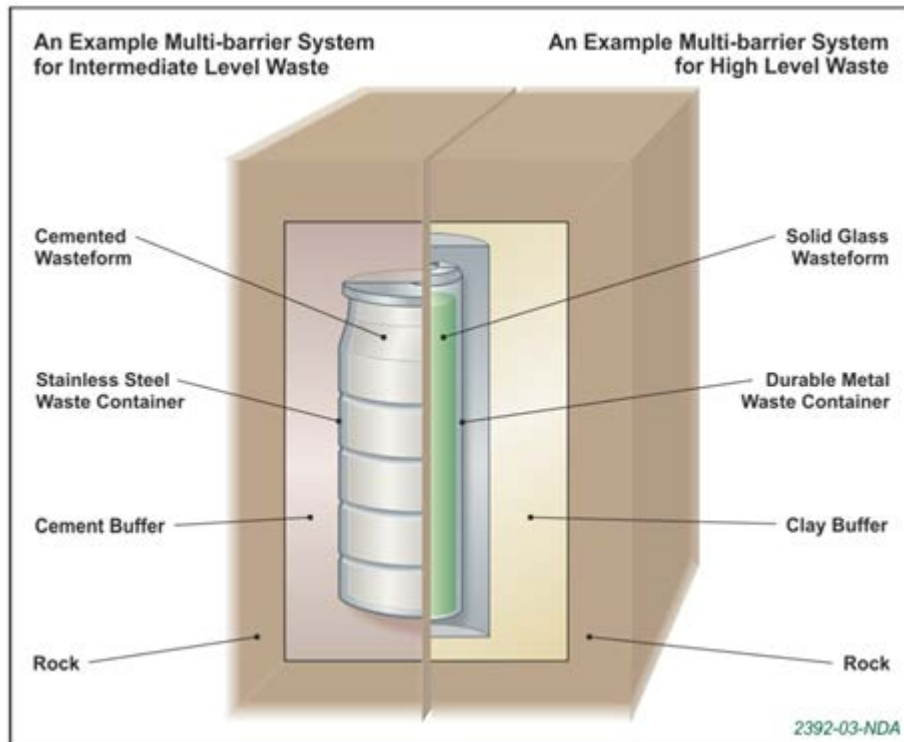


Figure 1.2 Examples of the multiple engineered barriers for a geological disposal facility (Department of Energy and Climate Change, 2014)

One geological setting that could host a GDF is higher strength rocks (Department of Energy and Climate Change, 2014), where groundwater flow is typically through fractures as these rocks have a low matrix porosity and permeability (Radioactive Waste Management Ltd., 2016c). Lower strength sedimentary rocks and evaporitic rocks are other geologies that can host a GDF (Department of Energy and Climate Change, 2014).

Three main pathways could form for the migration of radionuclides from a GDF post-closure (Radioactive Waste Management Ltd., 2016c): transport with and through groundwater; gas migration; and human intrusion. The safety of a GDF is demonstrated by a safety case, which covers the different phases of operation (e.g. construction, operation and post closure), assessing the performance of the different barriers over time (Radioactive Waste Management Ltd., 2016c). In the UK, a generic safety case has been maintained that

details the current science and engineering that supports the safety of a geological disposal facility (Radioactive Waste Management Ltd., 2016a).

As the radioactive waste management organisation (WMO) for the UK, Radioactive Waste Management Limited (RWM Ltd.) maintains a programme of research into knowledge gaps identified in its generic safety case (Radioactive Waste Management Ltd., 2016b). This includes topics such as engineered barrier evolution and radionuclide behaviour, and specific processes such as colloid-facilitated radionuclide transport (Nuclear Decommissioning Authority, 2010b; Radioactive Waste Management Ltd., 2016b).

### **1.3. Colloid-Facilitated Radionuclide Transport**

In higher strength rocks, radionuclides could migrate from a GDF by being transported through fractures by groundwater (Alexander et al., 2011). Radionuclide transport in these fractures can be retarded by processes including sorption to the rock, diffusion into adjacent rock matrix and precipitation (Alexander et al., 2011).

Colloids are usually defined as particles that are between 1 and 1000 nm in size, suspended in another substance (Schäfer et al., 2012; Slomkowski et al., 2011). There is potential for colloids to enhance the migration of radionuclides in groundwater away from a GDF (Alexander et al., 2011), as mobile colloids can provide an additional sorption surface for a radionuclide (Nuclear Decommissioning Authority, 2010b). Colloids have a high surface area per their unit mass, and can have a higher charge due to the presence of a diffuse cloud of ions surrounding the colloid (referred to as a double layer) (Ryan and Elimelech, 1996). This double layer controls the interaction of the colloid with ions, other colloids and rock surfaces (Albarran et al., 2011; Ryan and Elimelech, 1996).

If a radionuclide sorbs to a colloid, the radionuclide could undergo different migration processes. For instance, several radionuclides (e.g. thorium, plutonium) are expected to strongly sorb to rock surfaces. However, if these radionuclides sorb to mobile colloids instead they could be transported for greater distances than would be expected if this colloid phase was not considered (Ryan and Elimelech, 1996; Schäfer et al., 2012), effectively reducing the ability of the geology or engineered barriers to retard radionuclide migration from a GDF (Alexander et al., 2011). This process is referred to as colloid-facilitated radionuclide transport (CFRT), although colloids can also facilitate the transport of other species, such as heavy metals (Ryan and Elimelech, 1996). Figure 1.3 details some of the processes involved with colloid-facilitated radionuclide transport in groundwater flowing through a fracture. Colloids can be transported through groundwater (Process 1, Figure 1.3); undergoing attachment to rock surfaces (2), and interacting with other colloids through aggregation (9). Radionuclides can also be transported through groundwater (3), their transport retarded through sorption to rock surfaces (4) and diffusion into the adjacent rock matrix (5). Radionuclides can sorb and be transported by mobile colloids (6), but these colloids can become immobile (7), and radionuclides can desorb from immobile colloids (8). These processes are discussed in more detail in Chapter 2.

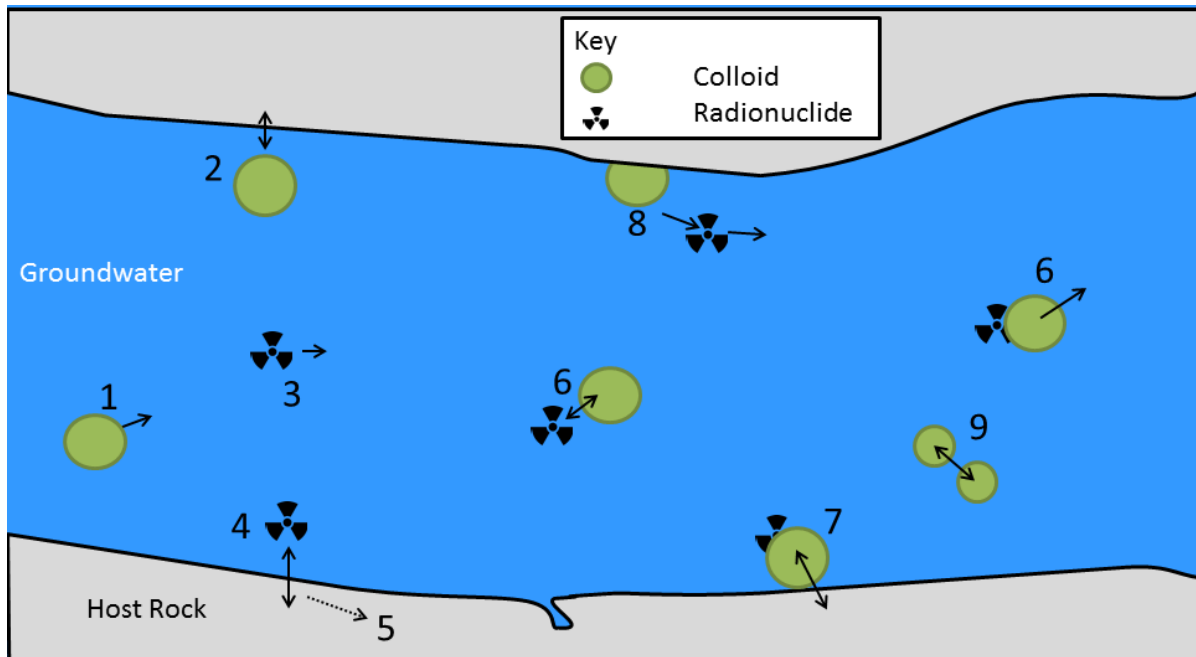


Figure 1.3 Diagram of different processes involved in colloid-facilitated radionuclide transport within a fracture. Processes: colloid transport (1); colloid attachment (2); radionuclide (RN) transport (3); RN sorption to rock surfaces (4); RN matrix diffusion (5); RN sorption to mobile colloids (6); attachment of colloids with RN sorbed (7); desorption of RN from colloid (8); colloid aggregation (9). Processes not shown include colloid sedimentation and straining.

Colloids are found naturally in groundwater (Degueldre et al., 1989), and can form from both organic and inorganic materials. There are many different sources of colloids in a GDF setting (Alexander et al., 2011), but the existing classification used for colloids in a GDF do not consider whether the colloids formed from solid or dissolved phases, and are sometimes poorly defined. Therefore, colloids in a GDF setting can be grouped broadly into the following two groups:

- Self-colloids, which are formed from radionuclides, their oxides and hydroxides. These are also referred to in the wider literature as true colloids (Malkovsky and Pek, 2009) or eigencolloids (Schäfer et al., 2012).
- Carrier colloids, which have formed from non-radioactive materials (e.g. clays). These are also referred to as pseudocolloids in the wider literature (Malkovsky and Pek, 2009; Alexander et al., 2011). Carrier colloids include bacteria, viruses (Ryan and

Elimelech, 1996), humic acids (Alexander et al., 2011), parts of host rocks, other secondary minerals (e.g. iron oxides), and materials from the degradation of the engineered barriers (Alexander et al., 2011). Carrier colloids also encompass pre-existing or indigenous colloids that were present before GDF construction.

These two definitions can be further subdivided based on whether the colloids are formed from the solid or dissolved phase, making either a suspension or an emulsion. Colloidal suspensions contain solid colloidal material contained within a liquid, whereas colloidal emulsions contain dissolved colloidal material within another liquid (Slomkowski et al., 2011).

Bentonite is a clay that can form by ash alteration, comprising mostly of montmorillonite (a smectite group mineral), with some additional accessory minerals (e.g. quartz, sulphides and organic carbon) (Nuclear Decommissioning Authority, 2014). Bentonite clay has a low permeability and porosity, high cation exchange capacity, and swells under contact with water (Nuclear Decommissioning Authority, 2014), which act together to reduce the advective flow of water, keeping the canister in position and limiting the rate of microbial activity and radionuclide transport, making it a suitable material for a buffer or backfill in a GDF in a fractured hard rock (Albarran et al., 2014; Nuclear Decommissioning Authority, 2014). However, it has been shown that bentonite can form colloids by the erosion of a gel that forms on the surface of hydrated bentonite (Missana et al., 2003).

The bentonite potentially represents a significant source of colloids in a GDF, which could lead to transport of safety-case relevant radionuclides. Because of this, there is an interest in developing understanding of colloid formation and colloid-facilitated radionuclide transport

caused by bentonite colloids. These processes have been investigated in experiments at the Grimsel Test Site (Alexander et al., 2011; Möri et al., 2004; Schlickenrieder et al., 2017), as detailed in the next section, and in Chapter 3.

Limited examples of quantified colloid-facilitated radionuclide transport exist from the field. At the Nevada Test Site, USA, plutonium was observed to migrate at greater distances (1.3km) from a nuclear test bunker than would otherwise be expected (Kersting et al., 1999). The exact cause of the migration has not been confirmed, as both the formation of plutonium self-colloids, or sorption of plutonium to carrier colloids could have facilitated its transport. At the same site, colloid-facilitated transport of cobalt, caesium and europium has also been observed, and is caused by carrier colloids forming from clays and zeolites facilitating transport (Kersting et al., 1999).

Other examples of field colloid-facilitated radionuclide transport exist in the United States at other national laboratory sites. For instance, the colloid-facilitated transport of americium and plutonium lead to waste from the Los Alamos National Laboratory migrating through a shallow alluvium aquifer up to 3km from the waste source (Penrose et al., 1990). Organic colloids are believed to be the cause of americium and curium migration from waste trenches from the Oak Ridge National Laboratory (McCarthy, 1998).

Another example of potential field colloid-facilitated radionuclide transport is the migration of plutonium in Mayak, Russia, which was caused by the formation of iron oxide and iron hydroxide carrier colloids, which facilitated the transport of plutonium, as well as the transport of uranium carbonates (Novikov et al., 2006).

## **1.4. The Grimsel Test Site, and the Colloid Formation and Migration Project (CFM)**

This section gives a brief introduction to the Grimsel Test Site and the Colloid Formation and Migration (CFM) project. More information on these is found in Chapter 3.

The Grimsel Test Site (GTS) is located in the Bernese Alps in Switzerland. Situated within the Grimsel granodiorite host rock at a depth of approximately 400 to 450m below ground, it has been operated by Nagra (the Swiss National Cooperative for the disposal of radioactive waste) since 1984 as a generic underground research laboratory (URL) (Delay et al., 2014; Blechschmidt and Vomvoris, 2009). Experiments investigating the performance of geological and engineered barriers in a realistic geological environment have been running since the 1980's (Delay et al., 2014). Uniquely, Grimsel contains an IAEA level B/C radiation controlled zone, allowing the use of radioactive tracers in *in situ* field experiments (Delay et al., 2014). One such experiment is the Colloid Formation and Migration (or CFM) project, which has been run as an international collaboration since 2004 (Schlickenrieder et al., 2017).

The CFM project builds on earlier experiments investigating radionuclide transport at the Grimsel Test Site, particularly the earlier Colloid and Radionuclide Retardation (CRR) experiment, which was carried out at the same location within the site (Schlickenrieder et al., 2017). The CFM project was set up to study the generation of bentonite colloids and the colloid facilitated radionuclide transport caused by these bentonite colloids under repository relevant flow conditions (Schlickenrieder et al., 2017).

Both CFM and CRR projects investigated radionuclide migration in the presence of bentonite colloids, carrying out migration experiments at the site, between different

boreholes that intersect the same series of fractures, referred to as the Migration Experiment or MI shear zone, up to a distance of 6 metres apart. During the CFM project, a mega-packer system was installed in the MI shear zone, allowing for greater control over hydraulic gradients and groundwater flow (Schlickerieder et al., 2017), allowing migration experiments to be carried out in low flow conditions. To date, three migration experiments have been carried out containing both bentonite colloids and radionuclides, summarised in Table 1.1.

<i>Experiment</i>	<b>CRR Run 32</b>	<b>CFM Run 12-02</b>	<b>CFM Run 13-05</b>
<i>Distance</i>	2.3 m	5.71 m	2.3 m
<i>Peak Arrival</i>	~1.5 hours	50 hours	44 hours
<i>Injected</i>	<sup>131</sup> I, Radionuclides and Colloids	Amino-G Acid, Radionuclides and Colloids	Amino-G Acid, Radionuclides and Colloids

**Table 1.1 Summary of the migration experiments investigating bentonite colloids and radionuclide migration carried out at the Grimsel Test Site**

The field experiments have been supported by a programme of laboratory experiments and modelling has been carried out to further investigate colloid generation and colloid-facilitated radionuclide transport. This thesis forms part of the supporting modelling work, aiming to improve understanding of these field migration experiments.

Although other models and modelling teams have modelled the migration experiments (see Chapter 3), these models largely consist of 1D or homogeneous 2D representations of the MI shear zone (where the experiments take place). The result of these models was that although good model matches were found, some per-experiment model calibrations were used, where model parameters were changed to model the same species in different

experiments. The need to change model parameters between experiments reduces the predictive ability of the models and confidence in the description used to describe chemical or physical processes occurring during the experiments. By including a more detailed representation of the shear zone structure and the flow geometry in models of colloid-facilitated radionuclide transport, the work in this thesis aims to develop a self-consistent understanding of different migration experiments thereby improving understanding of colloid-facilitated radionuclide transport in fractured hard rocks.

### **1.5. Aim and Objectives**

The aim of this research is to improve understanding of colloid-facilitated radionuclide transport in fractured hard rocks by making self-consistent interpretations of the migration experiments that have been carried out at the Grimsel Test Site. The following objectives were used to attempt to achieve the project's aim:

- to develop a 2D model of groundwater flow and conservative tracer transport for the MI shear zone at the Grimsel Test Site that includes more information on the geology of the shear zone and the various flow paths than previous modelling attempts;
- to build on the above and develop a model for colloid-facilitated radionuclide transport, to include processes such as colloid transport and attachment; radionuclide transport, sorption to mobile colloids and matrix diffusion;
- to validate and verify the transport model by applying it to two field experiments carried out in CRR Dipole 1 (CFM Run 13-05 and CRR Run 32), with the aim of including the same processes and finding consistent parameters between the

experiments that describe the transport of conservative tracers, bentonite colloids and radionuclides in the two experiments, to develop a self-consistent understanding of the experiments;

- to identify from the results of the modelling, important transport processes behind colloid-facilitated radionuclide transport in the geological and hydrogeological setting of the Grimsel Test Site.

The tools and methods developed in this project could then be applied to other experiments and geological settings, including for a potential GDF site in the UK.

## **1.6. Thesis Structure**

This chapter (Chapter 1) contains an introduction and overview of the issues behind geological disposal of radioactive wastes and colloid-facilitated radionuclide transport.

Chapter 2 provides a short literature review of some of the important transport processes behind colloid-facilitated radionuclide transport, and some of the previous models developed to describe it.

Chapter 3 details the geological and hydrogeological setting of the Grimsel Test Site, the experimental protocols used in the CRR and CFM migration experiments and previous models of the Grimsel migration experiments.

Chapter 4 describes the development of the transport model for colloid-facilitated radionuclide transport.

Chapter 5 details the results of the transport model calibration for conservative tracer and bentonite colloid breakthrough in CFM Run 13-05 and CRR Run 32. This chapter also

details a 'channel' model which was used to attempt to model the experiments using a homogenous 1D representation of the shear zone, and some blind predictions made of colloid transport in an additional colloid transport experiment carried out at the test site during the CFM project.

Chapter 6 details the results of the model calibration for the breakthrough of americium and plutonium in CFM Run 13-05 and CRR Run 32.

Chapter 7 details the results of the model calibration for caesium, uranium and neptunium breakthrough in the same experiments.

Finally, Chapter 8 details the conclusions of the project, the implications for colloid-facilitated radionuclide transport that can be drawn from modelling the two migration experiments and identifies areas for future work.

## 1.7. List of References

Albarran, N., Degueudre, C., Missana, T., Alonso, Ú., García-Gutiérrez, M. and López, T. (2014) Size distribution analysis of colloid generated from compacted bentonite in low ionic strength aqueous solutions. **Applied Clay Science**, 95: 284–293 DOI: 10.1016/j.clay.2014.04.025

Albarran, N., Missana, T., García-Gutiérrez, M., Alonso, Ú. and Mingarro, M. (2011) Strontium migration in a crystalline medium: Effects of the presence of bentonite colloids. **Journal of Contaminant Hydrology**, 122 (1–4): 76–85 DOI: 10.1016/j.jconhyd.2010.11.005

Alexander, W.R., Berry, J.A., Kelly, M.J. and Swanton, S.W. (2011) **Review of colloids in the geosphere and their treatment in performance assessments. NDA-RWMD report NPO003512.** Harwell: Nuclear Decommissioning Authority

Blechs Schmidt, I. and Vomvoris, S. (2009) **25 Years of Underground Research: Grimsel Test Site.** Wettingen, Switzerland: Nagra

Degueudre, C., Baeyens, B., Goerlich, W., Riga, J., Verbist, J. and Stadelmann, P. (1989) Colloids in water from a subsurface fracture in granitic rock, Grimsel Test Site, Switzerland. **Geochimica Et Cosmochimica Acta**, 53: 603–610

Delay, J., Bossart, P., Ling, L.I.X., Blechs Schmidt, I., Vinsot, A., Nussbaum, C., Maes, N. and Ohlsson, M. (2014) Three decades of underground research laboratories: what have we learned? Norris, S., Bruno, J., Cathelineau, M., Delage, P., Fairhurst, C., Gaucher, E.C., Hohn, E.H., Kalinichev, A., Lalieux,

P. and Sellin, P. (eds.). **Geological Society Special Publications**. 400 (Clays in Natural and Engineered Barriers for Radioactive Waste Confinement) pp. 7–32

Department of Business Energy and Industrial Strategy and Nuclear Decommissioning Authority (2017) **Radioactive Wastes in the UK: A Summary of the 2016 Inventory**. Moor Row, Cumbria

Department of Energy and Climate Change (2014) **Implementing Geological Disposal: A Framework for the long-term management of higher activity radioactive waste. White Paper URN 14D/235**. London

Kersting, A.B., Efurud, D.W., Finnegan, D.L., Rokop, D.J., Smith, D.K. and Thompson, J.L. (1999) Migration of plutonium in ground water at the Nevada Test Site. **Nature**, 397 (6714): 56–59 DOI: 10.1038/16231

Malkovsky, V.I. and Pek, A.A. (2009) Effect of colloids on transfer of radionuclides by subsurface water. **Geology of Ore Deposits**, 51 (2): 79–92 DOI: 10.1134/S1075701509020019

McCarthy, J.F. (1998) Colloid-Facilitated Transport of Contaminants in Groundwater: Mobilization of Transuranic Radionuclides from Disposal Trenches by Natural Organic Matter. **Physics and Chemistry of the Earth**, 23 (2): 171–178

Missana, T., Alonso, Ú. and Turrero, M.J. (2003) Generation and stability of bentonite colloids at the bentonite/granite interface of a deep geological radioactive waste repository. **Journal of Contaminant Hydrology**, 61 (1–4): 17–31 DOI: 10.1016/S0169-7722(02)00110-9

Möri, A., Alexander, W.R., Degueudre, C., Eikenberg, J., Fierz, T., Geckeis, H., Geier, F., Hauser, W., Schäfer, T. and Smith, P.A. (2004) **Nagra Technical Bulletin NTB 03-01: The CRR Final Project Report series 1 - Description of the Field Phase - Methodologies and Raw Data**. Wettingen, Switzerland

Novikov, A.P., Kalmykov, S.N., Utsunomiya, S., Ewing, R.C., Horreard, F., Merkulov, A., Clark, S.B., Tkachev, V. V. and Myasoedov, B.F. (2006) Colloid transport of plutonium in the far-field of the Mayak Production Association, Russia. **Science**, 314 (5799): 638–641 DOI: 10.1126/science.1131307

Nuclear Decommissioning Authority (2010a) **Geological Disposal: An introduction to the generic Disposal System Safety Case**. Harwell

Nuclear Decommissioning Authority (2010b) **Geological Disposal: Radionuclide behaviour status report. NDA Report NDA/RWMD/034**. Harwell

Nuclear Decommissioning Authority (2014) **A review of the Development of Bentonite Barriers in the KBS-3V Disposal Concept. NDA Technical Note 21665941**. Harwell

Nuclear Decommissioning Authority (2015) **Understanding activities that produce radioactive wastes in the UK. NDA Report 23527545**. Moor Row, Cumbria

Penrose, W.R., Polzer, W.L., Essington, E.H., Nelson, D.M. and Orlandin, K.A. (1990) Mobility of Plutonium and Americium through a Shallow Aquifer in a Semiarid Region. **Environmental Science and Technology**, 24 (2): 228–234 DOI: 10.1021/es00072a012

Radioactive Waste Management Ltd. (2016a) **Generic Environmental Safety Case - Main Report. NDA Report DSSC/203/01**. Harwell: Nuclear Decommissioning Authority

Radioactive Waste Management Ltd. (2016b) **Geological Disposal: Science and Technology Plan**.

**NDA Report NDA/RWM/121.** Harwell

Radioactive Waste Management Ltd. (2016c) **Implementing Geological Disposal: National Geological Screening Guidance.** Harwell: Nuclear Decommissioning Authority

Ryan, J.N. and Elimelech, M. (1996) Colloid mobilization and transport in groundwater. **Colloids and Surfaces A: Physicochemical and Engineering Aspects**, 107 (95): 1–56 DOI: 10.1016/0927-7757(95)03384-X

Schäfer, T., Huber, F., Seher, H., Missana, T., Alonso, Ú., Kumke, M., Eidner, S., Claret, F. and Enzmann, F. (2012) Nanoparticles and their influence on radionuclide mobility in deep geological formations. **Applied Geochemistry**, 27: 390–403 DOI: 10.1016/j.apgeochem.2011.09.009

Schlickenrieder, L., Lanyon, B., Kontar, K. and Blechschmidt, I. (2017) **Nagra Technical Report NTB 15-03: Colloid Formation and Migration Project: Site instrumentation and initiation of the long-term in-situ test.** Wettingen, Switzerland

Slomkowski, S., Alemán, J. V., Gilbert, R.G., Hess, M., Horie, K., Jones, R.G., Kubisa, P., Meisel, I., Mormann, W., Penczek, S. and Stepto, R.F.T. (2011) Terminology of polymers and polymerization processes in dispersed systems (IUPAC Recommendations 2011). **Pure and Applied Chemistry**, 83 (12): 2229–2259 DOI: 10.1351/PAC-REC-10-06-03

## 2. LITERATURE REVIEW

### 2.1. Introduction

The purpose of this chapter is to review the current understanding of the relevant transport processes that are involved in colloid and colloid-facilitated transport. Where possible, gaps in current understanding of these processes have been identified.

Additionally, models of colloid-facilitated radionuclide transport have been reviewed, identifying how these processes have been treated by the models and finding potential improvements to these models.

The simplest models of solute transport typically consider two transport phases; a mobile dissolved species, and an immobile phase, typically caused by sorption to aquifer materials (Schäfer et al., 2012). Colloid-facilitated transport means that colloids can act as a third phase of transport for certain species. As heavy metals and radionuclides are considered to strongly sorb to aquifer materials (Schäfer et al., 2012), a large contrast exists if this third phase is present, potentially making these contaminants more mobile, (e.g. plutonium at the Nevada Test Site, Kersting et al. (1999)).

Because of this, colloid-facilitated radionuclide transport is being investigated as a relevant radionuclide transport process to build process understanding and to inform an environmental safety case for geological disposal facilities. For colloid-facilitated transport to have a significant impact on the performance of a geological disposal facility, the conditions of the 'colloid ladder' (Figure 2.1) have to be met (Möri et al., 2004). Colloids have to be present, able to migrate without significant filtration or attachment in geochemical conditions that result in stable colloid populations (Möri et al., 2004). Radionuclides then

have to undergo sorption to the colloids, sorbing irreversibly in the timescale that the assessment is being made (as no process is truly irreversible) (Möri et al., 2004). These processes are reviewed in more detail in the following sections.

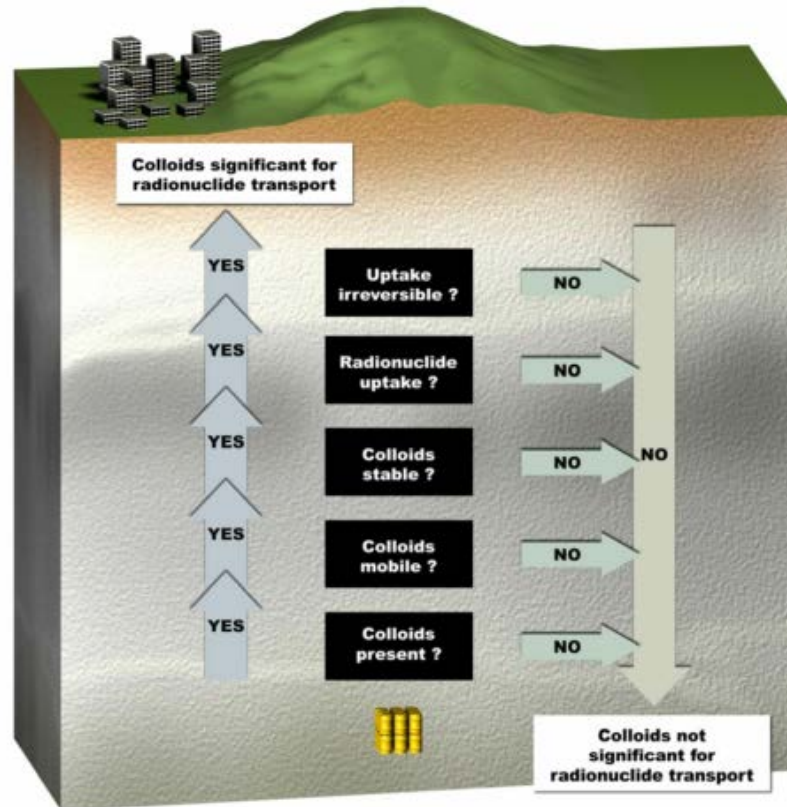


Figure 2.1 The ‘colloid ladder’ of conditions that if met will result in colloid-facilitated radionuclide transport being significant in an environmental safety case for a geological disposal facility (From: Möri et al. 2004)

## 2.2. Colloid transport processes

### 2.2.1. Colloid interaction

Colloid formation and attachment are key controls on colloid migration and so are important processes to consider for colloid-facilitated radionuclide transport. Predictions on whether colloids form and attach to rock surfaces typically consider the different attractive and repulsive forces that act between the colloid and other geological media.

As described in the previous chapter, colloids can have a diffuse cloud of ions surrounding them to balance out their surface charge, referred to as a double layer (Ryan and Elimelech, 1996). DLVO theory describes this double layer force, as well as the London/van der Waals attractive force and short range repulsive forces which also act on a colloid (Ryan and Elimelech, 1996), summarising these forces between a colloid and a surface over a particular interaction distance (Kanti Sen and Khilar, 2006). This results in an energy profile, such as that shown in Figure 2.2.

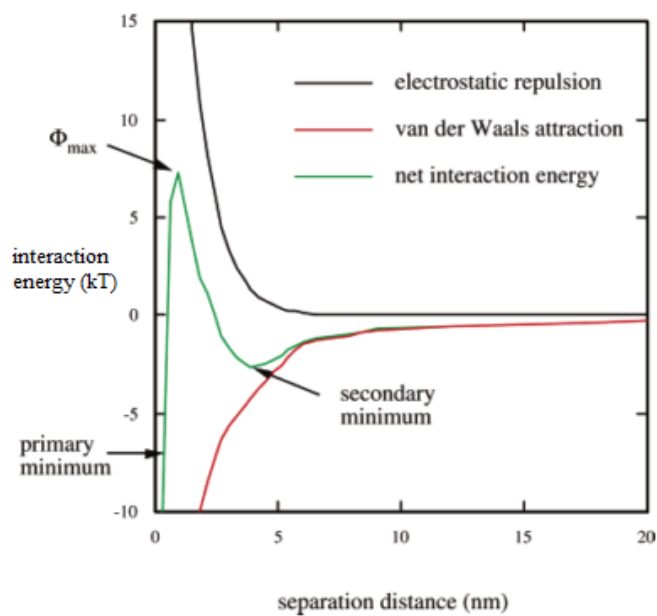


Figure 2.2 Component forces that make up DLVO energy profiles (Black = double layer repulsion, Red = van der Waals attraction, Green = Total forces) (From: Hahn and O'Melia, 2004)

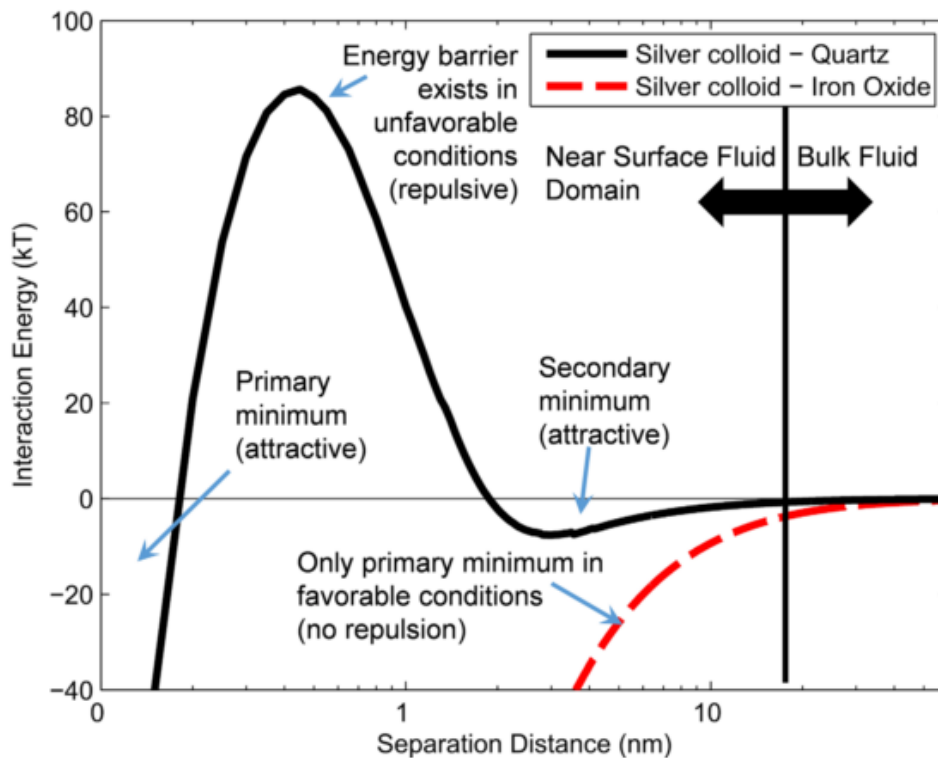


Figure 2.3 Calculated DLVO energy profiles showing attractive/ favourable (red line) and repulsive/ unfavourable (black line) conditions for deposition of silver colloids onto quartz and iron oxide (From: Molnar et al. 2015)

The double layer force can be attractive or repulsive depending on whether the charge of the surface is the same as the double layer forces (Ryan and Elimelech, 1996). Because of this, DLVO energy profiles can be attractive between colloids and surfaces (red line in Figure 2.3), or repulsive (black line in Figure 2.3). The double layer force is dependent on the surface potential of both the colloid and surface, the ionic strength of the solution that the colloids are contained in, and colloid size, (Ryan and Elimelech, 1996) as discussed further in the following sections.

### 2.2.2. Colloid formation

Colloids can form through the precipitation of oversaturated minerals, or through the mobilisation of immobile colloidal material, typically due to changes in physical or chemical conditions (Ryan and Elimelech, 1996). Changes in chemical conditions are the most likely to

cause the mobilisation of existing immobile colloids by lowering the ionic strength of groundwater, as this increases the thickness of the double layer (Ryan and Elimelech, 1996). This has the effect of increasing the range of the repulsive forces and reducing the effect of the attractive van der Waals attractive forces, potentially mobilising the immobile colloid. Ionic strength has been shown to be the major control on colloid formation in several laboratory experiments, controlling both colloid formation (Albarran et al., 2014; García-García et al., 2009) and the size distribution of colloids generated (Bessho and Degueudre, 2009).

The hydrogen ion activity is also a control on colloid mobilisation, as it can alter the surface (or zeta) potential on the colloid (Kanti Sen and Khilar, 2006). The surface potential arises as minerals on the colloid exchange hydrogen ions with the groundwater, through protonation or deprotonation reactions. At lower  $H^+$  activities the colloid is more likely to exhibit a positive charge, whereas at higher activities the colloid surface is likely to become negatively charged (Ryan and Elimelech, 1996), potentially mobilising the colloids as most natural geological media is also negatively charged. In addition, adding surfactants to groundwater has been shown to mobilise colloids (Ryan and Elimelech, 1996; Kanti Sen and Khilar, 2006).

Increased groundwater flow velocity also mobilises pre-existing immobile colloids, as increased lift and drag forces act on the colloid to counteract adhesive forces between colloid and surface (Ryan and Elimelech, 1996), causing additional rolling or sliding along a collector surface (Kanti Sen and Khilar, 2006). Increased groundwater flow through

sandstone cores mobilised pre-existing colloids in the experiments described in Torkzaban et al. (2015), although groundwater chemistry was still the major control on colloid formation.

### **2.2.3. Colloid attachment and straining**

The deposition of colloids on surfaces (through chemical attachment or physical straining) is a critical control on the migration of colloids in groundwater (Ryan and Elimelech, 1996). Chemical colloid attachment refers to when the double layer forces between colloid and surface are attractive and a colloid attaches itself to a collector (Ryan and Elimelech, 1996). Physical straining occurs when colloids get trapped in the junction between pore spaces (Bradford et al., 2006). This section focuses on the methods currently used to predict these two colloid removal mechanisms.

Colloid filtration theory is used to predict whether colloids will attach to particular surface and takes into account the transport of a colloid to a surface, considering forces such as diffusion, gravity and fluid drag as well as whether the double layer and van der Waals forces between colloid and collector surface allow attachment, as predicted by DLVO theory (Molnar et al., 2015).

Figure 2.3 shows examples of favourable and unfavourable energy profiles for attachment. Unfavourable environments result in limiting or stopping colloid attachment due to the presence of an energy barrier to attachment, i.e. repulsive forces dominate between colloid and surface (Molnar et al., 2015). However, as can be seen from Figure 2.3, colloids can still be deposited in a secondary minimum (Ryan and Elimelech, 1996), 10's of nm from a surface (Molnar et al., 2015). In favourable conditions, no energy barrier exists for colloid attachment and so can attach directly to the surface in the primary minimum.

Unfavourable attachment conditions are found in most environmental settings, as typically both colloids and surfaces are negatively charged (Molnar et al., 2015). Lower ionic strength groundwaters, such as glacial meltwaters, are less favourable for colloid attachment, as the thicker double layer on the colloid reduces the effect of the attractive forces between colloid and surface (Ryan and Elimelech, 1996).

Mechanistic models that use colloid filtration theory typically provide good predictions of colloid attachment where favourable conditions for attachment exist (Molnar et al., 2015). However, these models are unreliable when predicting colloid attachment in unfavourable attachment conditions (Ryan and Elimelech, 1996; Kanti Sen and Khilar, 2006). In unfavourable environments, predicted deposition rates are typically lower than found in experiments.

One of the potential causes of this discrepancy is that although the majority of colloid and collector surfaces are negatively charged in unfavourable attachment environments, small portions of the colloid (or the collector) surface could be positively charged, facilitating attachment at much higher rates than predicted. Elimelech et al. (2000) demonstrated that the presence of such chemical heterogeneity was a larger control on colloid deposition rates than the measured surface charge of the colloid, as this measurement averages the charge on the colloid.

There are also other potential causes of the discrepancy. Colloid filtration theory considers deposition in the primary minimum, however colloids can also attach to the secondary minimum (as shown in Figure 2.3) (Molnar et al., 2015). Unlike deposition in the primary minimum, deposition here however is easily reversible. In addition, colloids and

surfaces exhibit surface roughness, potentially requiring a range of interaction energies to describe colloid attachment accurately (Ryan and Elimelech, 1996).

Although mechanistic models that use colloid filtration theory could be altered using empirical factors to account for this discrepancy in predicted attachment rates, this would calibrate the model to a particular environment, reducing the models predictive capability. Further improvements to these mechanistic models are required to improve the predictive capability of these models. Models using continuum-based approaches to describe colloid attachment using kinetic approaches have been successful in describing colloid attachment, but have limited predictive capability as these are again calibrated to a particular environment (Molnar et al., 2015).

Colloid attachment is a dynamic process, with DLVO/ colloid filtration theory providing an approximate attachment rate at the initial stages of colloid attachment, known as 'clean bed filtration' (Ryan and Elimelech, 1996). Colloids already attached to a surface can either attract or repel other colloids. Ripening occurs when attached colloids enhance the attachment rate i.e. attracting other colloids to a surface (Ryan and Elimelech, 1996), typically occurring in favourable attachment conditions. Blocking occurs when attached colloids repel other colloids and can occur in low ionic strength groundwater (Ryan and Elimelech, 1996), such as found at the Grimsel Test Site. If blocking occurs, colloid attachment can be controlled by the rate at which these limited attachment sites are filled and blocked (Ryan and Elimelech, 1996).

Several laboratory column experiments show that colloid attachment increases with residence time, even in unfavourable environments for attachment (Missana et al., 2008;

Schäfer et al., 2012, 2004), as longer residence times allow for more interaction with potential attachment surfaces.

Colloid filtration theory describes colloid attachment to a single collector (Bradford et al., 2006). In practice, this would be scaled to account for the multiple collectors present in geological media. However, this means that colloid filtration theory does not account for the pore structure and junctions between grains that exist in geological media (Bradford et al., 2006), and as such colloid filtration theory does not account for the removal of colloids through physical processes such as mechanical filtration or straining. Mechanical filtration occurs when colloids are larger than all of the pores in a geological media and are retained with no colloids transported. Straining occurs when colloids are trapped in only the smallest pore junctions, so colloid transport can still take place (Bradford et al., 2006).

Straining has been successfully modelled using continuum based approaches (Bradford et al., 2003, 2011) where models require calibration to match specific experimental data. Mechanistic models of straining and filtration require knowledge of the sizes of the colloids and pore structure, which could be gained through imaging processes such as X-ray tomography (Molnar et al., 2015; Bradford et al., 2006).

#### **2.2.4. Colloid size**

Polydispersed colloidal suspensions refer to colloid suspensions made up from a distribution of colloid sizes. Where colloid suspensions are made up from the same size, the suspension is said to be monodispersed. Colloid sizes are important to consider as colloids undergo different processes based on their size (such as colloid straining and attachment). Colloid filtration theory predicts that colloid attachment rates are sensitive to different

colloid sizes. However, experiments show that colloid attachment may be independent of particle size (Elimelech and O'Melia, 1990). This discrepancy is thought to be caused by DLVO theory not taking into account transient colloid and surface charges during interactions with other colloids and attachment surfaces (Elimelech and O'Melia, 1990).

As well as interaction with surfaces through colloid attachment, colloids can also interact with other colloids, in a process called colloid aggregation. Colloid aggregation can be predicted with DLVO theory; colloid aggregation is more likely to occur in higher ionic strength groundwater where there are weaker repulsive forces and stronger attractive forces between colloids (Bertetti et al., 2006). Experiments show a positive correlation between colloid aggregation and increased colloid attachment rates (Chatterjee and Gupta, 2009). Aggregation can occur through attachment in both the primary and secondary minimum of another colloid (Hahn and O'Melia, 2004). Colloids can in theory aggregate with the same type of colloid (homoaggregation), or with different types of colloids (heteroaggregation) (Malkovsky and Pek, 2009).

Investigations of colloid migration have shown that colloid breakthrough can occur before a conservative tracer (Ryan and Elimelech, 1996). This is caused by size exclusion chromatography, where the large size of colloids excludes them from smaller paths. Therefore, as colloids do not sample the full velocity profile that a conservative tracer might, the colloid velocity is higher causing earlier breakthrough (Chrysikopoulos and Katzourakis, 2015), which also results in the colloids undergoing different dispersion than a tracer.

### **2.3. Radionuclide interaction with colloids**

This section reviews previous investigations of radionuclide interaction with clay colloids, as the migration experiments modelled in this thesis investigate colloid-facilitated transport caused by bentonite derived clay colloids. This is because the concentration of bentonite colloids used in the two migration experiments are orders of magnitude higher than the concentration of background colloids at the Grimsel Test Site (Degueldre et al., 1989), minimising the likelihood of significant amounts of radionuclides sorbing to the indigenous colloids during the experiments. A number of laboratory experiments are reviewed in this chapter, as summarised in Table 1.1.

As a key part of the 'colloid ladder' (Figure 2.1) for colloid-facilitated radionuclide transport, radionuclide sorption and reversibility have been investigated in detail as part of the CRR (Missana and Geckeis, 2006), and CFM projects (Schäfer et al., 2014). Other projects have also investigated radionuclide sorption to colloids, for instance the EC BELBaR project studied radionuclide sorption and reversibility to bulk and colloidal bentonite (Schäfer et al., 2016), or in reviews by or for radioactive waste management organisations (Wold, 2010; Bertetti et al., 2006; Alexander et al., 2011), as well as in the wider literature.

Radionuclide sorption to colloids will generally occur by the same processes as sorption to rock surfaces (i.e. surface complexation and ionic exchange) (Alexander et al., 2011). As colloids have a higher specific surface area, the sorption capacity (per mass of material) for colloids is typically higher than for rock surfaces (Alexander et al., 2011). Sorption of radionuclides is dependent on redox state, pH, ionic strength, other ions and chemical components and available surface area/ concentration of colloids (Bertetti et al., 2006).

Batch sorption studies are frequently used to investigate radionuclide sorption to colloids, for instance Missana et al. (2004) used batch experiments to investigate caesium and uranium sorption to bentonite colloids, finding that caesium showed a non-linear sorption isotherm in Grimsel groundwater, which was explored further by Missana et al. (2014) in experiments investigating the impact of ionic strength, pH and competing ions on sorption to bentonite derived smectite colloids. Other batch experiments include investigating neptunium (V) and plutonium (V) sorption to montmorillonite over a series of different pH (pH 3-8) and ionic strength solutions ( $I = 0.001\text{M}$  to  $1\text{M}$  NaCl) in Zavarin et al. (2012), which showed that under the conditions of the experiment, the presence of montmorillonite colloids meant plutonium (V) underwent potential reduction to plutonium (IV).

Column migration experiments also provide insight into radionuclide sorption processes in particular environments. For example, Schäfer et al. (2004) use column experiments in Grimsel granodiorite to show that thorium and europium migration was facilitated by bentonite colloids, but uranium migration was not, migrating as an aqueous species instead. Dittrich et al. (2015), showed that desorption kinetics from bentonite colloids were a key control on americium migration in Grimsel fracture fill material; similar results were found for strontium migration by Albarran et al. (2011). Batch studies can be combined with column migration experiments. For example Dittrich and Reimus, (2015), used batch experiments to find parameter values to successfully model caesium transport in column experiments with Grimsel fracture fill material and bentonite colloids, using a two-site sorption model on both the colloids and fracture fill material.

Experiments running with bulk clay instead of colloidal clay can provide information on radionuclide sorption. For instance Zavarin et al. (2012) showed that neptunium (V) weakly sorbed to montmorillonite, whereas plutonium (V) showed kinetic sorption effects, potentially because it had reduced to plutonium (IV). Marsac et al. (2015) showed that neptunium (V) sorption increased with reduction Eh values, potentially due to its reduction in that experiment.

Determining whether radionuclide sorption is reversible to the colloids is a key process in the 'colloid ladder'. Experiments have tested whether radionuclide sorption is reversible, using a variety of methods. Huber et al. (2011) and Huber et al. (2015) found that americium, plutonium and thorium sorption to bentonite and montmorillonite colloids was reversible, whereas uranium and neptunium showed limited sorption to the colloids and to Grimsel fracture fill material in the experiments. Sherriff et al. (2015) showed that europium sorption to bulk bentonite was reversible, with a fraction of the europium showing desorption kinetics. This was also shown in Schäfer et al. (2016) for americium, uranium and thorium sorption to bentonite.

Begg et al. (2015) showed that plutonium (IV) sorption to bentonite was reversible, showing desorption kinetics, which was also the case for montmorillonite (Begg et al., 2017). Durrant et al. (2018) investigated desorption of caesium from montmorillonite, Illite and kaolinite, showing that sorption to Illite was not fully reversible, but was fully reversible to montmorillonite and kaolinite.

Reference	Materials	Radionuclides	Key Finding	Timescale
Missana et al. (2004)	FEBEX Bentonite colloids	U (VI) and Cs	Cs sorption showed non-linear isotherm; sorption of both elements not completely reversible.	18 weeks
Missana et al. (2014)	Bentonite derived smectite colloids	Cs	Cs sorption non-linear, controlled by ion exchange to different sites on the clay. Competing ions important control on sorption.	1 week
Schäfer et al. (2004)	Grimsel granodiorite, FEBEX bentonite colloids	U (VI), Th (IV) , Eu (III)	Uranium transport not colloid-facilitated, Th and Eu transport colloid-facilitated. Colloid recovery decreases with increased residence time.	1000 hours
Dittrich et al. (2015)	Grimsel granodiorite, FEBEX bentonite colloids	Am	Desorption kinetics from single site key control on the transport of colloid-facilitated americium	600 hours
Albarran et al. (2011)	Grimsel granodiorite, FEBEX bentonite colloids	Sr	Sorption to colloids reversible, partial colloid-facilitated transport of Sr observed.	10 hours
Dittrich and Reimus (2015)	Grimsel granodiorite and FFM, FEBEX bentonite colloids	Cs	Sorption reversible, modelled with two sites on FFM and Colloids	250 hours
Zavarin et al. (2012)	Montmorillonite	Np (V) and Pu (V)	Weak pH-dependent sorption of Np(V), stronger sorption with kinetics for Pu (V) showing reduction to Pu(IV)	300 hours
Marsac et al. (2015)	Illite	Np (V)	Partial reduction of Np(V) in anaerobic conditions as K <sub>d</sub> values increase with decreasing Eh	63 days
Troyer et al. (2016)	Montmorillonite	U (VI)	At high pH values U(VI) carbonate-surface complexes control sorption behaviour, phosphate has influence on sorption behaviour.	48 hours
Elo et al. (2017)	Montmorillonite	Np (V)	pH dependent desorption behaviour due to formation of surface complex	30 days
Begg et al. (2015)	Bulk Bentonite (FEBEX)	Pu (IV) and Pu (V)	Linear sorption isotherm for Pu (IV) showing kinetic sorption. Reversible sorption indicated.	300 days
Begg et al. (2017)	Montmorillonite	Pu (IV)	Kinetic pH dependent sorption shown for Pu (IV). Desorption rate limited in experiment	6 months
Sherriff et al. (2015)	Na-Bentonite - bulk and colloidal. EDTA competitor	Eu (III)	No evidence for 'irreversible' Eu sorption, fast and slow Eu desorption for bulk and colloidal bentonite, but colloid dissociation occurred an order of magnitude faster.	350 days
Durrant et al. (2018)	Illite, montmorillonite and kaolinite	Cs	Linear sorption to montmorillonite and kaolinite, non-linear sorption to Illite. Nearly complete desorption from montmorillonite and kaolinite, slow desorption from Illite.	500 days
Huber et al. (2011)	FEBEX Bentonite colloids, Grimsel FFM competitor	Tc (VII), U (IV), Np (V), Am (III), Th (IV), Pu (IV)	Tc, U and Np did not bind to colloids, and U and Tc did not interact with FFM. Np did interact with FFM. Am, Th, Pu were strongly associated with colloids but did show slow dissociation.	365 days
Huber et al. (2015)	Artificially labelled Ni-/ Zn-montmorillonite colloids	Tc (VII), U (IV), Np (V), Am (III), Th (IV), Pu (IV)	Tc, U and Np did not sorb to colloids, but could have sorbed to FFM. Am, Pu and Th were strongly sorbed to colloids but showed desorption kinetics.	13 months

**Table 2.1 Summary of different laboratory investigations of radionuclide sorption to bentonite derived colloids, full details found in Chapters 6 and 7**

The majority of research described above into radionuclide sorption reversibility found that sorption to the colloids was reversible, that under the definitions of ‘colloid-ladder’ means that colloid-facilitated transport would not be significant (Möri et al., 2004). However, it has been shown that if radionuclides undergo slow desorption from colloids relative to colloid residence time, colloid-facilitated transport can still be significant (Sherriff et al., 2015; Bertetti et al., 2006; Schäfer et al., 2016).

## **2.4. Models of colloid-facilitated radionuclide transport**

This section briefly reviews previous models of colloid-facilitated radionuclide transport, identifying the processes that have been used to describe the different processes involved in colloid-facilitated radionuclide transport. The main difference between these models is that they use different representations of radionuclide sorption to the colloids. Chapter 3 reviews in detail the models applied to the CFM and CRR field experiments, although an outline of these models is also given in this section.

Ibaraki and Sudicky (1995a and 1995b) detail a two dimensional model of colloid-facilitated radionuclide transport that has been used previously in the JNC-COLFRAC model code that has been applied to the CRR experiment (Smith et al., 2006), and the descriptions of the different processes used as a conceptual model for the CFM migration experiments (Noseck et al., 2016). The model solves for colloid transport and attachment in a fracture, radionuclide transport in both the fracture and an adjacent porous medium, and allows for kinetic and equilibrium sorption (using either Freundlich or Langmuir isotherms) to mobile and immobile colloids, and fracture surfaces. Similar processes are included in the software package (HYDRUS) developed in Simunek et al., (2012), which additionally includes colloid

straining, and linear reversible kinetic sorption of radionuclides to mobile and immobile colloids, and two (one equilibrium and one kinetic) sorption sites on rock surfaces.

Cvetkovic et al. (2004) assumed that colloid concentration was steady-state across their 1D model, with colloid attachment balanced by a source of colloids. Radionuclides could sorb to colloids and rock surfaces using linear reversible sorption or kinetic sorption with a Langmuir or bilinear isotherm. Baek and Pitt, (1996) also used a 1D model which assumed equilibrium sorption of the colloids to rock surfaces (representing colloid attachment), and linear equilibrium sorption of the radionuclides to mobile and immobile colloids, and fracture surfaces. The model also accounts for diffusion of radionuclides into adjacent rock matrix, which can then undergo equilibrium sorption to the matrix. Li and Jen, (2001) detailed a similar model using either equilibrium or kinetic sorption to describe radionuclide sorption, and includes equilibrium colloid attachment.

Similar approaches were also used to model the CFM and CRR migration experiments. The models applied to the CRR migration experiments did not consider colloid attachment (apart from one model; which considered irreversible attachment) (Smith et al., 2006). These models also mostly assumed that radionuclide sorption to the colloids and rock surfaces could be described by equilibrium sorption and that radionuclide sorption to the colloid was irreversible, apart from one model which described sorption using 1<sup>st</sup> order kinetics (Smith et al., 2006).

The models that have been previously applied to model CFM migration experiments described radionuclide sorption to the colloids with linear kinetic sorption that was reversible (Noseck et al., 2016). One of the models (the LANL model) included more than

one sorption site on the colloid, and this model also had the ability to limit sorption capacity on these sites, and to set time-dependent desorption rates. All of these three models also included descriptions of first-order reversible and irreversible colloid attachment, matrix diffusion and either linear equilibrium or kinetic radionuclide sorption to rock surfaces.

These models have been successfully applied to the CFM and CRR migration experiments, however they mostly used 1D or homogeneous 2D model domains. However, some of these models required different parameter values to describe the same species in different migration experiments, also known as per-experiment calibrations. The migration experiments take place in a highly heterogeneous shear zone. As previous models have not included this complex geological structure in their models of the experiments, the model developed in this thesis will include a more detailed representation of the geological structure to attempt to model the experiments.

The models detailed in this section are all solved numerically, using either the finite element scheme (Ibaraki and Sudicky, 1995a; Simunek et al., 2012) or a finite difference scheme (Baek and Pitt, 1996; Li and Jen, 2001). Bryan and Sherriff, (2016) detail a different approach, which uses Damkohler numbers to consider whether colloid-facilitated transport is likely, based on the kinetic desorption rate of the radionuclide when compared to colloid residence time. The Damkohler numbers are then used to assess whether process level models of colloid-facilitated radionuclide transport need to be included in environmental safety cases for geological disposal facilities.

## 2.5. Summary

This chapter has reviewed the current understanding of the relevant processes involved in colloid and colloid-facilitated radionuclide transport, and how these processes are treated in models.

Mechanistic models of colloid transport and attachment using colloid-filtration theory have been successful in replicating colloid attachment in favourable conditions where there are no energy barriers for attachment. However, in unfavourable conditions such as the low-ionic strength glacial meltwater of the Grimsel Test Site, these mechanistic models require further calibration to match experimental results, limiting their predictive ability. Continuum-based models which require calibration to specific environments have also been successfully used to describe colloid attachment, but have limited predictive ability.

Laboratory experiments investigating the reversibility of radionuclide sorption to colloids have all shown that at least a fraction of the radionuclides undergo desorption from the colloids, with several showing that desorption kinetics are a key control on this process. As this has a key impact on whether colloid-facilitated radionuclide transport is significant for a GDF, reversible sorption from colloids is required to be included and investigated further in this modelling work.

Previous models of colloid-facilitated radionuclide transport have all included similar descriptions of colloid attachment and radionuclide sorption to colloids and rock surfaces. The models already applied to model the CFM and CRR migration experiments mostly used either 1D or homogenous 2D model domains, despite the highly heterogeneous geological structure of the shear zone where the migration experiments take place. Therefore, in order

to attempt to develop a self-consistent understanding of colloid-facilitated radionuclide transport in these experiments, a more detailed representation of the geological structure is to be included in the model.

## 2.6. List of References

Albarran, N., Degueldre, C., Missana, T., Alonso, Ú., García-Gutiérrez, M. and López, T. (2014) Size distribution analysis of colloid generated from compacted bentonite in low ionic strength aqueous solutions. **Applied Clay Science** [online], 95: 284–293 DOI: 10.1016/j.clay.2014.04.025. Available from: <http://dx.doi.org/10.1016/j.clay.2014.04.025>

Albarran, N., Missana, T., García-Gutiérrez, M., Alonso, Ú. and Mingarro, M. (2011) Strontium migration in a crystalline medium: Effects of the presence of bentonite colloids. **Journal of Contaminant Hydrology** [online], 122 (1–4): 76–85 DOI: 10.1016/j.jconhyd.2010.11.005. Available from: <http://www.ncbi.nlm.nih.gov/pubmed/21196062> [Accessed 18 July 2014]

Alexander, W.R., Berry, J.A., Kelly, M.J. and Swanton, S.W. (2011) **Review of colloids in the geosphere and their treatment in performance assessments. NDA-RWMD report NPO003512.** Harwell: Nuclear Decommissioning Authority

Baek, I. and Pitt, W.W. (1996) Colloid-facilitated radionuclide transport in fractured porous rock. **Waste Management**, 16 (4): 313–325 DOI: 10.1016/S0956-053X(96)00074-8

Begg, J.D., Zavarin, M. and Kersting, A.B. (2017) Desorption of plutonium from montmorillonite: An experimental and modeling study. **Geochimica et Cosmochimica Acta** [online], 197: 278–293 DOI: 10.1016/j.gca.2016.10.006. Available from: <http://dx.doi.org/10.1016/j.gca.2016.10.006>

Begg, J.D., Zavarin, M., Tumey, S.J. and Kersting, A.B. (2015) Plutonium sorption and desorption behavior on bentonite. **Journal of Environmental Radioactivity** [online], 141: 106–114 DOI: 10.1016/j.jenvrad.2014.12.002. Available from: <http://linkinghub.elsevier.com/retrieve/pii/S0265931X14003610>

Bertetti, P., Klar, R. V. and Vaught, M.M. (2006) **COLLOID-FACILITATED TRANSPORT OF RADIONUCLIDES IN NATURAL GROUNDWATER SYSTEMS — LITERATURE REVIEW.** San Antonio, Texas. p. 61

Bessho, K. and Degueldre, C. (2009) Generation and sedimentation of colloidal bentonite particles in water. **Applied Clay Science** [online], 43 (2): 253–259 DOI: 10.1016/j.clay.2008.08.006. Available from: <http://dx.doi.org/10.1016/j.clay.2008.08.006>

Bradford, S.A., Simunek, J., Bettahar, M., Van Genuchten, M.T. and Yates, S.R. (2003) Modeling colloid attachment, straining, and exclusion in saturated porous media. **Environmental Science and Technology**, 37: 2242–2250 DOI: 10.1021/es025899u

Bradford, S.A., Simunek, J., Bettahar, M., Van Genuchten, M.T. and Yates, S.R. (2006) Significance of straining in colloid deposition: Evidence and implications. **Water Resources Research**, 42 (December 2005): 1–16 DOI: 10.1029/2005WR004791

Bradford, S.A., Torkzaban, S. and Simunek, J. (2011) Modeling colloid transport and retention in

saturated porous media under unfavorable attachment conditions. **Water Resources Research**, 47 (10): 1–12 DOI: 10.1029/2011WR010812

Bryan, N. and Sherriff, N. (2016) **BELBaR D3.10 Mechanistic model of radionuclide colloid interaction**. Brussels

Chatterjee, J. and Gupta, S.K. (2009) An agglomeration-based model for colloid filtration. **Environmental Science and Technology**, 43 (10): 3694–3699 DOI: 10.1021/es8029973

Chrysikopoulos, C. V. and Katzourakis, V.E. (2015) Colloid particle size-dependent dispersivity. **Water Resources Research** [online], 51 (6): 4668–4683 DOI: 10.1002/2014WR016094. Available from: <http://doi.wiley.com/10.1002/2014WR016094>

Cvetkovic, V., Painter, S., Turner, D., Pickett, D. and Bertetti, P. (2004) Parameter and model sensitivities for colloid-facilitated radionuclide transport on the field scale. **Water Resources Research**, 40: 1–14 DOI: 10.1029/2004WR003048

Degeldre, C., Baeyens, B., Goerlich, W., Riga, J., Verbist, J. and Stadelmann, P. (1989) Colloids in water from a subsurface fracture in granitic rock, Grimsel Test Site, Switzerland. **Geochimica Et Cosmochimica Acta**, 53: 603–610

Dittrich, T.M., Boukhalfa, H., Ware, S.D. and Reimus, P.W. (2015) Laboratory investigation of the role of desorption kinetics on americium transport associated with bentonite colloids. **Journal of Environmental Radioactivity** [online], 148: 170–182 DOI: 10.1016/j.jenvrad.2015.07.001. Available from: <http://dx.doi.org/10.1016/j.jenvrad.2015.07.001>

Dittrich, T.M. and Reimus, P.W. (2015) **Nagra Arbeitsbericht NAB 15-09: Laboratory investigation of colloid-facilitated transport of caesium by bentonite colloids in a crystalline rock system**. Wettingen, Switzerland

Durrant, C.B., Begg, J.D., Kersting, A.B. and Zavarin, M. (2018) Cesium sorption reversibility and kinetics on illite, montmorillonite, and kaolinite. **Science of the Total Environment** [online], 610–611: 511–520 DOI: 10.1016/j.scitotenv.2017.08.122. Available from: <https://doi.org/10.1016/j.scitotenv.2017.08.122>

Elimelech, M., Nagai, M., Ko, C.-H. and Ryan, J.N. (2000) Relative insignificance of mineral grain zeta potential to colloid transport in geochemically heterogeneous porous media. **Environmental Science and Technology**, 34: 2143–2148 DOI: 10.1021/es9910309

Elimelech, M. and O'Melia, C. (1990) Effect of Particle Size on collision efficiency in the deposition of brownian particles with electrostatic energy barriers. **Langmuir**, 6 (6): 1153–1163

Elo, O., Muller, K., Ikeda-Ohno, A., Bok, F., Scheinost, A.C., Holtta, P. and Huittinen, N. (2017) Batch sorption and spectroscopic speciation studies of neptunium uptake by montmorillonite and corundum. **Geochimica et Cosmochimica Acta**, 198: 168–181 DOI: 10.1016/j.gca.2016.10.040

García-García, S., Degeldre, C., Wold, S. and Frick, S. (2009) Determining pseudo-equilibrium of montmorillonite colloids in generation and sedimentation experiments as a function of ionic strength, cationic form, and elevation. **Journal of Colloid and Interface Science** [online], 335 (1): 54–61 DOI: 10.1016/j.jcis.2009.02.048. Available from: <http://dx.doi.org/10.1016/j.jcis.2009.02.048>

Hahn, M.W. and O'Melia, C.R. (2004) Deposition and Reentrainment of Brownian Particles in Porous Media under Unfavorable Chemical Conditions: Some Concepts and Applications. **Environmental**

**Science and Technology**, 38 (1): 210–220 DOI: 10.1021/es030416n

Huber, F., Heck, S., Truche, L., Bouby, M., Brendle, J., Hoess, P. and Schäfer, T. (2015) Radionuclide desorption kinetics on synthetic Zn / Ni-labeled montmorillonite nanoparticles. **Geochimica et Cosmochimica Acta**, 148: 426–441 DOI: 10.1016/j.gca.2014.10.010

Huber, F., Kunze, P., Geckeis, H. and Schäfer, T. (2011) Sorption reversibility kinetics in the ternary system radionuclide-bentonite colloids/nanoparticles-granite fracture filling material. **Applied Geochemistry** [online], 26 (12): 2226–2237 DOI: 10.1016/j.apgeochem.2011.08.005. Available from: <http://dx.doi.org/10.1016/j.apgeochem.2011.08.005>

Ibaraki, M. and Sudicky, E.A. (1995a) Colloid-facilitated contaminant transport in discretely fractured porous media. 1. Numerical formulation and sensitivity analysis. **Water Resources Research**, 31 (12): 2945–2960 DOI: 10.1029/95WR02180

Ibaraki, M. and Sudicky, E.A. (1995b) Colloid-facilitated contaminant transport in discretely fractured porous media. 2. Fracture network examples. **Water Resources Research**, 31 (12): 2961–2969 DOI: 10.1029/95WR02181

Kanti Sen, T. and Khilar, K.C. (2006) Review on subsurface colloids and colloid-associated contaminant transport in saturated porous media. **Advances in Colloid and Interface Science** [online], 119 (2–3): 71–96 DOI: 10.1016/j.cis.2005.09.001. Available from: <http://www.ncbi.nlm.nih.gov/pubmed/16324681>

Kersting, A.B., Efurud, D.W., Finnegan, D.L., Rokop, D.J., Smith, D.K. and Thompson, J.L. (1999) Migration of plutonium in ground water at the Nevada Test Site. **Nature**, 397 (6714): 56–59 DOI: 10.1038/16231

Li, S.H. and Jen, C.P. (2001) Migration of radionuclides in porous rock in the presence of colloids: Effects of kinetic interactions. **Waste Management**, 21: 569–579 DOI: 10.1016/S0956-053X(00)00104-5

Malkovsky, V.I. and Pek, A.A. (2009) Effect of colloids on transfer of radionuclides by subsurface water. **Geology of Ore Deposits**, 51 (2): 79–92 DOI: 10.1134/S1075701509020019

Marsac, R., Banik, N. Ial, Lützenkirchen, J., Marquardt, C.M., Dardenne, K., Schild, D., Rothe, J., Diascorn, A., Kupcik, T., Schäfer, T. and Geckeis, H. (2015) Neptunium redox speciation at the illite surface. **Geochimica et Cosmochimica Acta**, 152: 39–51 DOI: 10.1016/j.gca.2014.12.021

Missana, T., Alonso, Ú., García-Gutiérrez, M. and Mingarro, M. (2008) Role of bentonite colloids on europium and plutonium migration in a granite fracture. **Applied Geochemistry** [online], 23 (6): 1484–1497 DOI: 10.1016/j.apgeochem.2008.01.008. Available from: <http://linkinghub.elsevier.com/retrieve/pii/S0883292708000565> [Accessed 12 December 2014]

Missana, T., Benedicto, A., García-Gutiérrez, M. and Alonso, U. (2014) Modeling cesium retention onto Na-, K- and Ca-smectite: Effects of ionic strength, exchange and competing cations on the determination of selectivity coefficients. **Geochimica et Cosmochimica Acta** [online], 128: 266–277 DOI: 10.1016/j.gca.2013.10.007. Available from: <http://dx.doi.org/10.1016/j.gca.2013.10.007>

Missana, T., García-Gutiérrez, M. and Alonso, Ú. (2004) Kinetics and irreversibility of cesium and uranium sorption onto bentonite colloids in a deep granitic environment. **Applied Clay Science**, 26 (1–4 SPEC. ISS.): 137–150 DOI: 10.1016/j.clay.2003.09.008

Missana, T. and Geckeis, H. (2006) **Nagra Technical Bulletin NTB 03-02: CRR Final Project Report 2 - Supporting Laboratory Experiments with Radionuclides and Bentonite Colloids**. Wettingen, Switzerland

Molnar, I.L., Johnson, W.P., Gerhard, J.I., Willson, C.S. and O'Carroll, D.M. (2015) Predicting colloid transport through saturated porous media: A critical review. **Water Resources Research** [online], 51 (9): 6804–6845 DOI: 10.1002/2015WR017318. Available from: <http://doi.wiley.com/10.1002/2015WR017318>

Möri, A., Alexander, W.R., Degueldre, C., Eikenberg, J., Fierz, T., Geckeis, H., Geier, F., Hauser, W., Schäfer, T. and Smith, P.A. (2004) **Nagra Technical Bulletin NTB 03-01: The CRR Final Project Report series 1 - Description of the Field Phase - Methodologies and Raw Data** [online]. Wettingen, Switzerland. Available from: <http://www.nagra.ch/en/cat/publikationen/technicalreports-ntbs/ntbs-2001-2012/downloadcentre.htm>

Noseck, U., Flügge, J., Reimus, P., Cvetkovic, V., Lanyon, B., Schäfer, T. and Blechschmidt, I. (2016) **Nagra Technical Report NTB 16-06: Colloid Formation and Migration Project: Modelling of tracer, colloid and radionuclide/homologue transport for dipole CFM 06.002- Pinkel surface packer**. Wettingen, Switzerland

Ryan, J.N. and Elimelech, M. (1996) Colloid mobilization and transport in groundwater. **Colloids and Surfaces A: Physicochemical and Engineering Aspects**, 107 (95): 1–56 DOI: 10.1016/0927-7757(95)03384-X

Schäfer, T., Darbha, G. and Iijima, K. (2014) **Nagra Arbeitsbericht NAB 13-79 CFM Phase 2: Status Report of the Laboratory Programme at the end of 2011**. Wettingen, Switzerland

Schäfer, T., Geckeis, H., Bouby, M. and Fanghänel, T. (2004) U, Th, Eu and colloid mobility in a granite fracture under near-natural flow conditions. **Radiochimica Acta**, 92 (9–11): 731–737 DOI: 10.1524/ract.92.9.731.54975

Schäfer, T., Huber, F., Seher, H., Missana, T., Alonso, Ú., Kumke, M., Eidner, S., Claret, F. and Enzmann, F. (2012) Nanoparticles and their influence on radionuclide mobility in deep geological formations. **Applied Geochemistry**, 27: 390–403 DOI: 10.1016/j.apgeochem.2011.09.009

Schäfer, T., Sherriff, N., Bryan, N., Livens, F., Bouby, M., Darbha, G., Stoll, M., Huber, F., Schafer, T., Holtta, P., Elo, O., Suorsa, V., Honkaniemi, E., Niemiaho, S., Missana, T., Alonso, Ú., Mayordomo, N., Koloma, K., Cervinka, R., et al. (2016) **BELBaR D3.11: WP3 partners final report on experimental results on micro to macroscale colloid rock interaction and colloid radionuclide interaction**. Brussels

Sherriff, N., Issa, R., Morris, K., Livens, F., Heath, S. and Bryan, N. (2015) Reversibility in radionuclide/bentonite bulk and colloidal ternary systems. **Mineralogical Magazine** [online], 79 (6): 1307–1315 DOI: 10.1180/minmag.2015.079.06. Available from: <http://openurl.ingenta.com/content/xref?genre=article&issn=0026-461X&volume=79&issue=6&spage=1307>

Simunek, J., Sejna, M. and Van Genuchten, M.T. (2012) **The C-Ride Module for HYDRUS (2D/3D) Simulating Two-Dimensional Colloid-Facilitated Solute Transport in Variably-Saturated Porous Media**. Riverside, CA

Smith, P.A., Guimera, J., Kosakowski, G., Pudewills, A. and Ibaraki, M. (2006) **Nagra Technical Bulletin**

**NTB 03-03: Grimsel Test Site Investigation Phase V - The CRR Final Project Report series 3: Results of the Supporting Modelling Programme.** Wettingen, Switzerland

Torkzaban, S., Bradford, S.A., Vanderzalm, J.L., Patterson, B.M., Harris, B. and Prommer, H. (2015) Colloid release and clogging in porous media: Effects of solution ionic strength and flow velocity. **Journal of Contaminant Hydrology** [online], 181: 161–71 DOI: 10.1016/j.jconhyd.2015.06.005. Available from: <http://www.sciencedirect.com/science/article/pii/S0169772215000881>

Troyer, L.D., Maillot, F., Wang, Z., Wang, Z., Mehta, V.S., Giammar, D.E. and Catalano, J.G. (2016) Effect of phosphate on U(VI) sorption to montmorillonite: Ternary complexation and precipitation barriers. **Geochimica et Cosmochimica Acta** [online], 175: 86–99 DOI: 10.1016/j.gca.2015.11.029. Available from: <http://dx.doi.org/10.1016/j.gca.2015.11.029>

Wold, S. (2010) **TR-10-20 Sorption of prioritized elements on montmorillonite colloids and their potential to transport radionuclides potential to transport radionuclides** [online]. Stockholm. Available from: <http://www.skb.se/upload/publications/pdf/TR-10-20.pdf>

Zavarin, M., Powell, B.A., Bourbin, M., Zhao, P. and Kersting, A.B. (2012) Np(V) and Pu(V) ion exchange and surface-mediated reduction mechanisms on montmorillonite. **Environmental Science and Technology**, 46 (5): 2692–2698 DOI: 10.1021/es203505g

### **3. FIELD MIGRATION EXPERIMENTS AT THE GRIMSEL TEST SITE**

#### **3.1. Introduction**

This chapter provides detail on the geological and hydrogeological setting of the Grimsel Test Site. The site has been run by Nagra (the Swiss co-operative for the disposal of radioactive waste) as a generic underground research laboratory (URL) since 1984, carrying out experiments investigating the performance of engineered and geological barriers for a GDF.

This chapter details the background on two projects, the Colloid Formation and Migration (CFM) project, and the Colloid and Radionuclide Retardation (CRR) project. These two projects have been investigating the migration of radionuclides in the presence of colloids generated from bentonite clay, through a programme of field, laboratory and modelling investigations. This thesis models two *in situ* migration experiments carried out during these projects, CFM Run 13-05 and CRR Run 32. These migration experiments were carried out between the same two boreholes that intersect the Migration Experiment shear zone (referred to as the MI shear zone). The main difference between the experiments is that they were carried out under different flow conditions and therefore different residence times.

This chapter provides information on the procedures used in these two experiments and on previous models of these experiments (and other migration experiments carried out during the CFM and CRR projects). Finally, details are given about the inverse modelling that was undertaken by Dr Lindsay McMillan, which resulted in a transmissivity distribution that was used in the transport model described in Chapter 4.

## **3.2. Grimsel Test Site**

### **3.2.1. Geological Setting**

The Grimsel Test Site (GTS) is situated in the Bernese Alps in Switzerland, located at a depth of approximately 400 to 450m below ground level within the Grimsel granodiorite host rock (Blechsmidt and Vomvoris, 2009). The granodiorite is a medium to coarse grained crystalline rock intersected by a series of dykes and shear zones (Möri et al., 2004). Figure 3.1 shows an aerial view of the GTS, where a number of lakes are present due to a nearby hydroelectric power station. A series of tunnels have been excavated using tunnel boring machines (TBMs) into the Grimsel granodiorite host rock, taking advantage of the hydroelectric power plant infrastructure, as shown in Figure 3.2.

The two migration experiments were carried out in the MI shear zone, in the section of shear zone that intersects the AU tunnel. The shear zone has a complex geological structure resulting from several stages of deformation. Early ductile mylonite shear zones were reactivated and overprinted by further brittle deformation (Gaus and Smith, 2008). The shear zone runs parallel to mineral cleavage and is steeply dipping to the south (approximately 70 degrees), extending laterally for over 100 metres (Gaus and Smith, 2008), intersecting other tunnels at the site (Lanyon and Blechsmidt, 2016) as shown in Figure 3.3.



Figure 3.1 Aerial view at the surface of the Grimsel Test Site looking west. 1: Grimsel Test Site, 2: Räterichsbodensee, 3: Grimselsee, 4: Juchlistock. (From: Schlickenrieder et al. 2017)

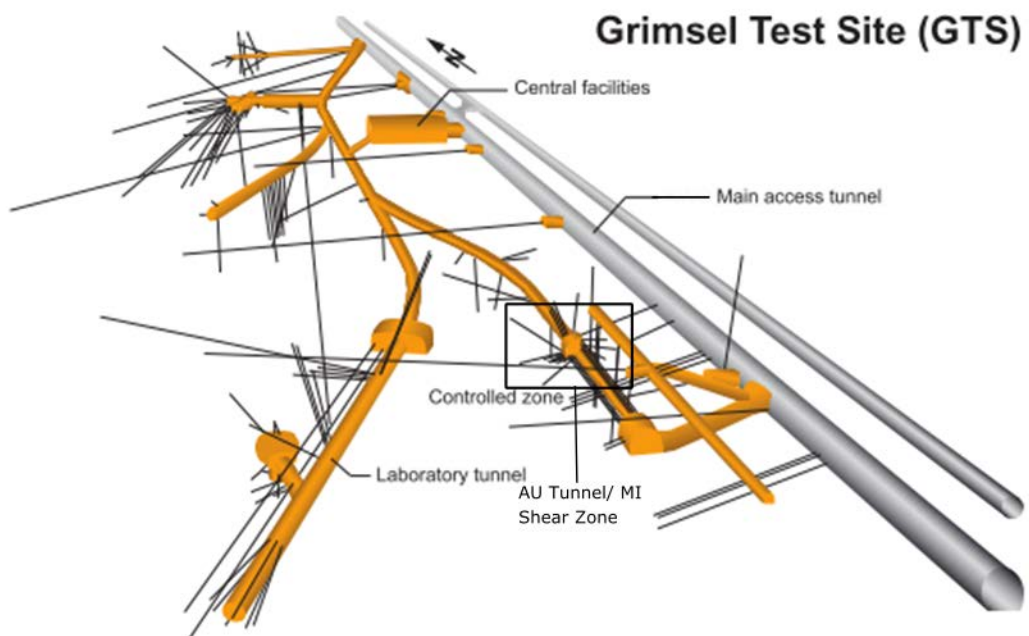


Figure 3.2 Schematic diagram of the different tunnels and boreholes drilled at the Grimsel Test Site (Altered from Schlickenrieder et al. 2017)

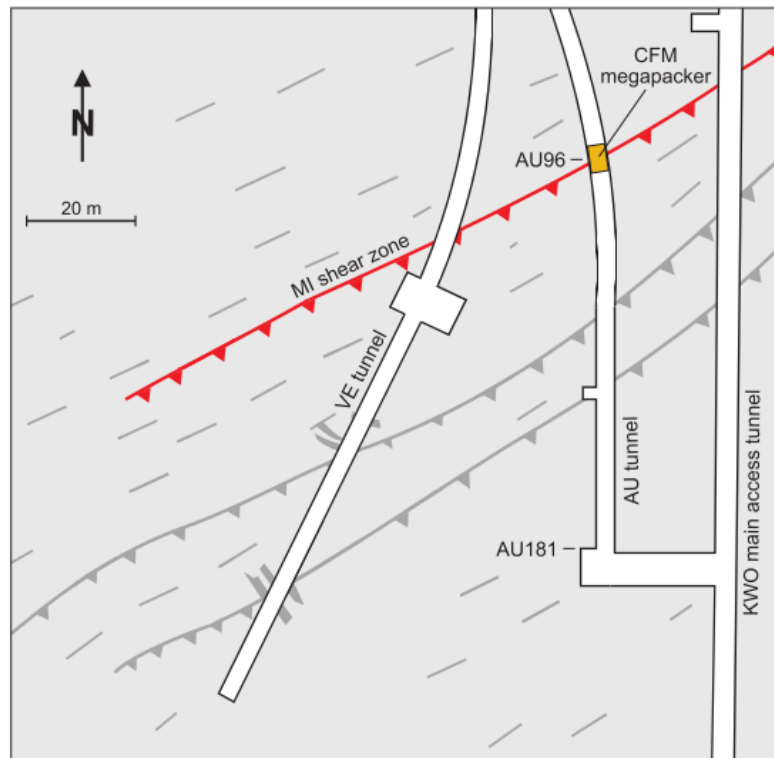


Figure 3.3 Map of the MI shear zone, showing the intersection with the AU tunnel (highlighted by the CFM megapacker), the VE Tunnel and the main KWO access tunnel (From: Schlickerieder et al. 2017)

The shear zone contains a series of between 1 and 3 braided shear planes termed water conducting features (WCFs) (Gaus and Smith, 2008). The thickness of these WCFs varies, but is typically around a few mm (Gaus and Smith, 2008). Figure 3.4 shows a map of the outcrop of the MI shear zone in the AU tunnel walls, clearly showing the braided structure. The lateral extent of the shear zone is much larger than its thickness, therefore it is normally conceptualised as a 2D structure for groundwater models (Smith et al., 2006).

The WCFs are variably filled with fracture fill material (FFM) generated by the latter brittle deformation of the shear zone. The main difference between the Grimsel granodiorite host rock, the mylonite shear zones and the FFM is that the granodiorite and mylonite is less porous (matrix porosity <1%), than the FFM (~40%) (Gaus and Smith, 2008).

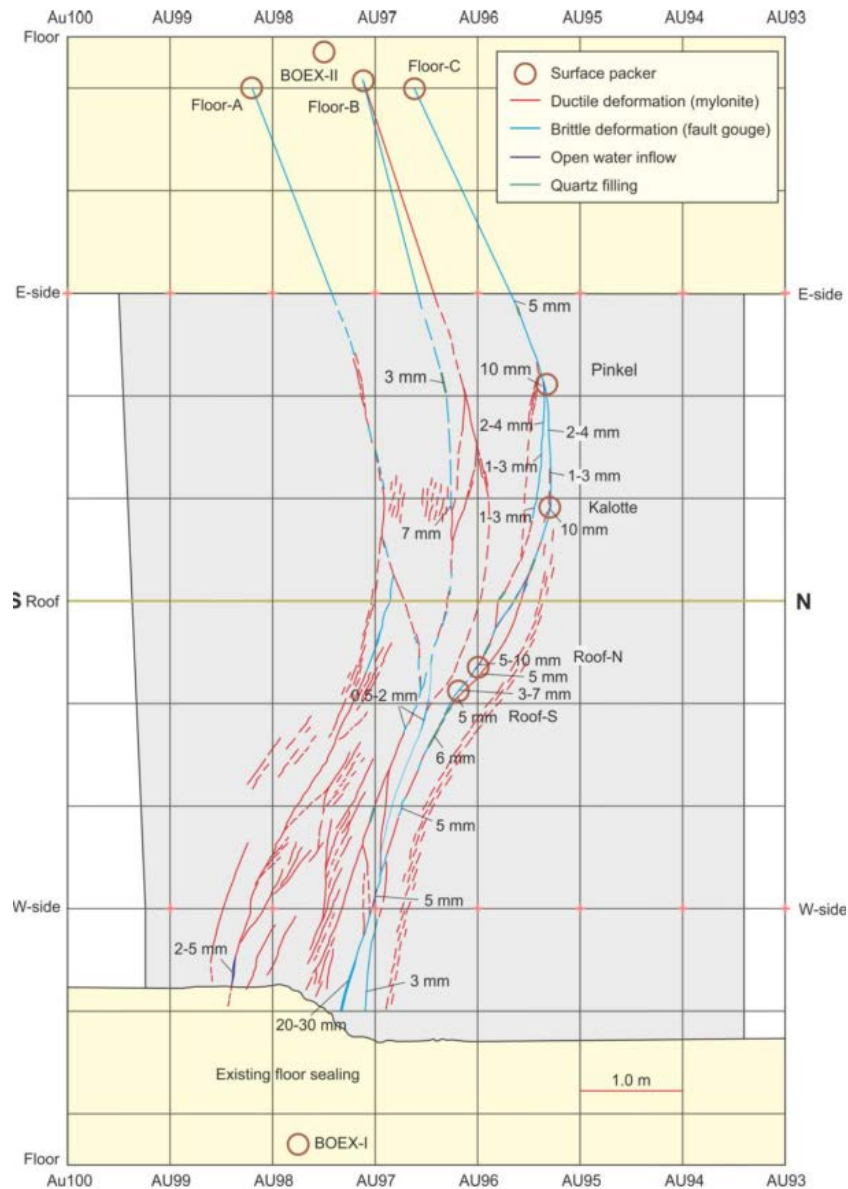


Figure 3.4 Map of the structure of the MI shear zone, as taken from the outcrop at the intersecting AU tunnel (From: Gaus and Smith 2008)

### 3.2.2. Hydrogeology

Groundwater flows in the MI shear zone through the multiple WCFs, which are highly heterogeneous and variably filled with FFM (Gaus and Smith, 2008), with transmissivity values measured locally at boreholes range between  $10^{-10}$  and  $10^{-6}$   $m^2/s$  (Schlickerieder et al., 2017). Regional groundwater head gradients mean that groundwater flows into the AU tunnel, flowing largely into six discrete points around the tunnel. Total inflows into the AU

tunnel are the largest in the southern part of the Grimsel test site (Gaus and Smith, 2008), measured between 400ml/min and 700 ml/min depending on the condition of tunnel sealing and whether flow rates had stabilised after drilling (Lanyon and Blechschmidt, 2016). Inflows from the MI shear zone into the neighbouring VE tunnel and the main access tunnel, both around 50 metres away from the AU tunnel, are less than 1 ml/min (Schlickenrieder et al., 2017).

One of the objectives of the CFM project was to investigate colloid-facilitated radionuclide transport under conditions that represent a repository flow system i.e. very low flow velocity (Schlickenrieder et al., 2017). A novel mega packer system was installed in the AU tunnel, to provide a greater control on flow and hydraulic gradients in the MI shear zone than in previous migration experiments. A diagram of the mega-packer is shown in Figure 3.5. More detail on the construction and design of the mega packer system is found in Schlickenrieder et al. (2017), but in summary the discrete inflow points into the tunnel are covered by surface packers. Once this was completed, the tunnel surface was resin-sealed. Finally, the tunnel was lined by a steel tunnel, with O-ring packers at each end. These combine with a water filled annulus to provide support and pressure on the resin sealing. Inflows into the tunnel from these inflow points are currently 25 ml/min (Lanyon and Blechschmidt, 2016), far lower than measured during previous experiments (~400-700 ml/min).

Situated at the surface above the Grimsel Test Site are multiple lakes and reservoirs (Figure 3.1) due to the nearby hydroelectric power station (Schlickenrieder et al., 2017). Hydraulic head values in the MI shear zone vary by approximately 1m with no changes to

inflows or extraction from the shear zone (Schlickenrieder et al., 2017). A strong correlation exists between lake levels in the Grimselsee reservoir to the south and hydraulic head values in the shear zone. Changes in lake levels alter head values by approximately 4% of the change in lake level (Schlickenrieder et al., 2017). It is believed that this is mainly caused by changes in rock stress in the mountain above the test site, compressing the shear zone and increasing pressure. It could also be caused by changes to hydraulic head in structures hydraulically connected to the Grimselsee, driving flow into the shear zone (Schlickenrieder et al., 2017). Changes in lake level can be caused by changes in pumping rates from the reservoir, seasonal changes or tides (Lanyon and Martin, 2014; Schlickenrieder et al., 2017). Changes in the water level in the Grimselsee have limited impact on differential head measurements within the shear zone, indicating that the changes in hydraulic head occur relatively uniformly within the shear zone (Schlickenrieder et al., 2017).

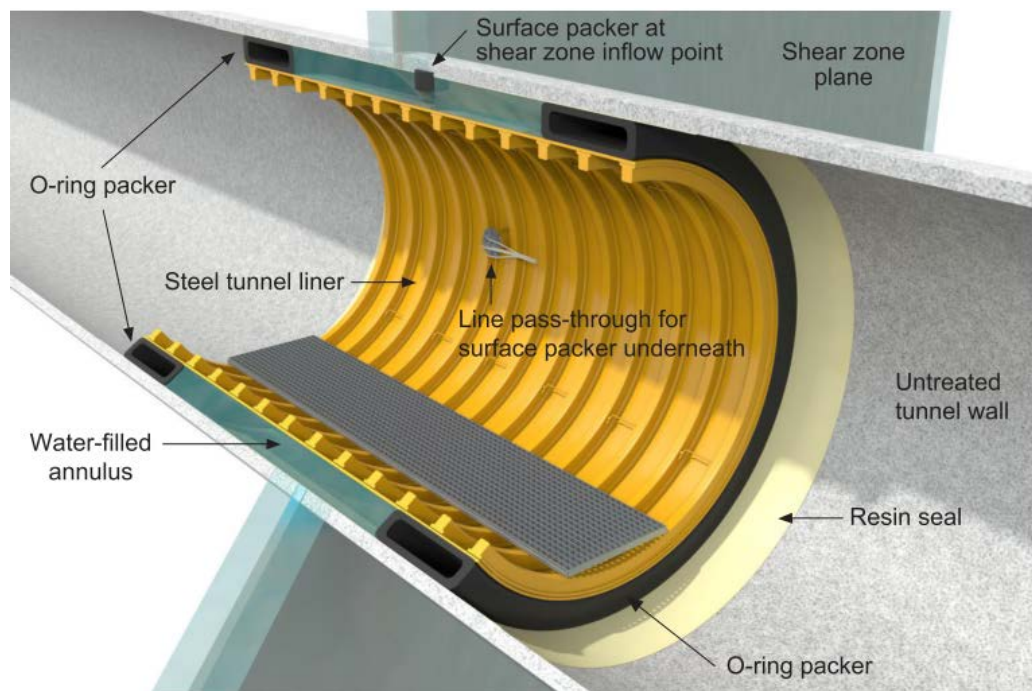


Figure 3.5 Schematic of the mega-packer system installed during the CFM project. Full details found in Schlickenrieder et al. (2017)

Several boreholes have been drilled to intersect the MI shear zone from different locations within the AU tunnel. These boreholes intersect the shear zone at different angles, and are all packed across the shear zone interval. The layout of where these boreholes intersect the shear zone are shown in Figure 3.6. CFM Run 13-05 and CRR Run 32 were carried out between boreholes CRR 99.002 and BOMI 87.010. The distance between these two boreholes is 2.3 metres, and is referred to as CRR Dipole 1 (Möri et al., 2004), (blue arrow on Figure 3.6).

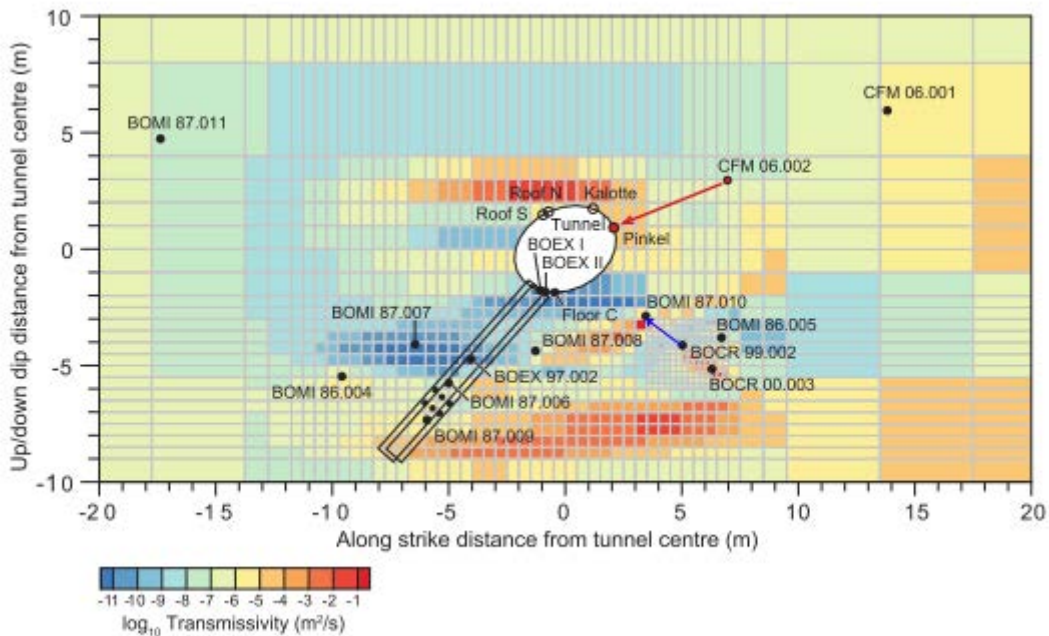


Figure 3.6 Map of the MI shear zone, with the transmissivity field generated by inverse modelling using a geostatistical approach during the CRR project, detailed in Jódar et al. (2002). Boreholes drilled from different locations in the AU tunnel, shown where they intersect with MI shear zone. BOCR 99.002 and BOCR 00.003 refer to boreholes CRR 99.002 and CRR 00.003. Red arrow shows CFM dipole between CFM 06.002 and Pinkel (used in CFM 12-02) and blue arrow shows CRR Dipole 1 between CRR 99.002 and BOMI 87.010 (used in CRR 31, 32 and CFM 13-05). Altered from: Schlickerieder et al. (2017).

Grimsel groundwater is low ionic strength ( $\sim 0.001M$ ), low carbonate concentration ( $<10^{-4} M$ ), high pH ( $\sim 9.6$ ) (Geckeis et al., 2004), and is commonly classified as Na-Ca- $HCO_3$  groundwater (Duro et al., 2000). Grimsel groundwater has been used as a reference water

for glacier melt water (for instance, in SKB's safety case, see Bennett (2014)). A typical composition of Grimsel groundwater is shown in Table 3.1.

Eh values for Grimsel groundwater are typically around -200mV (standard hydrogen electrode/ SHE), although measurements have been as high as -70 mV (Duro et al., 2000). Limited information exists as to the cause of the low Eh value. Redox speciation modelling carried out in Duro et al. (2000) did not definitively determine which redox couple was the cause of the low Eh, finding that the  $\text{SO}_4^{2-}/\text{HS}^-$  couple or the oxidation of Fe-bearing minerals are potential causes of the low Eh (Duro et al., 2000).

<i>Element</i>	<i>Concentration (M)</i>	<i>Element</i>	<i>Concentration (M)</i>
Al	2.63e-6	Mg	6.2e-7
Br	3.8e-7	Mn	5e-9
Ca	1.4e-4	Na	6.9e-4
Cl	1.6e-4	S	6.1e-5
F	3.6e-4	Si	2.5e-4
Fe	3e-9	Sr	2e-6
K	5e-6	$\text{HCO}_3^-$	4.5e-4

**Table 3.1 Composition of Grimsel groundwater, as used in Bennett (2014)**

Using the composition of all the elements detailed in Table 3.1, geochemical modelling using PHREEQC has been carried out to predict saturation indices for the precipitation of mineral phases. This modelling used the PSI/ Nagra thermodynamic database (TDB) (Thoenen et al., 2014), assuming a temperature of 12 degrees, using pH values between 9 and 11 and Eh values between -150mV and -300mV. Full details on the geochemical modelling methods are found in Appendix A. Figure 3.7 shows the variation in positive saturation indices for mineral phases in Grimsel groundwater with pH, and Figure 3.8 for changes in Eh. These figures show that at the pH and Eh values of reference Grimsel groundwater, and therefore expected to represent the conditions in the two migration

experiments (pH 9.6, Eh -220 mV), favourable conditions for precipitation are predicted for the precipitation of goethite, hematite and magnetite, kaolinite, aragonite and calcite. This is important as this may have an impact on radionuclide behaviour; especially if Fe(II) bearing mineral phases are precipitating (see Chapter 7 for further discussion).

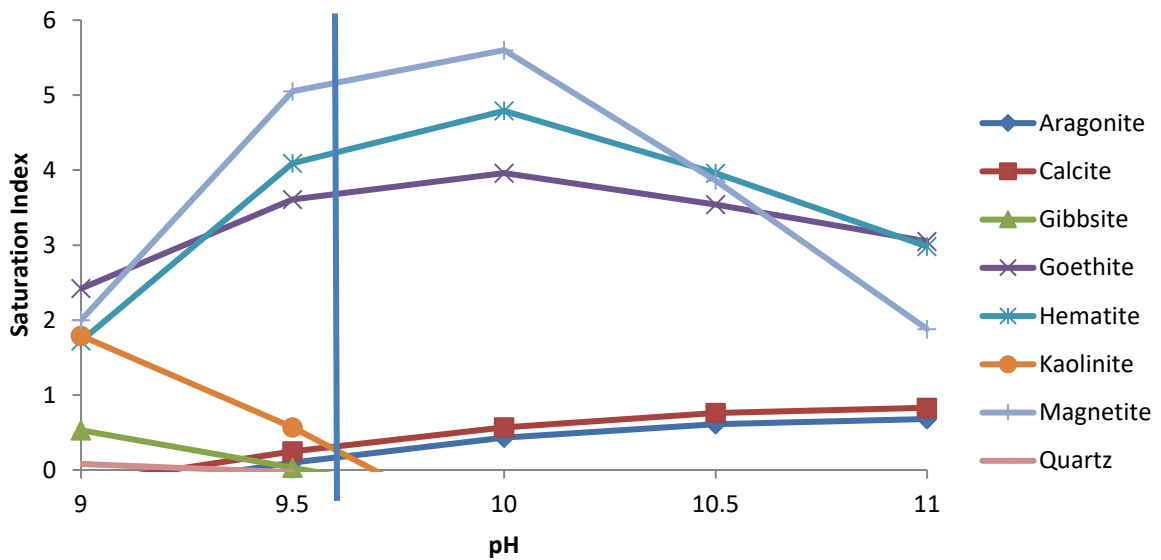


Figure 3.7 Positive saturation indices for mineral phases in Grimsel groundwater as a function of pH (Eh -220mV), as calculated using PHREEQC, using the PSI/ Nagra TDB. Blue line = pH 9.6, the average value for Grimsel groundwater.

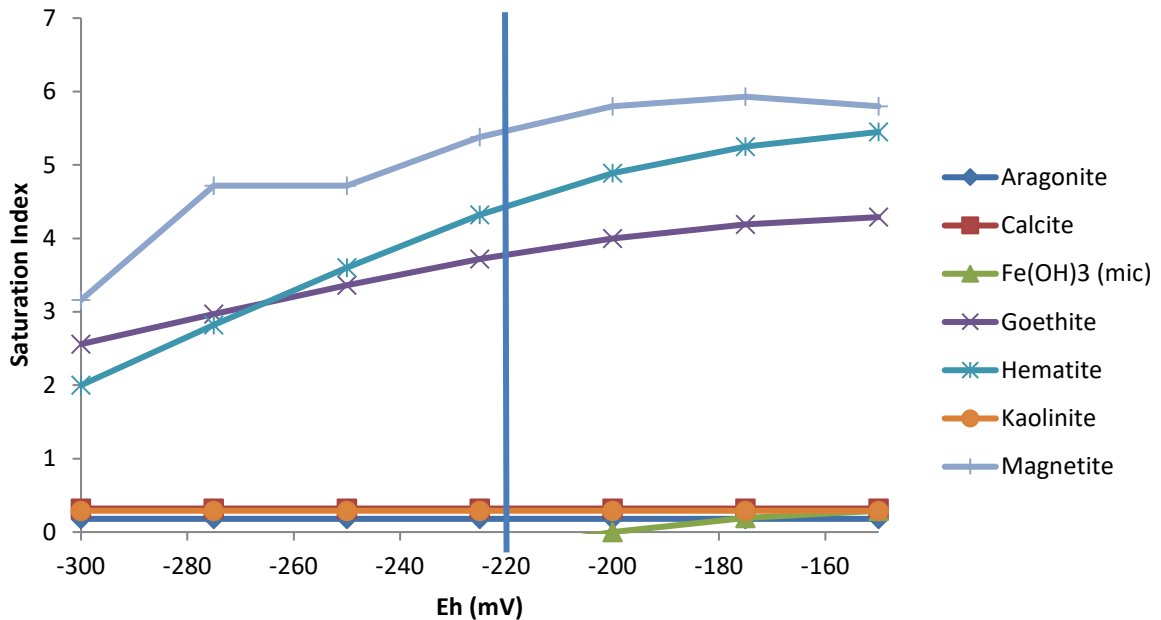


Figure 3.8 Positive saturation indices for mineral phases in Grimsel groundwater as a function of Eh (pH 9.6), as calculated using PHREEQC and PSI/Nagra TDB. Blue line = Eh -220mV, the average value measured in Grimsel groundwater.

### **3.3. Colloid Formation and Migration (CFM) Project**

#### **3.3.1. Background and Objectives**

The Colloid Formation and Migration (CFM) project has been run at the Grimsel Test Site since 2004. The project was set up to improve understanding of the impact of colloids generated from bentonite clay on radionuclide migration in low ionic strength groundwater.

The objectives of the experiment are (as listed by Schlickenrieder et al. (2017)):

- To examine colloid generation mechanisms and rates at the boundary between the engineered barrier and host rock under *in situ* conditions.
- Evaluate the migration of colloids derived from the engineered barrier under long-distance (~10m scale), repository relevant flow conditions (low flow velocities).
- Study long-term geochemical behaviour of radionuclides at the engineered barrier- host rock boundary.
- Examine the reversibility of radionuclide-colloid interactions.
- Gain experience in monitoring of radionuclide/colloid migration in long-term conditions near a repository.

#### **3.3.2. Previous Experiments in the MI Shear Zone**

This section summarises the relevant work that has been carried out in previous projects carried out in the MI shear zone, based on the summaries in Schlickenrieder et al. (2017) and Lanyon and Blechschmidt (2016).

The first experiment carried out in the MI shear zone was the Migration Experiment (MI) (1988-1996). Eight of the thirteen boreholes that have been drilled to intersect the MI shear zone were drilled during the MI experiment, and a large programme of hydraulic

characterisation was carried out for each borehole. Local transmissivity values were derived from short pulse tests, and longer constant rate pumping and pressure recovery tests determined larger scale properties and hydraulic connections in the shear zone (Schlickenrieder et al., 2017; Gaus and Smith, 2008). The effective transmissivity of the shear zone is estimated to be  $\sim 10^{-6}$  m<sup>2</sup>/s (on a 10m scale), with local transmissivity values varying between  $10^{-10}$  and  $5 \times 10^{-6}$  m<sup>2</sup>/s. Subsequent hydraulic tests were in a similar range to these results (Schlickenrieder et al., 2017). In addition, tracer tests were run using conservative and sorbing tracers in different dipoles during MI.

The Excavation Project (EP) (1996-1998) ran conservative and radionuclide tracer tests in a small dipole (1.76m) in the MI shear zone. After the radionuclide migration experiment, resin injection stabilised the shear zone and sorbed radionuclides, before overcoring for detailed characterisation of the shear zone. The section of overcored borehole has since been sealed with a mixture of sand and resin. During this project, a geostatistical inverse model of the shear zone was produced from the characterisation work from the MI experiment (see details in Gaus and Smith (2008)).

The CFM project directly builds on work from the Colloid and Radionuclide Retardation (CRR) project, (1999-2002). Two further boreholes were drilled and characterised during CRR. Initial tracer tests using conservative tracers, bentonite colloids and radionuclide homologues were carried out to determine the dipole and flow conditions that would result in the high recovery required to fulfil the license requirements for the main radionuclide migration experiments. As part of the CRR experiment the inverse model mentioned above was updated with new hydraulic data from the Excavation Project and

CRR, adding the new boreholes (see Jódar et al. (2002) and Section 3.6 for further details). Following this, two main field migration experiments CRR Run 31 and CRR Run 32, investigated radionuclide migration in the absence and presence of bentonite colloids respectively. Peak arrival times in these two experiments were around 1 hour. These experiments are discussed further in Section 3.4, but further detail can be found in Möri et al. (2004) for the field programme, and Missana and Geckeis (2006) for the laboratory programme. Modelling of the CRR experiments is reviewed in Section 3.5.

### **3.3.3. CFM Project**

The CFM project has been run since 2004. Early phases of the experiment focused on site selection and preparation of the MI shear zone around the AU tunnel, installing the novel mega-packer system which allowed for the reduction in water entering the tunnel and therefore lower hydraulic gradients within the shear zone (Schlickenrieder et al., 2017). Early migration experiments tested the mega-packer system by injecting conservative tracers, colloids and radionuclide homologues with steadily decreasing flow rates (Lanyon and Blechschmidt, 2016), to ensure that recovery values required by the license for Grimsel would be met in the radionuclide/colloid migration experiments. Two radionuclide/colloid migration experiments have been run in CFM to date, CFM Run 12-02 and CFM Run 13-05, which are discussed in Section 3.4.

The recent focus of the CFM project has been the Long-Term In-situ experiment (LIT), which has been running since May 2014 to investigate colloid formation, migration and radionuclide transport over long time periods. The LIT used a source of compacted bentonite rings which contained glass vials of radionuclides, conservative tracers and montmorillonite

clay (Schlickenrieder et al., 2017). The source is mounted on a special packer system and was emplaced in borehole CFM 06.002 within the shear zone. Groundwater flow during the LIT is controlled by the extraction of water from the Pinkel surface packer (kept constant at 25ml/min). Full information about the setup of the LIT is found in Schlickenrieder et al. (2017). It is expected that the experiment will continue (at time of writing) until early 2018 when the source will be stabilised with resin injection, and then overcored for detailed analysis (Schlickenrieder et al., 2017).

In addition to the extensive field programme, supporting laboratory experiments investigating bentonite erosion, colloid generation, colloid migration and stability and radionuclide sorption have been carried out (e.g. Schafer et al. (2014)). Previous modelling of the CFM migration experiments is discussed in more detail in Section 3.5. Planning for future work in the CFM project is underway at time of writing (Schlickenrieder et al., 2017).

### **3.4. Experimental Procedures**

#### **3.4.1. Introduction**

Three radionuclide-colloid migration experiments have been carried out at the MI Shear Zone at GTS; CRR Run 32, CFM Run 12-02, and CFM Run 13-05. In addition, CRR Run 31 was carried out without the presence of colloids, with identical injection and abstraction rates to CRR Run 32 (Möri et al., 2004). The two CRR experiments and CFM Run 13-05 were carried out between two boreholes referred to as CRR Dipole 1, with injection occurring at borehole CRR 99.002 and abstraction occurring at borehole BOMI 87.010 (Figure 3.4). In CFM Run 12-02 the experiment was run between borehole CFM 06.002, and the Pinkel surface packer (referred to as CFM Dipole 1), so colloid-facilitated radionuclide transport

could be investigated over a longer distance than the other experiments. These experiments were all carried out in asymmetric dipoles to ensure high radionuclide recovery, as required under the licensing for the experiments. Table 3.2 provides a summary of the background information and hydraulic parameters for the four experiments.

<i>Experiment</i>	<b>CRR Run 31<sup>1</sup></b>	<b>CRR Run 32</b>	<b>CFM Run 12-02<sup>1</sup></b>	<b>CFM Run 13-05</b>
<i>Dipole used</i>	CRR Dipole 1	CRR Dipole 1	CFM Dipole 1	CRR Dipole 1
<i>Distance</i>	2.3 m	2.3 m	5.7 m	2.3 m
<i>Tracer Injection Rate</i>	10 ml/min	10 ml/min	0.33 ml/min	0.33ml/min
<i>Abstraction Rate</i>	150 ml/min	150 ml/min	25ml/min	5ml/min <sup>2</sup>
<i>Peak Arrival</i>	~1.5 hours	~1.5 hours	50 hours	44 hours
<i>Type of Injection</i>	Direct	Direct	Re-circulation/ Dilution	Re-circulation/ Dilution
<i>Injected</i>	<sup>131</sup> I, Radionuclides	<sup>131</sup> I, Radionuclides and Colloids	Amino-G Acid, Radionuclides and Colloids	Amino-G Acid, Radionuclides and Colloids

<sup>1</sup>: Included for information, not modelled in thesis

<sup>2</sup>: Additional 25ml/min extracted from Pinkel surface packer

**Table 3.2 Summary of background and hydraulic parameters for radionuclide-colloid field migration experiments.**

In this thesis CRR Run 32 and CFM Run 13-05 have been modelled, which were carried out in the same dipole (CRR Dipole 1), but due to the installation of the mega packer in the CFM experiment, at very different flow rates (CRR Run 32 was carried out at ~30 times higher flow rates than CFM Run 13-05). These two experiments are described further in the following sections.

### **3.4.2. Injection Process**

The injection cocktails for both experiments were prepared by the experimental teams at KIT-INE. In CRR Run 32, a colloid suspension was made up from FEBEX bentonite, by equilibrating the bentonite in Grimsel groundwater taken from the MI shear zone, then centrifuging the suspension multiple times and diluting it with Grimsel groundwater until the

required colloid concentration (20 mg/l) was reached (Möri et al., 2004). This suspension was then spiked with nine radionuclides plus Iodine-131 (as a non-reacting tracer) at the concentrations shown in Table 3.3, five days before the experiment was run. More details of the cocktail preparation are found in Möri et al. (2004).

<i>Experiment</i>	<b>CRR Run 32</b>	<b>CFM Run 13-05<sup>1</sup></b>
<i>Conservative Tracer</i>	Iodine-131: $1.21 \times 10^{-4}$ µg/l	Amino-G Acid: 1980 µg/l
<i>Colloids</i>	FEBEX Bentonite: 20.1 mg/l	FEBEX Bentonite: 85.8 mg/l Ni-montmorillonite: 13.9 mg/l
<sup>22</sup> Na	N/A	$2.90 \times 10^{-3}$ µg/l
<sup>133</sup> Ba	N/A	0.45 µg/l
<sup>85</sup> Sr	$9.41 \times 10^{-4}$ µg/l	N/A
<sup>137</sup> Cs	1.9 µg/l	0.12 µg/l
<sup>99</sup> Tc	1.03 µg/l	N/A
<sup>232</sup> Th	2.55 µg/l	1.04 µg/l
<sup>233</sup> U	202 µg/l	0.1 µg/l
<sup>237</sup> Np	258 µg/l	2.04 µg/l
<sup>238</sup> Pu	0.01 µg/l	N/A
<sup>242</sup> Pu	N/A	0.48 µg/l
<sup>244</sup> Pu	1.64 µg/l	N/A
<sup>241</sup> Am	0.17 µg/l	N/A
<sup>243</sup> Am	N/A	0.10 µg/l

1: Concentrations as measured in 2.25L pressure vessel (see Figure 3.9)

**Table 3.3 Concentrations in the injection cocktails used in the two migration experiments.**

It is expected that the injection cocktail for CFM Run 13-05 was prepared using a similar method to CRR Run 32, as exact documentation on the preparation is not currently available at time of writing. However, there are some differences in the injection cocktail between the two experiments. In CFM Run 13-05, amino-G acid (AGA) was used as a conservative tracer. In addition to FEBEX bentonite, artificially labelled Ni-montmorillonite colloids were also included in the injection cocktail (Schäfer et al., 2013) to provide greater analytical certainty in the measurements of colloid concentration. Colloid concentration could then be measured by analysing nickel concentration (Lanyon and Blechschmidt, 2016),

which helps to determine whether bentonite colloids from previous experiments were being mobilised during the migration experiment. The colloid suspension was spiked with the amino-G acid and seven radionuclides, at the concentrations shown in Table 3.3, 35 days before the experiment was run.

The injection cocktails were both injected into borehole CRR 99.002, albeit using different methods. In CRR Run 32, a 100ml slug of the injection cocktail was injected by interrupting a 10 ml/min injection of Grimsel groundwater, injecting the cocktail at the same flow rate for 10 minutes (Möri et al., 2004). After the 10 minutes, injection was switched back to Grimsel groundwater.

For CFM Run 13-05, a 2.25L pressure vessel containing the injection cocktail was connected to a recirculation circuit intersecting the borehole interval, (total volume ~3.2L) (Kontar et al., 2013). Fluid in the circuit was then circulated at 20ml/min, and fresh Grimsel groundwater was injected into the circuit at 0.33 ml/min, maintaining a net inflow into the shear zone of 0.33 ml/min. The concentration of the conservative tracer was monitored in the circulation circuit by a fluorimeter providing a source term for modelling. A conceptual diagram summarising the injection process used in CFM Run 13-05 is shown in Figure 3.9.

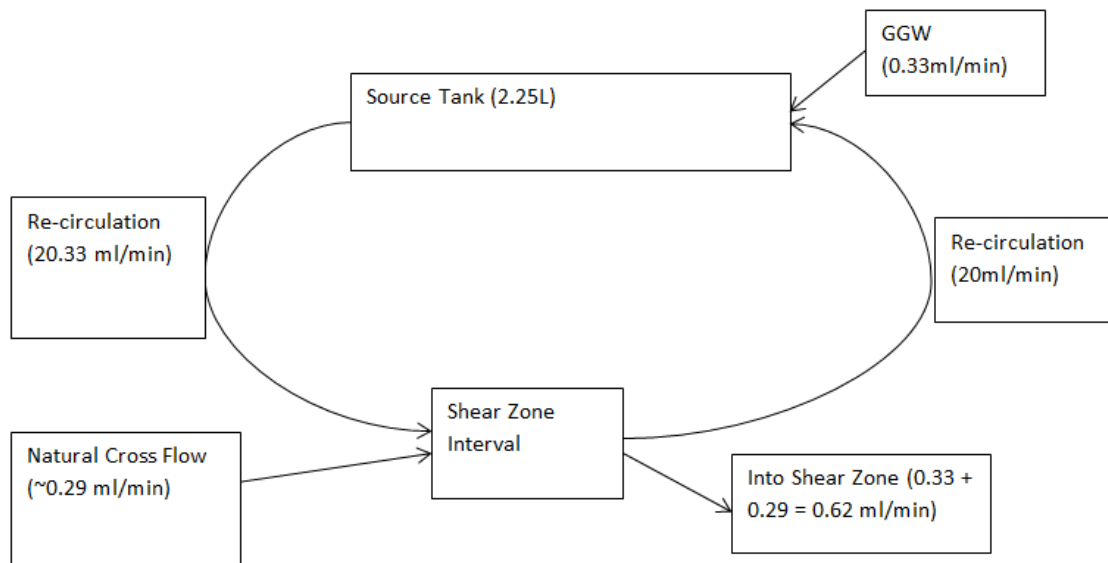


Figure 3.9 Conceptual diagram showing the injection used in CFM Run 13-05. Natural cross flow estimated by measuring the slope of the tracer concentration decline in the injection interval.

Discrepancies with the source term for CFM Run 13-05 were observed when the rate of concentration was compared to CFM Run 12-02 (which was carried out using the same method and flow rates), as the fall in concentration of tracer was occurring faster than expected. The discrepancy is caused by natural cross-flow occurring across the borehole/shear zone interval, causing further dilution and faster injection than originally intended. Estimates of the cross-flow give an average flow of 0.29 ml/min, as measured from the slope of the tracer concentration in the injection interval. Further discussion on this source term and how it is represented in the transport model is given in Chapter 4.

### 3.4.3. Monitoring Process

Details of the monitoring process for the two experiments are found in Möri et al. (2004) and Kontar et al. (2013); this section provides a short summary.

During CFM Run 13-05, pressure/ hydraulic head was measured in several boreholes. Differential pressure measurements were also made between the injection, extraction (and

other boreholes) and the Pinkel surface packer (Kontar et al., 2013). Flow measurements were made at both injection and extraction boreholes and the Pinkel surface packer. Within the injection and extraction lines, pH, turbidity, electric conductivity, temperature and Eh measurements were made (Kontar et al., 2013). Similar measurements were also made during CRR Run 32, although instead of turbidity and electrical conductivity, dissolved oxygen concentrations was measured (Möri et al., 2004).

Different methods of measuring the conservative tracer were used between the experiments due to the different tracers used. In CRR Run 32 iodine-131 concentrations were analysed by  $\gamma$ -spectroscopy and ICP-MS from samples from the extraction borehole, (Möri et al., 2004). There was no measurement of  $^{131}\text{I}$  concentrations in the injection borehole, so there is no direct measurement of the source term. However, the simple method used for injection in CRR Run 32 (see previous section) means that the source term can be easily replicated. For CFM Run 13-05, concentrations of amino-G acid were measured in both the injection and extraction boreholes by fluorimeters (Kontar et al., 2013).

Colloid concentrations in CFM Run 13-05 were measured by Laser Induced Breakdown Detection (LIBD) installed on the extraction borehole line (Kontar et al., 2013). Colloid concentrations were also measured by measuring the Al and Ni concentrations using ICP-MS (Lanyon and Blechschmidt, 2016). LIBD was also used in CRR Run 32, along with Photon Correlation Spectroscopy (PCS), ICP-MS measurements of Al concentrations and Single Particle Counting (SPC) of particular colloid size ranges (Möri et al., 2004). Colloid sizes were measured in CRR Run 32 by LIBD, PCS and SPC, and by LIBD in CFM Run 13-05, although this data was still being finalized at time of writing.

Radionuclide concentrations have been measured by ICP-MS,  $\alpha$ - or  $\gamma$ - spectroscopy, as indicated in Table 3.4. In addition, selected samples from CFM Run 13-05 were used for Accelerator Mass Spectroscopy (AMS) measurements of  $^{243}\text{Am}$ ,  $^{242}\text{Pu}$ ,  $^{237}\text{Np}$  and  $^{233}\text{U}$  concentrations (see Quinto et al. (2017) for more details). AMS provides greater resolution, allowing analysis of concentrations below parts per quadrillion levels (Lanyon and Blechschmidt, 2016), and has been used to provide long-term breakthrough data for the dissolved phase radionuclides (Lanyon and Blechschmidt, 2016).

Finally, in both experiments, the initial 'colloid bound fraction' of the injection cocktail was measured by determining the concentration of each radionuclide removed from solution after the injection cocktail was centrifuged. The colloid bound fraction was measured within a week after radionuclide spiking of the cocktail for CRR Run 32 (Reimus, 2016), but equipment issues meant that the initial bound fraction for CFM Run 13-05 was measured 401 days after radionuclide spiking (Schäfer et al., 2013). This could have led to different values in the two experiments.

<i>Experiment</i>	<b>CRR Run 32</b>	<b>CFM Run 13-05</b>
<i>Conservative tracer</i>	<sup>131</sup> I: Off-site ICP-MS, On and offsite $\gamma$ -spectroscopy	AGA: On-site fluorimeters in injection and abstraction boreholes
<i>Colloids</i>	Off-site: Laser Induced Breakdown Detection (LIBD) Al concentration (ICP-MS) Photon Correlation Spectroscopy (PCS) Single Particle Counting (SPC)	On-site Laser Induced Breakdown Detection (LIBD) Off-site Al/ Ni concentration (ICP-MS)
<sup>22</sup> Na	N/A	Off-site $\gamma$ -spectroscopy
<sup>133</sup> Ba	N/A	Off-site $\gamma$ -spectroscopy
<sup>85</sup> Sr	Off-site $\gamma$ -spectroscopy	N/A
<sup>137</sup> Cs	Off-site $\gamma$ -spectroscopy	Off-site $\gamma$ -spectroscopy
<sup>99</sup> Tc	Off-site ICP-MS	N/A
<sup>232</sup> Th	Off-site ICP-MS	Off-site ICP-MS
<sup>233</sup> U	Off-site ICP-MS Off-site $\alpha$ -spectroscopy (in pair with <sup>237</sup> Np)	Off-site ICP-MS Off-site Accelerator Mass Spectroscopy (AMS)
<sup>237</sup> Np	Off-site ICP-MS Off-site $\alpha$ -spectroscopy (in pair with <sup>233</sup> U)	Off-site ICP-MS Off-site AMS
<sup>238</sup> Pu	Off-site $\alpha$ -spectroscopy (in pair with <sup>241</sup> Am)	N/A
<sup>242</sup> Pu	N/A	Off-site ICP-MS Off-site AMS
<sup>244</sup> Pu	Off-site ICP-MS	N/A
<sup>241</sup> Am	Off-site ICP-MS Off-site $\alpha$ -spectroscopy (in pair with <sup>238</sup> Pu)	N/A
<sup>243</sup> Am	N/A	Off-site ICP-MS Off-site AMS

**Table 3.4 Analytical methods used to measure concentration of species in abstraction borehole (unless indicated) in CFM Run 13-05 and CRR Run 32.**

### **3.5.Previous Modelling**

This section reviews the models that have been previously applied to model the colloid-facilitated radionuclide transport experiments at the Grimsel Test Site.

Four modelling teams (PSI, Enviro, FZK-INE and JNC) were involved with modelling the CRR migration experiments. Table 3.5 summarises the models, including the representation of different processes and assumptions made, more detail is provided by Smith et al. (2006) and Kosakowski and Smith (2004).

Three modelling teams (GRS, LANL and KTH) have been modelling CFM migration experiments with documented model results. Table 3.6 summarises these models, but more information can be found in Noseck et al. (2016) which details the modelling of early CFM tracer, colloid and homologue migration experiments before modelling americium and plutonium transport in CFM Run 12-02. Reiche et al. (2015) describe the other model produced by the GRS modelling team, and Reimus (2016) details the modelling carried out by LANL of both CFM and CRR migration experiments, and is the only documented modelling of radionuclides other than americium and plutonium carried out during the CFM project. Early modelling by KIT-INE on conservative tracer migration is described in Huber et al. (2014) and Pudewills (2008). Finally, modelling teams from KAERI and NUMO are attempting to model the CFM migration experiments (Lanyon and Blechschmidt, 2016; Lanyon et al., 2017), but these models are in development at time of writing and are not discussed further.

<b>Model</b>	<b>FZK-INE</b>	<b>JNC: STAMMT-L</b>	<b>JNC: COLFRAC</b>	<b>Enviros</b>	<b>PSI: 1D/2D advection/dispersion</b>	<b>PSI: Non-fickian dispersion</b>
<i>Dimensions</i>	2D with symmetric domain (25m x 10m), anisotropic transmissivity	1D dual porosity model of dipole.	2D fracture network – multiple horizontal and vertical fractures.	2D model of the shear zone (exact dimensions unclear from published reports)	Multiple 1D paths representing the dipole/homogeneous 2D shear zone (40m x 40m)	1D model of the dipole
<i>Flow field</i>	Directly solved in porous medium	Directly solved in 'mobile zone' of fractures	Directly solved (1D flow in fractures, 2D flow in matrix)	Directly solved in porous medium	Directly solved in 2D porous medium models	Based on continuous time random walk approach
<i>Colloid attachment</i>	Breakthrough scaled to account for attachment	N/A (Tracer breakthrough only)	Irreversible attachment with empirical factor	N/A	Breakthrough scaled to account for attachment	Breakthrough scaled to account for attachment
<i>Radionuclide sorption to colloids</i>	Irreversible sorption to colloids using initial bound fraction	N/A (Tracer breakthrough only)	1 <sup>st</sup> order kinetics, no explicit desorption process	Equilibrium sorption, values based on equilibrium constants	Irreversible sorption to colloids using initial bound fraction	N/A (Colloid breakthrough only)
<i>Number of sorption sites on colloid</i>	1	N/A (Tracer breakthrough only)	1	1	1	N/A (Colloid breakthrough only)
<i>Radionuclide sorption to rock surfaces</i>	Reversible equilibrium using $K_d$	Reversible equilibrium using $K_d$	1 <sup>st</sup> order linear kinetics, no explicit desorption process	Reversible equilibrium using $K_d$	Reversible equilibrium using $K_d$	N/A (Colloid breakthrough only)
<i>Dispersivity</i>	Longitudinal and transverse dispersivity	Longitudinal dispersivity	Longitudinal and transverse dispersivity	Longitudinal and transverse dispersivity	Longitudinal (and transverse) dispersivity	Non-fickian dispersion
<i>Matrix diffusion</i>	N/A	Included	Included	N/A	Included	N/A (Colloid breakthrough only)

Table 3.5 Summary of model assumptions and processes in the CRR models. Information from Smith et al. (2006).

<b>Model</b>	<b>GRS-r<sup>3</sup>t</b>	<b>GRS-COFRAME</b>	<b>LANL-RELAP</b>	<b>KTH-Mathematica</b>	<b>KIT-INE</b>
<i>Dimensions</i>	2D (Homogenous K), symmetrical domain (20.5m x 6m)	1D fracture, dual domain model of dipole	1D model of dipole	1D model of dipole	2D domain (25m x 15m), anisotropic transmissivity
<i>Flow field</i>	Directly solved in porous medium	Directly solved in fracture	Black box (residence time and dispersivity altered)	Black box (residence time and dispersivity altered)	Directly solved in porous medium
<i>Colloid attachment</i>	Irreversible and reversible, 1 <sup>st</sup> order empirical attachment	Empirical reversible attachment (1 <sup>st</sup> order)	Irreversible and reversible, 1 <sup>st</sup> order empirical attachment	Irreversible and reversible, 1 <sup>st</sup> order empirical attachment	N/A (Used for conservative tracer)
<i>Radionuclide sorption to colloids</i>	Reversible kinetics	1 <sup>st</sup> order kinetics, no explicit desorption process	Reversible kinetics	Reversible kinetics	N/A (Used for conservative tracer)
<i>Number of RN sorption sites on colloid</i>	1	1	2	1	N/A (Used for conservative tracer)
<i>Radionuclide desorption rates from colloids</i>	Constant with time	Constant with time	Exponential decay can be specified	Exponential decay can be specified	N/A (Used for conservative tracer)
<i>Radionuclide sorption to rock surfaces</i>	Reversible kinetics	Linear equilibrium (K <sub>d</sub> ) or 1 <sup>st</sup> order kinetic	Reversible kinetics	Reversible equilibrium using K <sub>d</sub>	N/A (Used for conservative tracer)
<i>Rock surface sorption capacity</i>	Infinite	Infinite	Can be limited	Infinite	N/A (Used for conservative tracer)
<i>Dispersivity</i>	Longitudinal and transverse	Longitudinal	Longitudinal, varied for each experiment	Longitudinal	Longitudinal and transverse
<i>Matrix diffusion</i>	Included (but not used)	Included	Included (but not used)	Included (but not used)	N/A (Used for conservative tracer)

Table 3.6 Summary of model assumptions and processes in documented models used in the CFM project. Information from Noseck et al. (2016), Reiche et al. (2015), Pudewills (2008), and Huber et al. (2014).

As can be seen from both tables, both 1D and 2D model domains have been used to model the experiments. The majority of models used homogeneous representations of the MI Shear Zone, with only the FZK-INE model used in CRR including anisotropic transmissivity, this is despite measured transmissivity in the shear zone varying by up to five orders of magnitude.

All of the models assume steady state groundwater flow during the experiments. Some of the models directly solved for groundwater flow, although most of the 1D models inferred flow parameters by matching the residence time and dispersivity of conservative tracer breakthrough. Where a 1D model was used in CRR, an additional dilution factor is applied to the model output to account for diluting water drawn from the shear zone that the model is unable to replicate. The 1D models in CFM did not include this dilution factor, and therefore model outputs here did not account for the observed dilution.

Models in the CRR experiment used more varied representations of the shear zone than the CFM models, as models included multiple 1D flow pathways (PSI-1D), or a fracture network (JNC-COLFRAC). However, these models did not include as many processes as models used for the CFM project. The only model in CRR that includes colloid attachment processes is the JNC-COLFRAC model, which uses an empirical filtration coefficient to describe irreversible colloid attachment. Despite this, it is not clear how colloid attachment was modelled in the COLFRAC model, it appears that the colloid filtration co-efficient was calibrated on individual radionuclide breakthrough data and not colloid breakthrough, as different colloid attachment rates were used to model different radionuclide breakthroughs.

All of the other models of CRR scaled colloid (and corresponding radionuclide) breakthrough by the measured experimental colloid recovery. The Non-Fickian dispersion model was used by PSI to model colloid breakthrough only, as colloids are typically unable to sample the full velocity profile (which causes processes such as size exclusion chromatography). Although colloid breakthrough was accurately replicated by the other models (which assumed that Fickian dispersion accurately described colloid dispersion), it was thought that the non-Fickian dispersion model improved model fit (Smith et al., 2006), thought to be caused by the highly heterogeneous structure of the MI shear zone.

None of the CRR models explicitly include radionuclide desorption kinetics from colloids, with the models either using 1<sup>st</sup> order sorption kinetics (JNC), equilibrium sorption (Enviros) or assuming that radionuclide sorption to the colloids was irreversible, and that the measured colloid bound fraction remained constant (FZK-INE and PSI). These assumptions were made because it was thought that radionuclide desorption did not occur during the short time scales of the migration experiments in CRR.

A large effort was made when modelling the CRR experiments to make blind predictions based on initial homologue migration experiments, and on using  $K_d$  values from laboratory experiments within the models. However, despite this there is still some inconsistency with some model parameters, for instance the FZK-INE model assumes that 50% of Np and U is transported through the system unretarded. Although it did result in good model matches, it is not clear why this value was used, and what the cause of the unretarded transport is. If the unretarded transport is due to colloid-facilitated transport, this value is far above the measured colloid bound fraction and corresponding laboratory values.

The models used in CRR were able to replicate the transport of conservative tracers, and models that included matrix diffusion were able to replicate tracer tailing. These models were able to provide good matches for the transport of the different radionuclides, but parameters were changed to describe radionuclide sorption to rock surfaces from laboratory data to provide better fits to the experimental data. However, the models encountered difficulty modelling the transport of Am, Pu and Th in CRR Run 31, due to the unexpected transport behaviour of these radionuclides in the experiment, as partial colloid-facilitated transport occurred for these radionuclides, the exact cause of which is uncertain. The PSI model attempted to model caesium breakthrough for CRR Run 32, but differences between the predictions made by the model and the experimental data exist. The differences were attributed to the potential desorption of Cs from the colloids, or because of the non-linear sorption behaviour that Cs has (see Chapter 7).

The models used during the CFM project (Table 3.6) included more processes than previously included, as every model included empirical 1<sup>st</sup> order descriptions of irreversible and reversible colloid attachment, and explicitly included desorption kinetics for the radionuclides from colloids. However, only one of these models (the LANL model) has been applied to model radionuclides other than americium and plutonium (Reimus, 2016).

Two out of the three models used in CFM (the LANL and KTH models) inferred groundwater flow parameters by matching the residence time and dispersivity of a conservative tracer. Although these models were able to model the transport of tracers, colloids and radionuclides well, different parameters had to be used between different experiments.

The LANL model used different attachment rates and included different attachment processes between different migration experiments. Both the LANL and KTH models varied the desorption rate for the same radionuclides and homologues from colloids in different experiments. The LANL model could include multiple sorption sites on the colloids, resulting in five possible descriptions of radionuclide desorption, and different descriptions were used for the same homologues in different experiments, as well using different desorption rates.

Although the GRS-r<sup>3t</sup> model solved for the flow field of the experiments in a 2D porous medium, the model still resulted in different desorption rates being used for different experiments (Noseck et al., 2016), which could be related to the use of effective parameters to describe the shear zone. The other model developed by GRS (COFRAME) described the shear zone with a 1D dual porosity model. This model did not include irreversible colloid attachment and instead of explicitly modelling irreversible colloid attachment, colloid (and homologue) breakthroughs were scaled to account for the process (Reiche et al., 2015).

KIT-INE modelled conservative tracer breakthrough in migration experiments carried up to CFM Run 12-02 but could not find consistent parameters to describe the flow in different experiments under different flow fields, despite the inclusion of zones with different properties.

Although these models have generally resulted in good model matches to the experimental data, parameters describing colloid attachment and radionuclide desorption were changed between different experiments. This could be due to the difficulty in finding accurate effective properties that describe groundwater flow in the highly heterogeneous MI

shear zone (measured T values vary over five orders of magnitude (Schlickerieder et al., 2017)).

As described in Section 3.3.2, inverse models have been used to generate a transmissivity distribution of the shear zone, using a geostatistical approach. However, these transmissivity distributions have not been included in models of either the CFM or CRR migration experiments. The model developed in this thesis will include the transmissivity distribution to provide more information on the flow geometry and the geological structure of the shear zone. With this information the model aims to develop a self-consistent description of colloid and radionuclide transport, using the same parameters to describe transport in different experiments.

### **3.6. Inverse Model**

An inverse model was developed for the MI shear zone by Dr Lindsay McMillan; with the resulting transmissivity distribution used in the transport model detailed in Chapter 4. This section summarises the inverse model and its results, and further detail is provided in McMillan et al. (in prep.).

#### **3.6.1. Model overview**

The aim of the inverse model was to find a description of two-dimensional fracture transmissivity and porosity that honoured both varied hydraulic observations and simple metrics of conservative tracer transport. Fully distributed contaminant transport modelling is computationally costly, so alternative approaches to incorporating transport metrics that are appropriate to the repeated model runs required for inverse modelling were considered.

Numerical modelling of transport in the shear zone was undertaken using MODPATH to evaluate travel time (Pollock, 1994) and MT3DMS (Zheng and Wang, 1999), using MODFLOW (USGS, 2016) calculated velocity data. When attempting to model conservative tracer tests, Jódar et al. (2002, 2004) found that simulated dispersion resulted in significant mass loss to the AU tunnel that was not observed in reality. FlowSource (Foley and Black, 2013), a MODFLOW post-processor, provides a rough estimate of (primarily numerical) dispersive capture zones. Here, FlowSource was used to provide an estimate of recovery at the abstraction well under dispersive transport. MT3DMS was used to confirm FlowSource tracer recovery predictions and MODPATH travel times, and to undertake fully distributed contaminant transport modelling of the two tracer tests once inverse modelling had finished.

Inverse modelling was undertaken using PEST (Doherty, 2016a, 2016b). The problem of finding a transmissivity and porosity distribution in the MI shear zone is non-unique. Geostatistics provides one approach to reducing search space and is often perceived to be preferable due to its use of geological knowledge. However, in the MI shear zone geostatistical data is limited to observations in nine boreholes, and is insufficient to derive statistics. Jódar et al. (2002, 2004) used a wide variety of geostatistical varigrams in their model which were equally able to match observed hydraulic data. Here, PESTs parameter regularization approach is used, where highly correlated parameters are smoothed but no underlying geostatistical structure is assumed.

The fracture transmissivity is represented as a two-dimensional equivalent porous medium. The widely used cubic law (Tsang, 1992) is used to relate transmissivity (T) to fracture hydraulic aperture ( $b$ ) and hence porosity (Equation 3.1):

$$b = \left( \frac{12\mu T}{\rho g} \right)^{\frac{1}{3}}$$

**Equation 3.1 Cubic law derived fracture aperture**

The transmissivity obtained from the inverse modelling of hydraulic data is a macroscopic average of the underlying microscopic fracture structure. If transmissivity (and hence hydraulic aperture) is assumed to have a log normal distribution where  $\mu$  and  $\sigma$  are the mean and standard deviation of  $\ln T$ , then three different averages can be calculated (Equation 3.2 to Equation 3.4):

$$T_g = e^{\mu}$$

**Equation 3.2 The geometric mean of transmissivity**

$$T_a = T_g e^{\sigma^2/2}$$

**Equation 3.3 The arithmetic mean of transmissivity**

$$T_h = T_g e^{-\sigma^2/2}$$

**Equation 3.4 The harmonic mean of transmissivity**

where  $T_g$  is the geometric mean,  $T_a$  is the arithmetic mean and  $T_h$  is the harmonic mean ( $T_a \geq T_g \geq T_h$ ), (Dagan, 1979). The laboratory experiments of Zheng et al. (2008) confirmed theoretical analyses and showed that the arithmetic mean of fracture aperture is a good approximation for the mass balance aperture (which represents the flow volume and hence

porosity (Tsang, 1992)). This is the aperture which should be used to describe tracer transport (Zheng et al., 2008). By contrast, hydraulic aperture resulting from cubic law is weighted towards smaller apertures and lies somewhere between the geometric and harmonic mean of the underlying structure (Dagan, 1979; Gelhar and Axness, 1983; Tsang, 1992). Hence, the porosity resulting from the inverse modelling is likely to be an underestimate. Accordingly, after the approach of Jódar et al. (2002, 2004) porosity is scaled by assuming transmissivity is distributed over  $n$  parallel fractures, resulting in transmissivity  $T/n$  and effective aperture  $b_e/n$ . The effective aperture can be calculated by Equation 3.5, where the porosity scaling factor  $f$  is calculated by Equation 3.6:

$$\mathbf{b}_e = \mathbf{f} \cdot \mathbf{b}$$

**Equation 3.5 Effective fracture aperture**

$$f = n^{2/3}$$

**Equation 3.6 Porosity scaling factor**

Specific storage is calculated from the fracture aperture using Equation 3.7:

$$S_s = \gamma(\beta_p + \beta_w \cdot b_e)$$

**Equation 3.7 Specific storage from fracture aperture**

where  $\gamma$  is the specific weight of water ( $N/m^3$ ),  $\beta_p$  is the compressibility of the bulk matrix ( $m^2/N$ ) and  $\beta_w$  is the compressibility of water ( $m^2/N$ ) (Rutqvist et al., 1998).  $\beta_p$  is a model calibration parameter.

### 3.6.2. Data included in model

Ten second injection/recovery tests were carried out in the different boreholes drilled during the MI experiment to intersect the MI Shear Zone (referred to BM4, BM5, BM6, BM7, BM8, BM9 and BM10 in this model) (Meier, 1997). Analysis of these tests provided fixed point T values for the area surrounding each borehole. Tests were analysed by the Hvorslev and Cooper methods (Butler Jr, 1997), and by numerical inversion of the general Laplace transform solution of Barker (1988). These three methods provided an average that was then used in the model.

Steady-state head observations taken during the MI (Smith et al., 2001) and CRR projects (Möri et al., 2004), along with transient drawdown observations from 120 s cross-hole injection/recovery tests in BM6, BM9, CRR2 and CRR3 (Meier, 1997; Möri et al., 2004) were included in the inverse model. BM10 is the abstraction borehole used during one of the simulated tracer tests, but was not included in the injection/recovery test. Initial models wanted to include BM10 in a very low-T region, resulting in unphysically large drawdowns during tracer test simulation. To avoid this, steady-state drawdowns taken while BM10 was being used as a tracer test abstraction point (Möri et al., 2004) were also included in the model.

Two unequal-dipole conservative tracer tests, Run 2 (over CRR Dipole 1) and Run 4 (over CRR Dipole 2, between CRR2 and CRR3), were simulated in the inverse modelling (Möri et al., 2004). In both tests uranine was used as the tracer. A time delay exists between starting tracer injection and the arrival of the tracer at the packered borehole interval. During these tests, uranine concentration was monitored in the injection interval, with this

concentration being used as the input function in the model. The transport metrics used in the inverse modelling were: (1) the peak-peak tracer travel time (the difference between arrival time of the injection function concentration peak and the arrival time of the output function concentration peak); and (2) the percentage tracer recovery at the abstraction well.

### **3.6.3. Model setup**

The confined model domain is 63.25 m wide and 55 m high, centred on the 3.5 m wide AU tunnel. This is the same model domain used in the previous inverse modelling (Jódar et al., 2002, 2004). Figure 3.10 shows a summary of the model domain used.

The starting grid comprised 107 rows and 107 columns refined around the observation boreholes and the tunnel. The four tunnel inflow points were explicitly represented using MODFLOWs Well boundary condition. Head observations in the observation boreholes were inputted using MODFLOWs HOB package. Constant head boundary conditions were applied to the outer boundary of the model, where head values at the four corners of the model are calibration parameters and the intervening boundary cells set via linear interpolation.

Groundwater heads were solved for using MODFLOW's GMG solver with the head change criterion set to  $1e-7$  m. Transient simulations of the 120 second cross-hole injection/recovery tests in BM9, BM6, CRR2 and CRR3 had 20 time steps per stress period. Each injection/recovery test simulation had an initial steady-state head simulation to find starting background heads. Checks were made to ensure the model was solution, time step and grid converged.

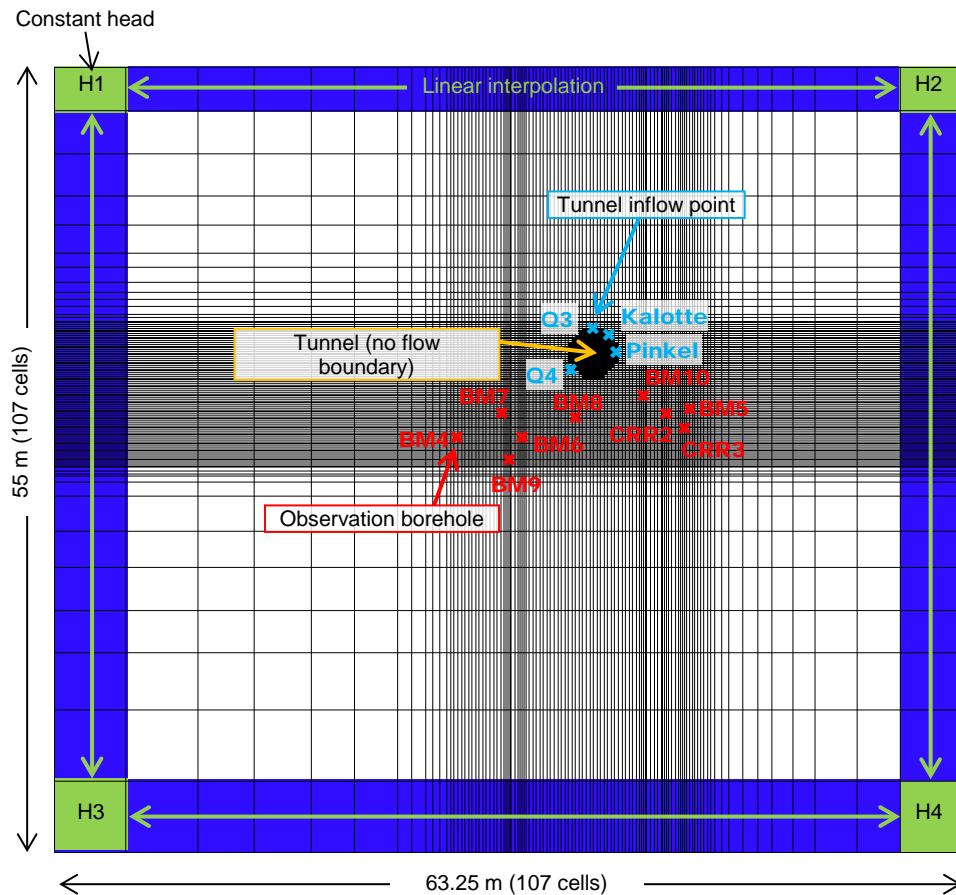


Figure 3.10 Summary of inverse model domain

During initial sensitivity testing, the results of different MT3DMS solvers were compared. The TVD solver was selected as the best option for solution accuracy and solver times. The concentration convergence criterion was  $1e-6$ . The heterogeneous T distribution in the model is expected to provide macrodispersion due to variation in flow paths. However, some additional dispersion was required to match breakthrough curves and to provide model stability. Starting values for dispersion lengths were 0.2 and 0.02 for longitudinal ( $\alpha_L$ ) and transverse dispersivity ( $\alpha_T$ ) respectively.

Model grid convergence checks were undertaken by iteratively refining the grid in the region surrounding the boreholes and tunnels and comparing the resulting breakthrough

curves. These checks suggest that, in such a heterogeneous model, grid refinement is very important. This is particularly the case for Run 2, the more heterogeneous of the two dipoles. The grid convergence checks suggested a minimum of  $1e5$  cells were required for solution accuracy. A similar result (not shown) was obtained for particle tracking. Hence, the starting model grid was refined to  $1e5$  cells for the final inverse modelling

#### **3.6.4. Model results**

The transmissivity field resulting from the model inversion is heterogeneous with over 6 orders of magnitude variation in transmissivity found in the area surrounding the tunnels and observation boreholes (Figure 3.11). A low transmissivity barrier exists between BM4, BM5, BM9, CRR2, CRR3 and the tunnel. This low T barrier is constrained by both cross-hole tests (BM10 shows little drawdown during the injection/recovery tests in CRR2, CRR3, BM6 and BM9) and head observations (heads in BM10 are significantly lower than those observed in CRR3, CRR2 and BM5).

A good match was achieved against observed steady-state heads (Figure 3.12a) and observed drawdowns during the injection/recovery tests (a summary of which is found in Figure 3.12b), plots of the results from each test are shown separately in McMillan et al. (in prep)). The exception to the good fit was steady-state heads observed in boreholes C and F (circled as the area of data scarcity in Figure 3.12a). C and F are two short boreholes drilled directly into the floor of the tunnel. These head measurements have a large uncertainty (Smith et al., 2001) and hence had low weights in the inverse model objective function.

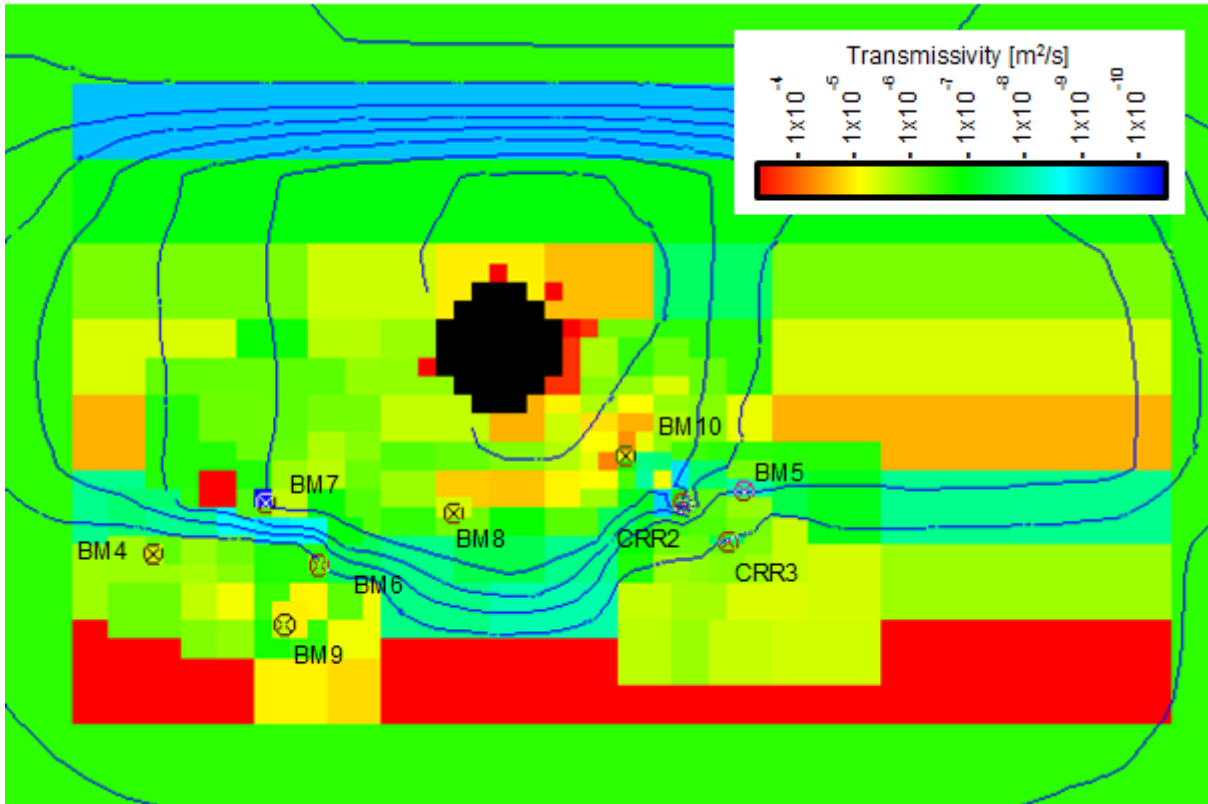


Figure 3.11 The resulting transmissivity distribution from the inverse model, with head contours representing CRR experimental conditions (McMillan et al., in prep.)

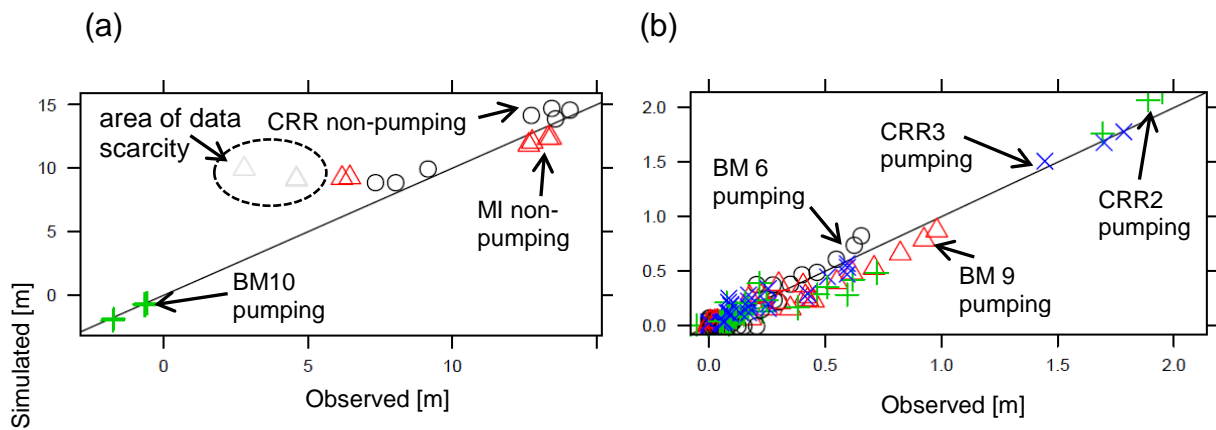


Figure 3.12 (a) Observed versus simulated steady-state heads; and (b) Observed versus simulated transient drawdowns

Final model parameters are summarised in Table 3.7. The boundary heads used may be model specific rather than representative of far field boundaries, nevertheless they are consistent with previous sub-regional modelling of Wyss (1990) and previous 2D modelling

of the tunnel by Jódar et al. (2002, 2004).  $\beta_p$  is within the range expected for fractures (Rutqvist et al., 1998). Although in the model, specific storage is aperture dependent, it is in fact relatively insensitive to variation in aperture. The reason is that the rock compressibility term dominates, with the product of aperture and water compressibility being almost negligible in comparison. Tunnel inflows during the CRR project are at the high end of the observed range. However, that range is fairly uncertain as tunnel inflows were measured only very infrequently during the project.

Parameter	Value	Units	Parameter	Value	Units
H1	18.68	m	Q3	52	ml/min
H2	17.36	m	Q4	35	ml/min
H3	18.60	m	QK	345	ml/min
H4	17.10	m	QP	263	ml/min
H1MI	15.79	m	QCRR	700	ml/min
H1MI	12.57	m	$\beta_p$	3.52E-10	m <sup>2</sup> N <sup>-1</sup>
H1MI	16.33	m	$f$	7	-
H1MI	13.11	m			

Table 3.7 Final value of calibration parameters used in inverse model

A good match is achieved for tracer test mass recovery (Table 3.8). However, peak-peak travel times over the two adjacent dipoles are not well matched. The low T barrier between CRR2 and BM10 results in a very small fracture aperture relative to the model average. This small aperture means porosity over this dipole is low and hence travel times are quick. However, observed travel times are in fact an order of magnitude lower than over the similarly apaced adjacent dipole, D2 (Table 3.8). The inverse modelling has attempted to slow travel times down over D1 as much as it can by (1) increasing porosity by including a high T zone immediately adjacent to the low T barrier intersecting D1 (Figure 3.11); and (2) by increasing the porosity scaling factor  $f$  to 7 (Table 3.7). Due to differences in porosity between the two modelled dipoles, it has not been possible to obtain good fits for tracer

transport using a consistent parameter set (Figure 3.13). Further discussion on the cause of this and the results from the model is found in McMillan et al. (in prep).

Metric	Observed	Simulated	Units
Run 2 peak-peak travel time	6120	6425	s
Run 4 peak-peak travel time	612	3100	s
Run 2 % recovery	93	100	%
Run 4 % recovery	98	100	%

Table 3.8 Inverse modelling transport metrics results

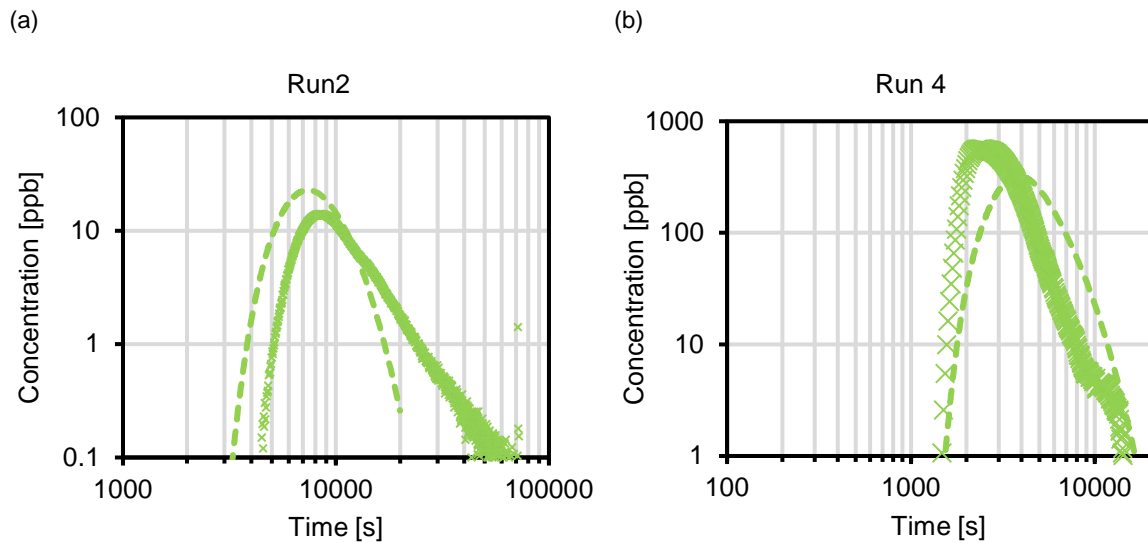


Figure 3.13 Best fit tracer breakthrough across adjacent dipoles D1 and D2 using MT3D.

### 3.7. Summary

This chapter has summarised the geological setting and hydrogeology of the Grimsel Test Site and the migration experiment (MI) Shear Zone. In summary, the Grimsel Test Site is situated 400 to 450 m below ground in the Grimsel Granodiorite host rock (Blechsmidt and Vomvoris, 2009). Groundwater flows in the shear zone through 1 to 3 variably filled water conducting features (WCFs) with variable apertures (Gaus and Smith, 2008). In the MI shear zone, high pH, low ionic strength glacial meltwater groundwater flows towards the AU

tunnel, which sees the highest inflow in this area of the Grimsel Test Site (Lanyon and Blechschmidt, 2016).

The Colloid Formation and Migration (CFM) project is the latest investigation of radionuclide transport that has been carried out in the MI shear zone. Building on the Colloid and Radionuclide Retardation (CRR) project, the CFM project was set up to investigate colloid generation, migration and colloid-facilitated radionuclide transport.

Two experiments (CFM Run 13-05 and CRR Run 32), were modelled in the present study. Both were carried out in CRR Dipole 1 (distance 2.3 metres) but under different flow rates: CRR Run 32 was carried out at a flow rate approximately 30 times higher than that applied in CFM Run 13-05. For both of these experiments the injection cocktail was prepared by KIT-INE, and a colloid population of FEBEX bentonite was made up (with Ni- labelled montmorillonite colloids in CFM Run 13-05) to which radionuclides were added. The time difference between the radionuclides being added to the cocktail and the experiment being run was different between the two experiments (CFM Run 13-05 – 35 days, CRR Run 32 – 5 days). The two experiments used different injection methods, with a 100ml slug directly injected in CRR Run 32, whereas in CFM Run 13-05 the cocktail was connected to a recirculation circuit and a dilution experiment was run (albeit with some slight injection).

Previous modelling has been carried out for both the CRR and CFM migration experiments. In the CRR project, models did not include processes such as colloid attachment or radionuclide desorption as it was thought that these processes would not be important during the short residence time migration experiments, but included several different representations of the shear zone. Models were typically able to replicate the

breakthrough curves of the radionuclides in the experiments, although the majority of them had to change the parameters describing radionuclide sorption from the laboratory derived values that were initially used to set them.

Models of CFM experiments included colloid attachment and radionuclide desorption and some included multiple radionuclide sorption sites on the colloid, but used simple model geometries (1D or homogeneous 2D model domains). Although the models typically achieved good model matches to experimental data, the models had difficulty with using the same parameters and descriptions of processes when modelling different experiments.

Inverse modelling has been used to generate a transmissivity distribution of the shear zone. The inverse model attempted to replicate hydraulic measurements from different tests carried out in the characterisation work from the MI and CRR experiments. In addition, the model included transport observations (arrival time and recovery) from two different tracer tests. The resulting transmissivity distribution is used in the transport model, as detailed in Chapter 4.

### **3.8. List of References**

Barker, J.A. (1988) A Generalized Radial Flow Model for Hydraulic Tests in Fractured Rock. **Water Resources**, 24 (10): 1796–1804 DOI: 10.1029/WR024i010p01796

Bennett, D.G. (2014) **SSM 2014:11 Radionuclide Solubility Limits in SKB's Safety Case**. p. 62

Blechs Schmidt, I. and Vomvoris, S. (2009) **25 Years of Underground Research: Grimsel Test Site**. Wettingen, Switzerland: Nagra

Butler Jr, J.J. (1997) **The Design, Performance, and Analysis of Slug Tests**. CRC Press

Dagan, G. (1979) Models of Groundwater Flow in Statistically Homogeneous Porous Formations. **Water Resources Research**, 15 (1): 47–63

Doherty, J. (2016a) **Model-Independent Parameter Estimation User Manual Part I: PEST, SENSAN and Global Optimisers**. 6th ed. Brisbane, Australia: Watermark Numerical Computing

Doherty, J. (2016b) **Model-Independent Parameter Estimation User Manual Part II: PEST Utility Support Software**. 6th ed. Brisbane, Australia: Watermark Numerical Computing

Duro, L., Bruno, J., Rollin, C. and Guimera, J. (2000) **AN 99-218: Prediction of the solubility and speciation of Radionuclides in Febex and Grimsel waters**. Wettingen, Switzerland

Foley, C. and Black, A. (2013) "Efficiently delineating volumetric capture areas and flow pathways using directed acyclic graphs and MODFLOW; description of the algorithms within FlowSource, MODFLOW And More." **In Translating Science into Practice**. Golden, Colorado School of Mines. **2013**

Gaus, I. and Smith, P.A. (2008) **Nagra Arbeitsbericht NAB 08-27: Modellers dataset for the Colloid Formation and Migration Project Status: End of CFM Phase 1**. Wettingen, Switzerland

Geckeis, H., Schafer, T., Hauser, W., Rabung, T., Missana, T., Degueldre, C., Möri, A., Eikenberg, J., Fierz, T. and Alexander, W.R. (2004) Results of the colloid and radionuclide retention experiment (CRR) at the Grimsel Test Site (GTS), Switzerland - Impact of reaction kinetics and speciation on radionuclide migration. **Radiochimica Acta**, 92 (9–11): 765–774 DOI: 10.1524/ract.92.9.765.54973

Gelhar, L.W. and Axness, C.L. (1983) Three-Dimensional Stochastic Analysis of Macrodispersion in Aquifers. **Water Resources Research** [online], 19 (1): 161–180 DOI: 10.1029/WR019i001p00161. Available from: <http://www.agu.org/pubs/crossref/1983/WR019i001p00161.shtml>

Huber, F., Noseck, U. and Schäfer, T. (2014) **Colloid / nanoparticle formation and mobility in the context of deep geological nuclear waste disposal** [online]. Karlsruhe, Germany. Available from: [http://www.ubka.uni-karlsruhe.de/dbkit/uv/getUvkaDocument.php?vv\\_id=1000035944](http://www.ubka.uni-karlsruhe.de/dbkit/uv/getUvkaDocument.php?vv_id=1000035944)

Jódar, J., Medina, A. and Carrera, J. (2002) **Actualisation of the geostatistical inverse model of the migration shear zone with new crosshole pumping tests and evaluation of non-sorbing tracer tests**. Unpublished Nagra Report

Jódar, J., Meier, P.M., Medina, A. and Carrera, J. (2004) "Geostatistical inversion of flow and transport data. Application to the CRR project." **In geoEnv IV - Geostaticstics for Environmental Applications**. pp. 512–513

Kontar, K., Grafe, K. and Rosli, U. (2013) **Nagra Aktennotiz AN 13-617: Tracer Test Run 13-05**. Monchaltorf, Switzerland

Kosakowski, G. and Smith, P. (2004) **Nagra Technical Bulletin NTB 04-01: Grimsel Test Site Investigation Phase V Modelling the transport of Solutes and Colloids in a Water Conducting Shear Zone at the Grimsel Test Site** [online]. Wettingen, Switzerland. Available from: <http://www.nagra.ch/en/cat/publikationen/technicalreports-ntbs/ntbs-2001-2012/downloadcentre.htm>

Lanyon, B. and Blechschmidt, I. (2016) **Nagra Aktennotiz AN16-102: Minutes of the CFM Modellers Workshop, 10-11 December 2015, San Francisco**. Wettingen, Switzerland

Lanyon, B., Blechschmidt, I. and Martin, A. (2017) **Nagra Aktennotiz AN 17-358: Minutes of the CFM Partner Meeting, 11-12 May 2017**. Wettingen, Switzerland

Lanyon, B. and Martin, A. (2014) **Nagra Aktennotiz AN 14-367: Minutes of the CFM Modellers Meeting, May 2014**. Wettingen, Switzerland

McMillan, L.A., Harvey, B.E. and Herbert, A.W. (n.d.) **Inverse modelling to understand contaminant transport experiments in a highly heterogeneous shear zone at the Grimsel Test Site in Switzerland.** In Preparation

Meier, P. (1997) **Nagra NIB 96-37: Grimsel Test Site: Migration Experiment and Radionuclide Retardation Project (RRP) - results of additional hydraulic test in the Migration Shear Zone.** Wettingen, Switzerland

Missana, T. and Geckeis, H. (2006) **Nagra Technical Bulletin NTB 03-02: CRR Final Project Report 2 - Supporting Laboratory Experiments with Radionuclides and Bentonite Colloids.** Wettingen, Switzerland

Möri, A., Alexander, W.R., Degueudre, C., Eikenberg, J., Fierz, T., Geckeis, H., Geier, F., Hauser, W., Schäfer, T. and Smith, P.A. (2004) **Nagra Technical Bulletin NTB 03-01: The CRR Final Project Report series 1 - Description of the Field Phase - Methodologies and Raw Data** [online]. Wettingen, Switzerland. Available from: <http://www.nagra.ch/en/cat/publikationen/technicalreports-ntbs/ntbs-2001-2012/downloadcentre.htm>

Noseck, U., Flügge, J., Reimus, P., Cvetkovic, V., Lanyon, B., Schäfer, T. and Blechschmidt, I. (2016) **Nagra Technical Report NTB 16-06: Colloid Formation and Migration Project: Modelling of tracer, colloid and radionuclide/homologue transport for dipole CFM 06.002- Pinkel surface packer.** Wettingen, Switzerland

Pollock, D.W. (1994) **User's Guide for MODPATH/ MODPATH-PLOT, Version 3: A particle tracking post-processing package for MODFLOW, the U.S. Geological Survey finite-difference groundwater flow model. USGS Open-file report 94-464.** [online]. Available from: <http://water.usgs.gov/nrp/gwsoftware/modpath5/ofr94464.pdf>

Pudewills, A. (2008) **Modelling of Tracer Tests in a Shear Zone at the Grimsel Test Site** [online]. Karlsruhe, Germany. Available from: <http://bibliothek.fzk.de/zb/berichte/FZKA7417.pdf>

Quinto, F., Blechschmidt, I., Garcia Perez, C., Geckeis, H., Geyer, F., Golser, R., Huber, F.M., Lagos, M., Lanyon, B., Plaschke, M., Steier, P., Schäfer, T., Perez, C.G., Geckeis, H., Geyer, F., Golser, R., Huber, F.M., Lagos, M., Lanyon, B., et al. (2017) Multi-actinide analysis with AMS for ultra-trace determination in small samples : application to an in situ radionuclide tracer test within the Colloid Formation and Migration (CFM) experiment at the Grimsel Test Site (GTS , Switzerland). **Analytical Chemistry**, 89 (13): 7182–7189 DOI: 10.1021/acs.analchem.7b01359

Reiche, T., Noseck, U. and Schäfer, T. (2015) Migration of Contaminants in Fractured-Porous Media in the Presence of Colloids: Effects of Kinetic Interactions. **Transport in Porous Media**, 111 (1): 143–170 DOI: 10.1007/s11242-015-0585-7

Reimus, P.W. (2016) **Nagra NAB 16-61: GTS Phase VI- CFM Phase 3: Interpretation of colloid-facilitated radionuclide transport experiments from the CRR and CFM projects.** Wettingen, Switzerland

Rutqvist, J., Noorishad, J., Tsang, C. and Stephansson, O. (1998) Determination of fracture storativity in hard rocks using high-pressure injection testing. **Water Resources Research**, 34 (10): 2551–2560

Schäfer, T., Darbha, G. and Iijima, K. (2014) **Nagra Arbeitsbericht NAB 13-79 CFM Phase 2: Status Report of the Laboratory Programme at the end of 2011.** Wettingen, Switzerland

Schäfer, T., Lanyon, B. and Blechschmidt, I. (2013) **CFM 13-05 Data Set.** pers comm.: Nagra/ KIT-INE

(Unpublished Dataset)

Schlickenrieder, L., Lanyon, B., Kontar, K. and Blechschmidt, I. (2017) **Nagra Technical Report NTB 15-03: Colloid Formation and Migration Project: Site instrumentation and initiation of the long-term in-situ test**. Wettingen, Switzerland

Smith, P.A., Alexander, W.R., Heer, W., Fierz, T., Meier, P.M., Baeyens, B., Bradbury, M.H., Mazurek, M. and McKinley, I.G. (2001) **Nagra Technical Report 00-09: Grimsel Test Site Phase IV: The Nagra-JNC in situ study of safety relevant radionuclide retardation in fracture crystalline rock I: Radionuclide Migration Experiment - Overview 1990-1996**. Wettingen, Switzerland

Smith, P.A., Guimera, J., Kosakowski, G., Pudewills, A. and Ibaraki, M. (2006) **Nagra Technical Bulletin NTB 03-03: Grimsel Test Site Investigation Phase V - The CRR Final Project Report series 3: Results of the Supporting Modelling Programme**. Wettingen, Switzerland

Thoenen, T., Hummel, W., Berner, U. and Curti, E. (2014) **The PSI / Nagra Chemical Thermodynamic Database 12 / 07**. Villigen, Switzerland

Tsang, Y.W. (1992) Usage of "Equivalent apertures" for rock fractures as derived from hydraulic and tracer tests. **Water Resources Research**, 28 (5): 1451–1455 DOI: 10.1029/92WR00361

USGS (2016) **MODFLOW and Related Programs** [online]. Available from: <http://water.usgs.gov/ogw/modflow/>

Wyss, E. (1990) **Nagra NIB 90-49 FLG Migration Test: Drei Beispiele für das weitere Verständnis des hydraulischen Verhaltens**. Wettingen, Switzerland

Zheng, B.C. and Wang, P.P. (1999) **A Modular Three - Dimensional Multispecies Transport Model**. Tuscaloosa, AL

Zheng, Q., Dickson, S.E. and Guo, Y. (2008) On the appropriate "equivalent aperture" for the description of solute transport in single fractures: Laboratory-scale experiments. **Water Resources Research**, 44 (4): 1–9 DOI: 10.1029/2007WR005970

## **4. DEVELOPMENT OF COLLOID-FACILITATED RADIONUCLIDE TRANSPORT MODEL**

### **4.1. Introduction**

This chapter details the development of the colloid-facilitated radionuclide transport model that is used to model the two in-situ migration experiments described in Chapter 3. The transport model uses a transmissivity distribution generated by an inverse modelling approach developed by Dr Lindsay McMillan, as described in more detail in Chapter 3. The distribution provides more information on the geological structure and flow path geometry than previous models of the experiments and is used to attempt to develop a self-consistent understanding of the transport processes and the processes involved in colloid-facilitated radionuclide transport within the experiments.

The transport model uses a flexible framework of equations, building on work carried out by Burns (2013) for the colloid transport and attachment equations, and on models detailed in Ibaraki and Sudicky (1995) and Noseck et al. (2016) for colloid-facilitated transport. This model uses a mainly 1<sup>st</sup> order kinetic approach to describe colloid attachment and radionuclide sorption to colloids. This continuum-based approach was used as a more mechanistic approach based on colloid filtration theory would have still required calibration to provide accurate predictions of colloid attachment. Kinetic sorption is used to describe radionuclide sorption to colloids as desorption kinetics played an important role in laboratory experiments which investigated radionuclide sorption reversibility (Dittrich et al. (2015), Missana and Geckeis (2006), Huber et al. (2011 and 2015)).

The aim of the transport model is to replicate the transport of conservative tracers, bentonite colloids and selected radionuclides in two field experiments (CFM Run 13-05 and CRR Run 32), using consistent parameter values. Previous models of these experiments have either used 1D or homogeneous 2D models to represent the shear zone in which the experiments are carried out (Chapter 3). These models were not able to use consistent parameter values in the different experiments, as the models used different rate constants to describe the transport of colloids and radionuclides in the experiments.

## **4.2. Conceptual Model**

### **4.2.1. Geology/ Hydrogeology**

The two field experiments are carried out at the Grimsel Test Site in Switzerland. The site is situated 400 to 450m below the surface in several tunnels in the Grimsel granodiorite host rock. The geology and hydrogeology of the test site is detailed in Chapter 3, but in summary the experiments are carried out in the MI shear zone at the test site. The shear zone consists of a number of fractures through which water flows, referred to as water-conducting features (WCFs) by Nagra (Gaus and Smith, 2008). These water-conducting features are variably filled with fracture fill material (FFM) and vary in aperture, but are typically around a few mm thick (Gaus and Smith, 2008). A large number of boreholes have been drilled from the tunnel (the AU tunnel) that intersects the shear zone, and high pH, low ionic strength groundwater generally flows towards the AU tunnel. The inflows into the tunnel are the highest in the southern part of the test site (Gaus and Smith, 2008).

#### 4.2.2. Experimental Processes

In the experiments, bentonite clay is used to generate colloids for the experiments, using colloids that have been prepared as part of the injection cocktail before the experiment has run. Other parts of the CFM project investigate bentonite erosion and colloid generation (Schäfer et al. (2014) detail several experiments for instance). Bentonite erosion and colloid formation is not the focus of this thesis, and as such bentonite erosion and colloid formation is not included in the model.

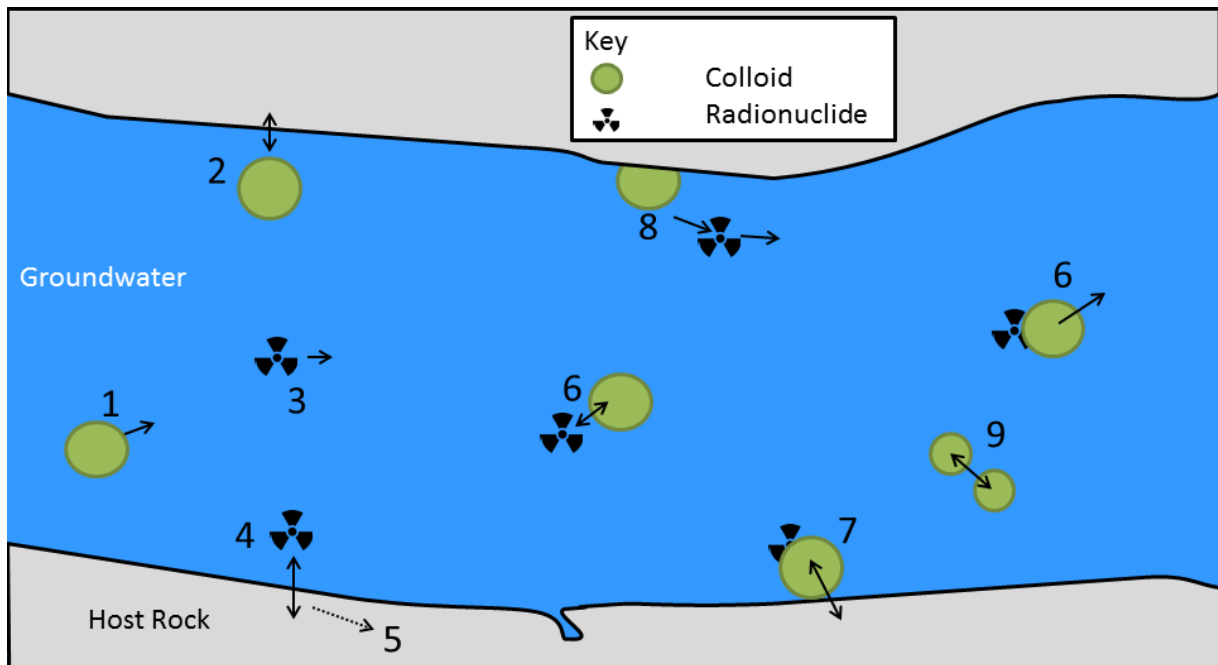


**Figure 4.1** Diagram of different processes involved in colloid-facilitated radionuclide transport within a fracture. Processes: colloid transport (1); colloid attachment (2); radionuclide (RN) transport (3); RN sorption to rock surfaces (4); RN matrix diffusion (5); RN sorption to mobile colloids (6); attachment of colloids with RN sorbed (7); desorption of RN from colloid (8); colloid aggregation (9). Processes not shown include colloid sedimentation and straining.

The injected concentration of colloids is much higher than the background colloid population, between 20 mg/l and ~100 mg/l for the experiments (Möri et al., 2004; Schäfer et al., 2013), and ~20 ppb for background colloids (Gaus and Smith, 2008). Although background colloid populations could act as a competitive sorption surface for the radionuclides (instead of the bentonite colloids), because the background colloid

concentration is much lower, the impact of natural background colloids acting as a competitive sorption surface is minimised, and so the transport model does not consider the natural background colloids.

Colloids can be transported through groundwater by advection and dispersion (Process 1, Figure 4.1). Colloid transport is limited by filtration processes (Process 2) to the rock surfaces, either by chemical attachment (Ryan and Elimelech, 1996), or by physical straining (Bradford et al., 2006). Although Burns (2013), (on which the colloid transport equations are based) include an equation describing straining, this had a similar formulation to the irreversible colloid attachment equation, and there is not enough information on the distribution of the throat size in the fractures to use a mechanistic colloid straining equation (for instance those found in Bradford et al. (2003)). Because of this, straining was not included as a specific equation in the transport model, but colloid attachment was.

Depending on the charge of the colloids and the rock surfaces, colloid attachment can either promote (ripening) or block further colloids from attachment to the rock surfaces (blocking) (Ryan and Elimelech, 1996). As Grimsel groundwater is low ionic strength, 'unfavourable' conditions are expected to exist for colloid attachment, meaning that blocking of attachment sites is more likely to occur (Ryan and Elimelech, 1996). Because of this, a blocking term is included in the model. Ripening is not included in the model due to the unfavourable attachment conditions.

Radionuclides can be transported through groundwater in the aqueous phase (Process 3), undergoing radioactive decay (although this will have limited impact on the migration experiments), sorption to the granodiorite surface or fracture fill material (Process 4).

Radionuclides may also diffuse into the adjacent granodiorite matrix, or into slower flow paths within the shear zone (Process 5). Sorption to the rock surface/ FFM may occur on multiple sites (e.g. Cs (Dittrich and Reimus, 2015b), U (Dittrich and Reimus, 2015a)). The residence times of the experiments (1.5 hours for CRR Run 32, 44 hours for CFM Run 13-05), mean that sorption of particular radionuclides may not have reached equilibrium during the experiments. In the model, both equilibrium and kinetic descriptions of radionuclide sorption to rock surfaces have been included, and can be applied based on the results of laboratory experiments testing sorption to Grimsel granodiorite and fracture fill material. Sorption kinetics have been included when modelling long-term, low concentration aqueous phase data from the CFM *in situ* migration experiments (Lanyon and Blechschmidt, 2016), however this data was not available for model calibration in this work.

Radionuclides can sorb to mobile colloids, and radionuclides that have sorbed to mobile colloids are transported through groundwater undergoing the same processes as colloids (e.g. colloid attachment) (Process 6 and 7). For the two *in situ* experiments, the radionuclides are added to the colloid suspension forming the injection cocktails. The time between radionuclide spiking and the experiment varies between 5 days for CRR Run 32 (Möri et al., 2004) and 35 days for CFM Run 13-05 (Schäfer et al., 2013). It depends on the sorption kinetics of each radionuclide as to how much sorption occurs in this time period, and although radionuclide sorption to colloids is included in the model, due to the time scales between experimental cocktail preparation and injection, the sorption process is unlikely to be important when modelling the two migration experiments as the majority of sorption is likely to have taken place already.

Sorption reversibility is a key factor in determining whether colloid-facilitated radionuclide transport is significant (Möri et al., 2003). Therefore, investigating sorption reversibility of radionuclides to bentonite colloids is a key part of the CFM and CRR experiments and associated laboratory work (e.g. Missana and Geckeis (2006); Huber et al. (2015); Dittrich et al. (2015)). Radionuclides can desorb from both mobile and attached colloids, with desorption kinetics providing a major control on the colloid-facilitated transport of several radionuclides, particularly if they undergo strong sorption to the colloids (e.g. Am, Pu and Th (Huber et al., 2011, 2015)).

It is possible that radionuclides could sorb to colloids that have been attached to the rock surface, and this process has been included in other CFRT models (Ibaraki and Sudicky, 1995; Noseck et al., 2016). However, in this model, it was assumed that radionuclides could only desorb from immobile colloids (Process 8), as rock surfaces were likely to provide more sorption sites for an aqueous radionuclide migrating through the shear zone.

The sorption and attachment processes in this model all assume that they can be described by first-order kinetics, or that the sorption process is dependent on the concentration of one species. For instance, the rate of radionuclide sorption to rock surfaces is dependent on the concentration of radionuclides in the system. The exception to this is radionuclide sorption to colloids, as this process is controlled by the concentration of both the radionuclide and colloids, making it a second-order reaction.

### 4.3. Governing Equations

Groundwater flow in the shear zone is assumed to have reached steady state in the experiments, and is described by Equation 4.1, which is a variable density formulation of Darcy's Law:

$$\mathbf{Q}' = -\frac{k}{\mu}b(\nabla P - \rho g)$$

#### Equation 4.1 Groundwater flow

where  $\mathbf{Q}'$  is discharge per unit width of fracture aperture [ $L^2T^{-1}$ ],  $k$  is intrinsic permeability [ $L^2$ ],  $\mu$  is water viscosity [ $ML^{-1}T^{-1}$ ],  $b$  is the hydraulic fracture aperture [ $L$ ],  $P$  is pressure [ $ML^{-1}T^{-2}$ ],  $\rho$  is water density [ $ML^{-3}$ ] and  $g$  is acceleration due to gravity [ $LT^{-2}$ ]. The density and viscosity of water is assumed to be constant when modelling the two in-situ experiments, allowing Equation 4.1 to be solved directly. The average linear velocity of groundwater is given by Equation 4.2, where  $\theta$  is porosity of the fracture [-]:

$$\mathbf{v} = \frac{\mathbf{Q}'}{\theta b}$$

#### Equation 4.2 Average linear velocity

The average linear velocity of groundwater provides an average velocity over the different flow paths, and does not give a velocity profile that would exist over the different flow paths situated in the shear zone.

The transport of colloids is described by Equation 4.3, which provides the mass conservation equation for colloids:

$$\theta b R_c \frac{\partial C}{\partial t} + (1 - \theta) b \rho_f \frac{\partial F}{\partial t} + (1 - \theta) b \rho_f \frac{\partial F_i}{\partial t} + \nabla \cdot (\theta b \mathbf{v} C - \theta b \mathbf{D} \nabla C) = 0$$

**Equation 4.3 Colloid transport**

where  $C$  is colloid concentration [ $\text{ML}^{-3}$ ],  $R_c$  is retardation factor for colloids [-] (used to model size exclusion chromatography if needed),  $\rho_f$  is fracture fill material density [ $\text{ML}^{-3}$ ],  $F$  and  $F_i$  are respectively the mass of reversibly and irreversibly attached colloids per mass of fracture fill material [-],  $\mathbf{D}$  is the hydrodynamic dispersion tensor [ $\text{L}^2\text{T}^{-1}$ ]. Equation 4.4 describes reversible colloid attachment and Equation 4.5 describes irreversible colloid attachment:

$$(1 - \theta) b \rho_f \frac{\partial F}{\partial t} = k_{att} \theta b \left(1 - \frac{F}{F_{max}}\right) C - k_{det} (1 - \theta) b \rho_f F$$

**Equation 4.4 Reversible colloid attachment**

$$(1 - \theta) b \rho_f \frac{\partial F_i}{\partial t} = k_{iat} \theta b \left(1 - \frac{F_i}{F_{imax}}\right) C$$

**Equation 4.5 Irreversible colloid attachment**

where  $k_{att}$  and  $k_{iat}$  are attachment rates for reversible and irreversible colloid attachment respectively [ $\text{T}^{-1}$ ],  $F_{max}$  and  $F_{imax}$  are the maximum values of  $F$  and  $F_i$  [-] and  $k_{det}$  is the detachment rate for reversibly attached colloids. These equations assume that the colloids in the experiment can be described as one equivalent colloid population.

The transport of an aqueous phase radionuclide that can sorb to a single type of sorption site on the bentonite colloids is described by Equation 4.6:

$$\begin{aligned}
& \theta b R \frac{\partial N}{\partial t} + \nabla \cdot (\theta b \mathbf{v} N - \theta b \mathbf{D} \nabla N) \\
& = -\theta b R \lambda_d N - k_{amc} \theta b \left( 1 - \frac{S_{mc}}{N_{mcmax}} \right) C N + k_{mca} \theta b S_{mc} \\
& + k_{ica} (1 - \theta) b \rho_f S_{ic} + k_{icai} (1 - \theta) \rho_f S_{ici}
\end{aligned}$$

**Equation 4.6 Aqueous phase radionuclide transport with one site sorption to colloids and equilibrium sorption to rock surfaces.**

where  $R$  is the equilibrium sorption retardation factor [-],  $N$  is aqueous radionuclide concentration [ $\text{ML}^{-3}$ ],  $\lambda_d$  is the radioactive decay constant [ $\text{T}^{-1}$ ],  $k_{amc}$  is the sorption rate to mobile colloids [ $\text{L}^3 \text{M}^{-1} \text{T}^{-1}$ ],  $S_{mc}$  is the concentration of radionuclides that are sorbed to mobile colloids [ $\text{ML}^{-3}$ ],  $N_{mcmax}$  is the maximum value of  $S_{mc}$  [ $\text{ML}^{-3}$ ],  $k_{mca}$  is the desorption rate for radionuclides from mobile colloids [ $\text{T}^{-1}$ ],  $k_{ica}$  and  $k_{icai}$  are the desorption rates for radionuclides from reversibly and irreversibly attached colloids respectively [ $\text{T}^{-1}$ ] and  $S_{ic}$  and  $S_{ici}$  are the mass of radionuclides sorbed to reversibly and irreversibly attached colloids per unit mass of fracture fill material [-].

The transport of radionuclides sorbed to mobile colloids is described by Equation 4.7. Initially in the model calibration it was assumed that only type of one sorption site was present on the colloid. However, Equation 4.7 can be duplicated to describe the presence of a different sorption site on the colloid if needed during the model calibration process. Equation 4.8 and Equation 4.9 describe radionuclides sorbed to colloids that are reversibly or irreversibly attached to rock surfaces:

$$\begin{aligned}
& \theta b R_c \frac{\partial S_{mc}}{\partial t} + \nabla \cdot (\theta b \mathbf{v} S_{mc} - \theta b \mathbf{D} \nabla S_{mc}) \\
& = -\theta b \lambda_d S_{mc} + k_{amc} \theta b \left(1 - \frac{S_{mc}}{N_{mcmax}}\right) CN - k_{mca} \theta b S_{mc} \\
& \quad - k_{att} \theta b \left(1 - \frac{F}{F_{max}}\right) S_{mc} + k_{det} (1 - \theta) b \rho_f S_{ic} - k_{iat} \theta b \left(1 - \frac{F_i}{F_{imax}}\right) S_{mc}
\end{aligned}$$

**Equation 4.7 Radionuclides sorbed to mobile colloids**

$$\begin{aligned}
& (1 - \theta) b \rho_f \frac{\partial S_{ic}}{\partial t} \\
& = -(1 - \theta) b \rho_f \lambda_d S_{ic} + k_{att} \theta b \left(1 - \frac{F}{F_{max}}\right) S_{mc} - k_{det} (1 - \theta) b \rho_f S_{ic} \\
& \quad - k_{ica} (1 - \theta) b \rho_f S_{ic}
\end{aligned}$$

**Equation 4.8 Radionuclides sorbed to reversibly attached colloids**

$$(1 - \theta) b \rho_f \frac{\partial S_{ici}}{\partial t} = -(1 - \theta) b \rho_f \lambda_d S_{ici} + k_{iat} \theta b \left(1 - \frac{F_i}{F_{imax}}\right) S_{mc} - k_{icai} (1 - \theta) b \rho_f S_{ici}$$

**Equation 4.9 Radionuclides sorbed to irreversibly attached colloids**

In the transport model, Equation 4.3 to Equation 4.9 are solved simultaneously. A summary of the different processes and the different couplings that the equations solve for are shown in Figure 4.2.

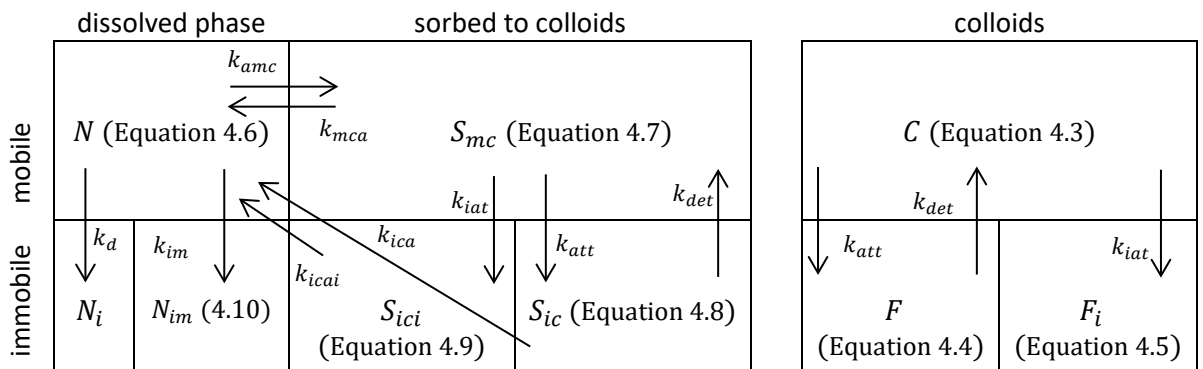


**Figure 4.2 Different phases solved in transport model (includes matrix diffusion, excludes kinetic sorption to rock surfaces)**

Matrix diffusion is described by Equation 4.10, which represents a dual porosity approach with a first-order transfer equation, and is similar to the approach used in Black and Kipp (1983). This equation provided a first approximation of matrix diffusion and was used as necessary during model calibration:

$$\theta_{im} b \frac{\partial N_{im}}{\partial t} = k_{im} b (N - N_{im}) - b \lambda_d N_{im}$$

**Equation 4.10 Radionuclide matrix diffusion**

where  $\theta_{im}$  is the matrix porosity multiplied by the matrix extinction depth (i.e. the depth within the rock matrix where matrix diffusion does not effectively occur) [-],  $N_{im}$  is the matrix radionuclide concentration [ML<sup>-3</sup>], and  $k_{im}$  is the first-order transfer rate that describes the matrix diffusion process [T<sup>-1</sup>]. If necessary, kinetic sorption to the rock surfaces or fracture fill material can be described by Equation 4.11:

$$(1 - \theta) b \rho_f \frac{\partial N_i}{\partial t} = k_{ai} \theta b \left( 1 - \frac{N_i}{N_{imax}} \right) N - k_{ia} (1 - \theta) b \rho_f N_i - (1 - \theta) b \rho_f \lambda_d N_i$$

**Equation 4.11 Radionuclide kinetic sorption to rock surfaces**

where  $N_i$  is the mass of sorbed radionuclide per mass of fracture fill material [-],  $k_{ai}$  is the first-order sorption rate constant [T<sup>-1</sup>],  $N_{imax}$  is the maximum value of  $N_i$  [-] and  $k_{ia}$  is the desorption rate constant [T<sup>-1</sup>]. It would be possible to duplicate this equation if multiple sorption sites on the rock surfaces need to be modelled. To use either Equation 4.10 or Equation 4.11 in the transport model, then the relevant coupling is added to Equation 4.6.

## 4.4. Model Verification

### 4.4.1. Advection-dispersion, retardation and radioactive decay

The model was verified initially by comparing conservative tracer breakthrough to an analytical solution for the advection-dispersion equation provided by Alan Herbert (pers. Comm.), which combines the Ogata-Banks solutions for the advection-dispersion equation with linear retardation and radioactive decay given in Domenico and Schwartz (1990).

The results of this analytical model were compared to a COMSOL model that solved the aqueous radionuclide equation (Equation 4.6), including linear equilibrium sorption (retardation) and radioactive decay, but without the terms for colloid-facilitated radionuclide transport.

Initially a 1D model was used, with a model domain of 0.1 metres with a constant groundwater velocity of 0.005 m/s with a constant source of contaminant and using the parameters in Table 4.1. An example comparison between the numerical and analytical model is shown in Figure 4.3. This shows that the numerical model was able to reproduce breakthrough curves generated by the analytical solution. The model was able to replicate the results when linear retardation and radioactive decay were included in the model.

Parameter	Value
x	0.1 m
u	0.005 m/s
$\alpha_l$	0.001 m
D	$5.01 \times 10^{-6} \text{ m}^2/\text{s}$
$D_d$	$1 \times 10^{-8} \text{ m}^2/\text{s}$
$C_0$	$0.01 \text{ kg}/\text{m}^3$
$\theta$	0.22

**Table 4.1** Parameters used in 1D COMSOL model to verify advection-dispersion, retardation and radioactive decay processes

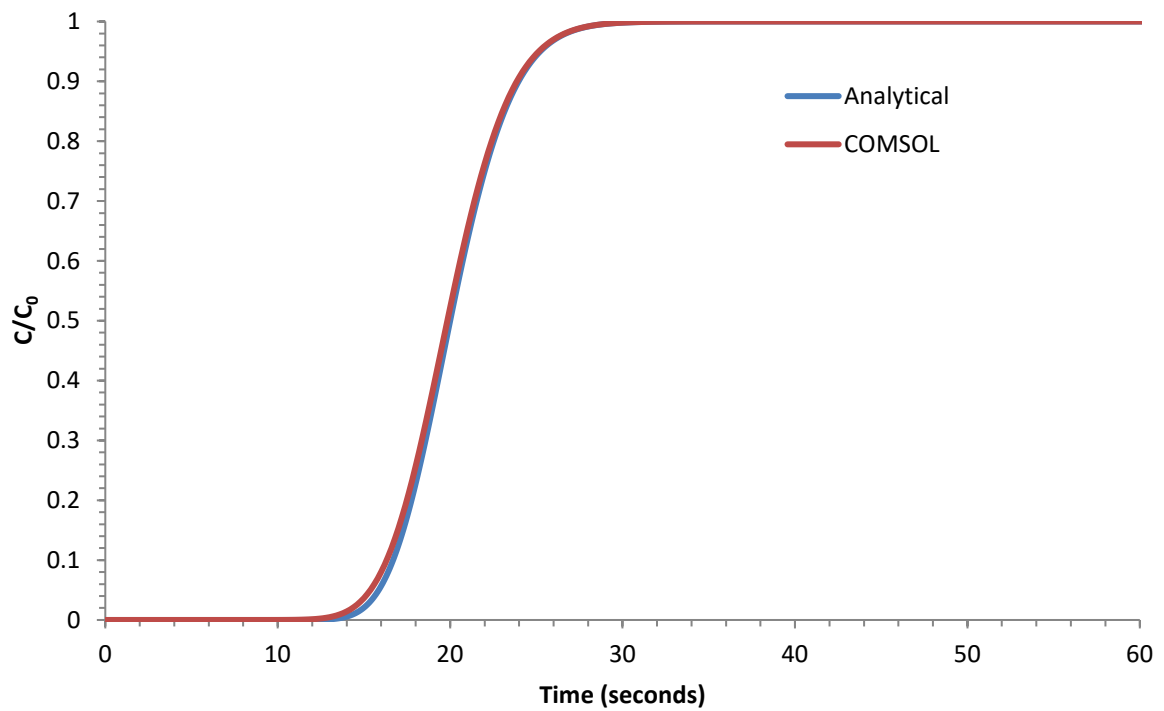


**Figure 4.3 Comparison between analytical solution using Ogata-Banks solution for advection dispersion equation with 1D Model in COMSOL Multiphysics**

Additional tests were carried out using a 2D model using the same parameters in Table 4.1, but including an additional term for transverse dispersion ( $\alpha_t = 0.0001$  m). The model domain used was 0.1 x 1 metre. Initial tests with this model applied the boundary conditions along the edge of the model (Figure 4.4), comparing the result to the 1D model to ensure that the model was coded correctly in 2D (Figure 4.5). The advection-dispersion equation would be further tested during the verification of the colloid transport equations.

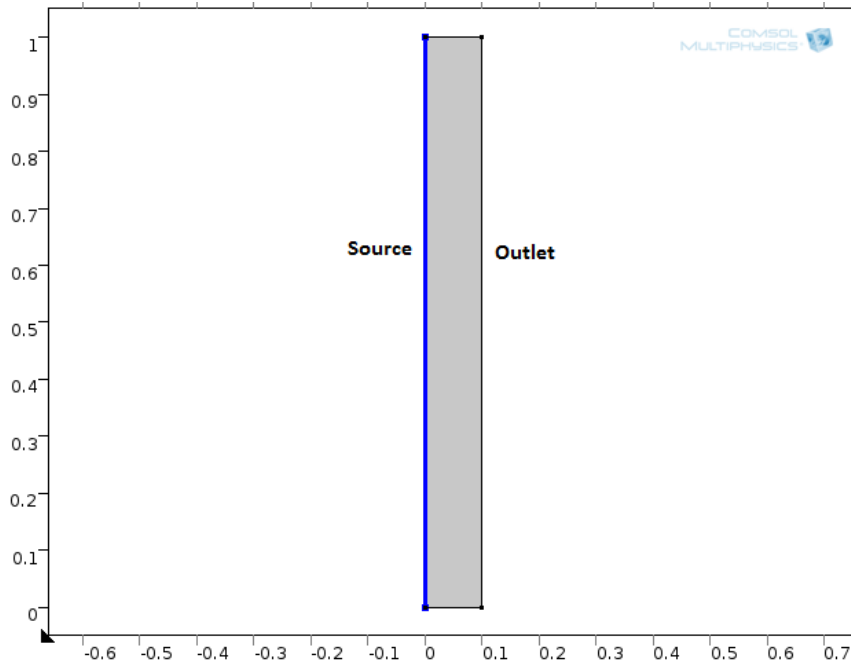


Figure 4.4 Initial 2D model for verification of ADE. Source term applied to left hand boundary, advective only flux applied to right hand boundary. Model domain 0.1 x 1 metre.

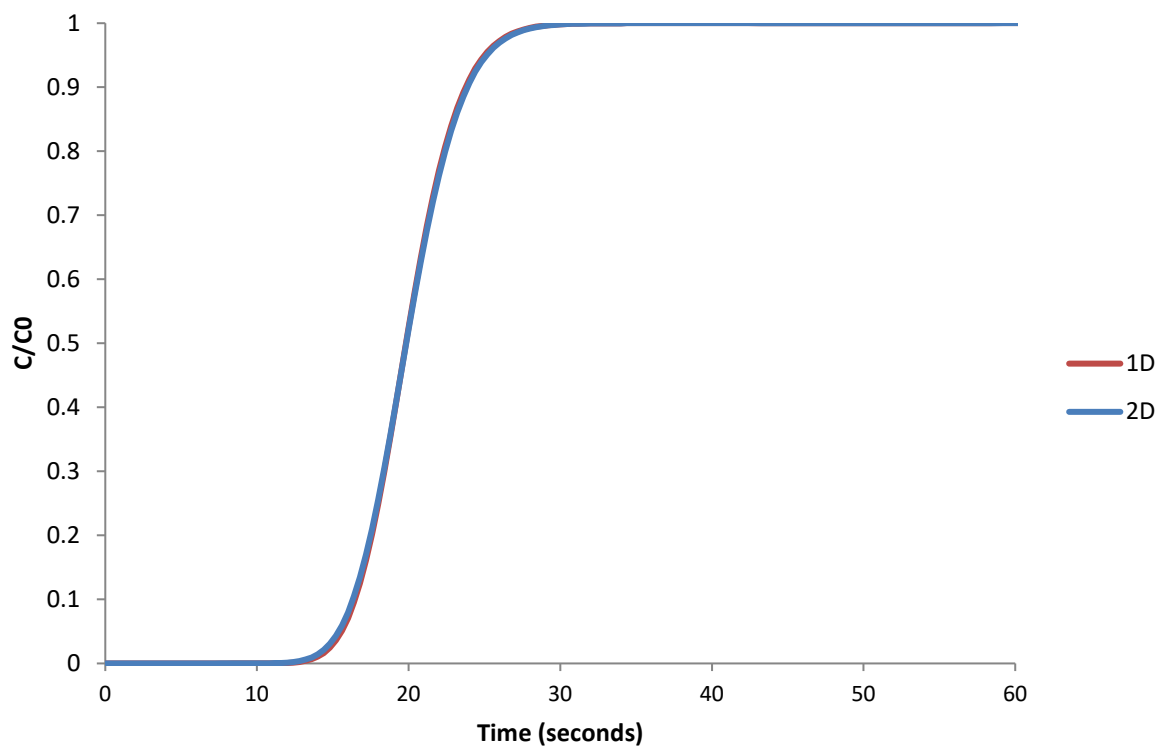


Figure 4.5 Comparison between 1D and 2D numerical models solving the advection-dispersion equation within COMSOL.

#### 4.4.2. Colloid transport and attachment

Initial verification of the colloid transport and attachment equations was carried out by attempting to replicate the results of the modelling carried out by Burns (2013). This was again carried out first in a 1D model, using the same model domain and parameters as above (Table 4.1), but including new parameters for colloid attachment (Table 4.2).

Parameter	Value
$k_{att}$	$0.005 \text{ s}^{-1}$
$k_{det}$	$0.005 \text{ s}^{-1}$
$\rho_b$	$2300 \text{ kg/m}^3$
$F_{max}$	0.1

Table 4.2 Parameters used in 1D COMSOL model to verify colloid transport and attachment equations

This model used a pulse injection of colloids for 50 seconds, after this fresh water was injected into the model, resulting in a good match to the previous model (Figure 4.6).

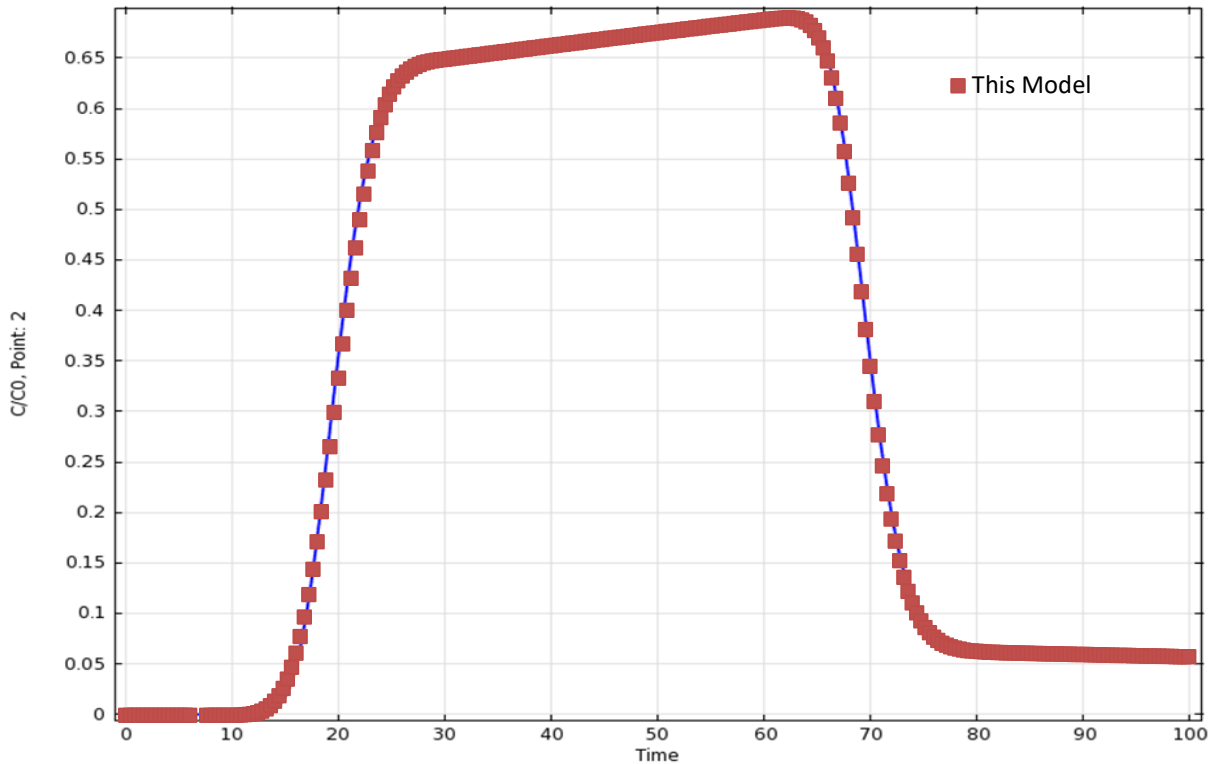


Figure 4.6 Comparison between colloid attachment modelling in Burns (2013), (blue line) and this model (red squares) using parameters in tables above. Time is in seconds, concentration in  $C/C_0$

Further verification was carried out by modelling laboratory migration experiments carried out on an artificial granite fracture with Na-bentonite by Walkden (2014), as detailed in Appendix C. This 2D model included a 30 x 14.9 cm model domain, which used the parameters in Table 4.3.

Parameter	Value
$\rho_b$ (granite bulk density)	2120 kg/m <sup>3</sup>
$\theta$ (porosity)	0.2
b (fracture aperture)	1 mm
k (intrinsic permeability)	1e-11 m <sup>2</sup>
$\mu$ (fluid viscosity)	0.001 Pa*s
$\rho$ (fluid density)	1000 kg/m <sup>3</sup>
$D_d^*$ (molecular diffusion co-efficient)	1e-8 m <sup>2</sup> /s
$g_x$ (acceleration due to gravity along strike)	0
$g_y$ (acceleration due to gravity down dip)	$-\sin(15^\circ)*9.82 \text{ m/s}^2$
$k_{att}$	<i>0.01 s<sup>-1</sup></i>
$k_{det}$	<i>0.04 s<sup>-1</sup></i>
$F_{max}$	5
$k_{iat}$	<i>4.2x10<sup>-5</sup> s<sup>-1</sup></i>
$F_{imax}$	<i>0.01</i>
$\lambda$	<i>750 m<sup>-1</sup></i>
$\alpha_l$	<i>0.01 m</i>
$\alpha_t$	<i>0.001 m</i>

**Table 4.3 Parameters used in 2D COMSOL model for modelling experiments carried out by Walkden (2014). Parameters in italics are calibration parameters.**

The model was calibrated through sensitivity analysis, which also allowed for the testing of different parameters, such as shown in Figure 4.7 where the irreversible

attachment rate was tested to make sure it worked as expected e.g. increased attachment rates result in reduced recovery of colloids. The model was also applied to model a migration experiment that used bentonite colloids across an artificial granite fracture, with the resulting breakthrough shown in Figure 4.8.

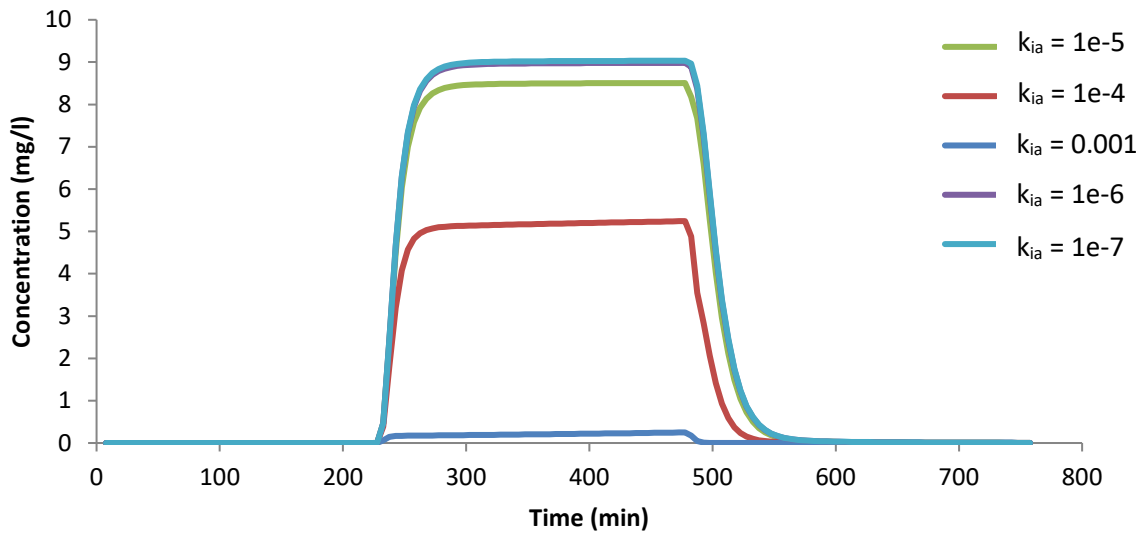


Figure 4.7 Sensitivity analysis of  $k_{iat}$  on COMSOL model using parameters in Table 4.3

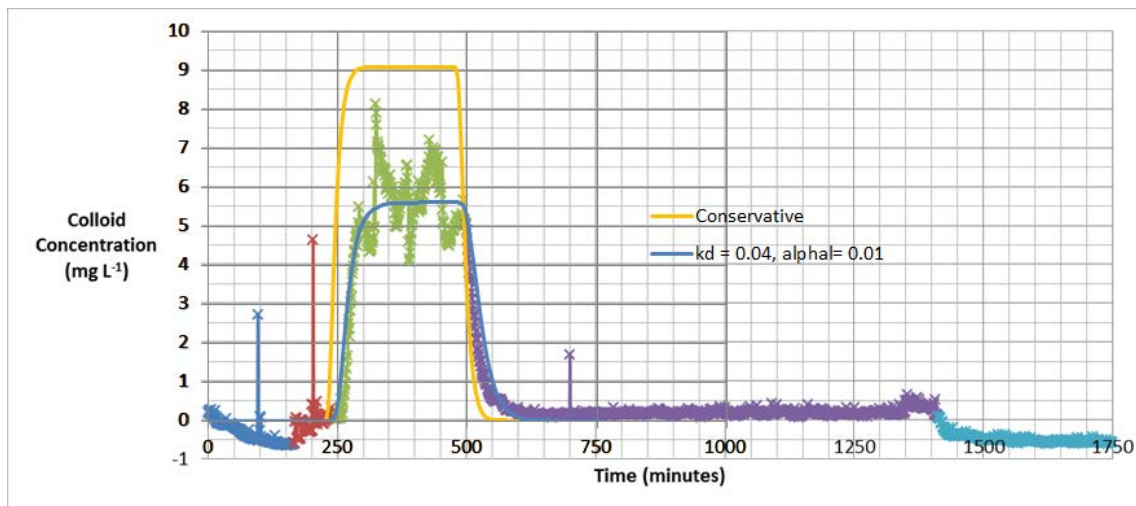


Figure 4.8 Result of calibrated model for Experiment B in Walkden (2014), using the parameters in Table 4.3. Full details of the model found in Appendix C.

As the parameters in the model worked as expected and were able to reproduce these experiments it was decided that the colloid attachment equations worked as expected.

### 4.4.3. Colloid-facilitated radionuclide transport

Due to the large number of processes involved in colloid-facilitated radionuclide transport, analytical solutions typically focus on radionuclide transport with radionuclides that undergo sorption to rock surfaces or transport in the absence of colloids (Baek and Pitt, 1996; Li and Jen, 2001), and therefore have not been used to verify this transport model. The model was first verified by running a sensitivity analysis in a simple model rather than in the full heterogeneous model described in the next section.

For this model, a 12 x 1 metre model domain was used (Figure 4.9), using the parameters in Table 4.4. As the purpose of this testing was to determine that the radionuclide sorption/ desorption equations were coded correctly, a constant colloid concentration was used to make it easier to notice if problems were present in the equations. Figure 4.10 shows the sensitivity to the sorption rate to colloids, which shows that the concentration of aqueous radionuclide decreases with faster sorption rates, as expected.



Figure 4.9 Model domain used for verification of CFRT attachment/ detachment equations. Inlet is on left hand side, right hand side is outlet. The centre line is the concentration measurement point.

Name	Value
k	1e-11 [m <sup>2</sup> ]
μ	0.001 [Pa*s]
b	1 [mm]
ρ	1000 [kg/m <sup>3</sup> ]
g	9.8067 [m/s <sup>2</sup> ]
g <sub>x</sub>	0*g
g <sub>y</sub>	0*g
θ	0.2
α <sub>l</sub>	0.6 [m]
α <sub>t</sub>	0.06 [m]
ρ <sub>f</sub>	2650 [kg/m <sup>3</sup> ]
D <sub>d</sub>	1e-10 [m/s <sup>2</sup> ]
k <sub>att</sub>	0 [1/s]
F <sub>max</sub>	5 [-]
k <sub>det</sub>	0 [1/s]
λ <sub>d</sub>	0 [1/s]
N <sub>mcm</sub>	1000000
C <sub>0</sub> / C	10 mg/l

Table 4.4 Parameters used in initial verification testing of radionuclide sorption and desorption

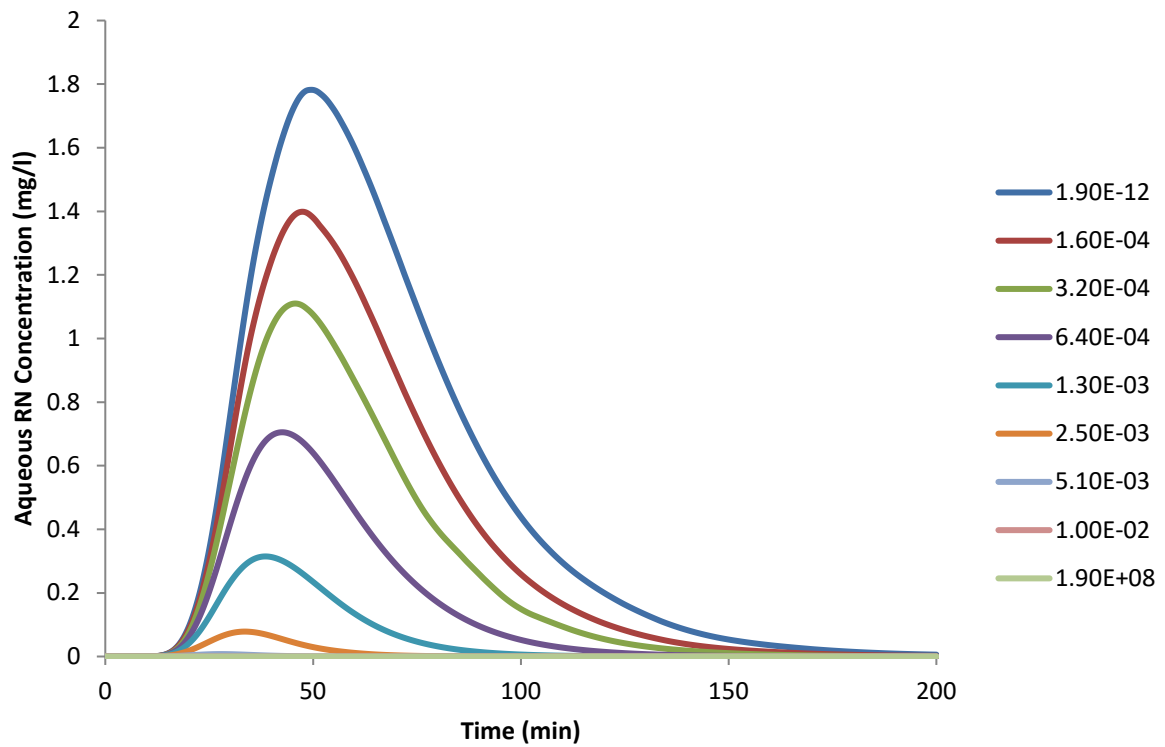
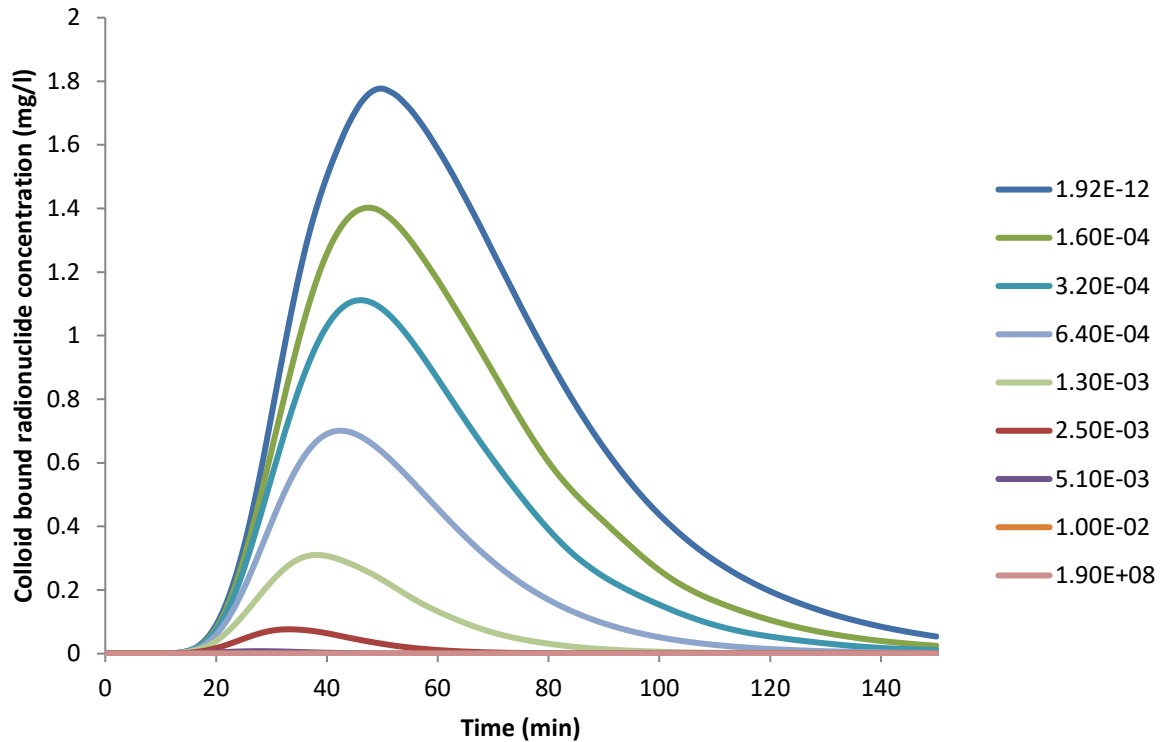


Figure 4.10 Sensitivity analysis for test case, values represent sorption rate  $k_{ams}$  (m<sup>3</sup>/kg.s), with 10 hour pulse injection.

Corresponding figures were also made to test the desorption rate from mobile colloids (Figure 4.11), which also showed the expected result i.e. increased desorption rates resulted in reduced recovery of colloid bound radionuclides.



**Figure 4.11 Sensitivity analysis for test case, values represent desorption rate  $k_{mca}$  (1/s), with 10 hour pulse injection.**

Similar tests were made at each model calibration stage when using the full numerical model described in the section below, to make sure that the equations were coded correctly and worked as intended when additional processes were added into the model, that the mass balance was correct and to ensure that the models were grid and time step converged.

#### **4.5. Numerical Model**

The equations detailed in Section 4.3 were coded into COMSOL Multiphysics v4.4 (COMSOL, 2013), a general-use finite element method equation solver, which specialises in

solving multiphysics problems. For this model, these equations were coded into a 2D model domain.

Initially, the full model domain used in the inverse model/ MODFLOW was imported into COMSOL. This model domain is shown in Figure 4.12 and is 55 m x 63.25 m in size. To save computational time, a sub region was selected for the transport model, 7 m x 5.5 m in size. This model domain centred around the injection and extraction boreholes used in the two modelled *in situ* dipole experiments (CRR 99.010-i2 and BOMI 87.010-i2), positioning the rectangle so that it was larger than the maximum plume extent as calculated from a MT3D model of CRR tracer tests (at least 2m from the boreholes). Figure 4.13 shows the transport model domain, highlighted in blue.

To ensure that the boundaries of the different zones of hydraulic conductivity were accurately represented in the COMSOL model, small rectangles were created that correspond to the different zones from the inverse model. The geometries of these rectangles were generated from .dxf files using a script written in R by Lindsay McMillan, a full copy of which is found in Appendix B.

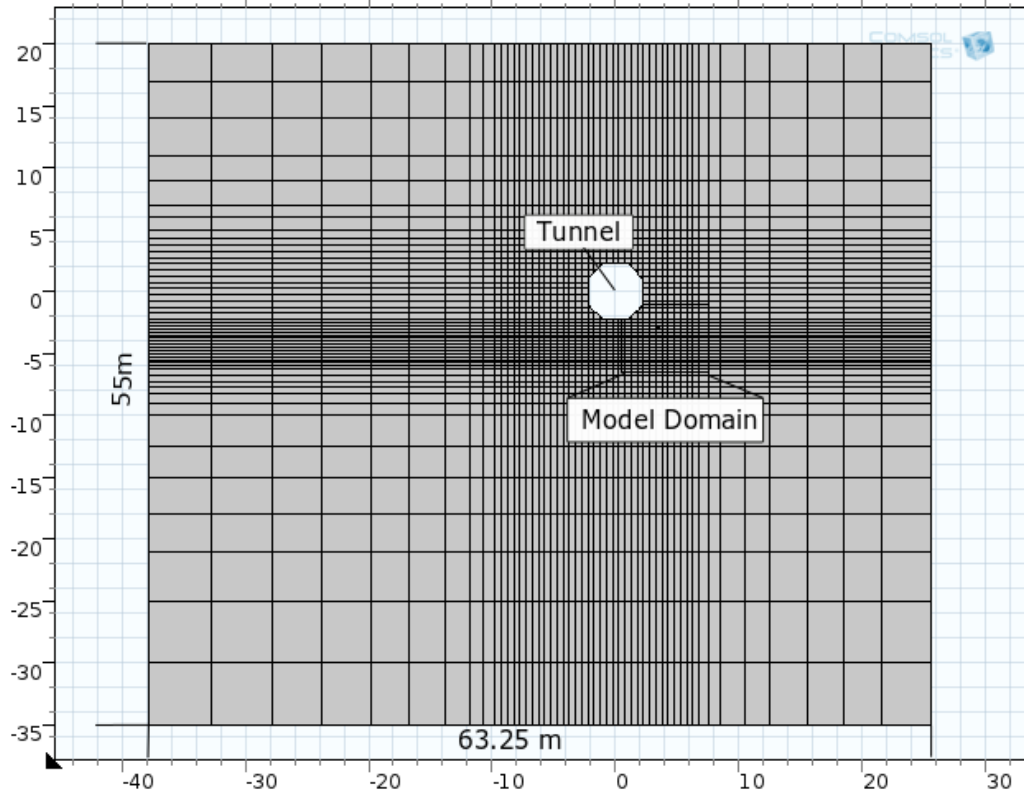


Figure 4.12 Geometry of 2D Transport Model (co-ordinate system centred on the centre of the tunnel, model domain represents plane view of shear zone dipping  $\sim 75^\circ$  to the south)

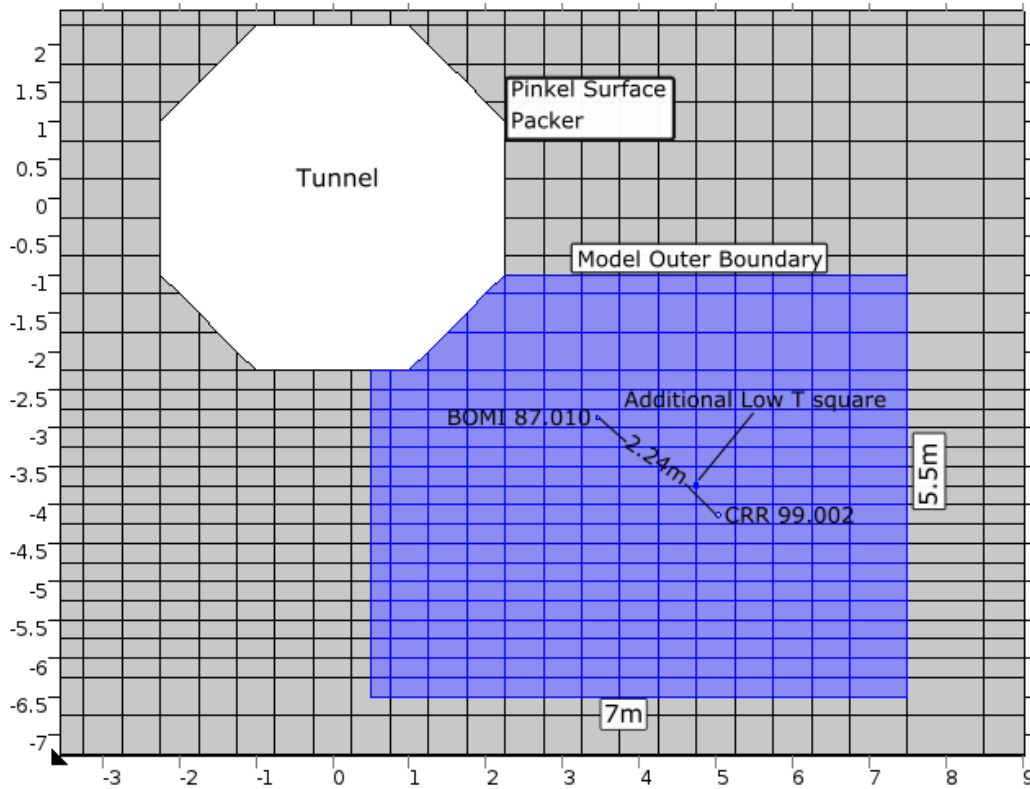


Figure 4.13 Close up of model domain (highlighted in blue, co-ordinate system centred on the centre of the tunnel). Explanation of low T square given in text below.

To represent the tunnel that intersects the MI shear zone, an octagon 4.5m wide by 4.5m high was placed in the model. The tunnel runs in a rough north-south direction, and is circular, so the octagon used in the model only approximates the tunnel shape, but was used as early versions of the model had difficulty generating a good quality mesh with a circular tunnel. For the two borehole intervals, two octagons with a side length of 2 cm with a radius of 2.5 cm were added to the model, again chosen so that the model was easier to mesh with a regular mapped grid while providing a good approximation of the borehole intervals. Within both the tunnel and the borehole intervals, the flow and transport equations were not solved.

In early stages of model calibration, it was noticed that the breakthrough of conservative tracer was occurring too early. This was believed to be caused by differences between the models used to solve for the groundwater flow field. MODFLOW (and the inverse model) uses the block-centred finite difference method, where each cell is linked to the adjacent rows and columns resulting in five equations being solved for each cell. COMSOL uses the finite element method, where more equations (nine) are generated to link different nodes within the mesh. This difference is important as the inverse model includes a low transmissivity barrier to match the tracer test results in the centre of the transport model domain. When the transmissivity field was applied in COMSOL, the low transmissivity barrier was less effective. To prevent the early breakthrough from occurring, an additional low transmissivity square was added into COMSOL. The additional square is 0.05m in size, and positioned so it overlaps between two low transmissivity areas from the inverse model. For convenience, this square was only added to the most significant pinch point. Figure 4.14

shows the transmissivity field between the two boreholes, with the low transmissivity block highlighted.

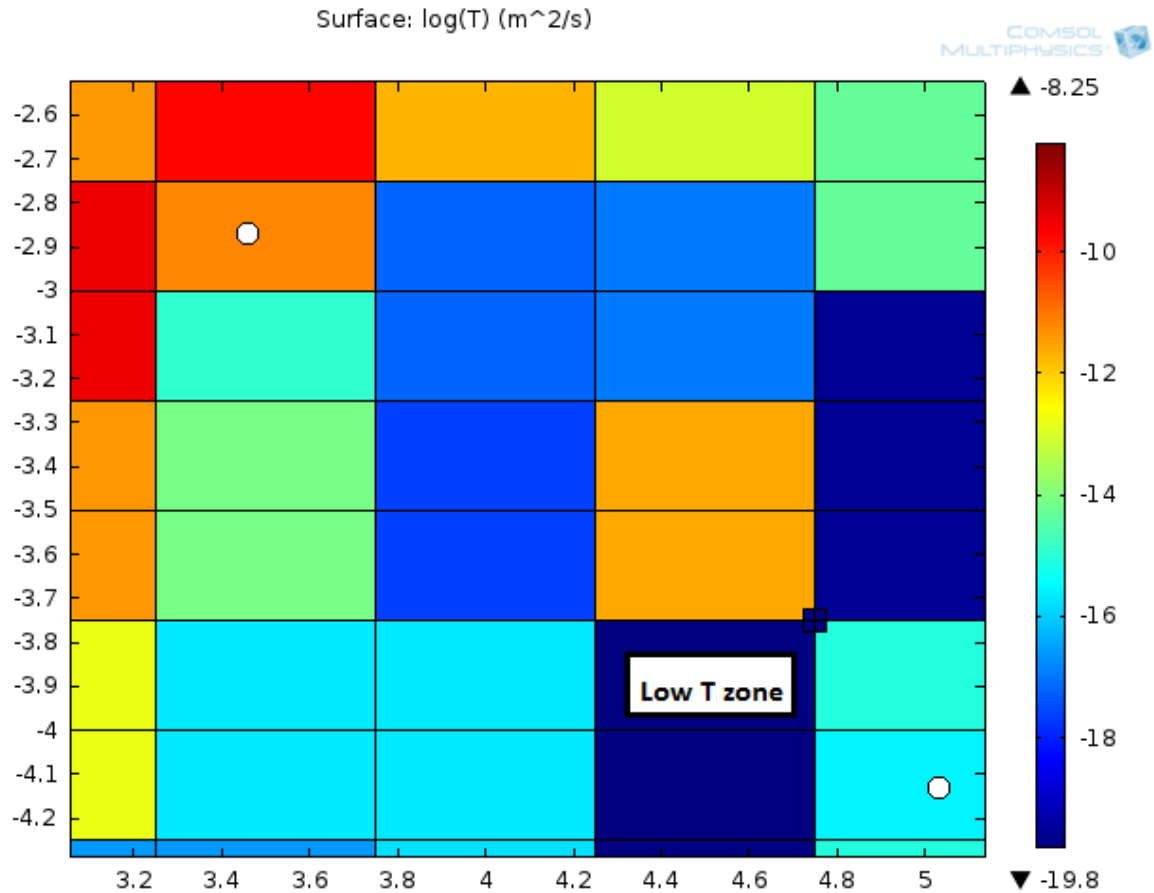


Figure 4.14 Transmissivity of part of model area (m<sup>2</sup>/s in log scale), including low transmissivity block highlighted.

A number of different boundary conditions are applied to the different equations in the model. For groundwater flow, (Equation 4.1), specified flux boundary conditions were applied to the injection and abstraction boreholes. As the boundary condition is applied over an area (the circumference of the borehole) within the model, the flow rates used in the experiments were divided to give a flow rate per unit circumference that is applied in the model.

A fixed pressure boundary condition is applied to the outer boundaries of the model, specifying a pressure value depending on the hydraulic head calculated in a MODFLOW model of the full shear zone that represents the flow conditions within each experiment. The exception to this is the model boundary with the tunnel, to which a no-flow boundary is applied. The hydraulic head is read from a MODFLOW .hds file (that has been converted into a .dat file); using a C function written by Dr Lindsay McMillan (a full copy of the function is found in Appendix B), and interpolated into the COMSOL model at the model boundary. This is then converted into a pressure in COMSOL. As COMSOL assumed that groundwater was constant density and viscosity the pressure values represent nominal values and are therefore consistent.

For the transport equations a specified flux boundary condition is applied to the injection borehole, based on the measured source term of the experiments, equal to the measured concentration multiplied by the injection flow rate per unit circumference ( $V_{in}$ ). For CRR Run 32, the source term applied was a ten minute pulse injection. For CFM Run 13-05, the method of injection used meant that the concentration of the injection cocktail declined roughly exponentially, but had to account for dilution that occurred across the injection interval.

This requires the alteration of the  $Q_{in}$  (and therefore  $V_{in}$ ) values used in CFM Run 13-05 as more water is entering the model than anticipated (this cross flow was not picked up by the inverse model due to uncertainty in far field boundary conditions). An estimate of the cross-flow in the experiment is an average of 0.29 ml/min (see Chapter 3). Therefore, the value for  $Q_{in}$  in CFM Run 13-05 is set as 0.62 ml/min (0.33 + 0.29 ml/min). As this water

entering the model represents both the injection cocktail and the natural cross flow, a different input flux for the transport boundary conditions has to be set, as the dilution results in a lower contaminant flux into the model. For CFM Run 13-05, the contaminant input flux term is set as  $Q_{inc}$ , and is equal to  $Q_{in}$  multiplied by the dilution factor. The dilution factor for the experiment is defined by Equation 4.12.

$$Dilution\ Factor = \frac{Original\ Flow\ Rate}{Total\ Flow\ Rate} = \frac{20.33}{20.33 + 0.29} (ml/min)$$

**Equation 4.12 Dilution Factor used to set CFM Run 13-05 boundary conditions**

For CFM 13-05, the dilution factor is equal to 0.985, and so  $Q_{inc}$  is set as 0.611 ml/min. The source term for CFM Run 13-05 used the actual injection concentration values measured in the recirculation circuit of conservative tracer. Due to data quality issues the actual injection concentrations could not be used from 275 hours after the injection started. After 275 hours through to the end of the model injection (700 hours) an approximation of the actual source term was used, as shown in Equation 4.13.

$$e^{-\frac{Q_{in}t}{Vol} C_0 V_{in}}$$

**Equation 4.13 Exponential source term factor**

where  $t$  is the time elapsed since injection started [T],  $Vol$  is the volume of the recirculation circuit [ $ML^{-3}$ ] and  $C_0$  is the initial concentration of tracer [ $ML^{-3}$ ].

For the radionuclide transport equations (Equation 4.6 and Equation 4.7), the concentration of aqueous and sorbed to mobile colloids used for the initial concentration depended on the initial bound fraction measured for both experiments by measuring the concentration of radionuclides removed by centrifugation. Zero dispersive flux (or advection

only) boundary conditions are applied to both the abstraction borehole, and the outer boundary of the model. Finally, the model assumes that the initial concentrations of colloids and radionuclides in all the phases are equal to zero.

For the model, a regular rectangular mesh (called the mapped mesh in COMSOL) was used where possible, i.e. in areas of the model with one-connected edge boundary. Where this rectangular mesh could not be applied, (in areas that intersected the boreholes or the tunnel) a triangular mesh (called free triangular in COMSOL) was used. The mesh used a maximum mesh size of 0.05 m, with a minimum size of 0.001 m, (other settings used default values; maximum element growth rate 1.05, curvature factor 0.2, narrow region resolution 1). Linear Lagrange elements were used throughout. These values gave a Peclet number of 0.5 (based on a longitudinal dispersivity of 0.1 m). The resulting mesh for the model is shown in Figure 4.15. Tests were carried out in the model to determine that the model was grid converged.

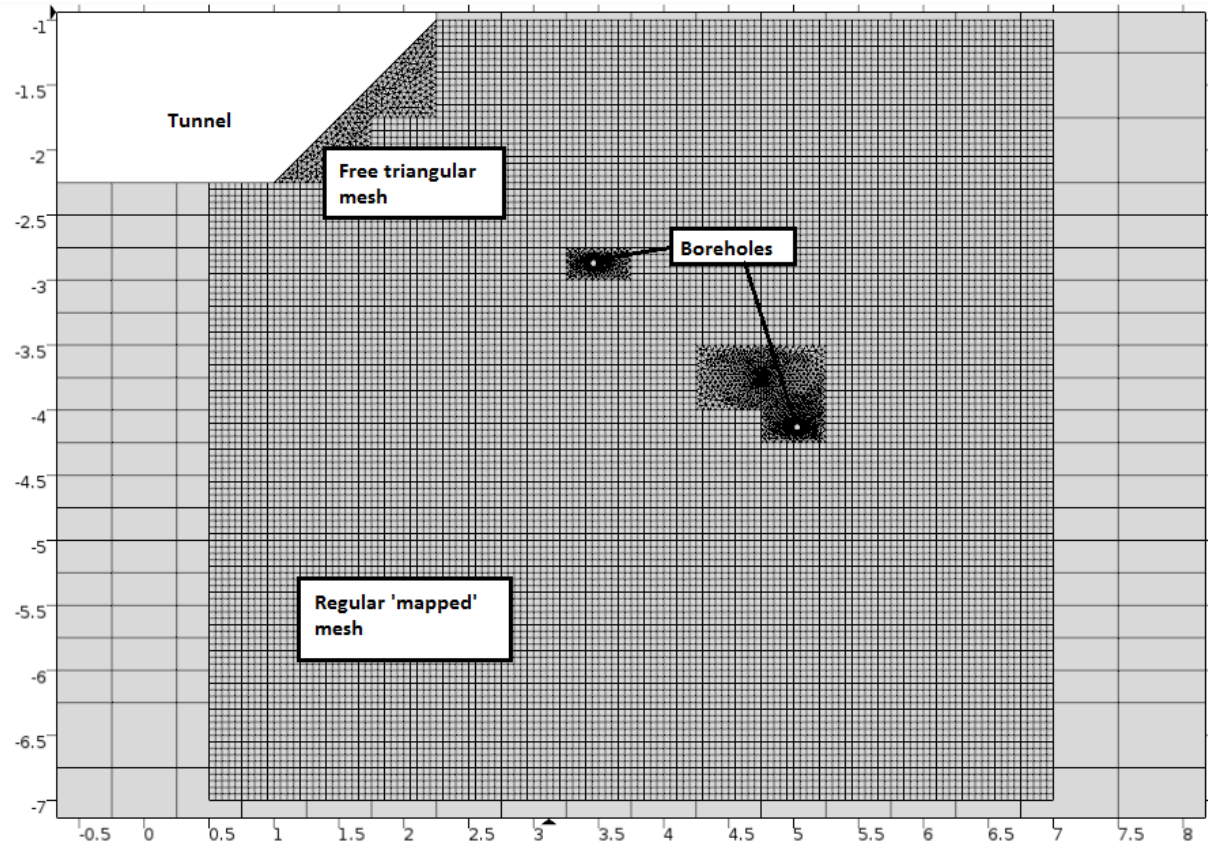


Figure 4.15 Mesh used in transport model, plane view of shear zone (co-ordinate system centred on tunnel in metres).

The model reads the transmissivity value of the different zones generated by the inverse model using an external function written in C by Dr Lindsay McMillan, a full copy of which is found in Appendix B. To provide greater accuracy on the import of the transmissivity field, an additional algebraic equation is solved (Equation 4.14) in a standalone steady state/ stationary solver, calling the external function data and storing the value of the transmissivity field within the model files before the other equations are solved.

$$trans - T = 0$$

**Equation 4.14** Equation to load transmissivity field into COMSOL model

where  $T$  is the transmissivity value read from the external function data [ $L^2T^{-1}$ ] and  $trans$  is the transmissivity value used in the transport model [ $L^2T^{-1}$ ].

The model then solves for steady-state groundwater flow using the transmissivity field and boundary conditions, using the stationary or steady-state solver in COMSOL. This groundwater flow field is then used by the time-dependent solver in COMSOL to solve the relevant transport equations. The 'MUMPS' solver was used (as the default solver), alongside the 'BDF' time stepping algorithm with strict time steps of 0.1 minutes for the CRR Run 32 model, and 0.1 hours for the CFM 13-05 model, giving Courant numbers of 0.06 for CRR Run 32 (using an average velocity of  $5 \times 10^{-4}$  m/s) and 0.144 for the CFM Run 13-05 model (using an average velocity of  $2 \times 10^{-5}$  m/s). Tests were carried out to ensure that the model was time-step converged. The model is run for 2000 minutes for CRR Run 32 and 1200 hours for CFM Run 13-05.

Finally, the COMSOL model generated the output data for the breakthrough curves using COMSOL's line integration tool to calculate the term:  $(\text{Concentration} * Q_{\text{out}}) / V_{\text{out}}$ , where  $V_{\text{out}}$  and  $Q_{\text{out}}$  are the abstraction discharge divided by the borehole circumference, and the abstraction discharge respectively.

#### **4.6. Transport Model Application**

The model was applied to two migration experiments (CRR Run 32 and CFM Run 13-05) that were carried out in the same dipole within the MI shear zone (CRR Dipole 1 between CRR 99.002 and BOMI 87.010), with the aim of replicating the transport of conservative tracers, bentonite colloids and selected radionuclides using a set of consistent transport parameters. The approach used to model these experiments is discussed below but was carried out to reduce the number of free parameters and degrees of freedom available during model calibration.

The model was first calibrated to the breakthrough of the conservative tracers used in the two experiments (Amino-G acid in CFM Run 13-05 and  $^{131}\text{I}$  in CRR Run 32). This stage of the calibration altered longitudinal dispersivity. In addition, differences between the fracture aperture used in the inverse model (generated by the cubic law, as described in Chapter 3) and the transport aperture (i.e. the aperture required for a transport velocity) mean that the fracture is represented by a series of parallel plates, leading to a scaling factor  $f$  which is a calibration parameter for conservative tracer in this model.

Once conservative tracer breakthrough was calibrated, breakthrough of bentonite colloids (as measured using LIBD in CRR Run 32, and the aluminium signal in CFM Run 13-05) was calibrated by altering the different colloid attachment parameters. Initially only reversible colloid attachment was included, with the option to include irreversible colloid attachment if required.

The final stage of the model calibration was to model radionuclides. The radionuclides represent a number of different redox states and have different initial colloid bound fractions. The radionuclides chosen were americium-241 and 243 ( $^{241}\text{Am}$  in CRR Run 32 and  $^{243}\text{Am}$  in CFM Run 13-05), plutonium-244 and 242 ( $^{242}\text{Pu}$  in CFM Run 13-05 and  $^{244}\text{Pu}$  in CRR Run 32), caesium-137, uranium-233 and neptunium-237.

Radionuclide transport was calibrated by initially altering sorption and desorption rates to a single sorption site on the bentonite colloids, and the aqueous phase retardation factor. Additional processes such as kinetic sorption to rock surfaces, matrix diffusion and additional sorption sites on the colloids were added as necessary to calibrate radionuclide breakthrough. This approach both limited the number of free calibration parameters, and

helped determine which processes needed to be included to accurately model the breakthrough of the radionuclide in question.

The model calibration at each stage was determined by visual match to the breakthrough curve data, and model calibration was carried out manually using sensitivity analysis. Where possible, parameters from laboratory experiments (for instance sorption/desorption batch experiments) were used in the model as initial estimates. Where laboratory data was not available, then parameters used from other models of the CFM/ CRR experiments were used to provide initial estimates of parameter values.

#### **4.7. Summary**

This chapter detailed the colloid-facilitated radionuclide transport model that has been used to model two in-situ migration experiments carried out at the Grimsel Test Site (CFM Run 13-05 and CRR Run 32). This model combines an inverse model generated transmissivity distribution with a flexible series of equations that describe the transport of tracers, bentonite colloids and various radionuclides, which can be switched on and off as necessary. Additional processes can also be added, for instance if additional types of sorption sites need to be included on colloids or rock surfaces.

The model is created in COMSOL Multiphysics, and uses similar descriptions of processes as previous models of the CFM experiments, but differs as it includes the transmissivity distribution and explicitly solves for groundwater flow, as the majority of the previous models are descriptive for groundwater flow, and use simplistic 1D or homogeneous 2D representations of the shear zone in which the experiments take place.

Colloid attachment is described using a continuum based approach which will allow comparisons to the other models and as mechanistic models of colloid attachment would also require alteration and calibration in the experiments. Radionuclide sorption to colloids is described using reversible second order kinetics, which can be limited and to multiple site types as necessary. The majority of the other processes are described by first-order kinetics.

This chapter shows how the equations were verified, either with comparisons between a numerical model built in COMSOL with appropriate analytical solutions (for advection-dispersion, retardation and radioactive decay); with comparisons to previous modelling (colloid attachment); modelling of previous laboratory experiments (colloid attachment; and testing that the parameters worked as expected during sensitivity analysis (colloid attachment and colloid-facilitated radionuclide transport).

Finally, this chapter details the setup and application process of the model in COMSOL that is applied to the field experiments at the Grimsel Test Site with the aim of describing the experiments in a self-consistent manner. The results of the modelling of conservative tracer and colloid transport are contained in the Chapter 5, the results of modelling americium and plutonium transport in Chapter 6 and the transport of caesium, uranium and neptunium in Chapter 7.

#### **4.8. List of References**

Baek, I. and Pitt, W.W. (1996) Colloid-facilitated radionuclide transport in fractured porous rock. **Waste Management**, 16 (4): 313–325 DOI: 10.1016/S0956-053X(96)00074-8

Black, J.H. and Kipp, K.L. (1983) Movement of tracers through dual-porosity media - Experiments and modelling in the Cretaceous Chalk, England. **Journal of Hydrology**, 62 (1–4): 287–312 DOI: 10.1016/0022-1694(83)90108-7

Bradford, S.A., Simunek, J., Bettahar, M., Van Genuchten, M.T. and Yates, S.R. (2003) Modeling

colloid attachment, straining, and exclusion in saturated porous media. **Environmental Science and Technology**, 37: 2242–2250 DOI: 10.1021/es025899u

Bradford, S.A., Simunek, J., Bettahar, M., Van Genuchten, M.T. and Yates, S.R. (2006) Significance of straining in colloid deposition: Evidence and implications. **Water Resources Research**, 42 (December 2005): 1–16 DOI: 10.1029/2005WR004791

Burns, D. (2013) **Modelling of experimental breakthrough curves of colloid injection**. Birmingham: Undergraduate Project, University of Birmingham

COMSOL (2013) **COMSOL Multiphysics**. v4.4 [online]. COMSOL Inc. Available from: [www.comsol.com](http://www.comsol.com)

Dittrich, T.M., Boukhalfa, H., Ware, S.D. and Reimus, P.W. (2015) Laboratory investigation of the role of desorption kinetics on americium transport associated with bentonite colloids. **Journal of Environmental Radioactivity** [online], 148: 170–182 DOI: 10.1016/j.jenvrad.2015.07.001. Available from: <http://dx.doi.org/10.1016/j.jenvrad.2015.07.001>

Dittrich, T.M. and Reimus, P. (2015a) Uranium transport in a crushed granodiorite: Experiments and reactive transport modeling. **Journal of Contaminant Hydrology** [online], 175–176: 44–59 DOI: 10.1016/j.jconhyd.2015.02.004. Available from: <http://dx.doi.org/10.1016/j.jconhyd.2015.02.004>

Dittrich, T.M. and Reimus, P.W. (2015b) **Nagra Arbeitsbericht NAB 15-09: Laboratory investigation of colloid-facilitated transport of caesium by bentonite colloids in a crystalline rock system**. Wettingen, Switzerland

Domenico, P. and Schwartz, F. (1990) **Chemical and Physical Hydrogeology**. 1st ed. New York: Wiley

Gaus, I. and Smith, P.A. (2008) **Nagra Arbeitsbericht NAB 08-27: Modellers dataset for the Colloid Formation and Migration Project Status: End of CFM Phase 1**. Wettingen, Switzerland

Huber, F., Heck, S., Truche, L., Bouby, M., Brendle, J., Hoess, P. and Schäfer, T. (2015) Radionuclide desorption kinetics on synthetic Zn / Ni-labeled montmorillonite nanoparticles. **Geochimica et Cosmochimica Acta**, 148: 426–441 DOI: 10.1016/j.gca.2014.10.010

Huber, F., Kunze, P., Geckeis, H. and Schäfer, T. (2011) Sorption reversibility kinetics in the ternary system radionuclide-bentonite colloids/nanoparticles-granite fracture filling material. **Applied Geochemistry** [online], 26 (12): 2226–2237 DOI: 10.1016/j.apgeochem.2011.08.005. Available from: <http://dx.doi.org/10.1016/j.apgeochem.2011.08.005>

Ibaraki, M. and Sudicky, E.A. (1995) Colloid-facilitated contaminant transport in discretely fractured porous media. 1. Numerical formulation and sensitivity analysis. **Water Resources Research**, 31 (12): 2945–2960 DOI: 10.1029/95WR02180

Lanyon, B. and Blechschmidt, I. (2016) **Nagra Aktennotiz AN16-102: Minutes of the CFM Modellers Workshop, 10-11 December 2015, San Francisco**. Wettingen, Switzerland

Li, S.H. and Jen, C.P. (2001) Migration of radionuclides in porous rock in the presence of colloids: Effects of kinetic interactions. **Waste Management**, 21: 569–579 DOI: 10.1016/S0956-053X(00)00104-5

Missana, T. and Geckeis, H. (2006) **Nagra Technical Bulletin NTB 03-02: CRR Final Project Report 2 - Supporting Laboratory Experiments with Radionuclides and Bentonite Colloids**. Wettingen, Switzerland

Möri, A., Alexander, W.R., Degueldre, C., Eikenberg, J., Fierz, T., Geckeis, H., Geier, F., Hauser, W., Schäfer, T. and Smith, P.A. (2004) **Nagra Technical Bulletin NTB 03-01: The CRR Final Project Report series 1 - Description of the Field Phase - Methodologies and Raw Data** [online]. Wetztingen, Switzerland. Available from: <http://www.nagra.ch/en/cat/publikationen/technicalreports-ntbs/ntbs-2001-2012/downloadcentre.htm>

Möri, A., Alexander, W.R., Geckeis, H., Hauser, W., Schäfer, T., Eikenberg, J., Fierz, T., Degueldre, C. and Missana, T. (2003) The colloid and radionuclide retardation experiment at the Grimsel Test Site: influence of bentonite colloids on radionuclide migration in a fractured rock. **Colloids and Surfaces A: Physicochemical and Engineering Aspects** [online], 217 (1–3): 33–47 DOI: 10.1016/S0927-7757(02)00556-3. Available from: <http://linkinghub.elsevier.com/retrieve/pii/S0927775702005563> [Accessed 12 December 2014]

Noseck, U., Flügge, J., Reimus, P., Cvetkovic, V., Lanyon, B., Schäfer, T. and Blechschmidt, I. (2016) **Nagra Technical Report NTB 16-06: Colloid Formation and Migration Project: Modelling of tracer, colloid and radionuclide/homologue transport for dipole CFM 06.002- Pinkel surface packer.** Wetztingen, Switzerland

Ryan, J.N. and Elimelech, M. (1996) Colloid mobilization and transport in groundwater. **Colloids and Surfaces A: Physicochemical and Engineering Aspects**, 107 (95): 1–56 DOI: 10.1016/0927-7757(95)03384-X

Schäfer, T., Darbha, G. and Iijima, K. (2014) **Nagra Arbeitsbericht NAB 13-79 CFM Phase 2: Status Report of the Laboratory Programme at the end of 2011.** Wetztingen, Switzerland

Schäfer, T., Lanyon, B. and Blechschmidt, I. (2013) **CFM 13-05 Data Set.** pers comm.: Nagra/ KIT-INE (Unpublished Dataset)

Walkden, S. (2014) **Bentonite Colloid Investigations on a granite fracture.** MSc Thesis, University of Birmingham

## **5. MODELLING CONSERVATIVE TRACER AND COLLOID TRANSPORT IN CFM RUN 13-05 AND CRR RUN 32**

### **5.1. Introduction**

This chapter presents the results of the transport model calibration for conservative tracer and bentonite colloid breakthrough for both CFM Run 13-05 and CRR Run 32, using the model described in the previous chapter. These experiments were carried out between the same two boreholes 2.24m apart, but under different flow conditions (CRR Run 32 was run at 30 times higher flow rates than CFM Run 13-05). The model used in this work includes a transmissivity distribution generated by an inverse model to attempt to describe the transport of tracers, bentonite colloids and radionuclides using self-consistent descriptions. Model calibration for tracers and colloids was carried out before modelling the radionuclides described in the next two chapters.

This chapter also details a homogeneous 1D channel model that was used to determine whether it was possible to find the same effective parameters to describe groundwater flow, conservative tracer and bentonite colloid transport in the two experiments.

Finally, this chapter details how the 2D model was applied to make blind predictions of the REMO-2 (colloid remobilisation) experiment carried out in the MI shear zone in 2017, which tested the ability of the model to make predictions about colloid transport in the MI shear zone.

Parts of this chapter have already been written up and presented as a conference paper at the American Nuclear Society International High Level Radioactive Waste Management conference (Harvey et al., 2017).

## 5.2. Numerical model setup

The COMSOL model has been described in Chapter 4. In addition to the calibration parameters for each species, Table 5.1 lists the parameters that were kept constant (i.e. non-calibration parameters). Figure 4.15 shows the grid used in the model (maximum size 0.05m), with maximum time steps of either 0.1 minutes (CRR Run 32) or 0.1 hours (CFM Run 13-05). A summary of the boundary conditions used in the model is provided in Table 5.2.

Parameter	Symbol	CFM 13-05	CRR 32	Justification
Water Viscosity	$\mu$	1.307x10 <sup>-3</sup> (kg/m.s)		Standard value for water at 10°C
Water Density	$\rho$	1000 (kg/m <sup>3</sup> )		Standard value for water at 10°C
Acceleration due to gravity <ul style="list-style-type: none"> <li>• X-direction</li> <li>• Y-direction</li> </ul>	$g_x$ $g_y$	0 (m/s <sup>2</sup> ) -9.8 (m/s <sup>2</sup> )		Based on model assumption that shear zone vertical in model co-ordinate system
Molecular diffusion co-efficient	$D_d^*$	1x10 <sup>-10</sup> (m <sup>2</sup> /s)		Standard value for ions in water
Input discharge	$Q_{in}$	0.62 (ml/min)	10 (ml/min)	Based on experimental protocol
Concentration input discharge <sup>1</sup>	$Q_{inc}$	0.611 (ml/min) <sup>1</sup>	10 (ml/min)	Based on experimental protocol
Output discharge	$Q_{out}$	5 (ml/min)	150 (ml/min)	Based on experimental protocol
Bulk density of FFM	$\rho_f$	2650 (kg/m <sup>3</sup> )		Experimentally measured for Grimsel FFM
Porosity	$\theta$	0.99		See text below
Transverse dispersivity	$\alpha_t$	1/10 of longitudinal dispersivity		Kept as non-calibration parameter as non-sensitive parameter

1: See discussion in Chapters 3 and 4 on changes made to reflect the source term in CFM 13-05

**Table 5.1 Transport model non-calibration parameters.**

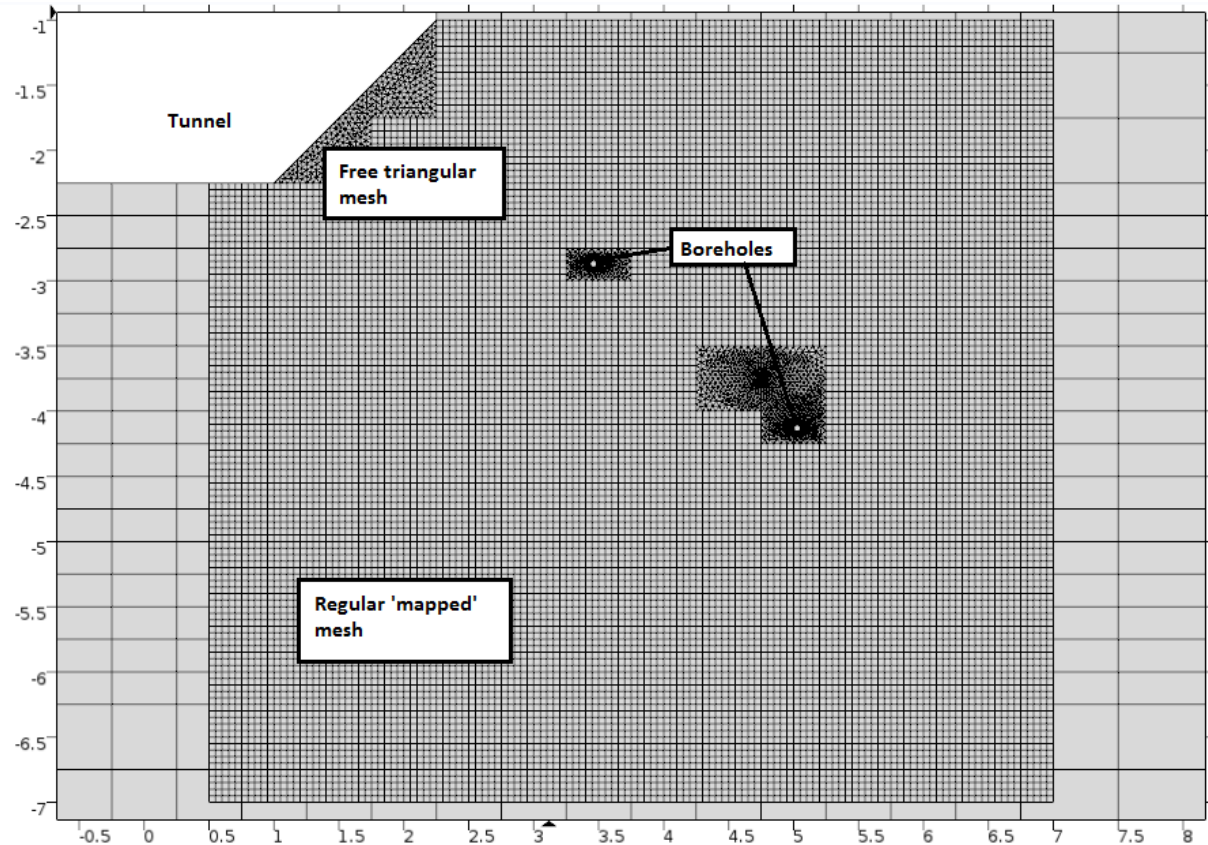


Figure 5.1 Mesh used in transport model, plane view of shear zone (co-ordinate system centred on tunnel in metres).

The cubic law is used to relate transmissivity to fracture aperture in the inverse model, however this does not accurately represent the mass balance fracture aperture for transport, and so the fracture aperture from the inverse model is likely to be an underestimate. The geological structure of the MI shear zone is represented by a series of stacked parallel plates, as used in the inverse model (Chapter 3), where a scaling factor ( $f$ ) is used as a calibration parameter in the conservative tracer modelling. The porosity value included in Table 5.1 represents the porosity of the fractures within the parallel plates, and so is set at 0.99 (it could not be set as 1 as this would cause a singularity when attempting to solve the colloid attachment equations).

Equation	Injection borehole	Abstraction borehole	Model outer boundary
Groundwater flow	Specified flux $V_{in}$	Specified flux $V_{out}$	Specified head based on full MODFLOW model/ No flow over tunnel boundary
Conservative tracer	Specified flux $V_{inc}$ (source term dependent)	Advective flux only	Advective flux only/ No flux over tunnel boundary
Colloid transport	Specified flux $V_{inc}$ (source term dependent)	Advective flux only	Advective flux only/ No flux over tunnel boundary
Attached colloids	No flux boundary	No flux boundary	No flux boundary
Irreversibly attached colloids	No flux boundary	No flux boundary	No flux boundary
Radionuclide transport	Specified flux $V_{inc}$ (dependent on source term and initial bound fraction)	Advective flux only	Advective flux only/ No flux over tunnel boundary
Radionuclides sorbed to mobile colloids	Specified flux $V_{inc}$ (dependent on source term and initial bound fraction)	Advective flux only	Advective flux only/ No flux over tunnel boundary
Radionuclides sorbed to rock surfaces	No flux boundary	No flux boundary	No flux boundary
Radionuclides sorbed to attached colloids	No flux boundary	No flux boundary	No flux boundary
Radionuclide sorbed to irreversibly attached colloids	No flux boundary	No flux boundary	No flux boundary
Radionuclide matrix diffusion	No flux boundary	No flux boundary	No flux boundary

Table 5.2 Transport model boundary conditions

### 5.3. Conservative tracer model calibration

Different conservative tracers were injected in the two experiments, amino-G acid (AGA) in CFM 13-05 and iodine-131 in CRR Run 32. The breakthrough of uranine in CRR Run 29 was also modelled to provide comparison for the iodine breakthrough in CRR Run 32. The concentration of conservative tracer used in both experiments is given in Table 5.3, as given in Möri et al. (2004) and Schäfer et al. (2013).

	<b>CFM Run 13-05: Amino-G acid (AGA)</b>	<b>CRR Run 32: <sup>131</sup>I</b>
Mass (M <sub>0</sub> )	4455 µg	1.21x10 <sup>-5</sup> µg
Concentration (C <sub>0</sub> )	1384.23 µg/l <sup>1</sup>	1.21x10 <sup>-4</sup> µg/l

1: Peak concentration in re-circulation circuit

**Table 5.3 Mass and concentration of conservative tracers used in CFM Run 13-05 and CRR Run 32**

Calibration of conservative tracer breakthrough was carried out by altering the longitudinal dispersivity ( $\alpha_l$ ) and the fracture aperture scaling factor described previously (f). The dispersivity length was initially set as 10% of the transport distance ( $\alpha_l = 0.22\text{m}$ ), and f was initially set as 1 (representing one fracture). The model was first calibrated by modelling CFM Run 13-05, and then determining whether the same parameters could be used to model CRR Run 32.

Figure 5.2 shows the model calibration for conservative tracers in CFM 13-05, CRR 32 and additionally the prediction of uranine breakthrough in CRR Run 29, using the final parameters shown in Table 5.4. These model calibrations are discussed further in the following sections.

	<b>CFM Run 13-05: Amino-G Acid (AGA)</b>	<b>CRR Run 32: <sup>131</sup>I</b>
Longitudinal Dispersivity ( $\alpha_l$ )	0.1 m	
Fracture aperture scaling (f)	7	

**Table 5.4 Calibrated parameters from Conservative tracer breakthrough**

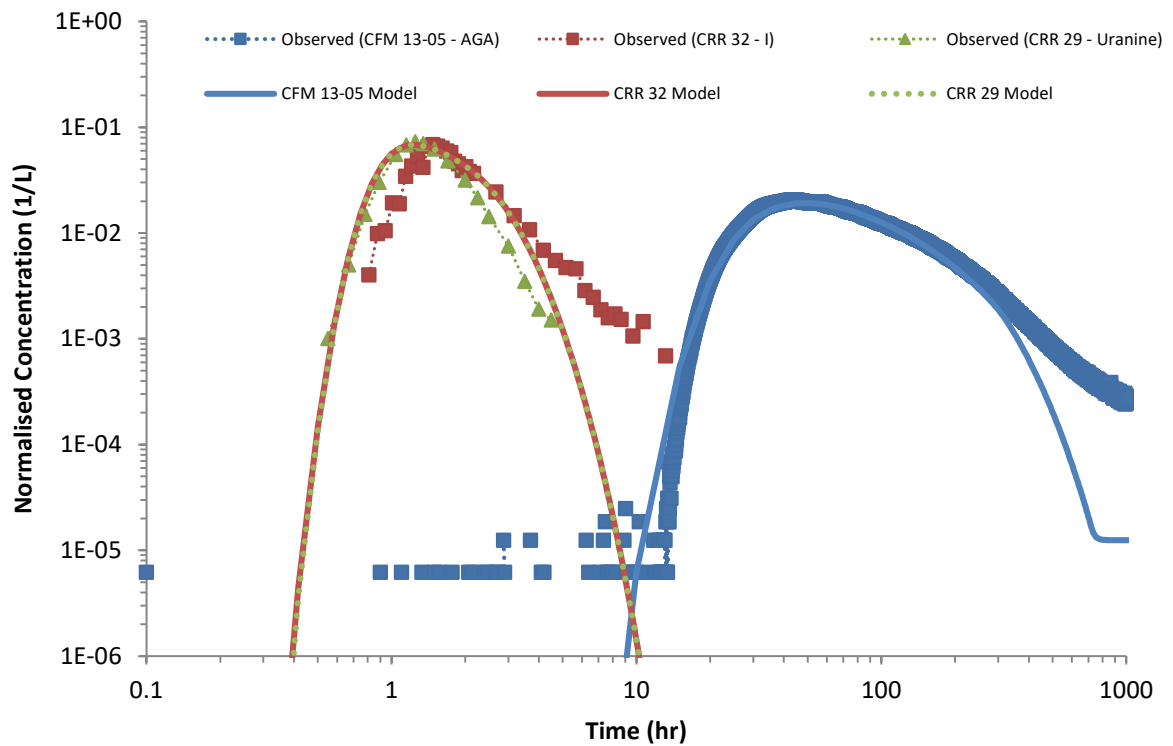


Figure 5.2 Model calibration for conservative tracer for CFM 13-05 (blue), CRR 32 (red) and CRR 29 (green). Concentrations normalised in this and all subsequent figures with normalised concentration against  $M_0$  (mass injected)

### 5.3.1. CFM Run 13-05

The calibrated model breakthrough for AGA in CFM 13-05 is shown in Figure 5.3, shown on a linear scale as it is easier to see the detail with the matches. Figure 5.3 shows that the model provided a good match to the arrival and peak of the experimental data. However, the modelled recovery is 76%, which is lower than the 92.6% recovery measured in the experiment (Kontar et al., 2013). A comparison of the cumulative recovery in Figure 5.4 shows that the lower recovery is caused by the model not being able to replicate the long tailing observed in the falling limb of the experimental dataset, as shown in the breakthrough curve in Figure 5.2. The discrepancy with the tailing could be caused by an additional diffusion process (akin to matrix diffusion) which occurs during the migration experiment but is not picked up in the model.

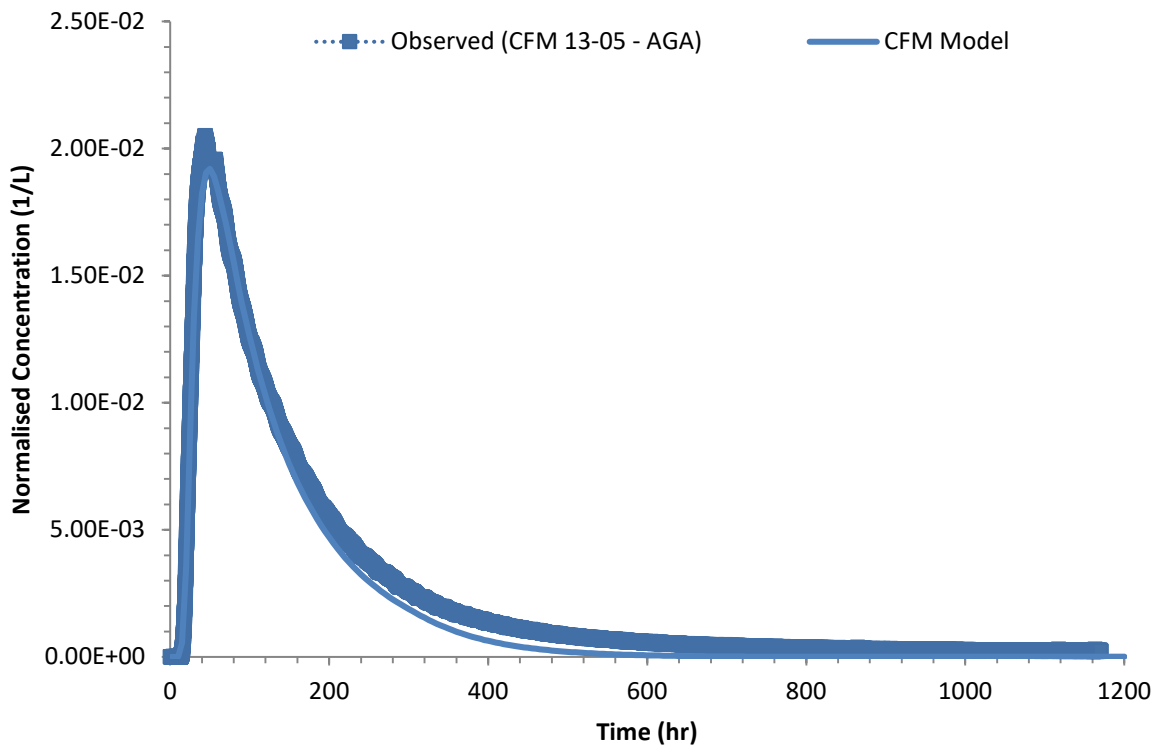


Figure 5.3 Calibrated model results for amino-G acid in CFM 13-05

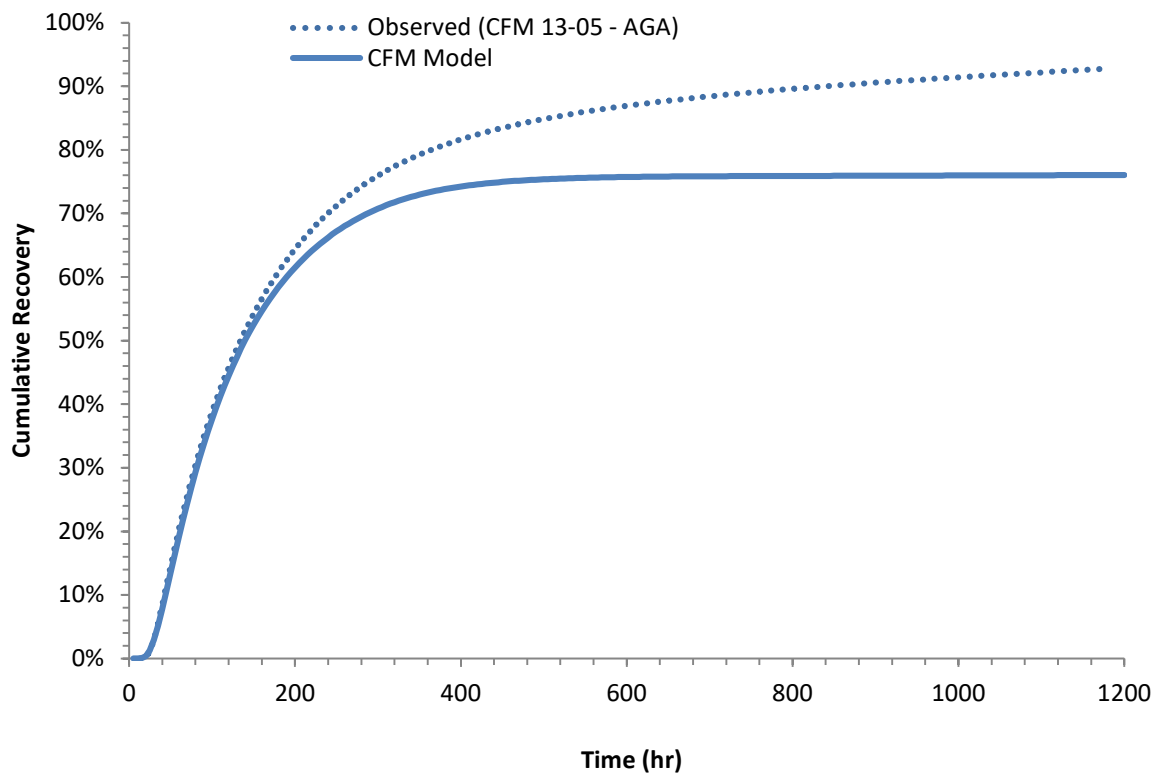


Figure 5.4 Comparison of cumulative recovery for observed and modelled data for CFM Run 13-05 conservative tracer

The lower recovery of tracer in the model could be caused by mass loss that does not occur in the experiment, as some mass in the model is lost towards the tunnel and the Pinkel surface packer and therefore not captured by the abstraction borehole. An additional reason is that the transmissivity distribution used in the model includes a low transmissivity barrier across the experimental dipole (as discussed in Chapter 3). At the end of the model run, some mass is trapped within this area (as shown in Figure 5.5).

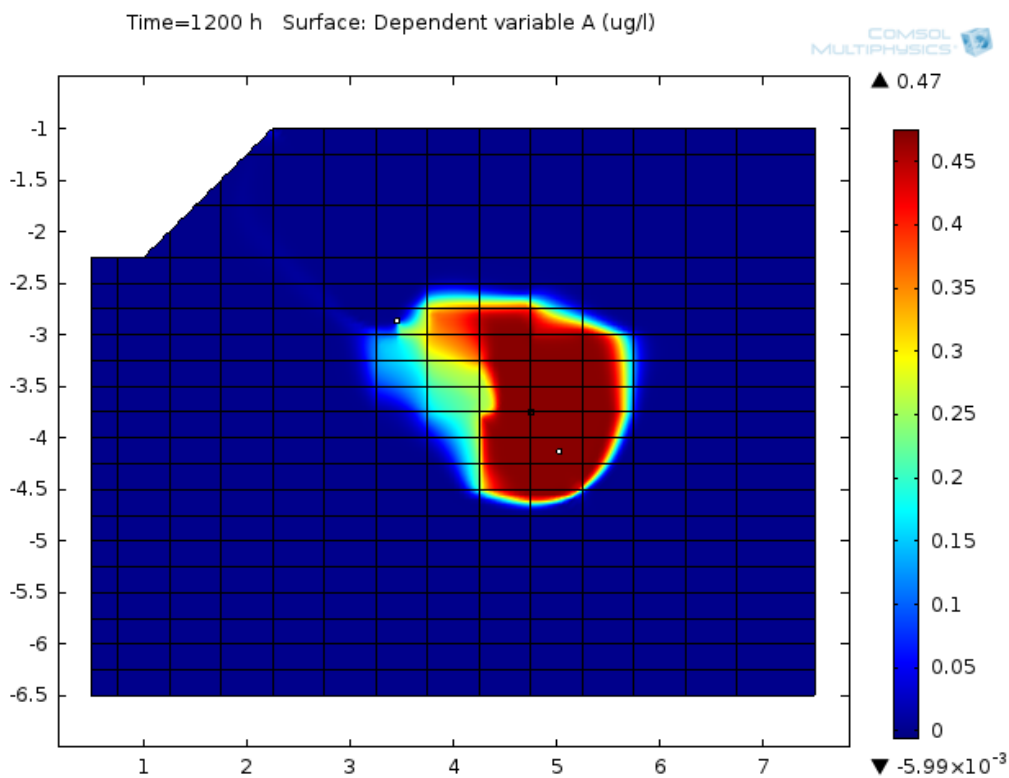


Figure 5.5 Concentration in  $\mu\text{g/l}$  of conservative tracer remaining in CFM Run 13-05 model after 1200 hours.

The single value used to represent the dilution of the source term caused by the cross-flow over the injection interval may overestimate the dilution past 50 hours as it is an average value, and the estimated dilution flow is expected to decrease as the experiment continues (Schäfer et al., 2013). These issues with the model calibration could have also been influenced by the groundwater flow model and transmissivity distribution used in the

model, however due to time issues a sensitivity analysis of the impact of the transmissivity distribution was not carried out to try and improve model calibration.

### 5.3.2. CRR Run 32

The calibrated model breakthrough for iodine-131 in CRR Run 32 is shown in Figure 5.6, with a comparison of the cumulative recovery shown in Figure 5.7. The breakthrough in the model occurs about 10 minutes earlier than the experimental data, but shows a good match to the peak concentration and the falling limb of the breakthrough curve. The modelled recovery of iodine in CRR Run 32 was 98%, higher than the measured recovery of 92%.

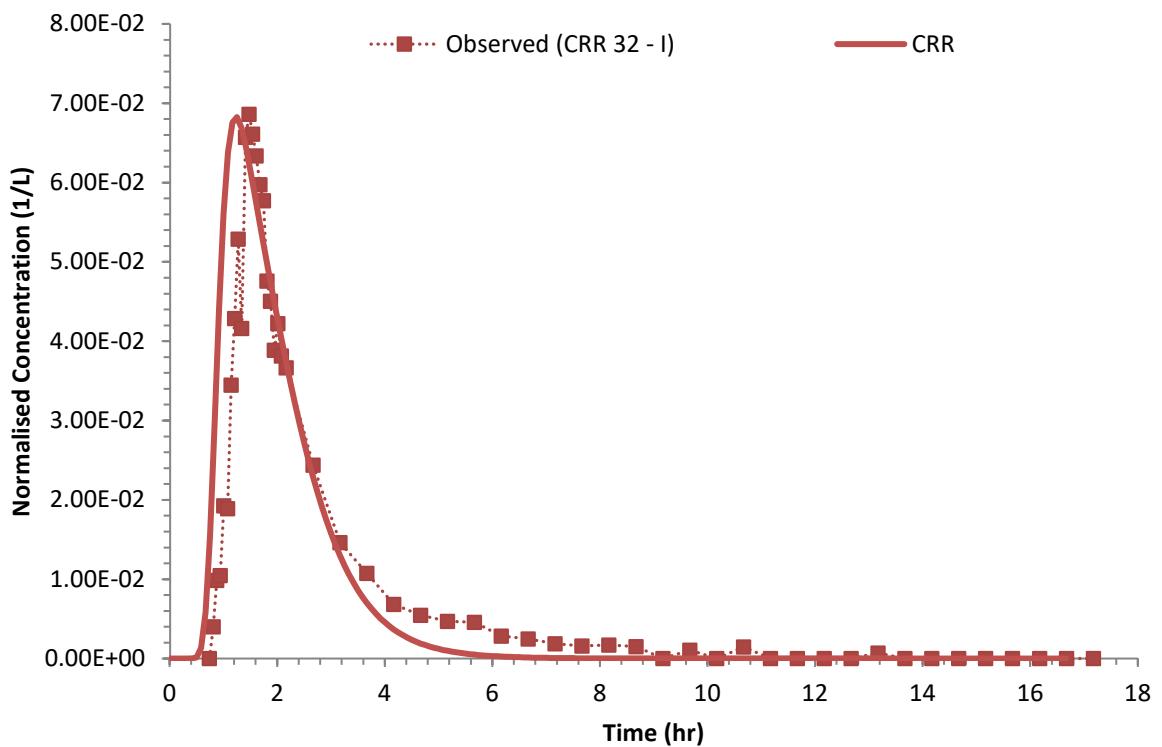


Figure 5.6 Calibrated model results for <sup>131</sup>I in CRR 32

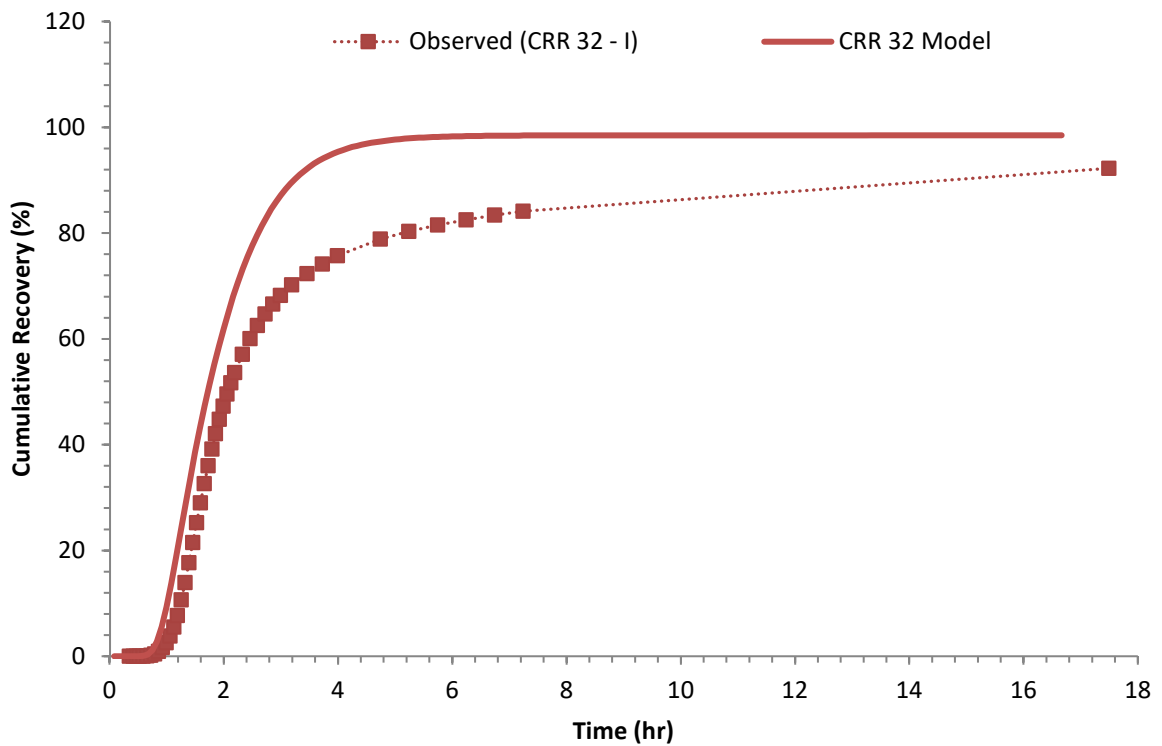


Figure 5.7 Comparison of cumulative recovery for observed and modelled data for CRR Run 32 conservative tracer

The model was also applied to the uranine breakthrough in CRR Run 29 (which was carried out in similar hydraulic conditions to CRR Run 32). The resulting breakthrough curve is shown in Figure 5.8, with a comparison of the cumulative recovery shown in Figure 5.9. The model match to the breakthrough in CRR Run 29 is better when compared to CRR Run 32 for the rising limb and the peak breakthrough, but the model is higher than the falling limb of the breakthrough curve.

This means that for conservative tracer breakthrough, the model both over-predicts (CRR Run 29) and under-predicts (CFM Run 13-05) the tailing of conservative tracers. The fact that the tracer tailing is under-predicted in CFM Run 13-05 could be due to the slower flow velocities of the experiment allowing for more diffusion processes, which do not occur

in the faster experiments carried out during CRR, but could also be due to the use of the transmissivity distribution in the groundwater flow model.

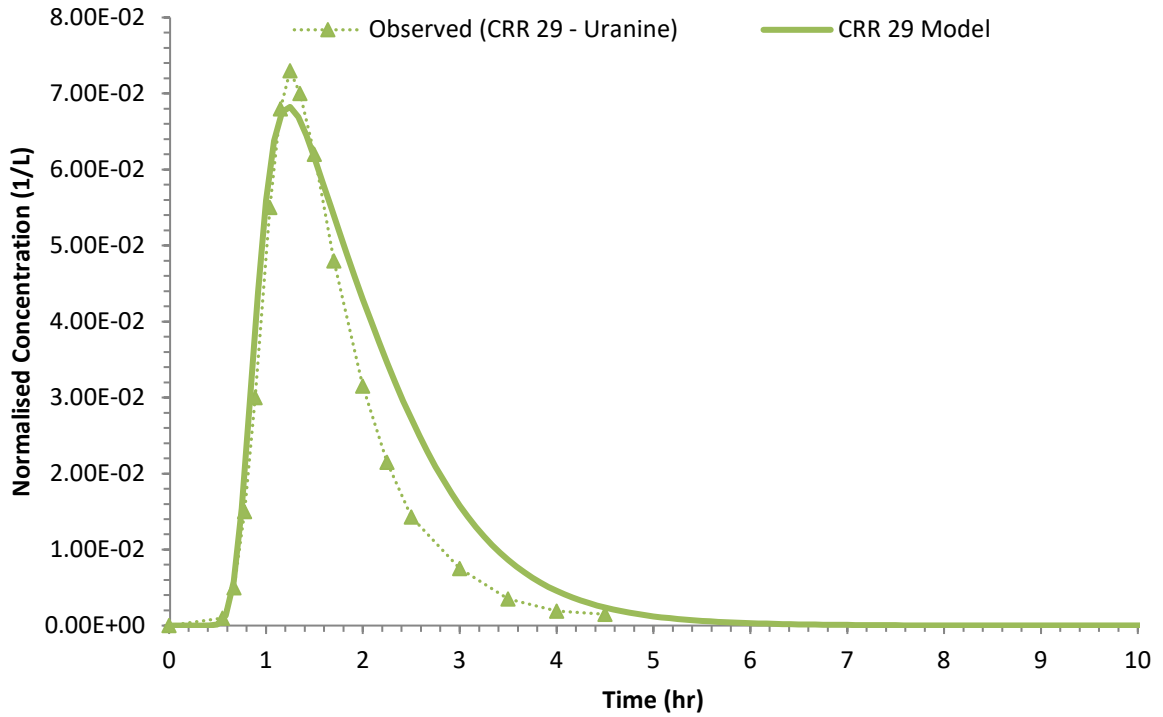


Figure 5.8 Predicted model results for uranine breakthrough in CRR 29

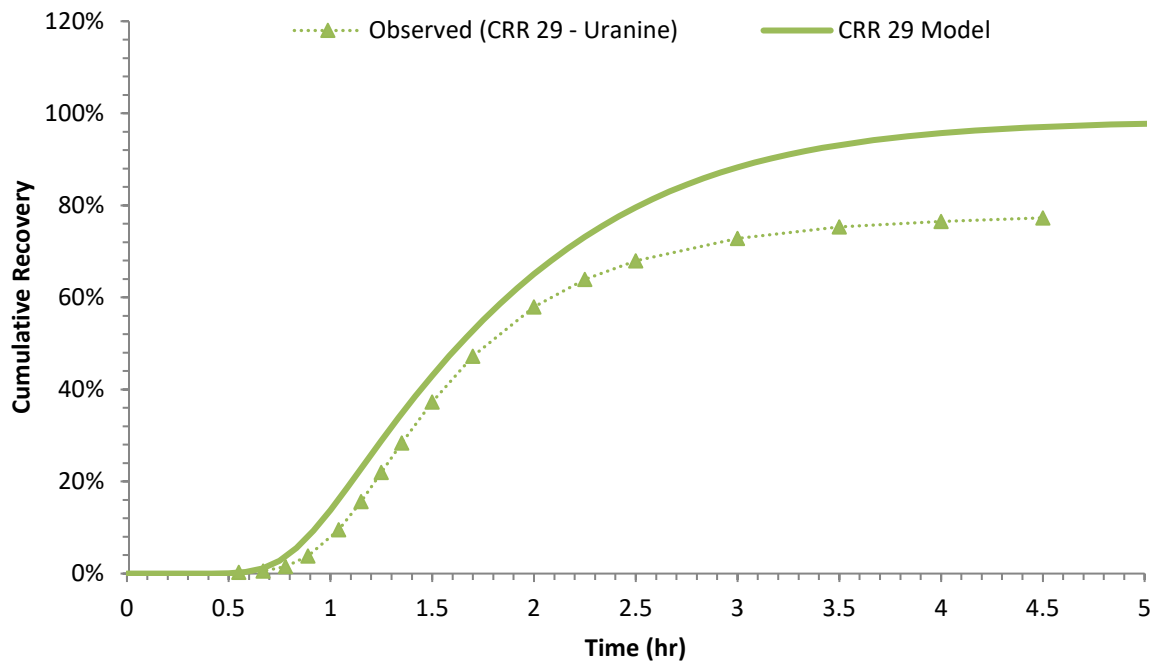


Figure 5.9 Comparison of cumulative recovery for observed and modelled data for CRR Run 32 conservative tracer

Comparing the model calibrations for iodine in CRR Run 32 and uranine in CRR Run 29, iodine breakthrough is slightly delayed compared to uranine. Peak recovery times for iodine are between 3 and 10 minutes longer than uranine in tracer tests carried out within the CRR project (Möri et al., 2004). The model match for uranine in CRR Run 29 is better than the model match for iodine in CRR Run 32 as this slight retardation ( $R = \sim 1.2$ ) is not included in the model for iodine. It would be possible to add a retardation factor (similar to the equation for radionuclide transport Equation 4.6); however due to time constraints this was not carried out.

### **5.3.3. Discussion of the calibration parameters**

Table 5.4 shows the parameters that resulted from the conservative tracer calibration process. Dispersivity values used in this model are roughly comparable to models of CRR experiments (Smith et al., 2006) which modelled the same dipole and section of shear zone. The longitudinal dispersivity is the same as used in the PSI 1D model, and similar to the PSI 2D model ( $\alpha_L = 0.075\text{m}$ ). However, the longitudinal dispersivity used in this model is lower than other models of CFM experiments (0.3-0.75m; Noseck et al. (2016)), possibly due to the fact that a larger (6m) dipole was used in these latter experiments.

In a transport model, the distribution of both transmissivity and fracture aperture has to be specified. This model uses a series of parallel plates to represent the shear zone, the fracture aperture being divided into a series of equal plates. This represents an approximation of the shear zone which is a complicated structure of between 1 to 5 braided 'water conducting features' (Gaus and Smith, 2008). The fracture aperture is calculated by Equation 5.1:

$$b = f \left( \frac{12\mu T}{\rho g} \right)^{\frac{1}{3}}$$

**Equation 5.1 Fracture aperture calculation**

The hydraulic (or cubic law) aperture used in the inverse model represents the geometric mean of aperture distribution, whereas the transport (or mass balance) aperture represents the arithmetic mean of the aperture distribution (Zheng et al., 2008). The presence of variable aperture causes the difference between the two values, as hydraulic aperture is more sensitive to smaller apertures. In a true parallel plate flow scenario, there would be no difference between the different apertures, (Hjerne and Nordqvist, 2014).

Forbes (2016) investigated the impact of heterogeneity on the relationship between hydraulic and transport apertures. This was carried out by generating stochastic distributions of hydraulic conductivity in a groundwater flow model, determining the number of parallel plates required to scale between hydraulic and transport aperture with different levels of transmissivity heterogeneity. The results of these investigations are shown in Figure 5.10, which shows that the number of parallel plates required to scale between hydraulic and transport aperture increases with transmissivity variability.

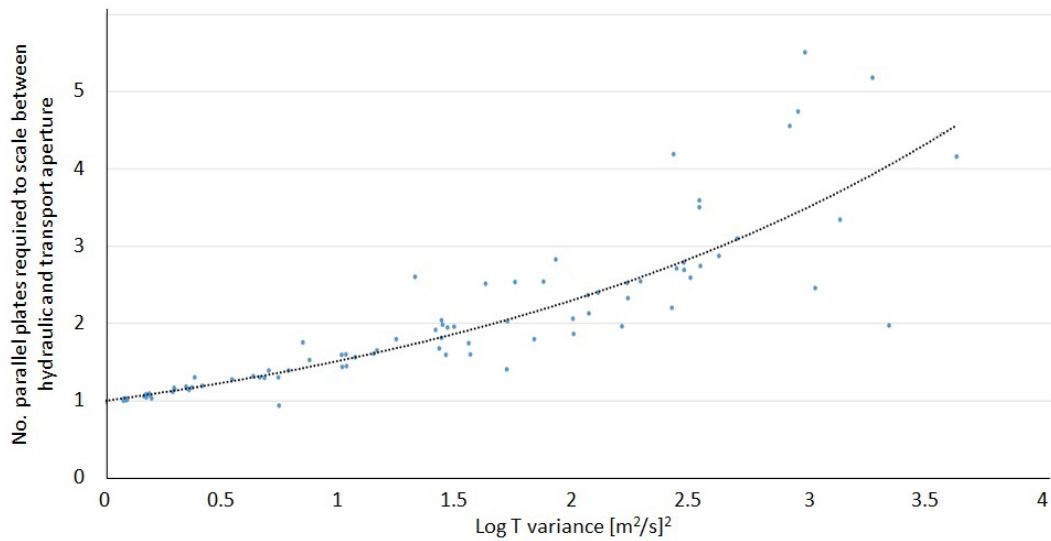


**Figure 5.10** Effect of heterogeneity on the number of parallel plates required to scale between transport and hydraulic aperture. From Forbes (2016).

The resulting scaling factor from the calibration of the conservative tracer ( $f = 7$ ) in this transport model results in the MI shear zone being represented by approximately 18 parallel plates, a much higher number than indicated by geological mapping. Transmissivity values in the inverse model vary by six orders of magnitude, necessitating the need to represent the shear zone by the high number of parallel plates in the transport model.

#### **5.4. Bentonite colloid model calibration**

The next stage of model calibration was to calibrate the breakthrough of bentonite colloids. It is important to note that due to the calibration process used, any error in the conservative tracer calibration described in the previous section is carried through to the colloid breakthrough calibration.

In both experiments, FEBEX bentonite colloids were used in the injection cocktail (albeit in different concentrations), but in CFM 13-05 artificially labelled Ni-montmorillonite colloids were also used, to improve confidence in breakthrough curve data (Lanyon and Blechschmidt, 2016). The concentration of colloids used in the two experiments is shown in

Table 5.5. For CFM 13-05, the aluminium signal as measured by ICP-MS was used for calibration, assuming a background signal of 20ppb (as determined by the CFM experimental team, Lanyon and Blechschmidt (2016)). For CRR 32, model calibration used the colloid concentration as determined by Laser Induced Breakdown Detection (LIBD) measurements.

	<b>CFM Run 13-05<sup>1</sup></b>	<b>CRR Run 32</b>
Mass ( $M_0$ )	FEBEX: 193 mg Ni-montmorillonite: 31.3 mg Total: 224.3 mg	2.01 mg
Concentration ( $C_0$ )	FEBEX: 60 mg/l Ni-montmorillonite: 9.71 mg/l Total: 69.7 mg/l	20.1 mg/l

*1: Concentration in re-circulation circuit*

**Table 5.5 Mass and concentration of Bentonite colloids used in CFM Run 13-05 and CRR Run 32**

Model calibration was carried out by altering the colloid reversible attachment ( $k_{att}$ ), detachment ( $k_{det}$ ) and irreversible attachment ( $k_{iat}$ ) rate constants. Initially, only reversible colloid attachment was included in the model. However, during calibration it was determined that including irreversible colloid attachment provided a better match to the breakthrough data.

During initial model calibration the experimental recovery was not known for CFM Run 13-05, so to help provide colloid attachment rates, colloid recovery maps of parameter space were generated to provide an insight into the resulting recovery from different colloid attachment and detachment rates. The full process is detailed in Appendix D, but the maps were created by running multiple models, and extrapolating the recovery value from those models to create a map of expected recovery. An example of a map is shown in Figure 5.11.

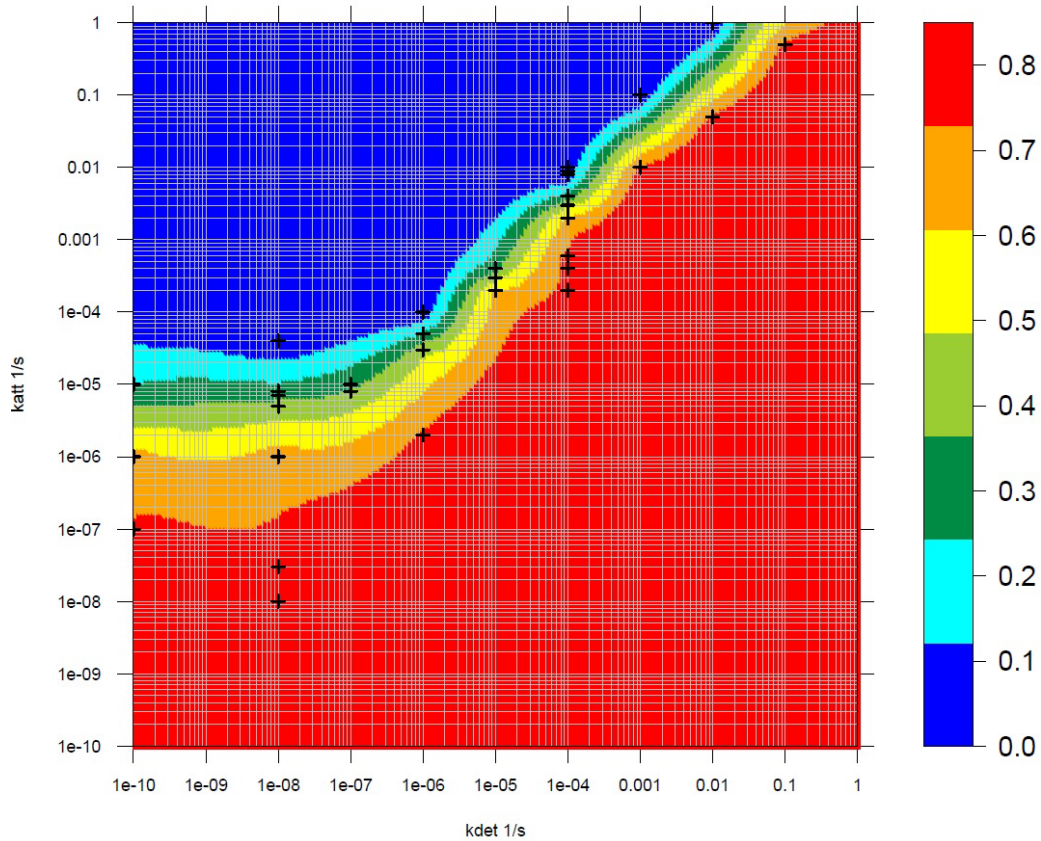


Figure 5.11 Example of a colloid recovery map for CFM Run 13-05,  $k_{iat} = 1e-6$  1/s, colours show the predicted colloid recovery. Arrows show where model values obtained. This map is a slice through a 3D parameter space due to the irreversible colloid attachment parameter.

Figure 5.12 shows the result of the calibration process for colloid breakthrough in both experiments, using the parameters in Table 5.6. The model is able to replicate the breakthrough of bentonite colloids in both experiments, using consistent parameters to describe irreversible and reversible colloid attachment. The following sections will discuss the individual calibrations for the two experiments.

	CFM Run 13-05	CRR Run 32
Reversible colloid attachment ( $k_{att}$ )	$5 \times 10^{-6}$ (1/s) ( $0.018 \text{ h}^{-1}$ )	
Reversible colloid detachment ( $k_{det}$ )	$5 \times 10^{-5}$ (1/s) ( $0.18 \text{ h}^{-1}$ )	
Irreversible colloid attachment ( $k_{iat}$ )	$4 \times 10^{-6}$ (1/s) ( $0.0144 \text{ h}^{-1}$ )	
Colloid retardation factor ( $R_c$ )	1 (-)	
Maximum concentration of F ( $F_{max}$ )	5 (-)	

Table 5.6 Calibrated parameters from bentonite colloid breakthrough

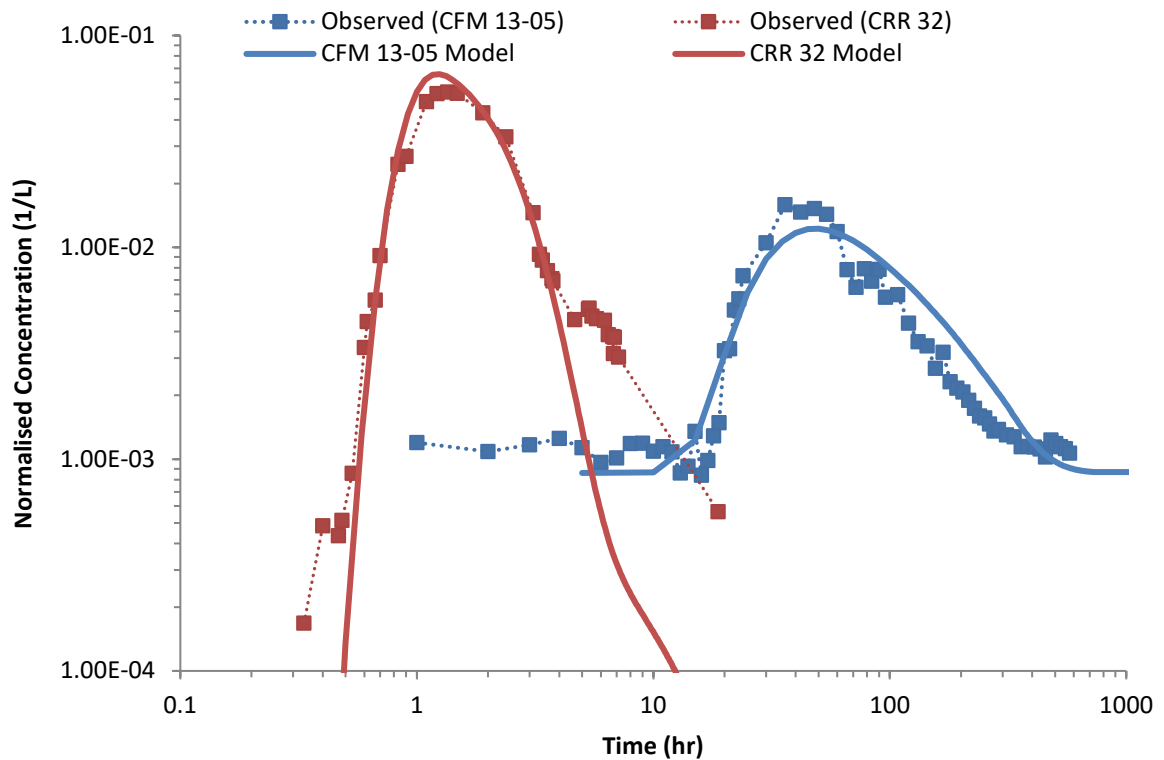


Figure 5.12 Model calibration for bentonite colloid breakthrough in CFM Run 13-05 (blue) and CRR Run 32 (red)

#### 5.4.1. CFM Run 13-05

The calibrated model breakthrough for bentonite colloids in CFM Run 13-05 (as calibrated against the ICP-MS measured Al concentration) is shown on a linear scale in Figure 5.13, with a comparison of the observed and modelled cumulative recovery in Figure 5.14.

The model calibration is a good match to the rising limb of the breakthrough curve, but is lower than the peak concentration and is higher than the falling limb of the curve. The modelled recovery of 43% is slightly higher than the experimental recovery of ~36% (Schäfer et al., 2013), due to the higher concentrations modelled in the falling limb of the breakthrough curve.

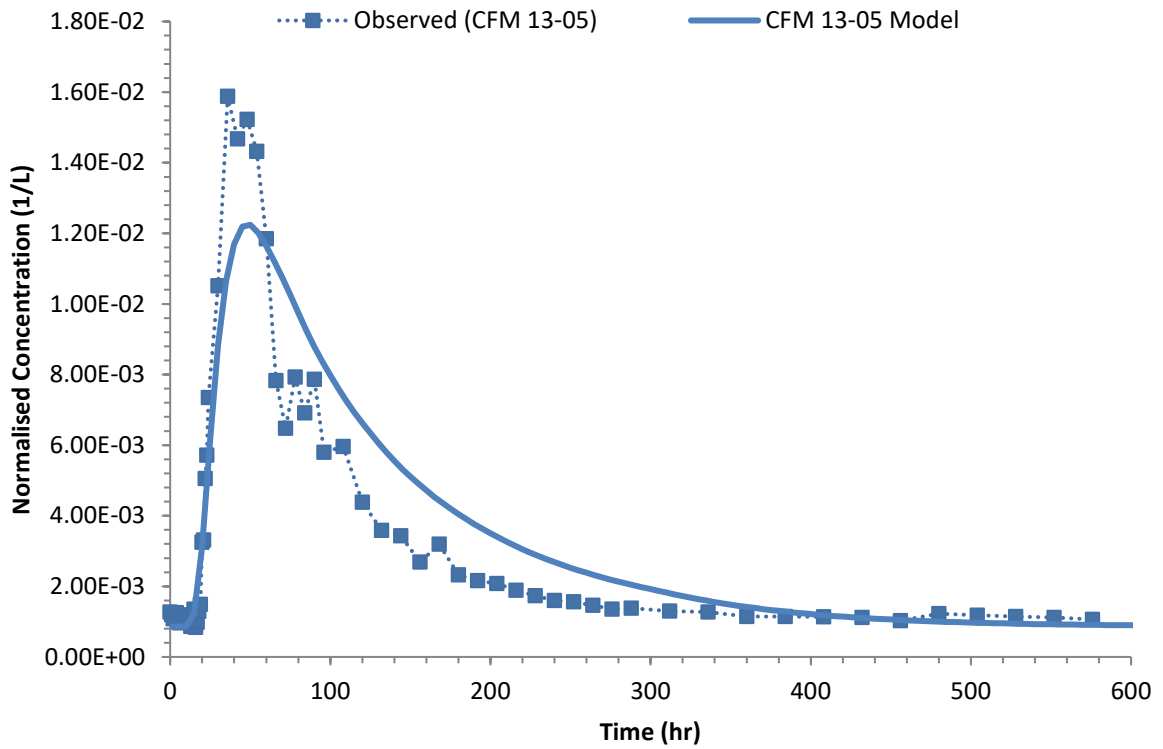


Figure 5.13 Model calibration result for bentonite colloids in CFM Run 13-05

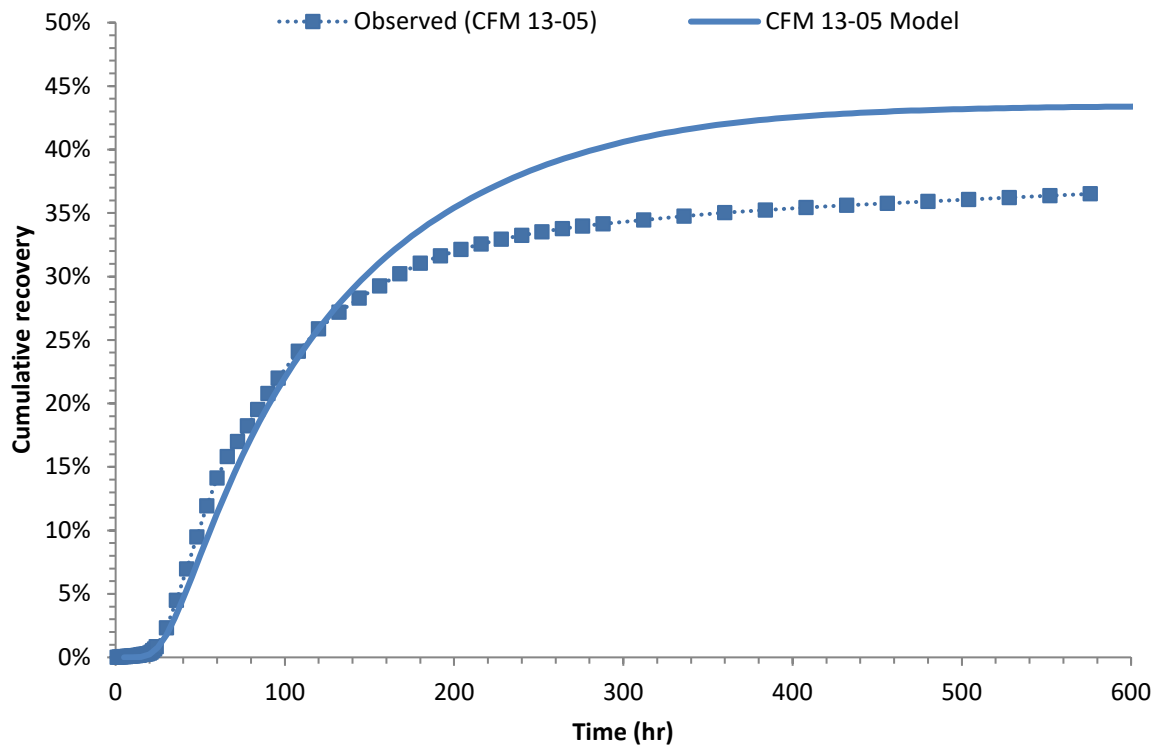


Figure 5.14 Comparison of observed and modelled cumulative recovery for CFM Run 13-05 bentonite colloids

The model is over-dispersed compared to the experimental data, as shown by the higher modelled concentration in the falling limb of the breakthrough curve. For this model, longitudinal dispersivity was set by calibrating conservative tracer breakthrough. This makes the assumption that the colloids have the same dispersive flux as the conservative tracer. However, colloids can be excluded from slower flow paths due to their size, resulting in earlier breakthrough than tracers (Ryan and Elimelech, 1996).

Column experiments with polystyrene microspheres in glass beads found that different dispersivity values exist for tracers (bromide) and different size classes of colloid (Chrysikopoulos and Katzourakis, 2015). This is because colloids undergoing size exclusion have a reduced dispersive flux. However, if significant numbers of colloids are excluded from flow paths, colloids will be more dispersed than tracers as the porosity that the colloids can enter is significantly reduced (Chrysikopoulos and Katzourakis, 2015).

In CFM Run 13-05, there was no significant size exclusion chromatography as colloid breakthrough was at the same time as conservative tracer. This indicates that colloids were not excluded from large areas of the shear zone, preventing the colloid longitudinal dispersivity value from being larger than the 0.1 m used for the conservative tracer. Although, longitudinal dispersivity of colloids could still be lower than the conservative tracer if limited numbers of colloids are excluded from slower flow paths. Changing the longitudinal dispersivity could improve the model calibration, but due to the limited evidence of size exclusion chromatography was not carried out.

The lower peak from the calibration is a direct consequence of the model being over dispersed on the falling limb of the breakthrough curve. It was attempted to increase the

peak concentration by reducing colloid attachment rates, but this resulted in even higher concentrations on the falling limb of the breakthrough curve. The colloid attachment parameters (in Table 5.6) were therefore chosen as a compromise between matching peak concentration and the recovery from the experiment.

#### **5.4.2. CRR Run 32**

The result of the model calibration for bentonite colloids in CRR Run 32 (as calibrated against the LIBD data) is shown in linear scale in Figure 5.15, with a comparison of observed and modelled cumulative recovery shown in Figure 5.16. Figure 5.15 shows a good model match to the rising and falling limbs of the breakthrough curves; however the model has a slightly higher peak concentration and is not able to replicate the tailing observed in the breakthrough curve after 6 hours. Unfortunately, sampling was interrupted between 7 and 18 hours (Möri et al., 2004), so there are no further data points to constrain the model as to when colloid concentration returned to background levels. It would have been possible to alter the reversible colloid attachment parameters to better replicate this tailing. This was not carried out due to the limited data points available for calibration, and the fact that this tailing is not replicated by the other analytical methods used to detect colloid breakthrough (Aluminium signal from ICP-MS, PCS or SPC; Möri et al. (2004)).

The model recovery of 95% compares well to the recovery as measured by LIBD, which varied between 85% and 100% depending on the value chosen to represent the natural colloid background (Möri et al., 2004). Although colloid recovery was high, colloid attachment processes did need to be included in the model to reduce peak concentration, unlike the previous CRR models which did not model colloid attachment (Smith et al., 2006).

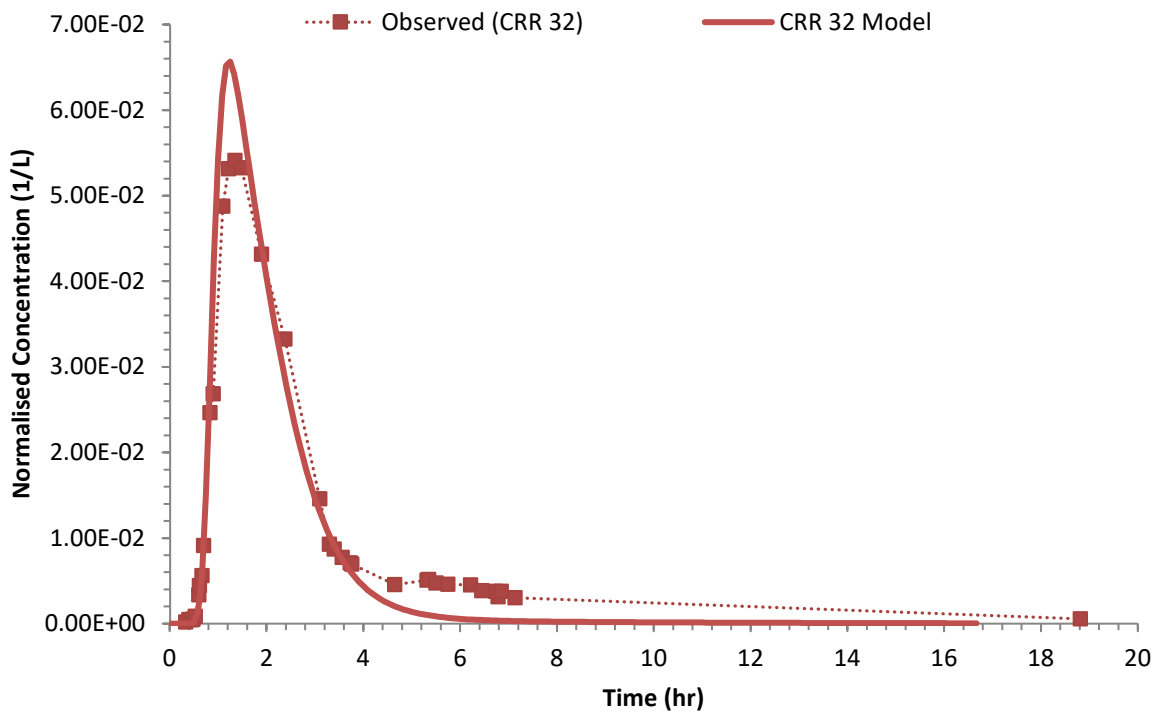


Figure 5.15 Model calibration for bentonite colloids in CRR Run 32

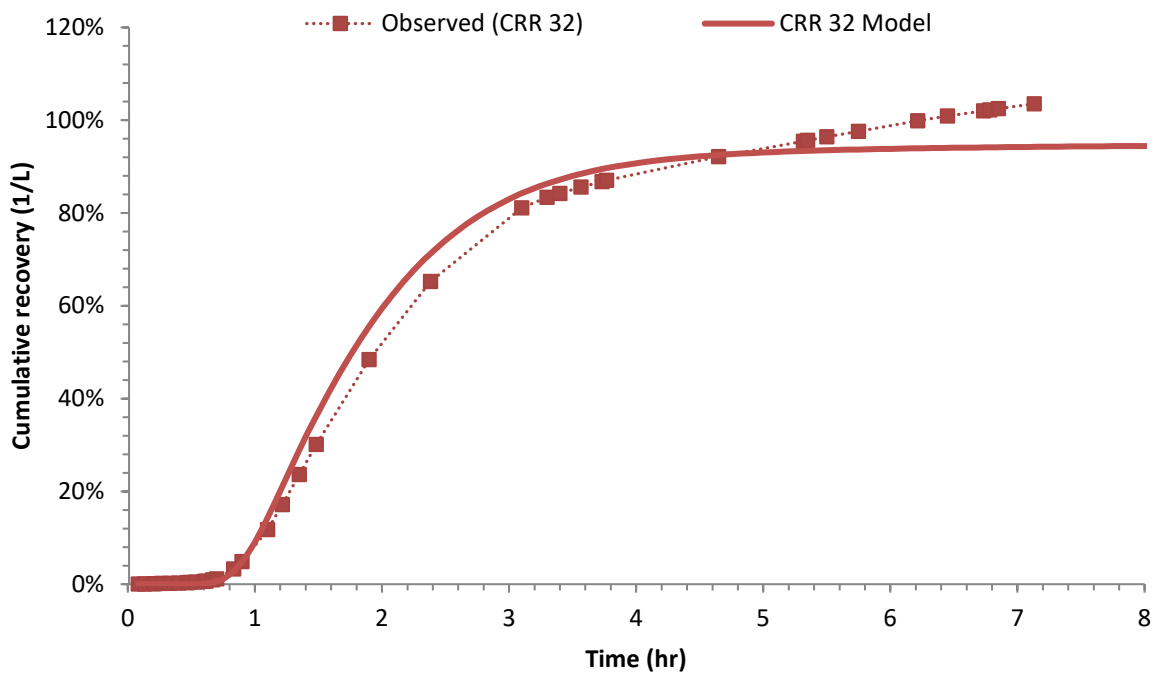


Figure 5.16 Comparison of observed and modelled cumulative recovery for CRR Run 32 bentonite colloids

### 5.4.3. Discussion on calibration parameters

The value of the calibration parameters used in this model are in the same order of magnitude with those resulting from previous models used to describe the CFM and CRR migration experiments. However, unlike the previous models, the same attachment and detachment rates and processes were used to describe colloid transport in the two migration experiments carried out in the same dipole.

Models of migration experiments carried out up to CFM Run 12-02 used a wide range of reversible attachment rates (between  $0.0065 \text{ h}^{-1}$  and  $0.054 \text{ h}^{-1}$  depending on the model and experiment) (Noseck et al., 2016). The rate used in the model ( $0.018 \text{ h}^{-1}$ ) is in this range despite these experiments taking place in a different dipole (CFM dipole 1). The detachment rates used in this model were again in the same range than those in Noseck et al. (2016). Irreversible attachment rates in Noseck et al. (2016) were in a wide range ( $0.0005 \text{ h}^{-1}$  and  $0.286 \text{ h}^{-1}$ ), and the rate used in this model ( $0.0144 \text{ h}^{-1}$ ) was within this range. It is important to note that both irreversible and reversible attachment was not included by the different modelling teams (Noseck et al., 2016), but during the calibration of this model it was found that including irreversible and reversible colloid attachment was necessary for a good quality model fit.

For the previous CRR models, only the JNC “Colfrac” model included an irreversible attachment mechanism for colloids, with the other models accounting for colloid attachment by simply scaling the solute breakthrough curve to give the correct colloid recovery (Smith et al., 2006; Kosakowski and Smith, 2004). Although the process was included, it is not apparent that the JNC model directly modelled the CRR Run 32 colloid

breakthrough, as different colloid attachment rates were used for when modelling different radionuclides in the same experiment, and so the parameters have not been compared.

Reimus (2016) only included irreversible colloid attachment, using an irreversible attachment rate between  $0.013 \text{ h}^{-1}$  and  $0.12 \text{ h}^{-1}$  (Reimus, 2016), depending on the CRR or CFM experiment modelled and the source term used. The irreversible attachment rate used in this model is comparable to the rates used in Reimus (2016).

During model calibration, the blocking factor ( $F_{\text{max}}$ ) was initially set at a high value (5), so that blocking did not occur during the experiment. This did not need to be changed during the model calibration to improve model fit, indicating that the processes either did not occur during the experiment, or had a limited impact on colloid breakthrough. Blocking (where attached colloids fill attachment sites) is more likely to occur in low ionic strength groundwater, such as Grimsel groundwater (Ryan and Elimelech, 1996; Gaus and Smith, 2008). The fact that this model did not include blocking shows there are a significant number of attachment sites in the multiple flow pathways that make up the MI shear zone, and that blocking has limited impact on colloid breakthrough in the two experiments.

In CRR Run 32, the colloid breakthrough did occur before the conservative tracer used in the experiment ( $^{131}\text{I}$ ) (Möri et al., 2004), which, at the time, was determined to be caused by size exclusion chromatography. However, this model has been able to match the peak breakthrough times of the colloids using consistent parameters, and the peak breakthroughs of AGA in CFM Run 13-05 and uranine in CRR Run 29 using the same parameters. Therefore, it is more likely that the cause of the early colloid breakthrough

(compared to  $^{131}\text{I}$ ) in CRR Run 32 is caused by slight retardation of the iodine in the experiment and not size exclusion causing the early breakthrough of colloids.

The model assumes that the colloid population can be described using the same effective attachment rates. Despite the different colloid populations in the two experiments, colloid transport and attachment can be described using the same parameters in the model. In addition, there is limited evidence of colloid aggregation during the experiments. In CRR Run 32, the average colloid diameter from the breakthrough curve measured by LIBD (100nm) was almost identical to the average measured in the injection cocktail (109nm) (Möri et al., 2004). Similar results were found for the initial colloid size distribution data in CFM Run 13-05 (Schäfer, pers. Comm.)<sup>1</sup>. This is expected as the low ionic strength Grimsel groundwater means that colloid aggregation was unlikely to occur (Ryan and Elimelech, 1996). The fact that size exclusion chromatography, multiple size-dependent deposition rates, or aggregation during the experiment were not included in the model suggests that the colloid population can be modelled using the same effective parameters.

In summary, the breakthrough of bentonite colloids in the two field experiments was modelled using consistent parameters to describe colloid attachment. The parameters and processes used in this model are similar to other models for the CFM and CRR experiments, but these models used a wide range of values to model the CFM experiments. The fact that this model was able to model colloid breakthrough with consistent parameters that are central in the range of other models gives confidence that the parameters used are more

---

<sup>1</sup> The finalised dataset for colloid size distribution in CFM 13-05 is not currently available.

realistic than other models and that the assumptions used to model colloid breakthrough are valid.

## **5.5. 1D 'channel' model**

### **5.5.1. Background**

To investigate the importance of the inverse-modelled transmissivity distribution in the ability to model the two field experiments using consistent parameters, it was decided to create a 1D model representing the shear zone to see if a simplified flow geometry could provide a similar level of accuracy when modelling the different experiments. This model replicates the approach of other models of the CFM and CRR experiments (Noseck et al., 2016; Reimus, 2016; Smith et al., 2006).

### **5.5.2. Model development**

An analytical model spreadsheet using the Ogata-Banks solution for the advection-dispersion equation (Domenico and Schwartz, 1990) was initially used to determine initial properties for the 1D transport model. The spreadsheet was designed by Dr Alan Herbert, and was used to calibrate hydraulic conductivity and longitudinal dispersivity. As the model represents a soil pollution source (e.g. a landfill), a contaminant flux and dilution factor which alters the concentration of contaminant when it enters the 'aquifer' were also specified in the spreadsheet. These were specified by altering the source length and width (which altered the contaminant flux), and mixing depth (which alters the 'dilution'), and so these parameters were also calibration parameters. The spreadsheet model is shown in Figure 5.17.

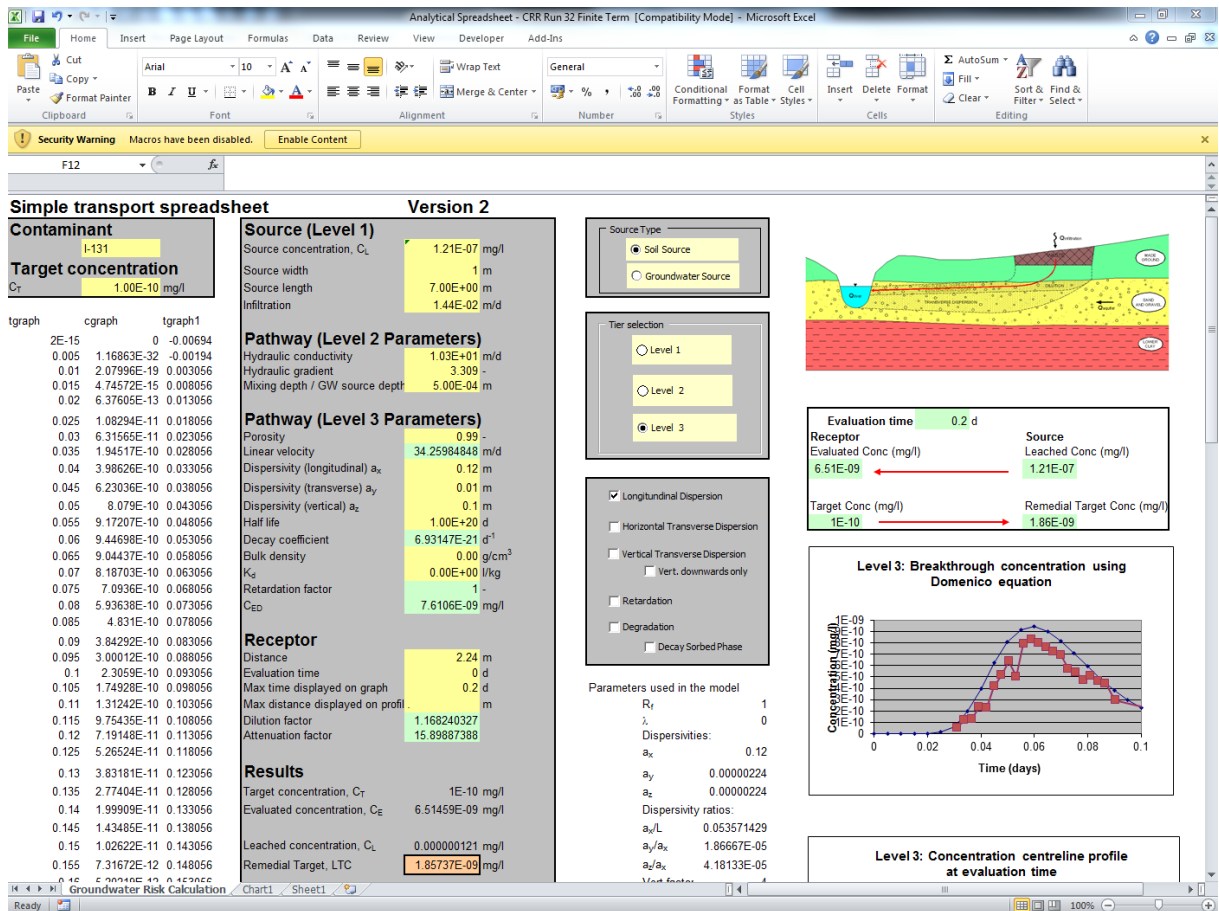


Figure 5.17 Layout and input of analytical spreadsheet model (showing results from CRR Run 32 calibration)

The source term for CRR Run 32 was approximated by a ‘tophat’ pulse injection directly in the spreadsheet. For CFM Run 13-05, the source term was approximated by using several pulse injections with different concentrations to attempt to match the decline of the experimental source term, using the principle of superposition to add up the effect of the multiple injections. The source term used in the spreadsheet model is shown in Figure 5.18, which also shows a comparison with the experimental data.

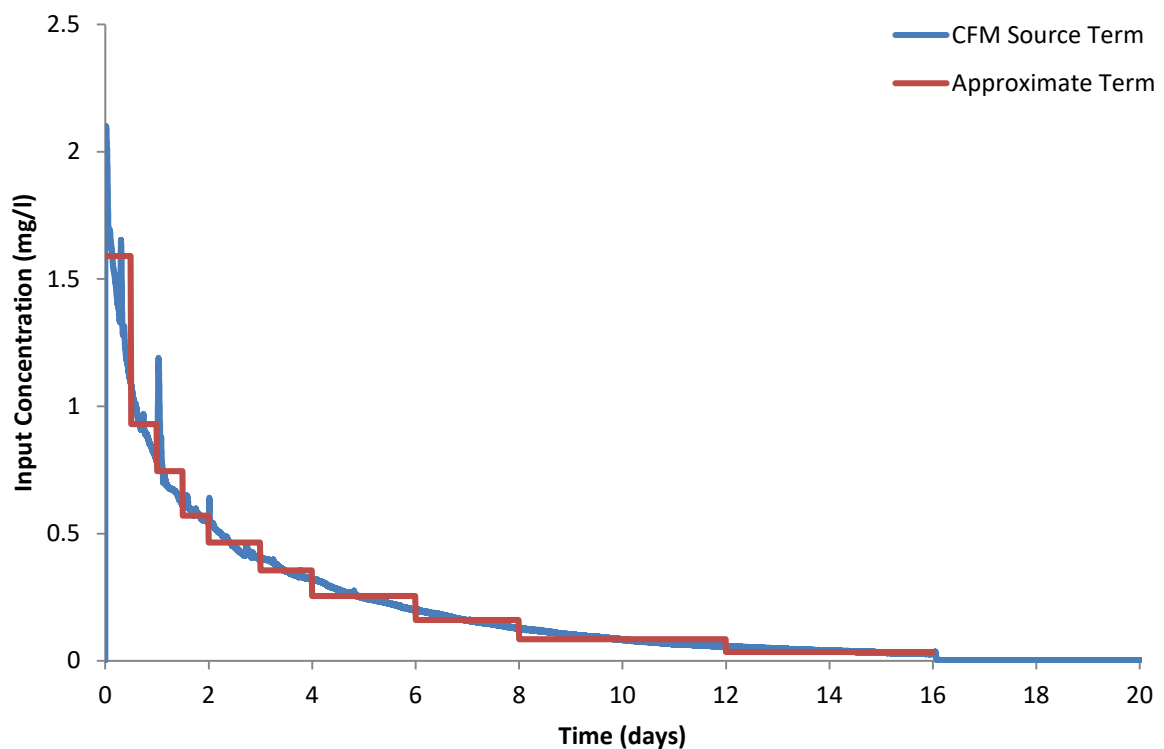


Figure 5.18 Approximate source term used in analytical model for CFM Run 13-05

Once the analytical model was calibrated for conservative tracer breakthrough, the parameters generated were used in a COMSOL Multiphysics 1D model using the same equations described in Chapter 4. The model used the advective velocity calculated by the spreadsheet making the model descriptive for groundwater flow.

To represent the dipole used in CRR Run 32 and CFM Run 13-05 (referred to as CRR Dipole 1), an interval of 2.23 m was created, which had maximum element size of 0.01 m when meshing. A specified flux boundary condition was applied to the left boundary of the 1D model, with an advective only flux boundary condition applied to the right hand model boundary. No other boundary conditions were applied. Finally, the point evaluation tool in COMSOL was applied to the outlet boundary to determine the breakthrough instead of the line integration used in the 2D model. The COMSOL model was applied to both conservative

tracer and colloid breakthrough, attempting to find consistent parameters to describe the transport of the respective species.

### 5.5.3. Model Results

The results of the conservative tracer calibration for the 1D model from the analytical spreadsheet model and the 1D COMSOL model are shown in Figure 5.19 for amino-G acid in CFM Run 13-05 and Figure 5.20 for  $^{131}\text{I}$  in CRR Run 32. The parameters used in the final calibrated 1D model are shown in Table 5.7. The results of the conservative tracer calibrations were then used to model colloid breakthrough, resulting in the breakthrough curves shown in Figure 5.21 for CFM Run 13-05 and Figure 5.22 for CRR Run 32, using the colloid attachment parameters shown in Table 5.8.

Parameter	CFM Run 13-05	CRR Run 32
Hydraulic Conductivity (K) (m/d)	15	10.25
Longitudinal Dispersivity ( $\alpha_l$ ) (m)	0.12	
Source width (m)	1	
Source length (m)	10	7
Mixing depth (m)	5e-5	5e-4
Linear velocity (m/d)	1.8939	36.76
Dilution factor (-)	1.01	1.18

Table 5.7 Parameters derived from analytical model calibration for conservative tracer breakthrough

Parameter	CFM Run 13-05	CRR Run 32
Reversible colloid attachment ( $k_{att}$ )	$9 \times 10^{-5}$ (1/s) (0.324 h $^{-1}$ )	
Reversible colloid detachment ( $k_{det}$ )	$3 \times 10^{-4}$ (1/s) (1.08 h $^{-1}$ )	
Irreversible colloid attachment ( $k_{iat}$ )	$7 \times 10^{-6}$ (1/s) (0.025 h $^{-1}$ )	
Colloid retardation factor ( $R_c$ )	1	
Maximum value of F ( $F_{max}$ )	5	

Table 5.8 Parameters used in COMSOL 1D model of colloid breakthrough

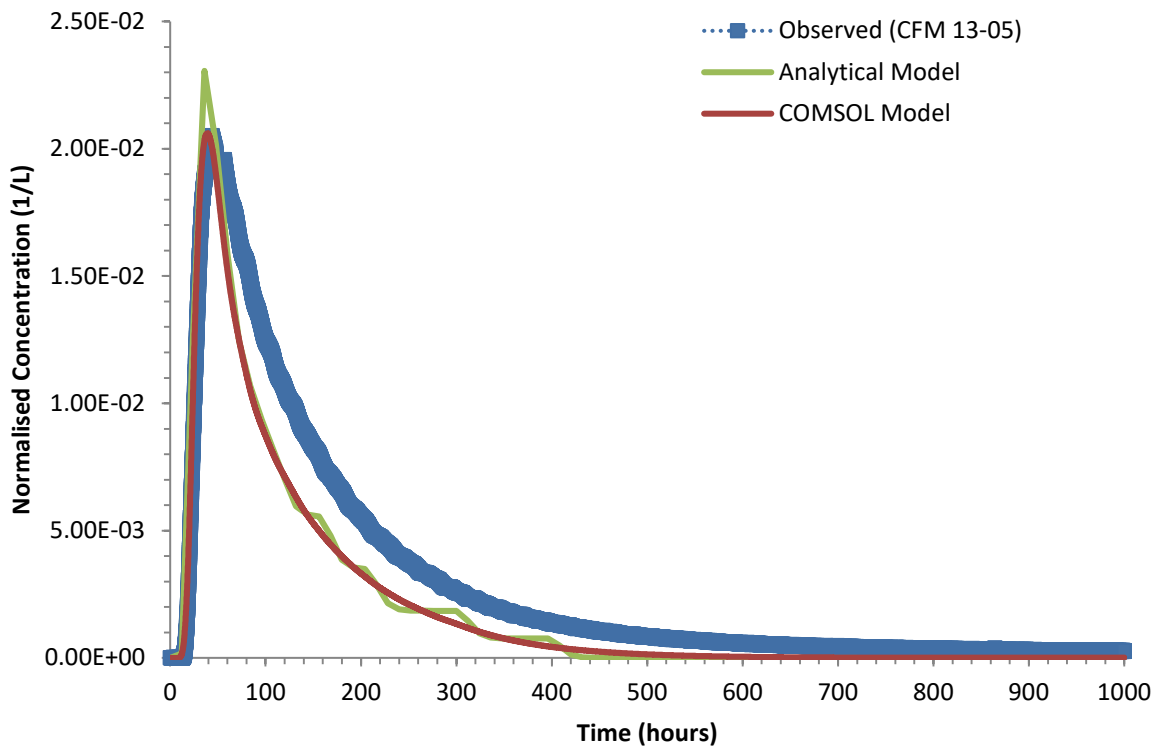


Figure 5.19 Model calibration from 1D analytical and COMSOL models for CFM Run 13-05 conservative tracer

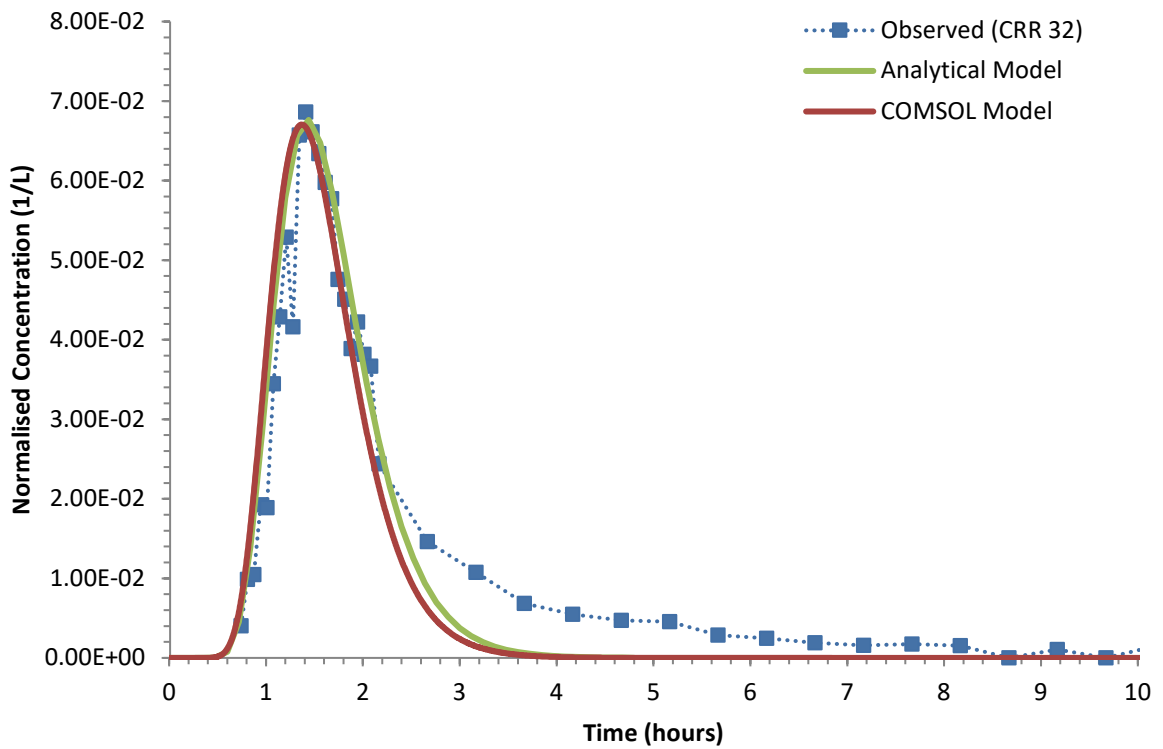


Figure 5.20 Model calibration from 1D Analytical and COMSOL models for CRR Run 32 conservative tracer

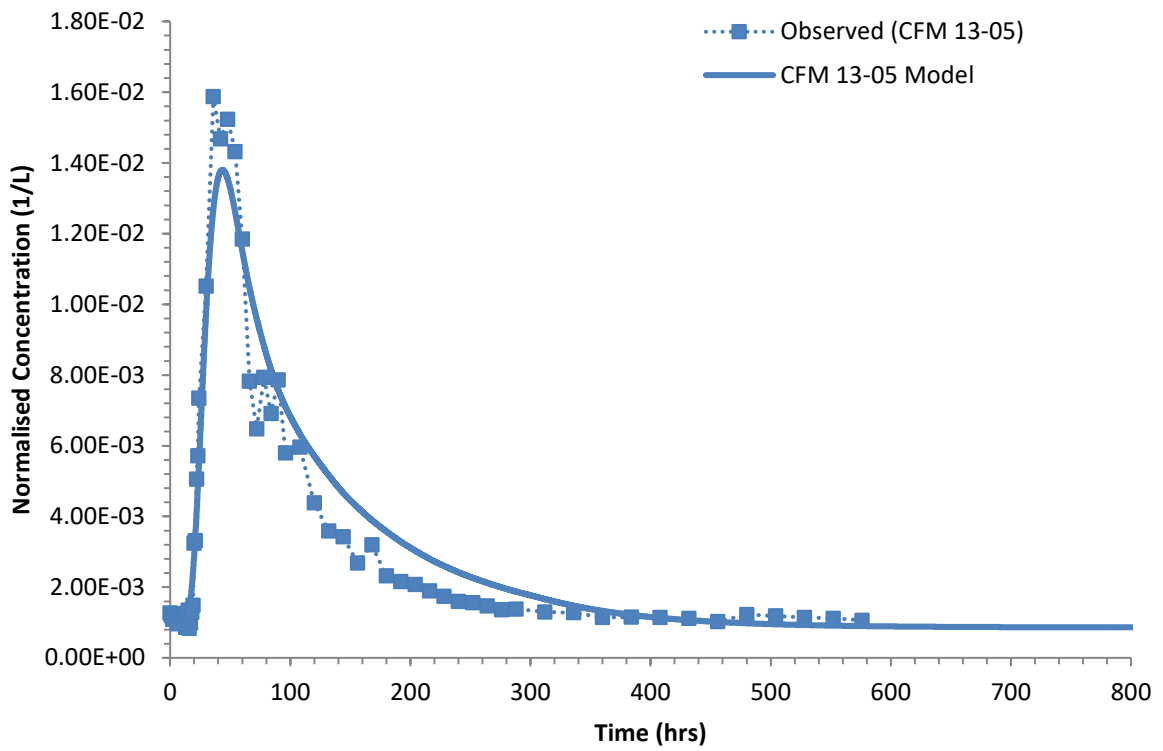


Figure 5.21 Model calibration for 1D bentonite colloid model in CFM Run 13-05

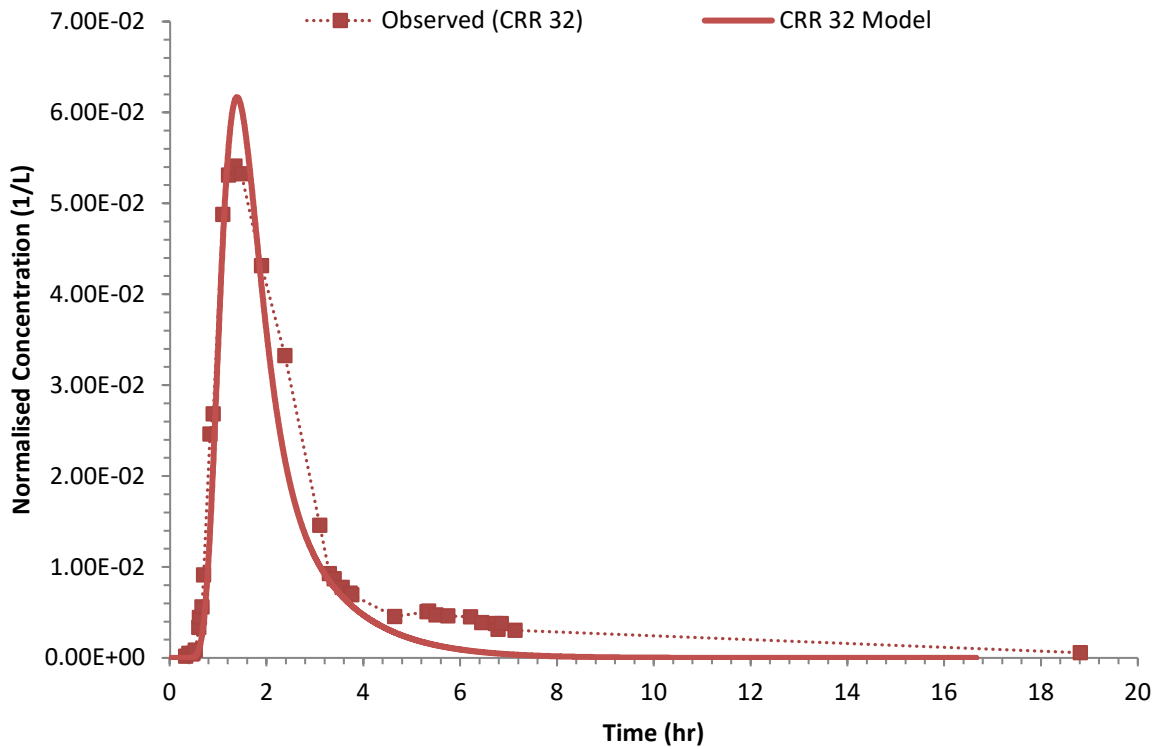


Figure 5.22 Model calibration for 1D bentonite colloid model in CRR Run 32

#### 5.5.4. Discussion and Conclusions

Figure 5.19 and Figure 5.20 both show reasonable matches for conservative tracer breakthrough for the 1D model in both experiments. Figure 5.19 shows a good match to the rising limb and peak of the breakthrough curve for CFM Run 13-05. However, the falling limb of the model is under-dispersed compared with the experimental data, as was found in the 2D model. Similar observations can be made for the breakthrough of conservative tracer in CRR Run 32 in Figure 5.20. The 2D model deals with mass loss and dispersion of the tracer better; this is because it includes both longitudinal and transverse dispersion, but also the inverse modelled transmissivity distribution, which generates macro-dispersion due to the different flow paths.

Although the 1D model provided relatively good matches to conservative tracer transport, this required the addition of an unphysical dilution term to match the experiments. In addition, Table 5.7 shows that unlike the 2D model, it was not possible to find consistent parameters to describe the transport of the conservative tracers, despite efforts to do so. The 1D model was not able to use the same effective flow parameters between the two experiments (as different hydraulic conductivity values were used), reducing the predictive ability of the model to describe groundwater flow in the MI shear zone.

Previous modelling of the CFM and CRR experiments used 1D and homogeneous 2D models (Noseck et al., 2016; Smith et al., 2006; Kosakowski and Smith, 2004; Reimus, 2016; Reiche et al., 2015), and while these models resulted in good model calibrations to experimental data, these models had difficulty in finding effective properties that accurately

described groundwater flow and tracer transport, resulting in the models requiring individual calibrations for each experiment.

The colloid breakthroughs shown in Figure 5.21 and Figure 5.22 both show good model matches to experimental data from the COMSOL 1D Model. The model matches are of similar quality to the 2D model (Figure 5.12) and used consistent rate constants for the two experiments. When comparing attachment rate constants used in the 1D and 2D models, the colloid attachment and detachment rates were higher in the 1D model than in the 2D model. This is unsurprising, as the 2D model gives a better representation of the different flow paths available for colloid transport, and therefore replicates the fact that colloids were not recovered by the abstraction borehole during the different experiments. The 1D model does not replicate this and therefore requires higher colloid attachment rates to accurately match colloid recovery.

In summary, it has not been possible to find consistent parameters to describe the transport of tracers using the 1D model, due to the highly heterogeneous nature of the MI shear zone. This demonstrates the importance of including information on the flow geometry and geological structure of the shear zone when modelling transport experiments, as the 2D model with a transmissivity distribution has been able to model tracer and colloid transport using consistent parameters. Including the transmissivity distribution in the 2D model also allows the model to reflect more accurately the influence of the heterogeneous geological structure on transport processes, namely dispersion and the mass loss caused by the different flow paths available in the shear zone.

## 5.6. Blind predictions for the REMO-2 experiment

### 5.6.1. Background

In addition to the *in situ* migration tests carried out as part of the CFM project, two further experiments studying colloid remobilisation have been carried out, led by the teams at KIT-INE. These additional experiments were termed the colloid remobilisation experiments (REMO).

The aim of REMO-1 was to hydraulically shock attached colloids that were not recovered in CFM Run 13-05 (and previous migration experiments) in CRR Dipole 1. Carried out in April 2016, two hydraulic shocks (of 58ml/min and 192 ml/min) were injected into the CRR 99.002 borehole (the injection borehole used in CRR Run 32 and CFM Run 13-05) (Lanyon et al., 2017). Although some colloids were mobilised, it is believed that these colloids were natural background colloids, and no radionuclides were mobilised within the experiment (as detected by ICP-MS) (Lanyon et al., 2017).

REMO-2 was carried out in May 2017, and as part of designing the experimental protocols, the 2D model was used to carry out blind predictions of colloid transport in the experiment, which also tested the ability of the transport model to make predictions of colloid transport. The aim of REMO-2 was to study the impact of fresh competing surfaces on remobilising radionuclides that have sorbed to the rock surfaces or to attached colloids from previous experiments (including CFM Run 13-05) (B. Lanyon, pers. Comm.). For REMO-2, a suspension of amino-G acid, FEBEX bentonite and Ni- and Zn- labelled montmorillonite colloids were made up under oxic conditions (unlike the migration experiments) and injected into CRR 99.002 at 25 ml/min. After a rest period in CRR 99.002, water was extracted from

the same borehole at 25 ml/min, sampling for colloid and tracer concentrations. Throughout the experiment, the Pinkel packer extracted at 25 ml/min of water, as it did throughout CFM Run 13-05 and subsequent experiments. The oxic suspension was also intended to test the effect of an oxic plume in the MI shear zone (which may have an impact on the behaviour of redox-sensitive radionuclides such as Np and U, see discussion in Chapter 7).

The aim of the modelling was to make predictions of the colloid breakthrough and recovery, at both CRR 99.002 and Pinkel for different potential rest times to help determine experimental protocols. This was done by carrying out groundwater flow modelling in Groundwater Vistas (and MODFLOW) and using the resulting flow field in the 2D COMSOL model for colloid transport.

#### **5.6.2. Alterations to Model**

The MODFLOW model (in Groundwater Vistas) for groundwater flow in the main transport experiments was altered by adding different stress periods (all assuming steady state flow) representing the single well injection-withdrawal (SWIW) experimental procedure that was planned to be used in REMO-2. This model was used to model groundwater flow across the full model domain used in the inverse model, extracting hydraulic heads for the COMSOL model. Table 5.9 shows the stress periods used in the MODFLOW model. All other aspects of the model remained the same. The resulting groundwater head contours are shown in Figure 5.23, Figure 5.24 and Figure 5.25.

Stress Period	Period Length (hours)	No of Time Steps	TS Multiplier	Notes
1	1	1	1.2	Steady State stress period (pre experiment) CRR 99.002 = 0 ml/min
2	1.5	2	1.2	Injection of colloids CRR 99.002 = 25ml/min Concentration= 273 mg/l
3	0.33	1	1.2	Injection of freshwater CRR 99.002 = 25ml/min
4	12-48	6-12	1.2	Rest Period. Period length depends on rest time CRR 99.002 = 0 ml/min
5	10	5	1.2	Extraction period CRR 99.002 = -25ml/min

Table 5.9 Stress period setup for REMO-2 MODFLOW model. Pinkel flow = -25ml/min throughout experiment

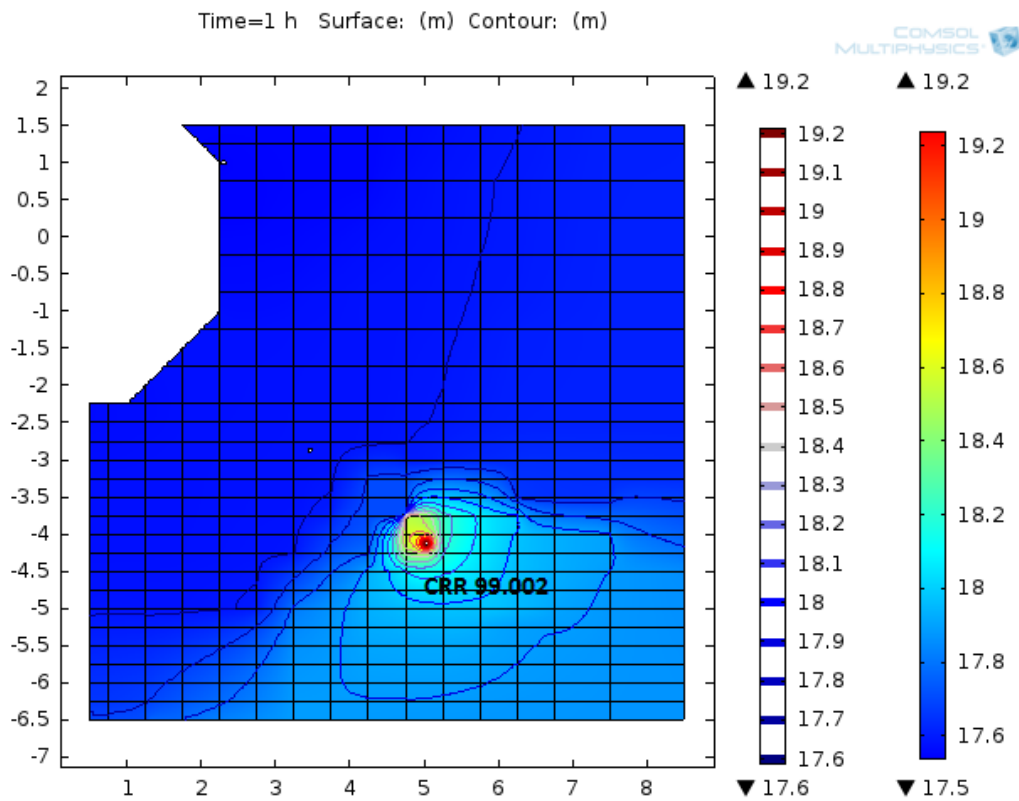


Figure 5.23 Groundwater head colour flood (with contours) during injection of colloids for REMO-2. Co-ordinate system centred on tunnel in metres.

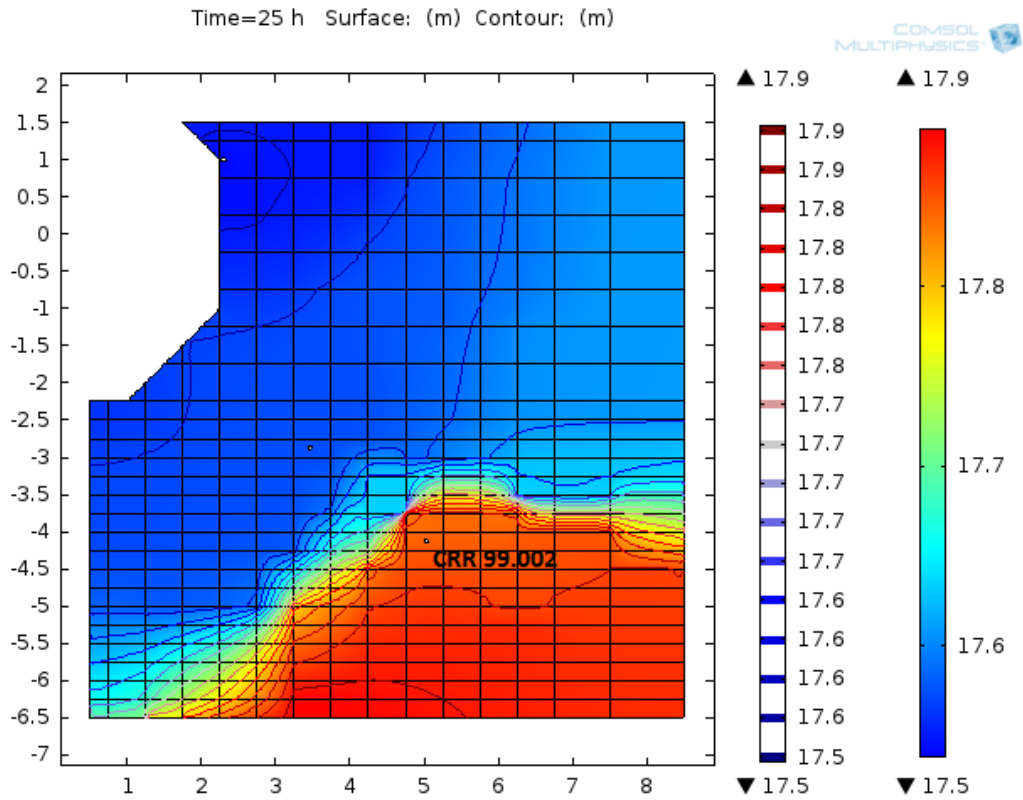


Figure 5.24 Groundwater head colour flood (with contours) during rest period for REMO-2. Co-ordinate system centred on tunnel in metres.

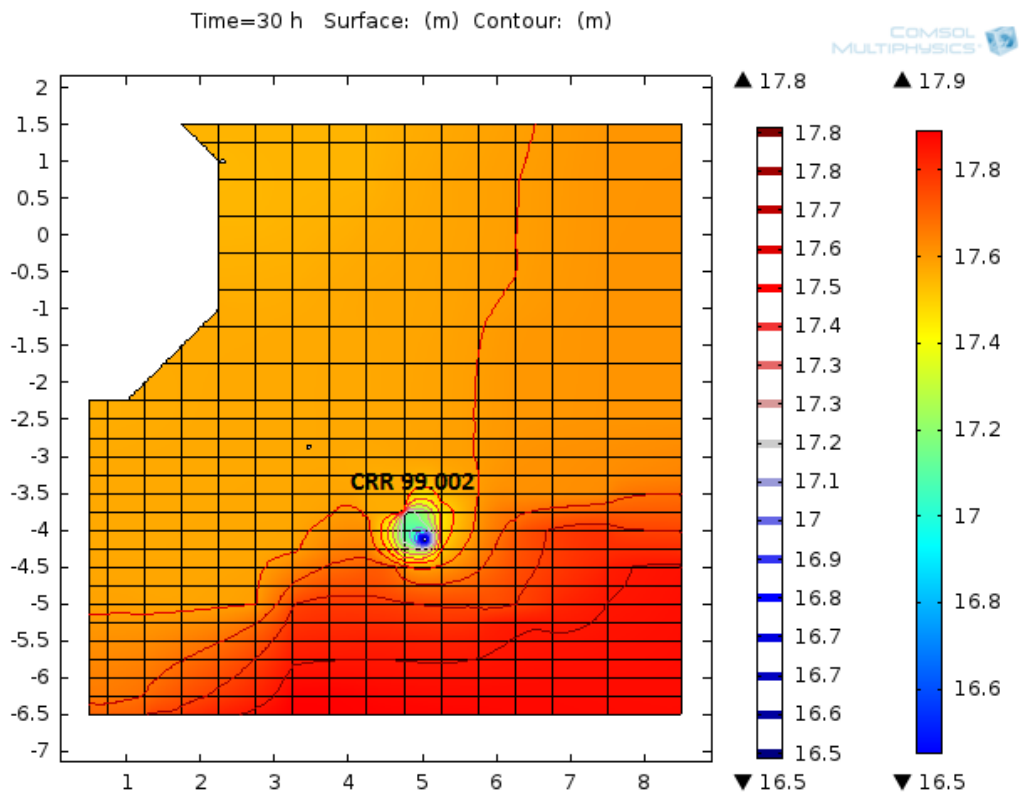


Figure 5.25 Groundwater head colour flood (with contours) during extraction of colloids for REMO-2. Co-ordinate system centred on tunnel in metres.

The COMSOL model for colloid transport used the steady state heads generated from the MODFLOW model, and includes the 2D transmissivity distribution. As one of the main purposes of the model was to determine whether colloid breakthrough would be observed at the Pinkel packer during the experiment, the model geometry was altered so that Pinkel was included. The model domain was altered so that it was an 8 x 8 m square so that it extended past Pinkel. Pinkel was modelled as an octagon, the same as other boreholes. The model was re-meshed using the same settings as the 2D model, and was set to run for 100 hours with the same time step settings.

Colloid transport including reversible and irreversible colloid attachment was included in the model, using the colloid attachment parameters given in Table 5.6. Darcy's Law was solved using COMSOL's time dependent solver at the same time as the colloid transport equations. For groundwater flow, specified flux boundary conditions were applied to both CRR 99.002 and Pinkel based on the flow rates specified in Table 5.9. For colloid transport, advective flux only boundary conditions were applied to Pinkel and the outer boundary of the model, and a specified flux condition applied to CRR 99.002. The model only considered the breakthrough of FEBEX bentonite colloids ( $C_0 = 273.23$  mg/l) and not the additional ~20 mg/l of artificially labelled Zn- and Ni- montmorillonite colloids. The model did not consider the presence of attached colloids from previous experiments or natural background colloids, as limited numbers of colloids were mobilised during REMO-1, which was conducted at much higher flow rates than the rates planned to be used in REMO-2. All other parameters in the model used values in Table 5.1.

### 5.6.3. Model Predictions

The model predictions are shown in Figure 5.26 and Figure 5.27 as breakthrough curves for both CRR 99.002 and Pinkel in linear and log scale, with the recovery of the FEBEX bentonite detailed in Table 5.10 for the different rest periods. Example contour plots showing the migration of the colloids are shown in Figure 5.28 to Figure 5.30.

Rest Period	Recovery at CRR 99.002	Recovery at Pinkel
12 hours	21.9%	3.6%
<b>24 hours</b>	<b>5.5%</b>	<b>5.5%</b>
36 hours	1.47%	6.4%
48 hours	0.42%	6.2%

Table 5.10 Recovery of bentonite colloids as calculated after 100 hours.

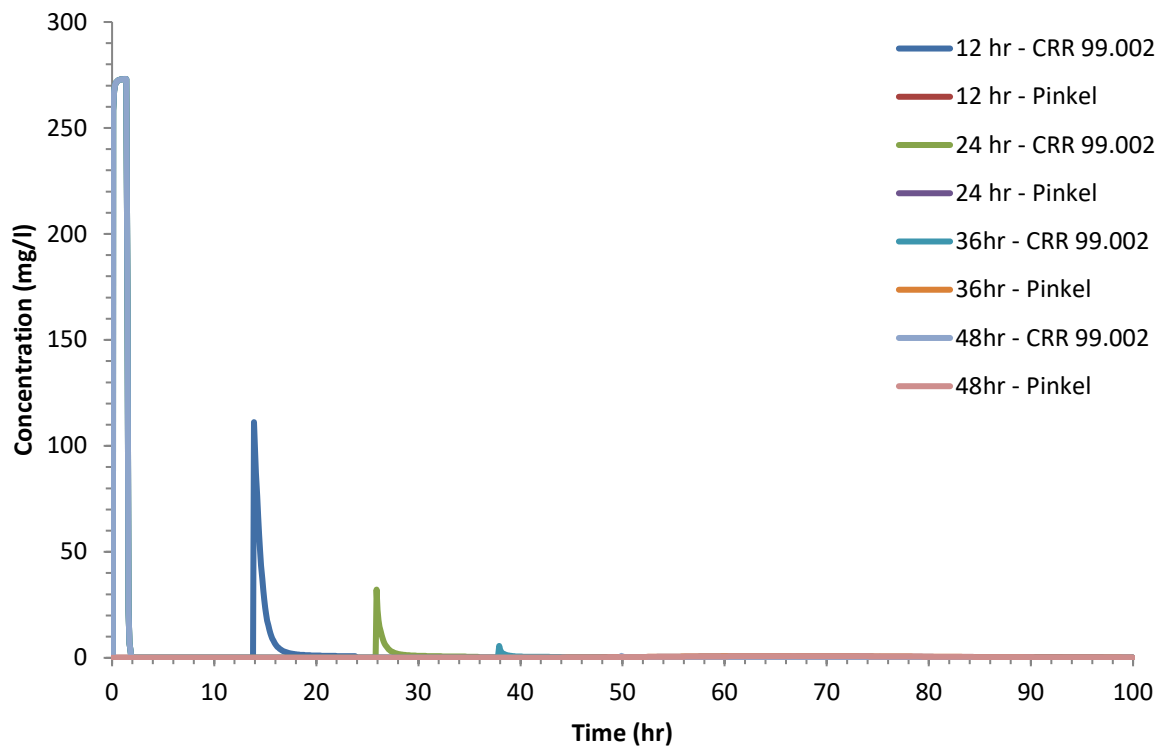


Figure 5.26 Predicted breakthrough for bentonite colloids in REMO-2 (for CRR 99.002 and Pinkel)

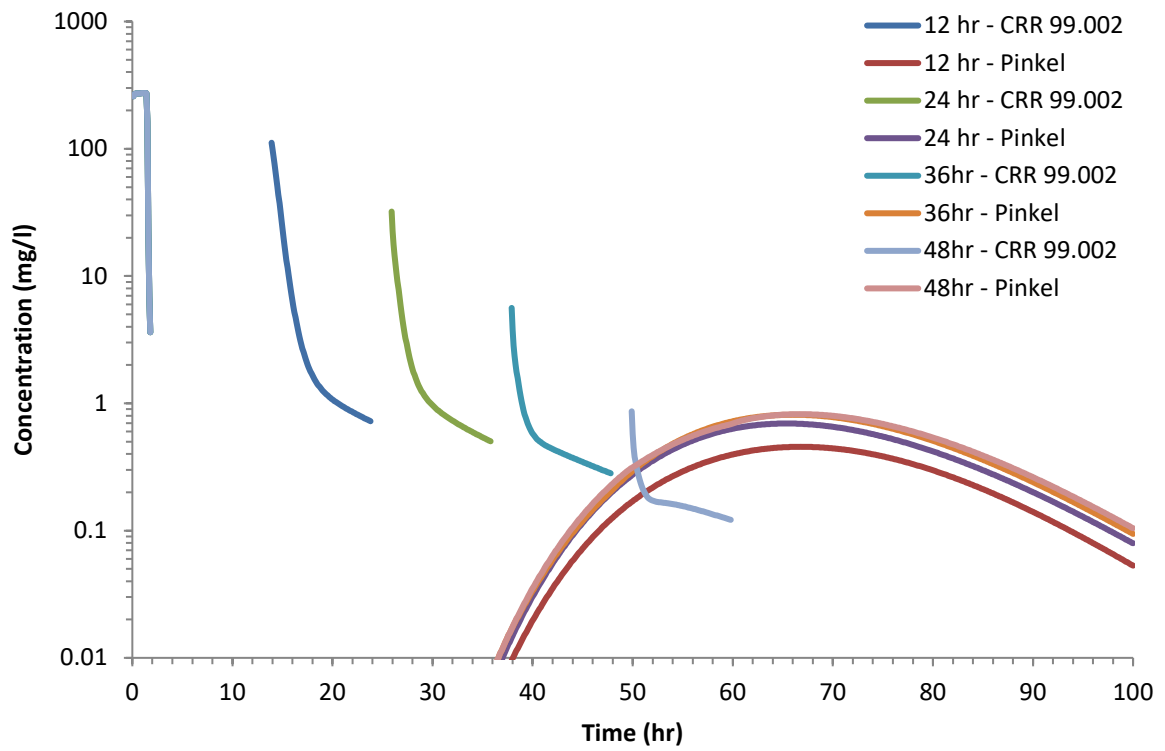


Figure 5.27 Predicted breakthrough curves for bentonite colloids in REMO-2 (for CRR 99.002 and Pinkel)

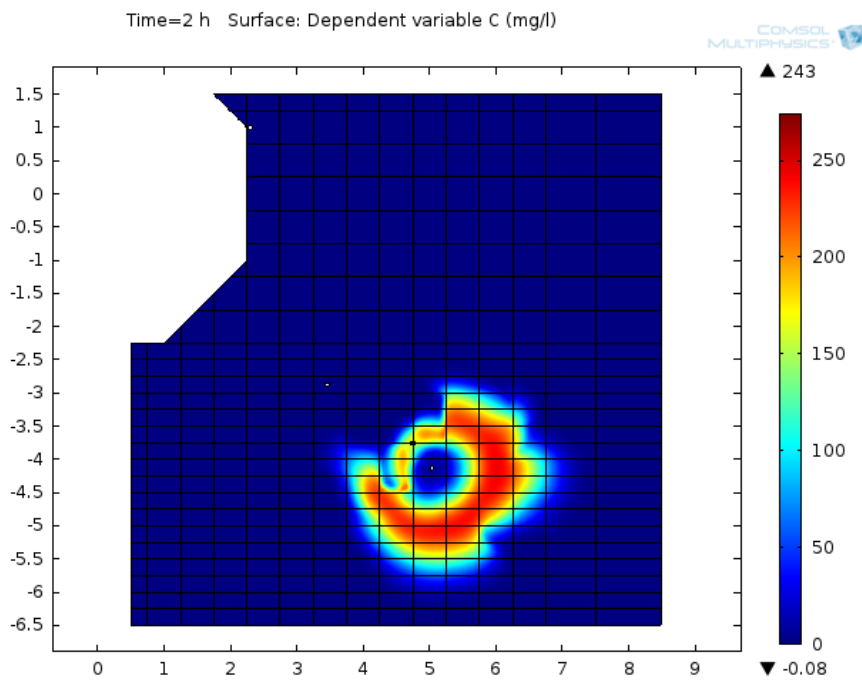


Figure 5.28 Predicted colloid concentration at 2hr in REMO-2 (end of injection of freshwater)

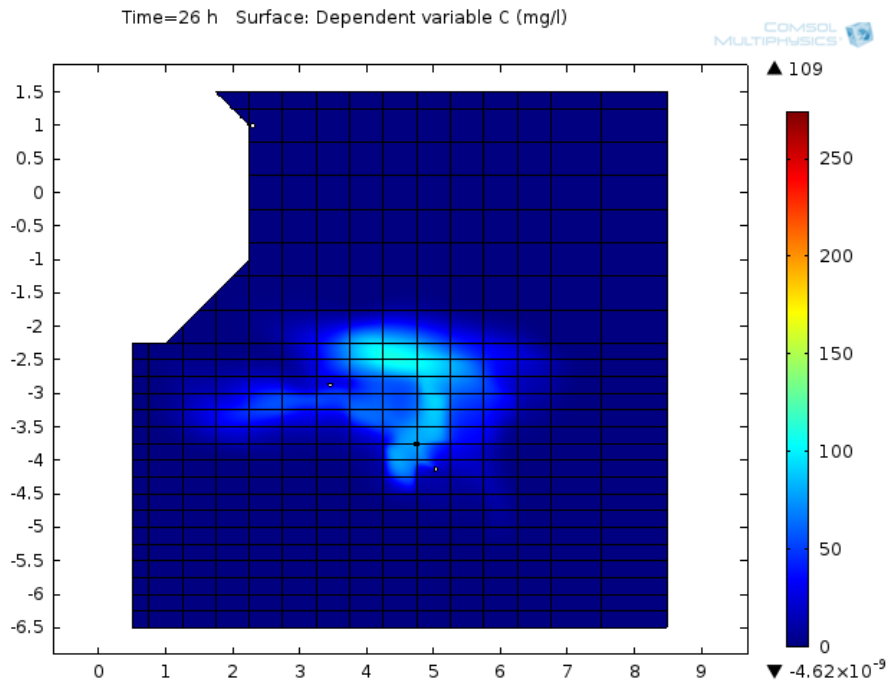


Figure 5.29 Predicted colloid concentration at 26 hr in REMO-2 (end of 24hr rest period)

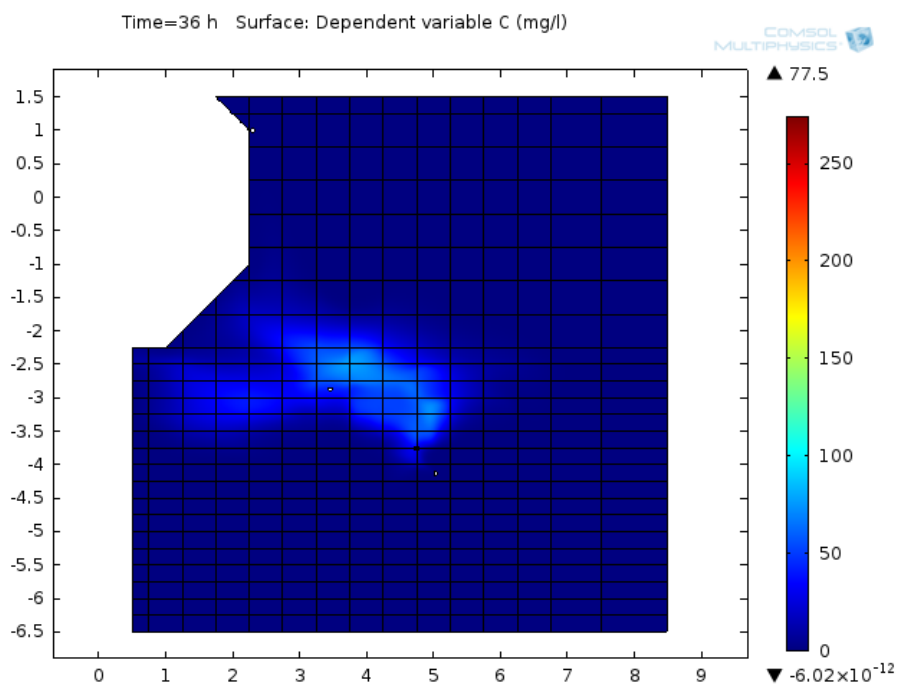


Figure 5.30 Predicted colloid concentration at 36 hours in REMO-2 (end of 10 hr extraction) in REMO-2

#### 5.6.4. Discussion and Conclusions

Table 5.10 shows that colloid recovery, as calculated at 100 hour model run time, at CRR 99.002 is controlled by rest time (recovery varied between 21% for a 12hr rest, to 0.4% for a 48hr rest). The rest time is less of a control on recovery at Pinkel (recovery at Pinkel varied between 3% and 6%). In contrast with CRR 99.002, the highest recovery at Pinkel (6.4%) was calculated for the 36hr rest period (the 48 hour rest period had slightly lower recovery of 6.2%). This is the result of the competing impacts of longer time for attachment and longer time for advection to Pinkel. However, the model does not account for colloid remobilisation caused by hydraulic shocks after the rest period when extraction starts so different colloid recovery values could be found experimentally due to this missing process.

The predictions were used to choose the rest period used in the experiment. To maximise colloid recovery, while also allowing the colloids to act as a fresh sorption surface for radionuclides, a 24hr rest period was chosen. At time of writing, experimental data for REMO-2 was not available to compare against the model predictions so it is unknown whether the predictions were of good quality.

In summary, the 2D model of colloid transport has been used to make predictions for colloid transport in the REMO-2 experiment to help with developing experimental protocols. The model has not accounted for previously attached or mobile colloids which could act as further sorption surfaces if mobilised. As the experimental data are not currently available, it is not possible to assess the quality of the model prediction, or determine whether sorbed radionuclides were mobilised by the colloids in this experiment, which this model could be used to predict if further alterations were made.

## 5.7. Summary

This chapter has detailed results of the model calibration for tracer and colloid transport in CFM Run 13-05 and CRR Run 32. Using the 2D transport model, with the inverse-modelled transmissivity distribution, it has been possible to model the transport of both conservative tracers and bentonite colloids in the two experiments using consistent parameters to describe their transport.

In a transport model, the distribution of both transmissivity and porosity has to be specified. In this model, fracture aperture (and therefore porosity) is related to transmissivity by a parallel plate model, with the shear zone represented by a number of parallel plates with equal apertures. Due to the highly heterogeneous nature of the MI shear zone, more parallel plates had to be specified than are present in the MI shear zone to accurately match the conservative tracer in the different migration experiments. However, using this approach, a consistent number of parallel plates and the same dispersivity values were used to model conservative tracers in CFM Run 13-05, CRR Run 32 (and CRR Run 29); with the model producing good matches to the experimental data.

Colloid breakthrough has been modelled accurately using the same colloid attachment rates for both CFM Run 13-05 and CRR Run 32, using values that are within the ranges used in previous models of CFM experiments. The model had to include both reversible and irreversible colloid attachment, but did not have to consider colloid exclusion chromatography or colloid attachment blocking mechanisms to model breakthrough, indicating that these processes did not occur. The model also assumed that the colloid populations in the two experiments could be described by the same effective properties.

These assumptions were not changed during model calibration. The colloid model was then used to predict colloid migration and recovery in the recent REMO-2 experiment that was carried out at Grimsel in the MI Shear Zone.

A 1D channel model was built to attempt to model conservative tracers and colloids, but consistent flow parameters could not be found to describe tracer transport accurately, demonstrating the importance of including information on the geological structure and flow geometry of the MI shear zone in models of the CFM and CRR experiments. The heterogeneous nature of the shear zone also has implications for both dispersion and colloid attachment, as the 1D model required higher parameter values for longitudinal dispersivity and colloid attachment rates than the 2D model.

The parameters derived from the calibration of both conservative tracer and colloid breakthrough will be used in the model calibration of the radionuclides that will be discussed in the next two chapters.

## 5.8. List of References

- Chrysikopoulos, C. V. and Katzourakis, V.E. (2015) Colloid particle size-dependent dispersivity. **Water Resources Research** [online], 51 (6): 4668–4683 DOI: 10.1002/2014WR016094. Available from: <http://doi.wiley.com/10.1002/2014WR016094>
- Domenico, P. and Schwartz, F. (1990) **Chemical and Physical Hydrogeology**. 1st ed. New York: Wiley
- Forbes, A. (2016) **Examining the Effects of Small Scale Heterogeneity on the Effective Apertures Calculated from Flow and Transport Data**. MSc Nuclear Decommissioning and Waste Management Project Report, University of Birmingham
- Gaus, I. and Smith, P.A. (2008) **Nagra Arbeitsbericht NAB 08-27: Modellers dataset for the Colloid Formation and Migration Project Status: End of CFM Phase 1**. Wettingen, Switzerland
- Harvey, B.E., McMillan, L.A. and Herbert, A.W. (2017) “Modelling colloid-facilitated Americium transport at Grimsel Test site, Switzerland.” **In International High Level Radioactive Waste Management 2017. Charlotte, NC, USA. 2017**. American Nuclear Society. pp. 273–280
- Hjerne, C. and Nordqvist, R. (2014) Relation between mass balance aperture and hydraulic properties

from field experiments in fractured rock in Sweden. **Hydrogeology Journal** [online], 22 (6): 1285–1292 DOI: 10.1007/s10040-014-1132-2. Available from: <http://link.springer.com/10.1007/s10040-014-1132-2>

Kontar, K., Grafe, K. and Rosli, U. (2013) **Nagra Aktennotiz AN 13-617: Tracer Test Run 13-05**. Monchaltorf, Switzerland

Kosakowski, G. and Smith, P. (2004) **Nagra Technical Bulletin NTB 04-01: Grimsel Test Site Investigation Phase V Modelling the transport of Solutes and Colloids in a Water Conducting Shear Zone at the Grimsel Test Site** [online]. Wettingen, Switzerland. Available from: <http://www.nagra.ch/en/cat/publikationen/technicalreports-ntbs/ntbs-2001-2012/downloadcentre.htm>

Lanyon, B. and Blechschmidt, I. (2016) **Nagra Aktennotiz AN16-102: Minutes of the CFM Modellers Workshop, 10-11 December 2015, San Francisco**. Wettingen, Switzerland

Lanyon, B., Blechschmidt, I. and Martin, A. (2017) **Nagra Aktennotiz AN 17-358: Minutes of the CFM Partner Meeting, 11-12 May 2017**. Wettingen, Switzerland

Möri, A., Alexander, W.R., Degueldre, C., Eikenberg, J., Fierz, T., Geckeis, H., Geier, F., Hauser, W., Schäfer, T. and Smith, P.A. (2004) **Nagra Technical Bulletin NTB 03-01: The CRR Final Project Report series 1 - Description of the Field Phase - Methodologies and Raw Data** [online]. Wettingen, Switzerland. Available from: <http://www.nagra.ch/en/cat/publikationen/technicalreports-ntbs/ntbs-2001-2012/downloadcentre.htm>

Noseck, U., Flügge, J., Reimus, P., Cvetkovic, V., Lanyon, B., Schäfer, T. and Blechschmidt, I. (2016) **Nagra Technical Report NTB 16-06: Colloid Formation and Migration Project: Modelling of tracer, colloid and radionuclide/homologue transport for dipole CFM 06.002- Pinkel surface packer**. Wettingen, Switzerland

Reiche, T., Noseck, U. and Schäfer, T. (2015) Migration of Contaminants in Fractured-Porous Media in the Presence of Colloids: Effects of Kinetic Interactions. **Transport in Porous Media**, 111 (1): 143–170 DOI: 10.1007/s11242-015-0585-7

Reimus, P.W. (2016) **Nagra NAB 16-61: GTS Phase VI- CFM Phase 3: Interpretation of colloid-facilitated radionuclide transport experiments from the CRR and CFM projects**. Wettingen, Switzerland

Ryan, J.N. and Elimelech, M. (1996) Colloid mobilization and transport in groundwater. **Colloids and Surfaces A: Physicochemical and Engineering Aspects**, 107 (95): 1–56 DOI: 10.1016/0927-7757(95)03384-X

Schäfer, T., Lanyon, B. and Blechschmidt, I. (2013) **CFM 13-05 Data Set**. pers comm.: Nagra/ KIT-INE (Unpublished Dataset)

Smith, P.A., Guimera, J., Kosakowski, G., Pudewills, A. and Ibaraki, M. (2006) **Nagra Technical Bulletin NTB 03-03: Grimsel Test Site Investigation Phase V - The CRR Final Project Report series 3: Results of the Supporting Modelling Programme**. Wettingen, Switzerland

Zheng, Q., Dickson, S.E. and Guo, Y. (2008) On the appropriate “equivalent aperture” for the description of solute transport in single fractures: Laboratory-scale experiments. **Water Resources Research**, 44 (4): 1–9 DOI: 10.1029/2007WR005970

## **6. MODELLING THE MIGRATION OF AMERICIUM AND PLUTONIUM IN CFM 13-05 AND CRR 32**

### **6.1. Introduction**

This chapter details the results from modelling the americium and plutonium breakthrough in CFM Run 13-05 and CRR Run 32, using the transport model (described in Chapter 4), and the results of the model calibration for conservative tracers and colloids (Chapter 5). It is important to note that any error in the results of the conservative tracer and colloid calibration are carried through to the results of these radionuclides. These radionuclides both had high initial bound fractions as measured in the experimental injection cocktails, and were the focus of the other CFM modelling teams when this project was started (e.g. Noseck et al. (2016); Reiche et al. (2015)).

This chapter also shows some geochemical modelling of the injection cocktail in the two migration experiments. The modelling was used to help understand the processes that the two radionuclides are undergoing in the transport experiments, and to help validate the conceptual model of the processes that need to be included in the transport model.

Both americium and plutonium were modelled using the same conceptual model that colloids facilitated the transport of both radionuclides, and that the rate at which the radionuclides desorbed from the colloids formed a major control on their transport. The transport model used consistent parameters to describe the transport of the two radionuclides in both experiments.

Part of this chapter (the americium model calibration results) has already been presented as a conference paper at the American Nuclear Society International High Level Radioactive Waste Management conference (Harvey et al., 2017).

## 6.2. Americium model calibration

Different isotopes of americium were used in the two experiments,  $^{243}\text{Am}$  in CFM Run 13-05 and  $^{241}\text{Am}$  in CRR Run 32. The transport model assumes that both isotopes have the same transport behaviour. The mass and concentrations of americium used in the experiments are shown in Table 6.1.

Before the beginning of both experiments, the amount of mass removed from solution after centrifugation is measured. This measurement is referred as the initial bound fraction, as the centrifugation process removes radionuclides from solution that are in colloidal form (either sorbed to carrier colloids or radionuclides as self-colloids).

The measured bound fraction for americium was 99.6% in CFM Run 13-05 and 99% in CRR Run 32. Because of this, americium was expected to have similar transport characteristics in both experiments.

	<b>CFM Run 13-05:</b> $^{243}\text{Am}$	<b>CRR Run 32:</b> $^{241}\text{Am}$
Mass ( $M_0$ )	0.235 $\mu\text{g}$	0.0167 $\mu\text{g}$
Concentration ( $C_0$ )	0.073 $\mu\text{g}/\text{l}^1$	0.167 $\mu\text{g}/\text{l}$
Initial bound fraction/ Mass removed by centrifugation	99.6%/ 0.234 $\mu\text{g}^2$	99%/ 0.0165 $\mu\text{g}$
Cocktail equilibration time	35 days	5 days
Colloid mass	Total: 224.3 mg	2.01 mg

1: Peak concentration in re-circulation circuit

2: Value measured after 401 days due to equipment problems

**Table 6.1 Mass and concentration of americium isotopes used in CFM Run 13-05 and CRR Run 32**

### 6.2.1. Conceptual Model

PHREEQC was used to model the injection cocktail in both experiments in order, to provide information about radionuclide speciation, precipitates and redox states. Dr Janice Kenney, researcher on the RATE project at the University of Birmingham, carried out the PHREEQC modelling work, and full details are provided in Appendix A. In summary, measured concentrations of all the radionuclides were added to reference Grimsel Groundwater (GGW), using the concentrations in Table 6.2. Initial calculations used the PSI-NAGRA thermodynamic database (Thoenen et al., 2014), but then the SIT/ ANDRA database (Giffaut et al., 2014) was used for the final results as more relevant precipitates and species were included in this database. The modelling used a fixed pe of -3.73 (equivalent of an Eh of -220mV, which is the value for reference Grimsel groundwater), and used pH values between 9 and 12.

The geochemical model represented the cocktail as a solution, and did not include the bentonite colloids due to the large amount of data required to add the interactions between radionuclide and colloid surfaces. This means that the model will not account for processes that occur in the clay surfaces, such as surface-mediated reduction (as observed for plutonium in Banik et al. (2016) and Zavarin et al. (2012)). The model assumes thermodynamic equilibrium, which may not be appropriate as sorption and precipitation equilibrium may not have been reached during the experiment. This means that the model may not represent the full nature of the injection cocktail, but nevertheless gives insight into relevant processes that may need to be included in the transport model.

<i>Element</i>	<b>Concentration (M)</b>	<i>Element</i>	<b>CFM Run 13-05 Concentration (M)</b>	<b>CRR Run 32 Concentration (M)</b>
<i>Al</i>	2.63e-6	<i>Am</i>	4.3e-10	6.66e-10
<i>Br</i>	3.8e-7	<i>Ba</i>	3.41e-9	N/A
<i>Ca</i>	1.4e-4	<i>Cs</i>	8.8e-10	1.38e-8
<i>Cl</i>	1.6e-4	<i>Np</i>	8.6e-9	1.09e-6
<i>F</i>	3.6e-4	<i>Pu</i>	2e-9	6.74e-9
<i>Fe</i>	3e-9	<i>Th</i>	4.5e-9	1.1e-8
<i>K</i>	5e-6	<i>U</i>	4.3e-10	8.69e-7
<i>Mg</i>	6.2e-7	<i>I</i>	N/A	9.23e-13
<i>Mn</i>	5e-9	<i>Tc</i>	N/A	1.04e-8
<i>Na</i>	6.9e-4	<i>Sr</i>	N/A	1.11e-11
<i>S</i>	6.1e-5			
<i>Si</i>	2.5e-4			
<i>Sr</i>	2e-6			
<i>HCO<sub>3</sub><sup>-</sup></i>	4.5e-4			

**Table 6.2** Concentration of elements used in PHREEQC calculations, Grimsel groundwater concentrations taken from Bennett (2014)

The speciation of americium as predicted by PHREEQC is shown in Figure 6.1 for the injection cocktail used in CFM Run 13-05, and Figure 6.2 for the injection cocktail in CRR Run 32. Americium is expected to be trivalent with similar speciation in both experiments. At the pH of reference Grimsel groundwater (pH 9.6 (Bennett, 2014)), americium forms carbonate or hydroxide complexes, and is mostly present as  $\text{Am}(\text{CO}_3)_2^-$ ,  $\text{Am}(\text{OH})_2^+$ ,  $\text{Am}(\text{CO}_3)^+$  and  $\text{AmOSi}(\text{OH})_3^{2+}$ . As both cation and anion species are predicted to be present, sorption to colloids would be facilitated at a wide range of pH values.

Figure 6.3 shows predicted saturation indices for americium precipitates in the CFM Run 13-05 cocktail; Figure 6.4 is the corresponding figure for CRR Run 32.  $\text{Am}(\text{CO}_3)(\text{OH})$  is the only precipitate with a positive saturation index at pH 9.6. The saturation index in CRR Run 32 is slightly higher than CFM Run 13-05, due to the higher concentration of americium used in the experiment.

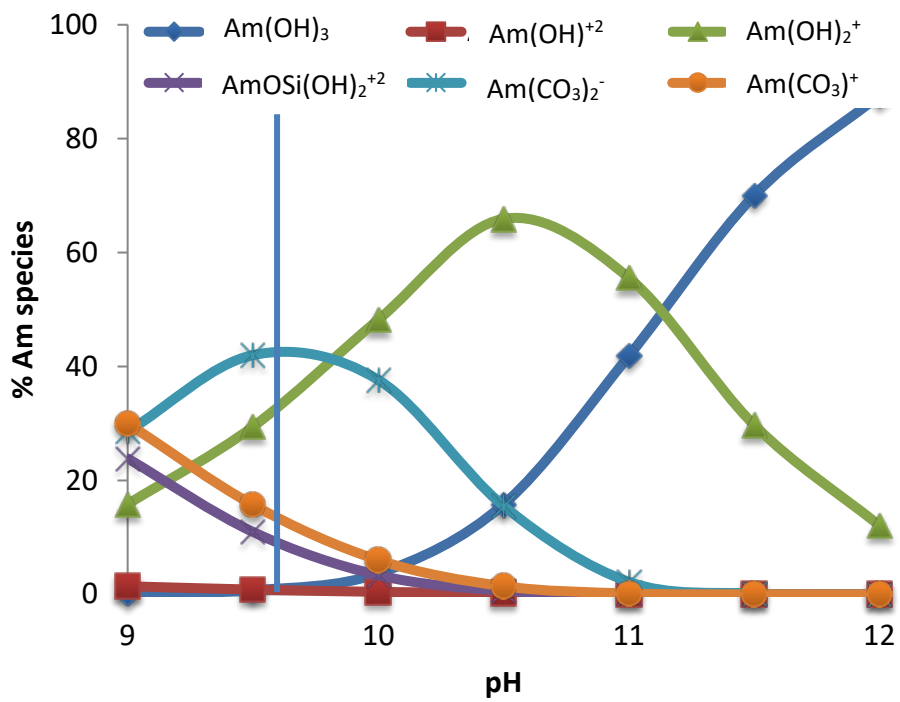


Figure 6.1 Speciation of americium in the CFM Run 13-05 injection cocktail as predicted by PHREEQC. Blue line = Grimsel groundwater (pH 9.6)

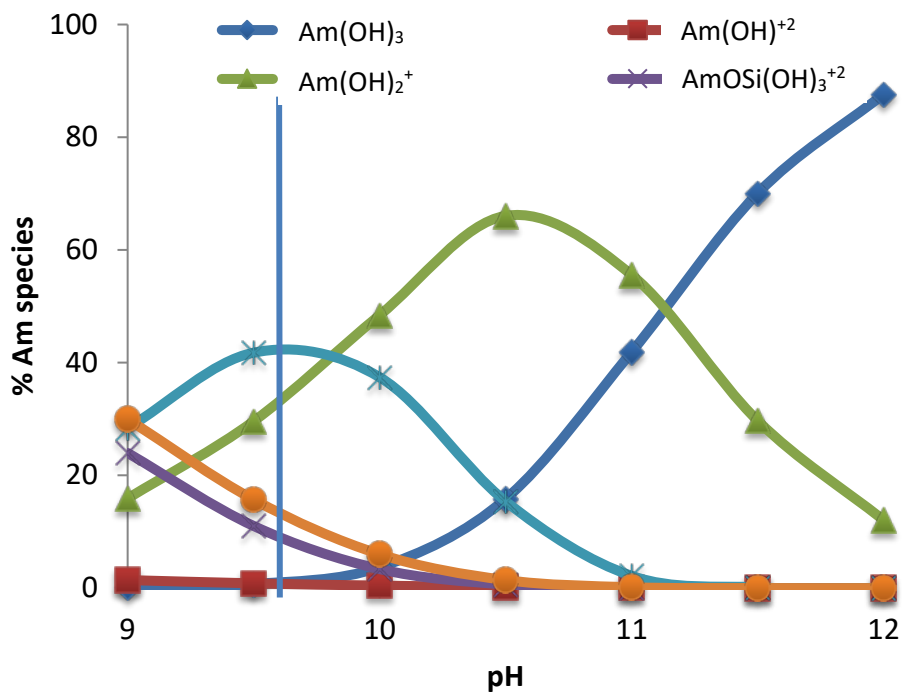


Figure 6.2 Speciation of americium in the CRR Run 32 injection cocktail as predicted by PHREEQC. Blue line = Grimsel groundwater (pH 9.6)

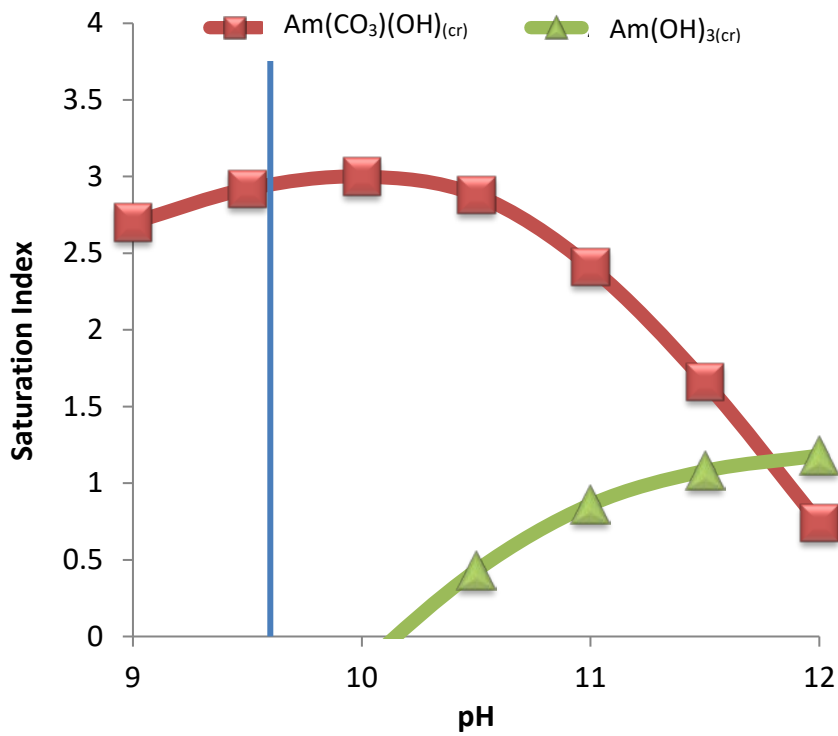


Figure 6.3 Predicted saturation indexes of americium precipitates in CFM Run 13-05 injection cocktail from PHREEQC. Blue line = pH (9.6) of the reference Grimsel groundwater

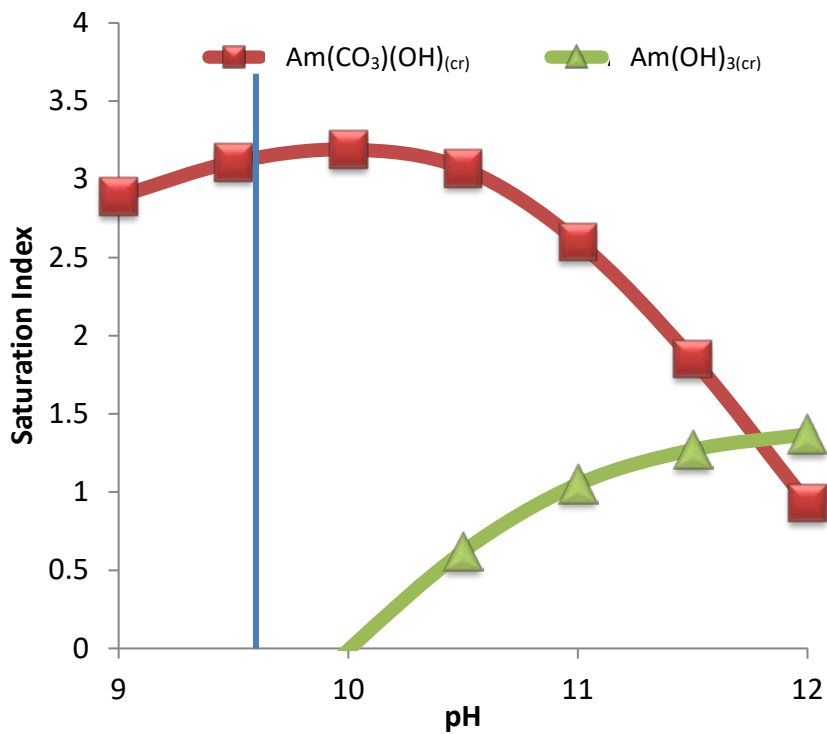


Figure 6.4 Predicted saturation indexes of americium precipitates in the CRR Run 32 injection cocktail from PHREEQC. Blue line = pH (9.6) of reference Grimsel groundwater.

A large proportion of americium is removed from the injection cocktail when centrifuged, as shown by the high initial bound fraction in both experiments (>99%). It is important to note that there is some uncertainty with the initial bound fraction measurement as the two experiments were prepared differently. For CRR Run 32, after the injection cocktail was prepared, the cocktail was left to equilibrate for 5 days before the experiment was run, and the initial bound fraction was measured at that same time. In CFM Run 13-05, the equilibration time was 35 days, but due to equipment issues the initial bound fraction was not measured until 401 days after the cocktail was prepared. This could provide some uncertainty in the data if processes such as sorption or precipitation had not reached equilibrium during the 35 days before the experiment.

Measured  $K_d$  values for americium sorption to bentonite colloids are very high (in the order of  $10^6$  L/kg (Missana and Geckeis, 2006)). It is commonly thought that the high initial bound fraction in the two experiments is caused by high amounts of sorption to the colloids in the injection cocktail (Möri et al., 2004; Schäfer et al., 2013). Huber et al. (2011) found that americium showed a high level of association to bentonite colloids, but when Grimsel FFM was added, slow desorption from the colloids occurred (due to the higher surface area of the FFM in this laboratory experiment). The rate at which desorption from the colloids occur was also demonstrated to be a key control on americium transport in column experiments in Grimsel FFM in Dittrich et al. (2015). This is despite the measured  $K_d$  value to Grimsel FFM being orders of magnitude lower than to the bentonite colloids ( $K_d$  to FFM  $10^3$  L/kg (Missana and Geckeis, 2006)).

Although in reality there will be multiple types of sorption site on a bentonite colloid, models have successfully represented americium transport using one (e.g. Noseck et al. 2016; Dittrich et al. 2015). To make the calibration process simpler, initially only one sorption site was included in the transport model, keeping the option open for an additional site if needed.

The PHREEQC model predicts that it is also possible for precipitates to form in the injection cocktail. In CRR Run 31, which was run under similar hydraulic conditions to CRR Run 32, but without bentonite colloids, it is thought that either americium radiocolloids formed, or americium sorbed to natural colloids in Grimsel groundwater. Although the initial bound fraction contained some significant uncertainty for americium in CRR Run 31 (measured between 6 and 51%), this was much higher than expected (Möri et al., 2004), which indicates that some americium was in colloidal form during the experiment despite the lack of bentonite colloids. The americium recovery was also higher (40%) than expected (Möri et al., 2004). In CRR Run 31, americium breakthrough (and plutonium and thorium) was approximately 10 minutes earlier than iodine-131, uranium and neptunium. Earlier breakthrough of these species was also observed in CRR Run 32 (Möri et al., 2004), which is believed to be caused by the colloids undergoing size exclusion, and indicating that americium underwent similar transport and retardation processes in both CRR Run 31 and 32. It is possible that any precipitates that formed in CRR Run 32 or CFM Run 13-05 were transported as if they were colloid bound. Unfortunately, imaging of the injection cocktails has not been carried out, and therefore it cannot be confirmed whether precipitates had formed. Because of this, it was decided to model americium self-colloids with the same

processes as if they were sorbing to the bentonite colloids, with its transport being controlled by colloid attachment and desorption kinetics.

Due to the high initial bound fraction for americium, it was decided that only 'colloid-bound' americium would be observed in the breakthrough curve data. In the transport model, a large equilibrium sorption retardation factor ( $R = 1000$ ), was used so that aqueous americium did not breakthrough during experimental timescales. Similarly large parameters were used in previous models of the CFM migration experiments (Noseck et al., 2016); however there is a lack of experimental data to confirm that no aqueous americium breaks through in this current data. Ideally, samples taken from the abstraction borehole would have also been centrifuged to determine an 'end bound fraction' and further investigation to determine the colloidal form of each radionuclide (if self-colloids could have formed), but this was not carried out.

There is some experimental evidence of slower sorption during batch experiments investigating americium sorption to Grimsel granodiorite and fracture fill material, as during the experiments of Missana and Geckeis (2006) sorption equilibrium had not been reached in experiments lasting 2 weeks, but still resulting in relatively high  $K_d$  values ( $10^3$  L/kg). However, as this model assumes that no aqueous americium is observed in the ICP-MS data used to calibrate americium breakthrough, the slow sorption kinetics are not added into the model.

### 6.2.2. Transport Model setup

Equations for colloid transport and attachment (Equation 4.3, Equation 4.4 and Equation 4.5), aqueous americium transport (Equation 4.6), americium sorbed to mobile (Equation 4.7) and immobile colloids (Equation 4.8 and Equation 4.9) were solved simultaneously using the COMSOL time dependent solver. All settings and boundary and initial conditions are kept as described in Chapter 4. The source term in the model used the concentration removed from solution (the bound fraction) as the initial concentration for the americium sorbed to mobile colloids boundary condition, with the remaining concentration being used for the initial concentration of aqueous americium.

Non calibration parameters used in the previous chapter (Table 5.1) are kept the same, as are the parameters calibrated in the models of conservative tracer and colloid breakthrough (Table 5.3 and Table 5.5). Table 6.3 shows the non-calibration parameters for americium transport.

Parameter	Symbol	CFM Run 13-05	CRR Run 32	Justification
Radioactive decay constant	$\lambda_d$	$2.98 \times 10^{-12}$ (1/s)	$5.08 \times 10^{-11}$ (1/s)	Based on isotope values
Bound Fraction		99.6%	99%	Experimentally measured
Unbound Fraction		0.4%	1%	Experimentally measured

Table 6.3 Non-calibration parameters for americium model

The calibration parameters are the sorption and desorption rate constants for americium to mobile colloids ( $k_{amc}$  and  $k_{mca}$ ), the desorption rate constant from immobile colloids ( $k_{ica}$  and  $k_{icai}$ ), and the aqueous phase retardation factor (R). The desorption rate from immobile colloids were initially set to be the same as the desorption rate from mobile colloids. This is a relatively restricted set of freedoms, so that this model is testing the

conceptual model of the relevant processes for americium transport in the two migration experiments.

### **6.2.3. Model Results**

Figure 6.5 shows the calibrated breakthrough curves for americium in CFM Run 13-05 and CRR Run 32, using the same processes and sorption and desorption rate constants in both experiments, as given in Table 6.4. The results of each model calibration are discussed further in the following sections.

During model calibration it was observed that americium breakthrough was insensitive to changes in sorption rate to mobile colloids, unless at very high values ( $\sim 1 \text{ m}^3/\text{kg}\cdot\text{s}$  or  $3600 \text{ m}^3/\text{kg}\cdot\text{h}$ ), due to the large initial bound fraction in both experiments and the use of the high aqueous retardation factor. Although the sorption rate has been included in Table 6.4 as a calibration parameter, it was not changed from the initial value used in the model. In addition, the model only includes a single sorption site on the colloid; this was not changed during model calibration.

It is important to note that the high retardation factor given in Table 6.4 ( $>1000$ ) is specified as it was the minimum value that resulted in no breakthrough of aqueous americium in either migration experiment, however the actual retardation factor could be a different value, but without breakthrough data for aqueous americium this parameter could not be calibrated further.

Parameter	Symbol	CFM Run 13-05	CRR Run 32
Sorption rate to mobile colloids	$k_{amc}$	$5.89 \times 10^{-5} \text{ m}^3/\text{kg}\cdot\text{s}$ ( $0.21 \text{ m}^3/\text{kg}\cdot\text{hr}$ )	
Desorption rate from mobile colloids	$k_{mca}$	$4.53 \times 10^{-6} \text{ 1/s}$ ( $0.016 \text{ h}^{-1}$ )	
Desorption rate from immobile colloids	$k_{ica}/k_{icai}$	$4.53 \times 10^{-6} \text{ 1/s}$ ( $0.016 \text{ h}^{-1}$ )	
Aqueous phase retardation factor	R	$>1000$ (-)	

Table 6.4 Calibration parameters resulting from model calibration to americium transport

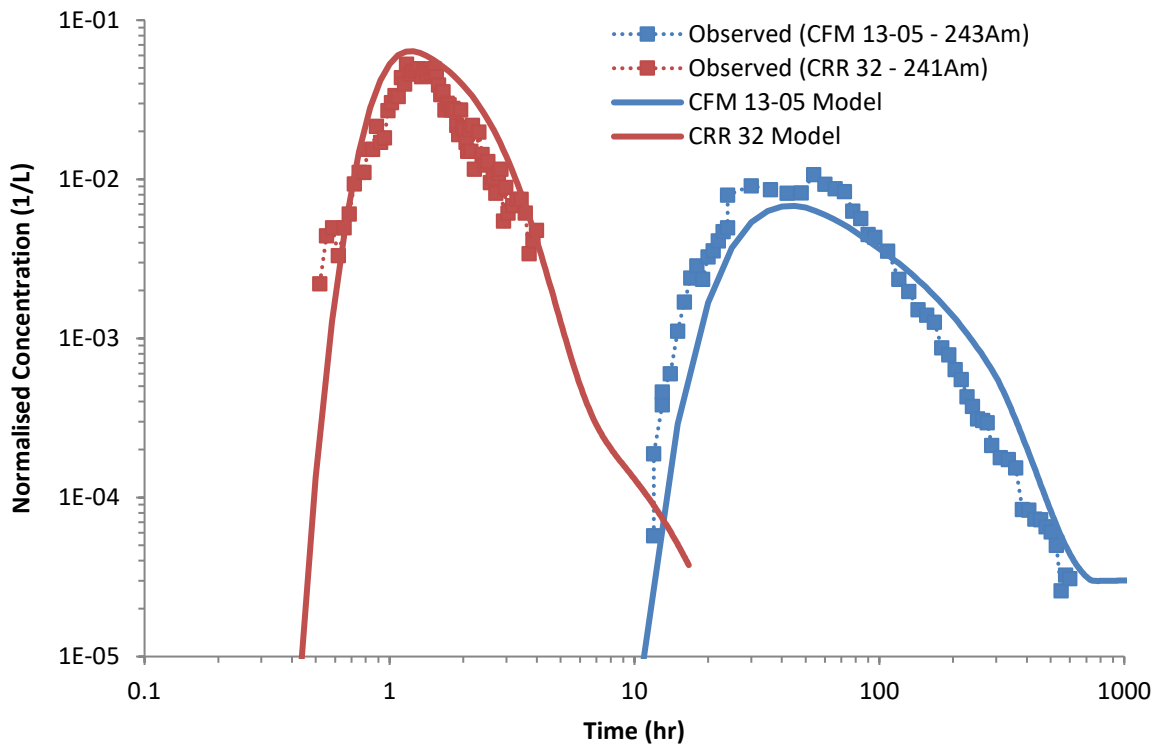


Figure 6.5 Calibrated breakthrough curves for americium in CFM Run 13-05 and CRR Run 32

### CFM Run 13-05

Figure 6.6 shows the modelled breakthrough for  $^{243}\text{Am}$  on a linear scale in CFM Run 13-05, with a comparison of the observed and modelled cumulative recovery shown in Figure 6.7. The breakthrough curve is similar to the colloid breakthrough from the previous chapter, which is expected as the model assumes americium transport is largely controlled by colloid transport processes. The modelled peak concentration is lower than the experimental data, but the falling limb of the breakthrough curve is higher than the

experimental data. This was also the case for the colloid breakthrough calibration described in the previous chapter and the errors from that model calibration have been carried forward here. Despite this, the modelled recovery (24%) compares extremely well to the experimental recovery of 25%. It is likely that the model match for americium would be improved by reducing any error from the model calibration for colloid breakthrough described in the previous chapter.

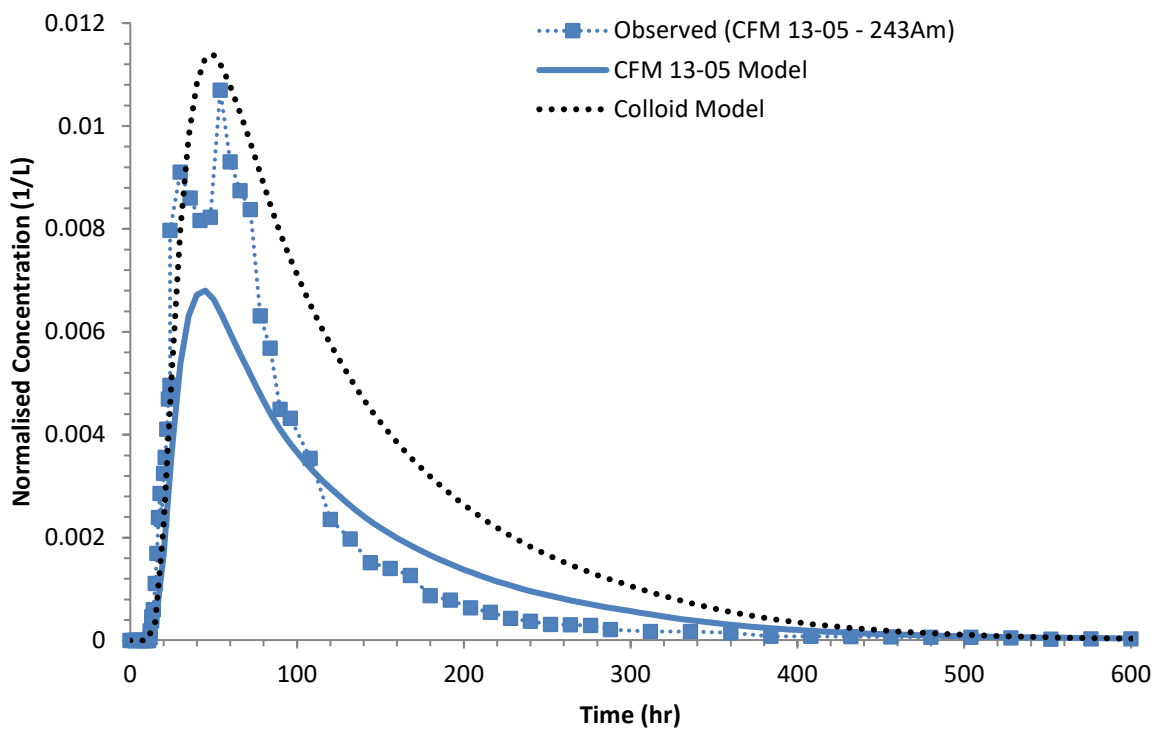


Figure 6.6 Calibrated breakthrough curve for  $^{243}\text{Am}$  in CFM Run 13-05. Includes the modelled colloid breakthrough for comparison, dotted black line.

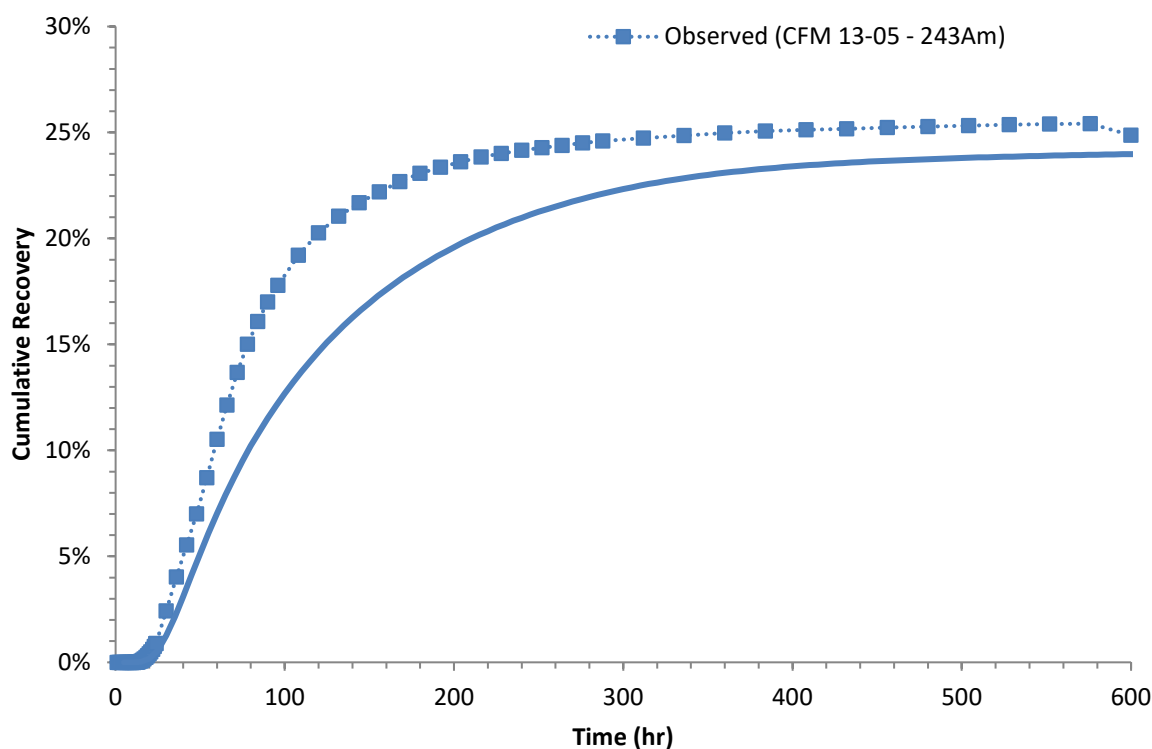


Figure 6.7 Comparison of cumulative recovery for observed and modelled data for  $^{243}\text{Am}$  in CFM Run 13-05

### ***CRR Run 32***

Figure 6.8 shows the calibrated breakthrough of  $^{241}\text{Am}$  in CRR Run 32 on a linear scale, with Figure 6.9 showing a comparison of modelled and observed cumulative recovery. Peak concentration in the model is slightly higher than the experimental data; this is due to error carried through from the colloid breakthrough calibration in the previous chapter.

The modelled recovery (87%) is higher than the experimental recovery (70%), measured by  $\alpha$ -spectroscopy analysed as a pair with plutonium-238 (Möri et al., 2004). Recovery could not be measured using ICP-MS in CRR Run 32 due to scatter in the experimental data. As the model was calibrated against the ICP-MS data, this provides some uncertainty in the experimental recovery data as the  $\alpha$ -spectroscopy data assumes that americium and plutonium had the same recovery values.

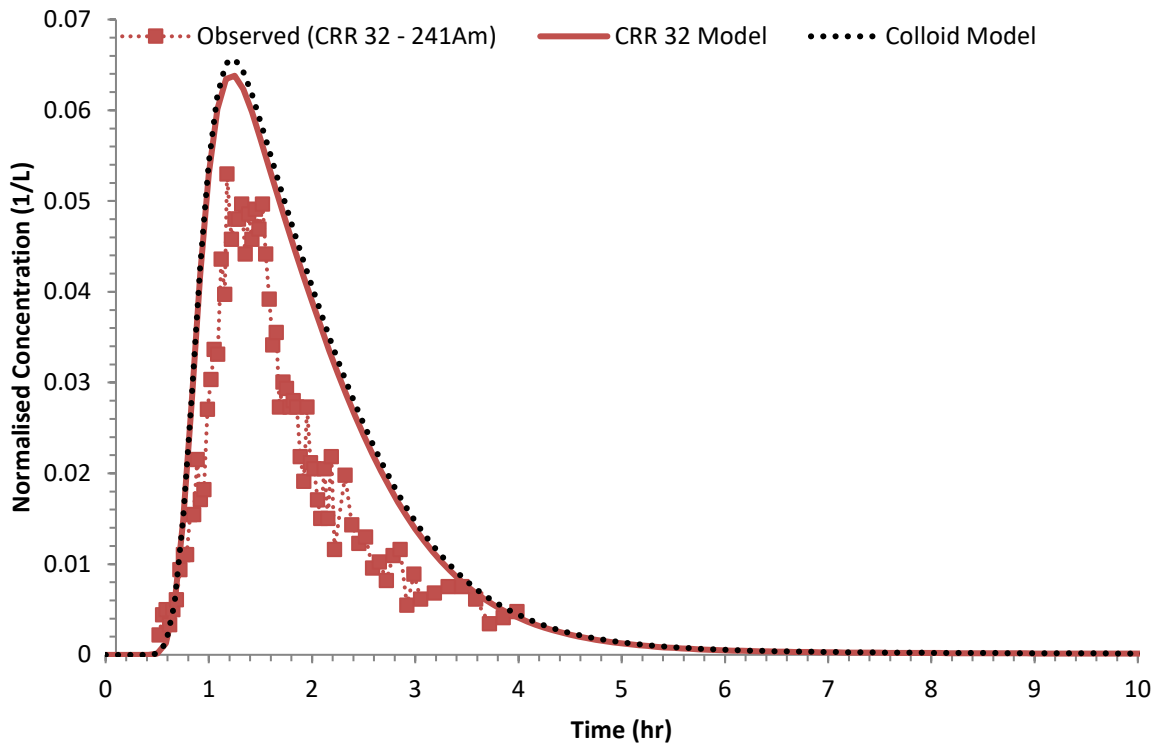


Figure 6.8 Calibrated breakthrough curve for  $^{241}\text{Am}$  in CRR Run 32. Includes the modelled colloid breakthrough for comparison, dotted black line.

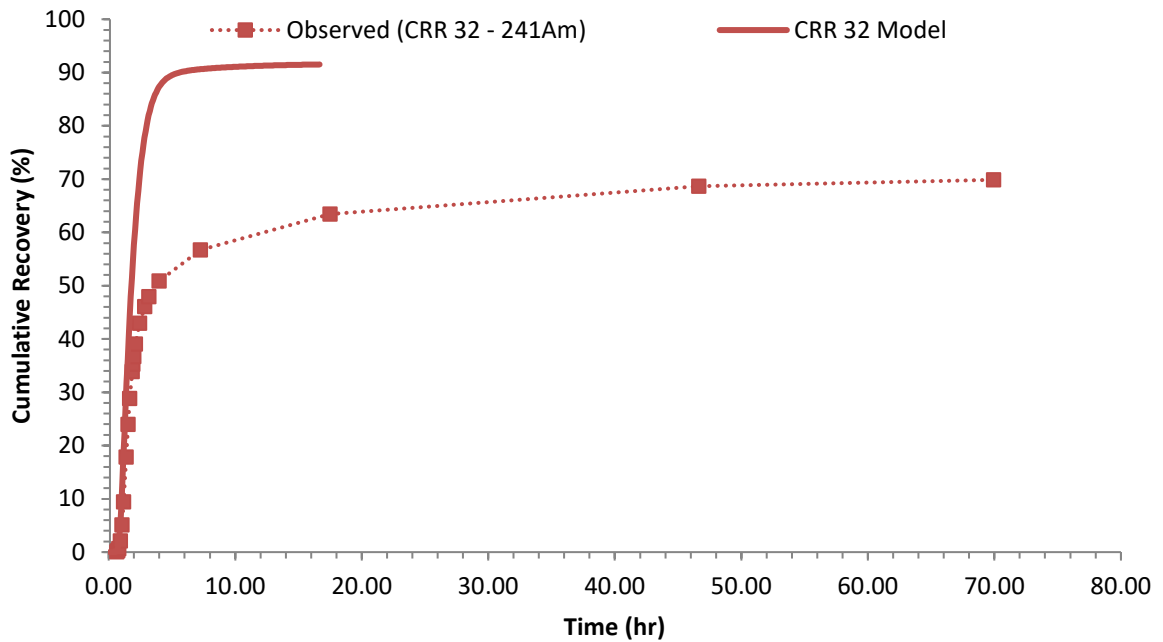


Figure 6.9 Comparison of cumulative recovery for observed and modelled data for  $^{241}\text{Am}$  in CRR Run 32. Note that the modelled data was compared to the ICP-MS data, but the observed recovery used the  $\alpha$ -spectroscopy data, analysed in a pair with  $^{238}\text{Pu}$  due to issues calculating recovery with ICP-MS.

Improvements to the model results for americium again could have been made if the colloid attachment rates had been altered, reducing the error from the colloid breakthrough calibration. Alternatively, the desorption rate for americium from mobile colloids could be increased to improve the model fit. This has not been carried out as the main cause of the higher modelled recovery is likely to be the colloid breakthrough from the previous chapter, and as there is some uncertainty in the  $\alpha$ -spectroscopy recovery data as it has been measured in a pair with plutonium (Möri et al., 2004). In addition, precipitation of self-colloids could not be discounted, and a measurement of the 'final bound fraction' and determination of the form of the colloidal americium would be useful to constrain model calibration further.

#### **6.2.4. Discussion and Conclusions**

Colloid transport and attachment are key processes controlling americium transport in CFM Run 13-05 and CRR Run 32, with desorption from the colloids forming a key rate control on americium recovery. This assumes that any self-colloids that have formed in the injection cocktail are transported with similar processes.

It is possible to compare both sorption and desorption rates used in this model with other models and experimental data from column and batch experiments involving americium and bentonite colloids. The desorption rate constant used here ( $0.016 \text{ h}^{-1}$ ) is the same rate as used in the LANL model, and is similar to the GRS ( $0.02 \text{ h}^{-1}$ ) and KTH ( $0.025 \text{ h}^{-1}$ ) models of americium in CFM Run 12-02 (Noseck et al., 2016). Similar desorption rates were used in LANL modelling of CRR and CFM migration experiments, which varied between 0 and  $0.29 \text{ h}^{-1}$  depending on the experiment (Reimus, 2016). These models all made the same

assumption with aqueous americium, applying high sorption rates to the rock surfaces/ fracture fill material. Unlike the previous models, which used different desorption rates (and sometimes different descriptions of desorption) to describe americium or other trivalent homologue transport in different experiments, this model used the same desorption rate in the two experiments.

The desorption rate used in this model is an order of magnitude larger than the desorption rate derived from modelling batch experiments investigating desorption kinetics of americium from FEBEX bentonite colloids (which varied between  $0.0037\text{h}^{-1}$  and  $0.009\text{h}^{-1}$ ) (Huber et al., 2011). The modelled desorption rate is also higher than desorption rates from similar batch experiments with artificially labelled Zn- or Ni- montmorillonite colloids ( $0.0012\text{h}^{-1}$ ) (Huber et al., 2015). Modelling of column experiments with Grimsel FFM, americium and FEBEX bentonite colloids used desorption rates between  $0.091$  and  $0.098\text{h}^{-1}$  (Dittrich et al., 2015), which is almost a magnitude higher than the desorption rate used in this model. The differing desorption rates are due to different solid: liquid ratios in the different experiments. A higher solid: liquid ratio was used in the column experiments of Dittrich et al. (2015) than the batch experiments of Huber et al. (2011, 2015), and when normalised to mass to solution ratio the desorption rates are in good agreement (Dittrich et al., 2015). The fact that the desorption rate used in this model falls between the different experiments demonstrates consistency with the laboratory data, with the differences caused by the different mass to solution ratio in the laboratory and field experiments.

The desorption rate for americium from both mobile and immobile colloids are the same value in this model as different rates were not set as there is limited evidence that

these desorption rates would be different. In addition, different desorption rates for mobile and immobile colloids were not used in previous models of CFM experiments (Noseck et al., 2016; Reimus, 2016).

The sorption rate to mobile colloids was found to have little impact on the americium breakthrough curve. This was also found by the previous models (Noseck et al., 2016; Reimus, 2016). This is unsurprising due to the high sorption rates used for aqueous americium to rock surfaces in each model. Direct comparisons between the different models show that the sorption rate used in this model ( $0.21 \text{ m}^3/\text{kg}\cdot\text{hr}$ ) are higher than the rates used to model CRR and CFM experiments ( $0.01\text{-}0.03 \text{ m}^3/\text{kg}\cdot\text{hr}$ ) (Reimus, 2016), but lower than the sorption rate ( $5.6 \text{ m}^3/\text{kg}\cdot\text{hr}$ ) used to calculate  $K_d$  values from models of CFM Run 12-02 in Noseck et al. (2016).

The high retardation factor used for aqueous americium ( $>1000$ ) is the minimum value that results in only colloid bound americium being predicted in the breakthrough curves, as shown in Figure 6.10. Longer term breakthrough curve data for CFM Run 13-05 (past 1000 hours after injection) showing aqueous americium breakthrough has been generated by measuring americium concentration using accelerator mass spectroscopy (AMS), (Quinto et al., 2017). However, this data were not available for calibration of this model, and so the retardation factor was kept at this value. Had this data been available, it would have been possible to include sorption kinetics of aqueous americium to fracture surfaces/ fill material instead of assuming equilibrium sorption, as has been done when modelling the AMS data from CFM Run 13-05 in other models (Lanyon and Blechschmidt, 2016), and to calibrate the breakthrough of aqueous americium.

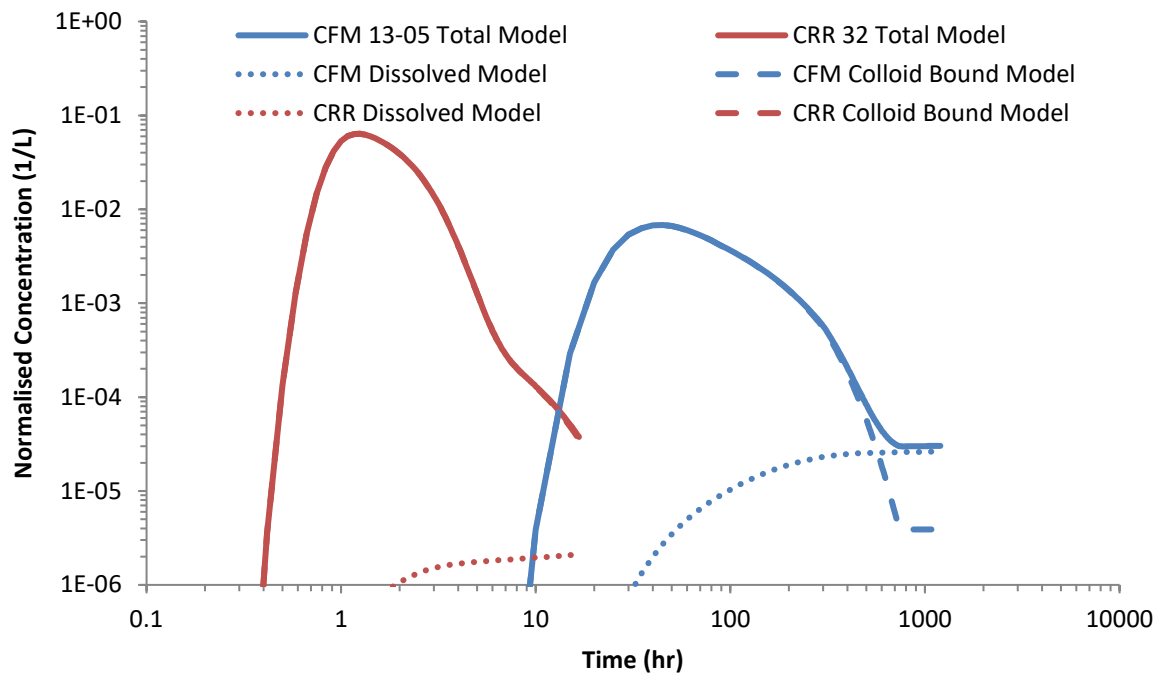


Figure 6.10 Breakthrough of aqueous and colloid bound americium in CFM Run 13-05 and CRR Run 32 (Solid = total; Dotted = aqueous phase; Dashed = colloid bound)

In summary, the model assumed that americium transport is controlled by colloid bound americium, and that any potential precipitates in the injection cocktail act as colloid bound americium. The model also assumed that aqueous americium is quickly and strongly sorbed to rock surfaces and therefore not observed in the current experimental dataset. The good model results for americium show that this conceptual model accurately describes americium transport in the two experiments using rate constants that are consistent in both experiments and using similar values to other models of the experiments and laboratory experiments.

### 6.3. Plutonium model calibration

Different plutonium isotopes were used in CFM Run 13-05 ( $^{242}\text{Pu}$ ) and CRR Run 32 ( $^{238}\text{Pu}$  and  $^{244}\text{Pu}$ ). The transport model assumes that the different isotopes have the same transport behaviour.  $^{244}\text{Pu}$  was modelled in CRR Run 32 as ICP-MS was used to measure its concentration ( $^{238}\text{Pu}$  was analysed by  $\alpha$ -spectroscopy in a pair with  $^{241}\text{Am}$ , which leads to uncertainty with the dataset as it assumes the two radionuclides are transported the same). The mass and concentration of the two plutonium isotopes is shown in Table 6.5. The high initial bound fractions measured at the beginning of the two experiments meant that the conceptual model used to describe americium transport in the previous section was also expected to be used for plutonium transport.

	<b>CFM Run 13-05:</b> $^{242}\text{Pu}$	<b>CRR Run 32:</b> $^{244}\text{Pu}$
Mass ( $M_0$ )	1.09 $\mu\text{g}$	0.164 $\mu\text{g}$
Concentration ( $C_0$ )	0.34 $\mu\text{g}/\text{l}^1$	1.64 $\mu\text{g}/\text{l}$
Initial bound fraction/ Mass removed by centrifugation	99.6%/ 1.08 $\mu\text{g}$	84%/ 0.14 $\mu\text{g}$
Cocktail equilibration time	35 days <sup>2</sup>	5 days
Colloid mass	Total: 224.3 mg	2.01 mg

1: Peak concentration in re-circulation circuit

2: Value measured after 401 days due to equipment problems

**Table 6.5 Mass and concentration of plutonium isotopes in CFM Run 13-05 and CRR Run 32**

#### 6.3.1. Conceptual Model

Geochemical modelling of the injection cocktail using PHREEQC (as detailed in Appendix A) provided information on the speciation, redox state and potential precipitates for plutonium in the two experiments. The speciation of plutonium in the injection cocktail of CFM Run 13-05 is shown in Figure 6.11, while Figure 6.12 shows speciation in CRR Run 32. Almost all of the plutonium is expected to be present as  $\text{Pu}(\text{OH})_4$  at pH 9.6. As this is a neutral species, less sorption would be expected to occur than for americium (which was

predicted to be both anion and cation species), although anionic sorption of the minor  $\text{Pu}(\text{CO}_3)_2(\text{OH})_2^{2-}$  species to the colloids would occur, potentially redistributing the concentrations of each species. Sorption of this species will be pH dependent, increasing at lower pH. Because of this, the method of plutonium addition to the injection cocktail (as acidic Pu(III) at a low pH and undergoing pH adjustment to match the pH of Grimsel groundwater (Schäfer, pers. Comm.), may have an important influence on sorption in the two experiments.

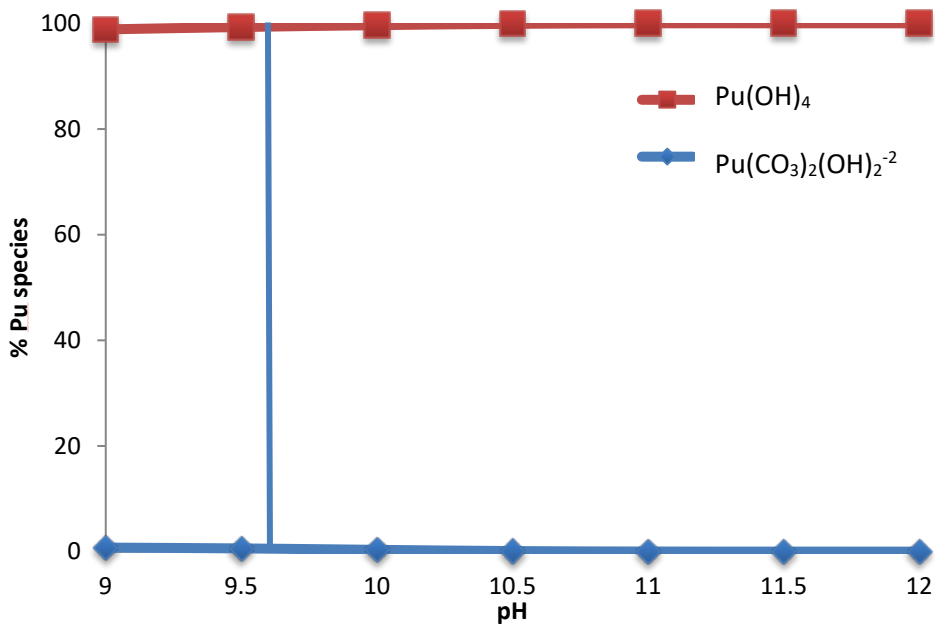


Figure 6.11 Speciation of plutonium in the CFM Run 13-05 injection cocktail as predicted by PHREEQC. Blue line = Grimsel groundwater pH (pH 9.6)

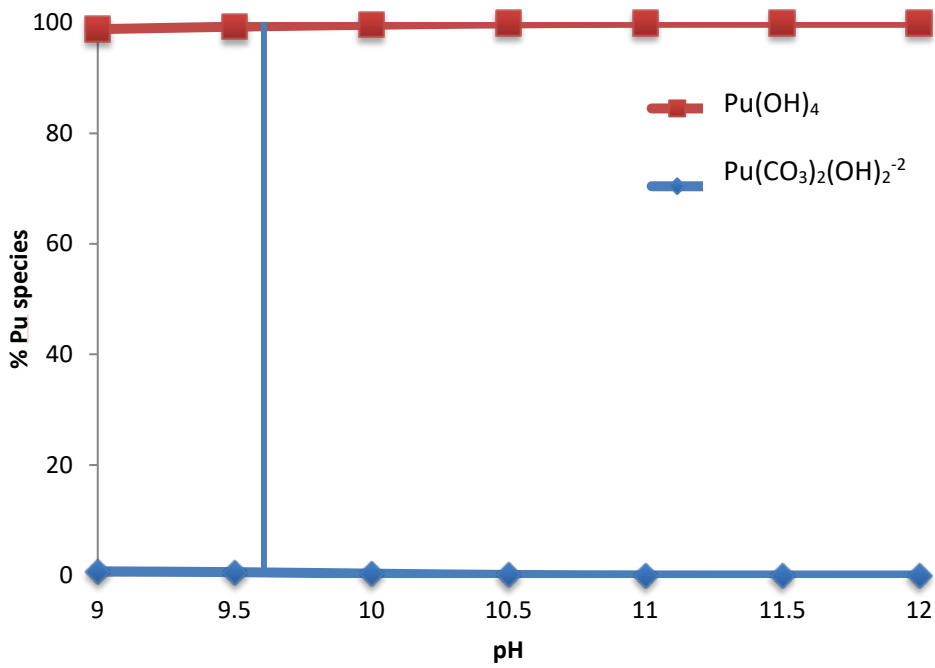


Figure 6.12 Speciation of plutonium in the CRR Run 32 injection cocktail as predicted by PHREEQC. Blue line = Grimsel groundwater pH (pH 9.6)

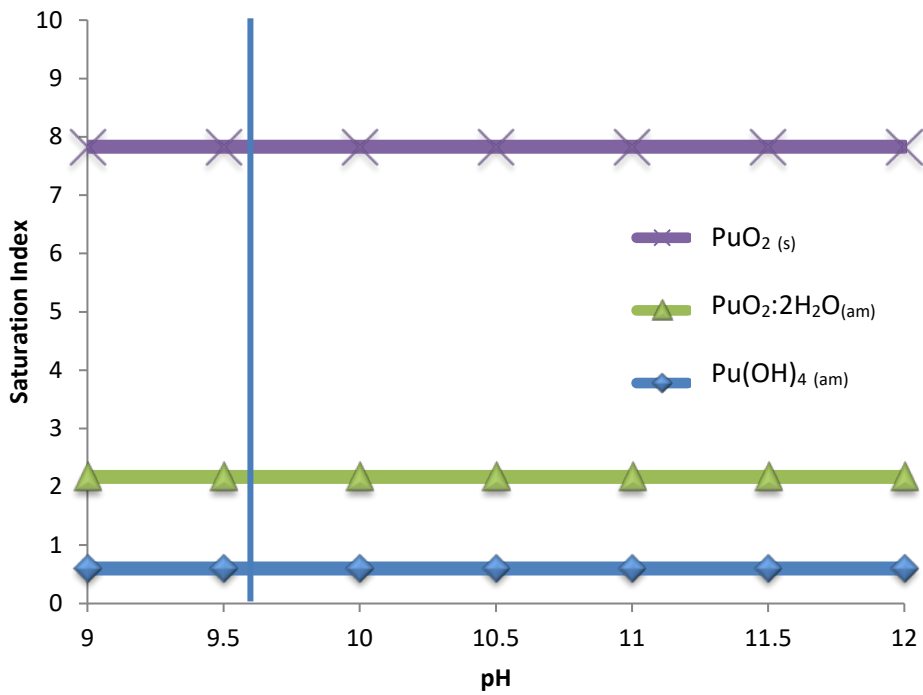


Figure 6.13 Predicted saturation indexes of plutonium precipitates in the injection cocktail of CFM Run 13-05 from PHREEQC. Blue line = pH 9.6 of reference Grimsel groundwater

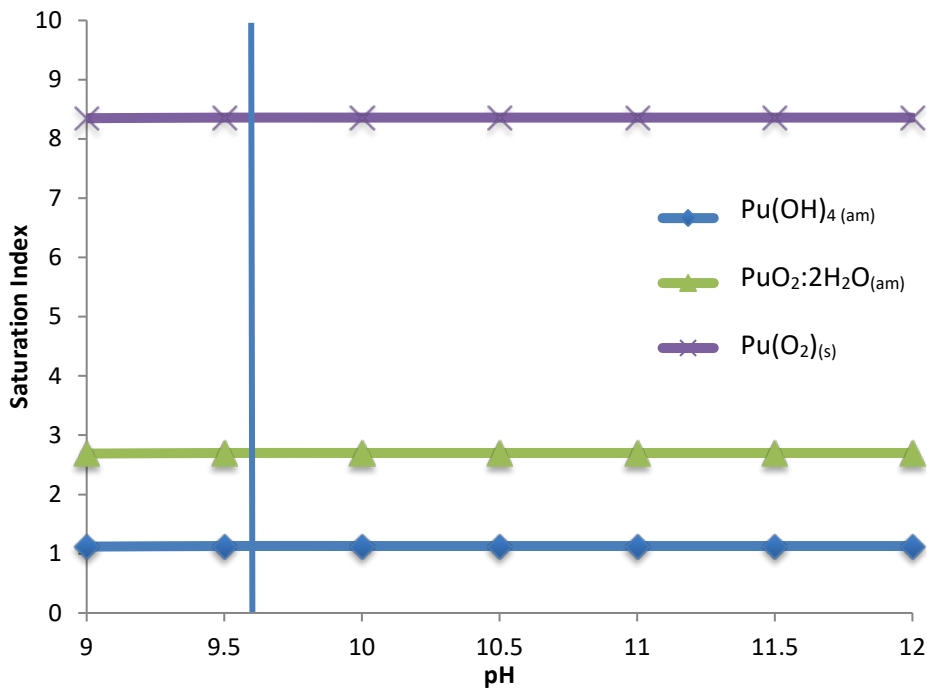


Figure 6.14 Predicted saturation indexes of plutonium precipitates in the injection cocktail of CRR Run 32 from PHREEQC. Blue line = pH 9.6 of reference Grimsel groundwater.

Figure 6.13 shows the predicted saturation indices for plutonium precipitates in the injection cocktail for CFM Run 13-05, and Figure 6.14 shows this for CRR Run 32. At the pH value of Grimsel groundwater in both experiments, PHREEQC predicts positive saturation indices for three potential precipitates PuO<sub>2(s)</sub>, PuO<sub>2</sub>:2H<sub>2</sub>O<sub>(am)</sub>, and Pu(OH)<sub>4(am)</sub>. Slightly higher saturation indices are present in CRR Run 32 than CFM Run 13-05; this is likely to be due to the higher Pu concentration used in this experiment.

A similar conceptual model to americium can be applied to plutonium in the experiments. Plutonium can be present in more redox states than americium (between Pu (III) and Pu (V)), which is important as the transport behaviour of plutonium changes depending on redox state (for instance Pu (V) undergoes weaker sorption to bentonite (Begg et al., 2015)). PHREEQC predicts that Pu (IV) is present in the injection cocktail, with a small amount of Pu (III) additionally present (<0.001%). This assumes that the Eh value in the

injection cocktails is close to the average found in reference Grimsel groundwater (Eh -220mV). Plutonium is initially added to the injection cocktail as acidic Pu (III), undergoing pH adjustment until it is expected to be present as Pu (IV) (Schäfer, pers. Comm.). One drawback of the PHREEQC model is that the colloid surfaces are not explicitly included, due to the large amount of data required to be collected. This means that the model will not include processes such as surface-mediated reduction, which has been observed for Pu(IV) to Pu(III) at illite surfaces (Banik et al., 2016), and for Pu(V) to Pu(IV) on montmorillonite surfaces (Zavarin et al., 2012), albeit at lower pH than Grimsel groundwater. As PHREEQC assumes thermodynamic equilibrium, does not consider different pH values used in cocktail preparation, and surface-mediated reduction, it is possible that larger concentrations of plutonium could be present as Pu(III) (or Pu(V)) than predicted by PHREEQC.

In both experiments, large amounts of plutonium have been removed from solution when centrifuged, giving high initial bound fractions.  $K_d$  values for plutonium sorption to bentonite colloids are in the order of  $10^5$  L/kg (Missana and Geckeis, 2006), and it is traditionally thought that the high initial bound fraction is caused by sorption. In this case, the different initial bound fractions could be caused by the different times between radionuclide spiking and the experiment (5 days for CRR Run 32; 35 days for CFM Run 13-05, although the initial bound fraction was measured after 401 days), allowing for more sorption to occur in CFM Run 13-05. Experiments testing Pu(IV) sorption to FEBEX bentonite found that it took up to 100 days for sorption equilibrium to be reached (Begg et al., 2015), which was due to the reduction of Pu(V) to Pu(IV). It is possible that redox processes in the injection cocktail act as a rate limiting step for sorption to the colloids (Missana and Geckeis, 2006).

PHREEQC predicts positive saturation indices for a number of plutonium solid phases in the injection cocktail. This is despite lower concentrations of plutonium being used in the injection cocktail ( $\sim 10^9$  M) than laboratory experiments where precipitation reactions were previously noted ( $>10^8$  M) (Missana et al., 2008; Begg et al., 2015; Huber et al., 2011). However, in CRR Run 31 (which did not include bentonite colloids) higher than expected initial bound fractions (5-58%) and recovery of plutonium ( $\sim 40\%$ ) is thought to be caused by the precipitation of self-colloids in the injection cocktail (although sorption to natural colloids could have also occurred) (Möri et al., 2004). As the plutonium concentration used in CRR Run 31 is similar, self-colloids could have formed in CRR Run 32 or CFM Run 13-05.

Imaging of the injection cocktail has not been carried out; therefore it has not been possible to confirm whether any precipitates formed. Because of this, plutonium is modelled as if the initial bound fraction is caused by sorption and plutonium transport is controlled by colloid processes and desorption kinetics, assuming that any plutonium self-colloids were transported by similar processes.

Multiple types of sorption site will be present on a bentonite colloid, and descriptions of multiple sites have been used in the LANL model for plutonium in CFM Run 12-02 (Noseck et al., 2016). However the same model used different descriptions for the same tetravalent homologues between previous CFM experiments (i.e. including multiple sorption sites in particular experiments only). Two-site models were also used for plutonium/montmorillonite colloid laboratory experiments (Begg et al., 2017). Other models of the CFM and CRR experiments (Chapter 3) were able reproduce plutonium breakthrough using a

single sorption site on the bentonite colloids. For this model, it was decided to initially use a single sorption site on the bentonite colloids and then add an additional site if necessary.

Finally, the model assumed that only ‘colloid-bound’ plutonium would be observed in the breakthrough curves of both experiments, as aqueous plutonium was expected to undergo strong sorption to the Grimsel FFM and granodiorite ( $K_d$  values for FFM  $\sim 10^2$  L/kg). As was included for americium, a large retardation factor was included ( $\sim 1000$ ) for aqueous plutonium.

### 6.3.2. Transport Model setup

The same model set up as used for americium (see previous section) was used for plutonium, with the non-calibration parameters for plutonium shown in Table 6.6. The calibration parameters were: sorption and desorption rate constants for plutonium to mobile colloids ( $k_{amc}$  and  $k_{mca}$ ), desorption rate constants from immobile colloids ( $k_{ica}$  and  $k_{cai}$ ) and the aqueous phase retardation factor ( $R$ ). The desorption rate for mobile and immobile colloids were initially set to be the same.

Parameter	Symbol	CFM Run 13-05	CRR Run 32	Justification
Radioactive decay constant	$\lambda_d$	$5.88 \times 10^{-14}$ (1/s)	$2.75 \times 10^{-16}$ (1/s)	Based on isotope value
Bound Fraction		99.6%	84%	Experimentally measured
Unbound Fraction		0.4%	16%	Experimentally measured

Table 6.6 Non-calibration parameters for plutonium model

### 6.3.3. Model Results

Figure 6.15 shows the calibrated breakthrough curves for plutonium transport in both CFM Run 13-05 and CRR Run 32. Table 6.7 shows the calibration parameters used in the

model, and shows that consistent parameters were used to model both experiments. The results of the model calibration are discussed further in the following sections.

Parameter	Symbol	CFM Run 13-05	CRR Run 32
Sorption rate to mobile colloids	$k_{amc}$	$1 \times 10^{-8} \text{ m}^3/\text{kg}\cdot\text{s}$ ( $3.6 \times 10^{-5} \text{ m}^3/\text{kg}\cdot\text{hr}$ )	
Desorption rate from mobile colloids	$k_{mca}$	$1 \times 10^{-6} \text{ s}^{-1}$ ( $0.0036 \text{ h}^{-1}$ )	
Desorption rate from immobile colloids	$k_{ica}/k_{icai}$	$1 \times 10^{-6} \text{ s}^{-1}$ ( $0.0036 \text{ h}^{-1}$ )	
Aqueous phase retardation factor	R	>1000 (-)	

Table 6.7 Calibration parameters resulting from model calibration to plutonium transport

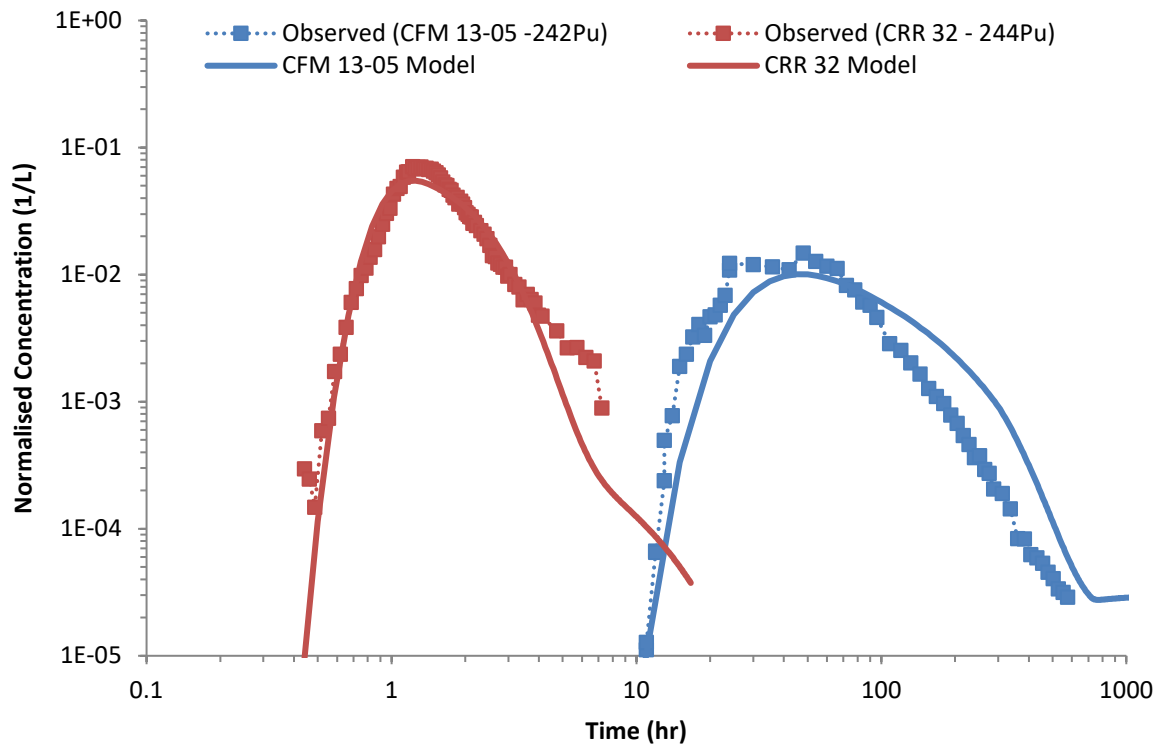


Figure 6.15 Calibrated breakthrough curves for plutonium in CFM Run 13-05 and CRR Run 32

Although included as a calibration parameter, changes to the sorption rate to bentonite colloids had limited impact to the breakthrough curve, apart from at high values (this was also the case for americium), and so was not changed from the initial value. This is

expected due to the high initial bound fraction and the use of the high aqueous retardation factor.

Although other models of plutonium transport have used multiple sorption sites on the colloid (the LANL model in Noseck et al., (2016)), a further sorption site was not included in this model as it was thought not be needed to improve model calibration.

#### ***CFM Run 13-05***

Figure 6.16 shows the results of the model calibration for  $^{242}\text{Pu}$  in CFM Run 13-05 on a linear scale, with a comparison of the modelled and observed cumulative recovery shown in Figure 6.17. The modelled recovery of 38% is higher than the measured experimental recovery of 28%. The modelled breakthrough has a good match to the rising limb of the breakthrough curve, the model has a lower peak breakthrough than the experimental data, and has higher values on the falling limb of the breakthrough curve. These differences are likely caused by the error carried forward from the colloid breakthrough calibration described in the previous chapter. It is likely that an improvement to the colloid breakthrough data from the previous chapter would also improve the model fit to the plutonium data.

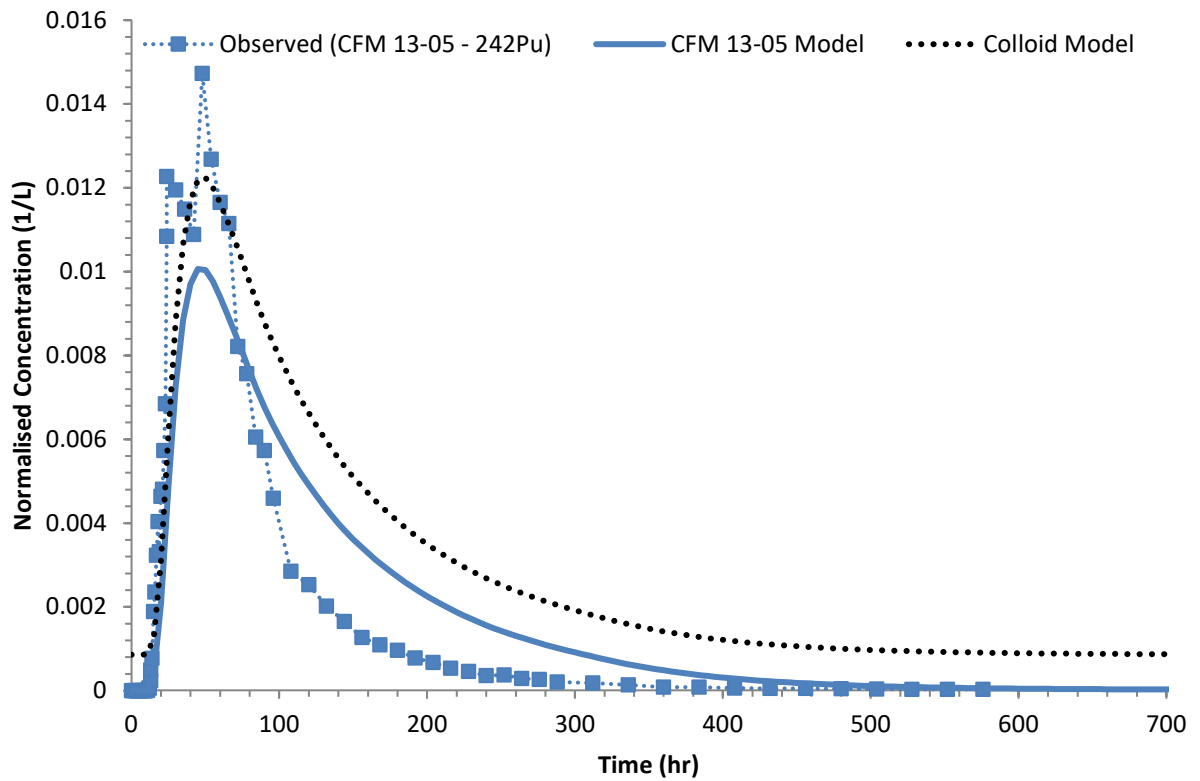


Figure 6.16 Calibrated breakthrough curve for  $^{242}\text{Pu}$  in CFM Run 13-05. Includes the modelled colloid breakthrough for comparison, dotted black line.

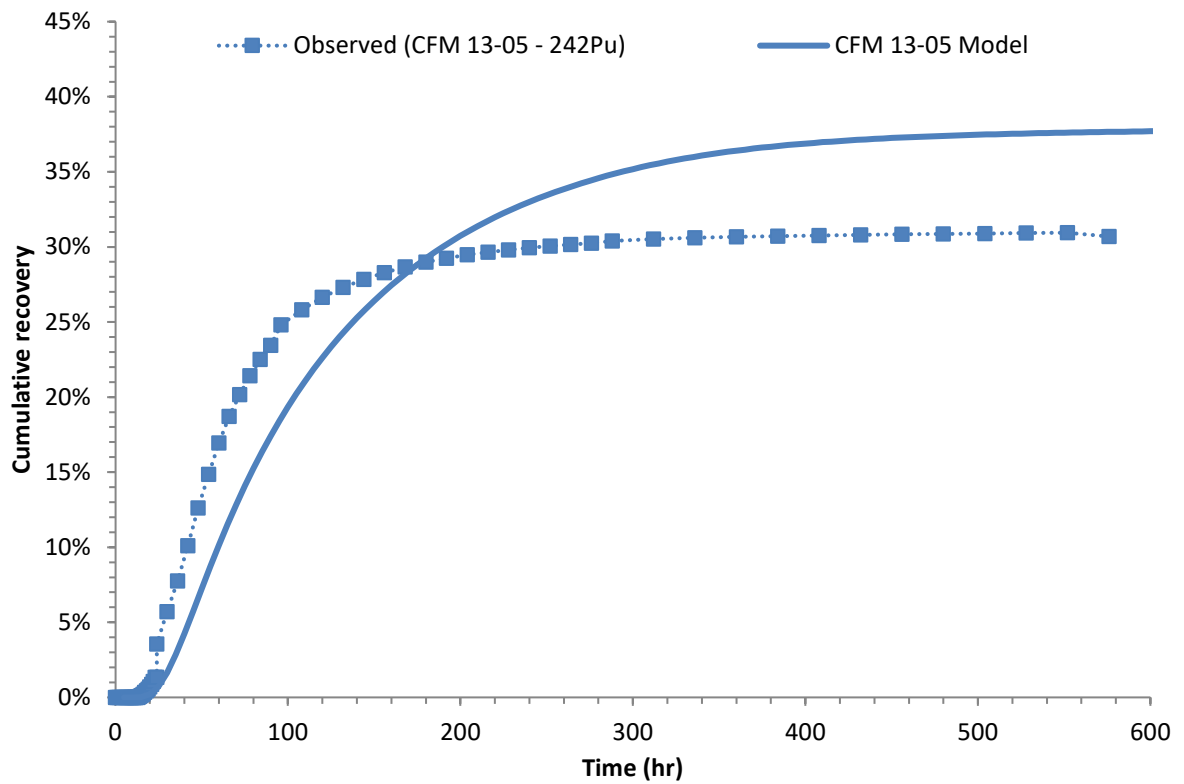


Figure 6.17 Comparison of cumulative recovery between observed and modelled data for  $^{242}\text{Pu}$  in CFM Run 13-05

### CRR Run 32

Figure 6.18 shows the results of the model calibration for  $^{244}\text{Pu}$  in CRR Run 32 on a linear scale, with a comparison of modelled and observed cumulative recovery shown in Figure 6.19. The model match produced a lower peak breakthrough than the experimental data, but produced good matches to both the rising and falling limbs of the breakthrough curve. The modelled recovery (78%) is lower than the experimental recovery (86%), as measured using ICP-MS (Möri et al., 2004), although is higher than the recovery of  $^{238}\text{Pu}$  measured by  $\alpha$ -spectroscopy (70%). An improvement to the model fit would have most likely resulted in different desorption rates or processes being used in the two experiments, and for this reason, has not been carried out.

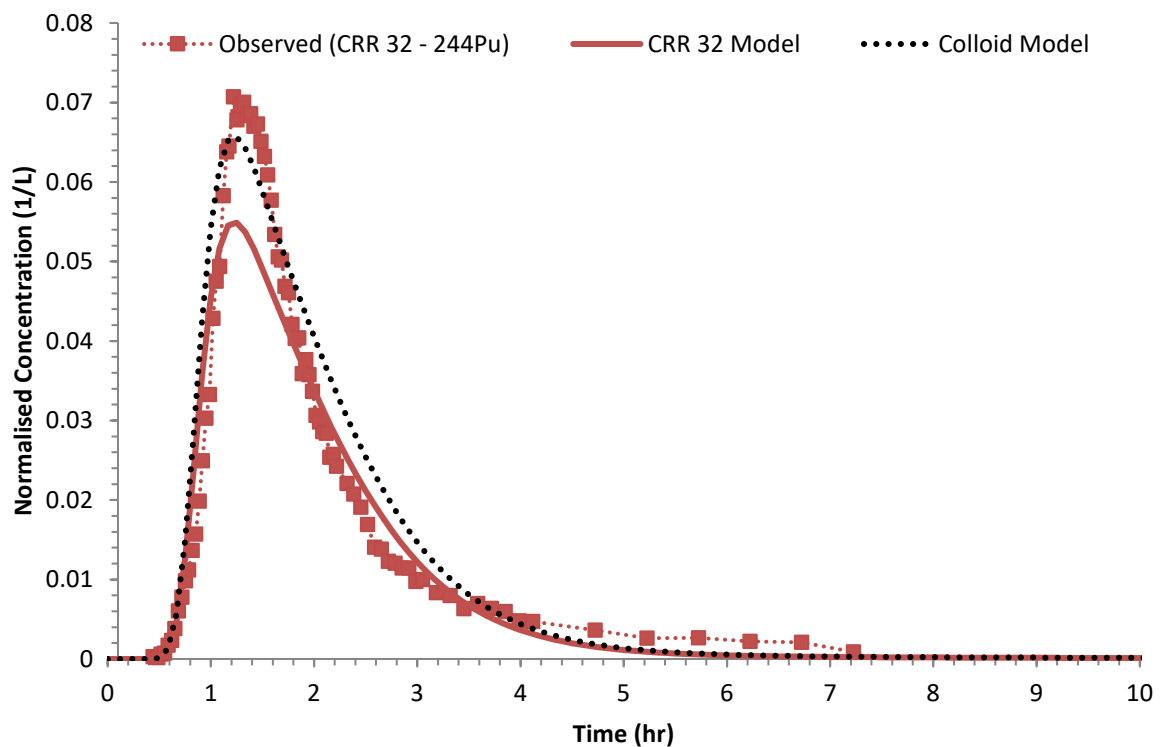


Figure 6.18 Calibrated breakthrough curve for  $^{244}\text{Pu}$  in CRR Run 32. Includes the modelled colloid breakthrough for comparison, dotted black line.

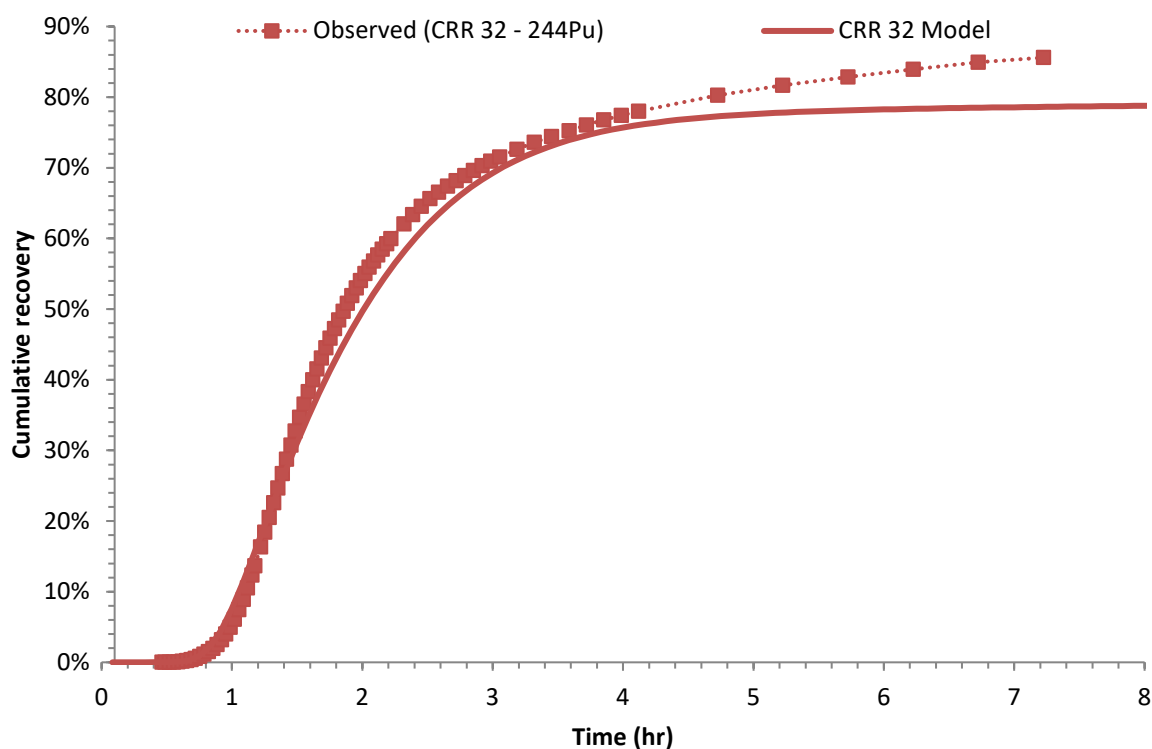


Figure 6.19 Comparison of cumulative recovery between observed and modelled data for  $^{244}\text{Pu}$  (measured by ICP-MS) in CRR Run 32

### 6.3.4. Discussion and Conclusions

As for americium, colloid transport and attachment processes are key controls on plutonium transport in both CFM Run 13-05 and CRR Run 32, and the desorption from the bentonite colloids forms a key control on plutonium recovery.

Comparing the desorption rate from bentonite colloids used in this model ( $0.0036 \text{ h}^{-1}$ ), the rate is smaller than rates used in models of plutonium transport in CFM Run 12-02, CFM Run 13-05 ( $0.01 \text{ h}^{-1}$ ), and CRR Run 32 ( $0.07 \text{ h}^{-1}$ ), as detailed in Reimus (2016). These models also used time-dependent desorption rates which varied with the experiment duration, however these had little chemical justification, as they were used to match the source term used in that model run. The lower end of the time dependent desorption rate used to model CFM Run 12-02 ( $0.005 \text{ h}^{-1}$ ) (Reimus, 2016), is close to the constant desorption

rate used in this model. The desorption rate used in this model ( $0.0036\text{h}^{-1}$ ) is slightly lower than the values used in the single site LANL model ( $0.0077\text{h}^{-1}$ ), the GRS ( $0.025\text{h}^{-1}$ ) and the KTH ( $0.035\text{h}^{-1}$ ) models of plutonium transport in CFM Run 12-02 (Noseck et al., 2016).

Results of batch desorption experiments carried out with plutonium and FEBEX bentonite were interpreted to give desorption rates between  $0.0014\text{h}^{-1}$  and  $0.0085\text{h}^{-1}$  depending on plutonium concentration (Huber et al., 2011). The desorption rate used in the model is between these two values, potentially due to the plutonium concentration in the two migration experiments being between the total plutonium concentrations used in the two laboratory experiments. Similar laboratory experiments using Ni-montmorillonite interpreted a desorption rate of  $0.0012\text{h}^{-1}$  (Huber et al., 2015), which is similar to the desorption rate used in this model.

PHREEQC predicts positive saturation indices for several solid plutonium phases, but it has not been possible to confirm whether these formed in the injection cocktail of the two experiments. The positive saturation indices are despite plutonium concentration being an order of magnitude lower than laboratory experiments where plutonium precipitation has been observed in similar redox conditions (Begg et al., 2015; Missana et al., 2008). The transport model assumed that any precipitates were transported during the migration experiments with the same processes as plutonium sorbed to the bentonite colloids. Further investigation in future migration experiments of the formation of precipitates, the 'final bound fraction' and determining the type of plutonium colloids would be useful to help test whether this assumption is valid and to help constrain the transport model for future migration experiments.

This model only included a single sorption site on the colloids, unlike some previous models (LANL model, Noseck et al. (2016)). Different sorption sites will be present due to the sheet silicate structure of the bentonite and montmorillonite, with sites present on both the edge and plane of the clay. Caesium shows non-linear sorption to bentonite clay due to the different sites (Missana et al., 2004) (see discussion in next chapter). However, for plutonium, linear sorption isotherms have been observed for Pu(IV) to bentonite (Begg et al., 2015; Missana et al., 2008) and montmorillonite (Begg et al., 2013), up to concentrations where precipitation reactions are observed. This indicates that plutonium sorption is the same for the different sites, or that plutonium sorption is not reaching limited site capacities as was found for caesium. Because of limited experimental data and evidence for multiple site sorption, and the fact that this model was able to reproduce plutonium breakthrough accurately using a single site, an additional site was not added to the model.

The model assumes that in the ICP-MS breakthrough data only colloid bound plutonium is observed, applying a large aqueous retardation factor ( $>1000$ ), which again represents the minimum value so that very limited concentrations of aqueous plutonium was modelled (as shown in Figure 6.20). Additional long term breakthrough data for plutonium in CFM Run 13-05 has been measured using AMS (Quinto et al., 2017), but the data was not available for model calibration. If this data was available, it would have been possible to calibrate aqueous plutonium breakthrough further, potentially including kinetic sorption of aqueous plutonium to rock surfaces/ fracture fill material as included in the GRS model of the AMS dataset (Lanyon and Blechschmidt, 2016).

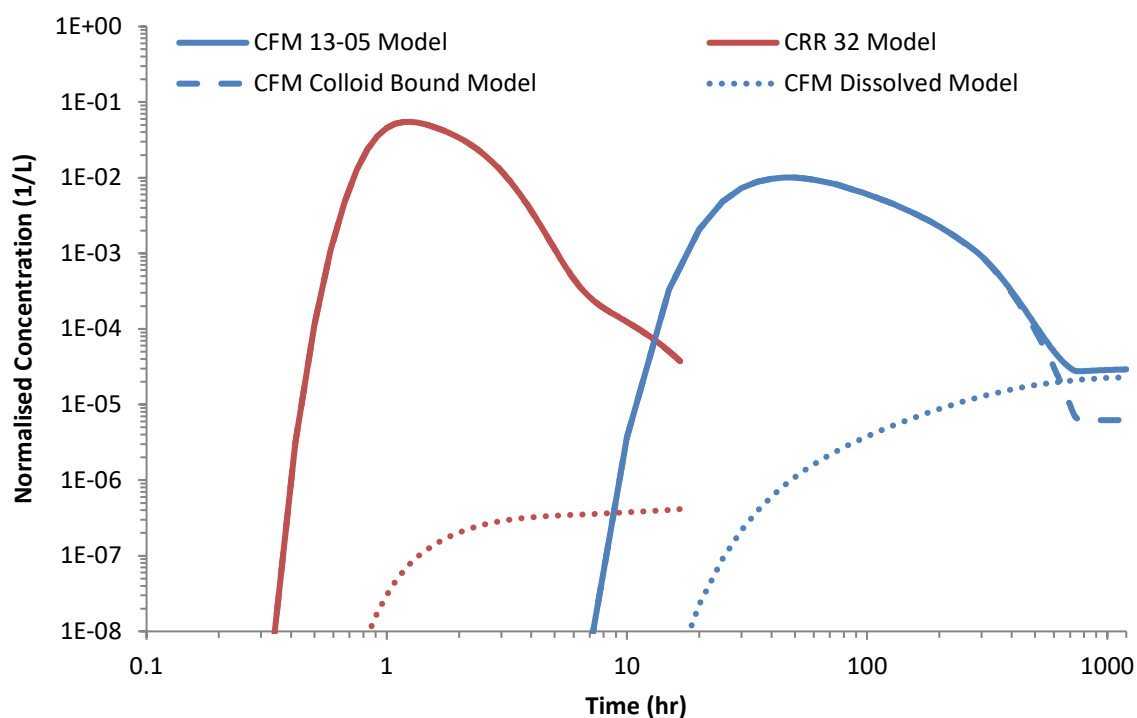


Figure 6.20 Contribution of aqueous and colloid bound plutonium in CFM Run 13-05 and CRR Run 32 (Solid = total concentration; Dotted = aqueous phase; Dashed = colloid bound)

In summary, the transport model assumed that plutonium underwent similar transport processes to americium, i.e. that transport is controlled by colloid-bound plutonium, and that aqueous plutonium quickly and strongly sorbed to rock surfaces/ FFM. In addition, any precipitates that formed in the injection cocktail acted as colloid bound plutonium. The good model matches for plutonium, using consistent parameters and descriptions, show that this conceptual model can be used to describe the transport of plutonium in both experiments accurately.

## 6.4. Summary

This chapter has presented the results of the calibration of the transport model for the breakthrough of americium and plutonium in CFM Run 13-05 and CRR Run 32. Supported by observations from laboratory experiments, previous models of the experiments and PHREEQC modelling, it has been possible to successfully model the transport of both

radionuclides using a similar conceptual model, using consistent parameters in the different experiments. Transport of these radionuclides in the two experiments is facilitated by the colloids, with the radionuclides sorbing to the colloids in the injection cocktail before both field experiments. Colloid transport and attachment are therefore important controls on the transport of americium and plutonium in the two experiments. The sorption of the two radionuclides to the colloids is not irreversible during the experiments, and the desorption rate is a key control on radionuclide recovery. Desorption rates used in this model are typically close to experimental data from laboratory batch and column experiments, or from other models of the CFM and CRR field experiments.

In both experiments geochemical modelling using PHREEQC predicts the formation of precipitates in the injection cocktail. The transport model assumes that these precipitates undergo the same processes (or can be represented by the same models) as a radionuclide sorbed to the bentonite colloids, as it has not been possible to confirm whether precipitates have formed in either experiment. As the model has been able to replicate the transport of the two radionuclides in both experiments, it is likely that these assumptions were valid, but further investigation is needed to determine whether the precipitates formed in the injection cocktail and whether they are transported by the same processes.

This transport model applied a large retardation factor ( $R > 1000$ ) to both aqueous americium and plutonium. This is consistent with the previous models of the CFM experiment, which applied large sorption rates to rock surfaces (Noseck et al., 2016; Reimus, 2016). In this model, the large retardation factor was applied so that the majority of the breakthrough of these radionuclides is caused by colloid bound radionuclide. There is limited

experimental evidence that this assumption is valid, and it would be useful in future migration experiments for a ‘final bound fraction’ measurement to be taken of samples abstracted from the shear zone. This measurement, along with a determination of the colloidal type if self-colloids could form, would help to constrain future model runs.

## 6.5. List of References

- Banik, N.L., Marsac, R., Luetzenkirchen, J., Diascorn, A., Bender, K., Marquardt, C.M. and Geckeis, H. (2016) Sorption and Redox Speciation of Plutonium at the Illite Surface. **Environmental Science & Technology**, 50 (January): 2092–2098 DOI: 10.1021/acs.est.5b05129
- Begg, J.D., Zavarin, M. and Kersting, A.B. (2017) Desorption of plutonium from montmorillonite: An experimental and modeling study. **Geochimica et Cosmochimica Acta** [online], 197: 278–293 DOI: 10.1016/j.gca.2016.10.006. Available from: <http://dx.doi.org/10.1016/j.gca.2016.10.006>
- Begg, J.D., Zavarin, M., Tumey, S.J. and Kersting, A.B. (2015) Plutonium sorption and desorption behavior on bentonite. **Journal of Environmental Radioactivity** [online], 141: 106–114 DOI: 10.1016/j.jenvrad.2014.12.002. Available from: <http://linkinghub.elsevier.com/retrieve/pii/S0265931X14003610>
- Begg, J.D., Zavarin, M., Zhao, P., Tumey, S.J., Powell, B. and Kersting, A.B. (2013) Pu(V) and Pu(IV) sorption to montmorillonite. **Environmental Science and Technology**, 47 (10): 5146–5153 DOI: 10.1021/es305257s
- Bennett, D.G. (2014) **SSM 2014:11 Radionuclide Solubility Limits in SKB’s Safety Case**. p. 62
- Dittrich, T.M., Boukhalfa, H., Ware, S.D. and Reimus, P.W. (2015) Laboratory investigation of the role of desorption kinetics on americium transport associated with bentonite colloids. **Journal of Environmental Radioactivity** [online], 148: 170–182 DOI: 10.1016/j.jenvrad.2015.07.001. Available from: <http://dx.doi.org/10.1016/j.jenvrad.2015.07.001>
- Giffaut, E., Grivé, M., Blanc, P., Vieillard, P., Colàs, E., Gailhanou, H., Gaboreau, S., Marty, N., Madé, B. and Duro, L. (2014) Andra thermodynamic database for performance assessment: ThermoChimie. **Applied Geochemistry** [online], 49: 225–236 DOI: 10.1016/j.apgeochem.2014.05.007. Available from: <http://dx.doi.org/10.1016/j.apgeochem.2014.05.007>
- Harvey, B.E., McMillan, L.A. and Herbert, A.W. (2017) “Modelling colloid-facilitated Americium transport at Grimsel Test site, Switzerland.” **In International High Level Radioactive Waste Management 2017. Charlotte, NC, USA. 2017**. American Nuclear Society. pp. 273–280
- Huber, F., Heck, S., Truche, L., Bouby, M., Brendle, J., Hoess, P. and Schäfer, T. (2015) Radionuclide desorption kinetics on synthetic Zn / Ni-labeled montmorillonite nanoparticles. **Geochimica et Cosmochimica Acta**, 148: 426–441 DOI: 10.1016/j.gca.2014.10.010
- Huber, F., Kunze, P., Geckeis, H. and Schäfer, T. (2011) Sorption reversibility kinetics in the ternary system radionuclide-bentonite colloids/nanoparticles-granite fracture filling material. **Applied Geochemistry** [online], 26 (12): 2226–2237 DOI: 10.1016/j.apgeochem.2011.08.005. Available from:

<http://dx.doi.org/10.1016/j.apgeochem.2011.08.005>

Lanyon, B. and Blechschmidt, I. (2016) **Nagra Aktennotiz AN16-102: Minutes of the CFM Modellers Workshop, 10-11 December 2015, San Francisco**. Wettingen, Switzerland

Missana, T., Alonso, Ú., García-Gutiérrez, M. and Mingarro, M. (2008) Role of bentonite colloids on europium and plutonium migration in a granite fracture. **Applied Geochemistry** [online], 23 (6): 1484–1497 DOI: 10.1016/j.apgeochem.2008.01.008. Available from: <http://linkinghub.elsevier.com/retrieve/pii/S0883292708000565> [Accessed 12 December 2014]

Missana, T., García-Gutiérrez, M. and Alonso, Ú. (2004) Kinetics and irreversibility of cesium and uranium sorption onto bentonite colloids in a deep granitic environment. **Applied Clay Science**, 26 (1–4 SPEC. ISS.): 137–150 DOI: 10.1016/j.clay.2003.09.008

Missana, T. and Geckeis, H. (2006) **Nagra Technical Bulletin NTB 03-02: CRR Final Project Report 2 - Supporting Laboratory Experiments with Radionuclides and Bentonite Colloids**. Wettingen, Switzerland

Möri, A., Alexander, W.R., Degueldre, C., Eikenberg, J., Fierz, T., Geckeis, H., Geier, F., Hauser, W., Schäfer, T. and Smith, P.A. (2004) **Nagra Technical Bulletin NTB 03-01: The CRR Final Project Report series 1 - Description of the Field Phase - Methodologies and Raw Data** [online]. Wettingen, Switzerland. Available from: <http://www.nagra.ch/en/cat/publikationen/technicalreports-ntbs/ntbs-2001-2012/downloadcentre.htm>

Noseck, U., Flügge, J., Reimus, P., Cvetkovic, V., Lanyon, B., Schäfer, T. and Blechschmidt, I. (2016) **Nagra Technical Report NTB 16-06: Colloid Formation and Migration Project: Modelling of tracer, colloid and radionuclide/homologue transport for dipole CFM 06.002- Pinkel surface packer**. Wettingen, Switzerland

Quinto, F., Blechschmidt, I., Garcia Perez, C., Geckeis, H., Geyer, F., Golser, R., Huber, F.M., Lagos, M., Lanyon, B., Plaschke, M., Steier, P., Schäfer, T., Perez, C.G., Geckeis, H., Geyer, F., Golser, R., Huber, F.M., Lagos, M., Lanyon, B., et al. (2017) Multi-actinide analysis with AMS for ultra-trace determination in small samples : application to an in situ radionuclide tracer test within the Colloid Formation and Migration (CFM) experiment at the Grimsel Test Site (GTS , Switzerland). **Analytical Chemistry**, 89 (13): 7182–7189 DOI: 10.1021/acs.analchem.7b01359

Reiche, T., Noseck, U. and Schäfer, T. (2015) Migration of Contaminants in Fractured-Porous Media in the Presence of Colloids: Effects of Kinetic Interactions. **Transport in Porous Media**, 111 (1): 143–170 DOI: 10.1007/s11242-015-0585-7

Reimus, P.W. (2016) **Nagra NAB 16-61: GTS Phase VI- CFM Phase 3: Interpretation of colloid-facilitated radionuclide transport experiments from the CRR and CFM projects**. Wettingen, Switzerland

Schäfer, T., Lanyon, B. and Blechschmidt, I. (2013) **CFM 13-05 Data Set**. pers comm.: Nagra/ KIT-INE (Unpublished Dataset)

Thoenen, T., Hummel, W., Berner, U. and Curti, E. (2014) **The PSI / Nagra Chemical Thermodynamic Database 12 / 07**. Villigen, Switzerland

Zavarin, M., Powell, B.A., Bourbin, M., Zhao, P. and Kersting, A.B. (2012) Np(V) and Pu(V) ion exchange and surface-mediated reduction mechanisms on montmorillonite. **Environmental Science and Technology**, 46 (5): 2692–2698 DOI: 10.1021/es203505g

## **7. MODELLING THE TRANSPORT OF CAESIUM, URANIUM AND NEPTUNIUM IN CFM RUN 13-05 AND CRR RUN 32**

### **7.1. Introduction**

This chapter details the modelling of caesium, uranium and neptunium in two field migration experiments carried out at the Grimsel Test Site, CFM Run 13-05 and CRR Run 32. This was carried out using the transport model detailed in Chapter 4. These experiments measured the transport of radionuclides in the presence of bentonite colloids, injecting an injection cocktail made up of these (and other) radionuclides in a bentonite colloid suspension. Measurements of caesium, uranium and neptunium before the experiments showed significantly different 'initial bound' fractions between the two experiments for each radionuclide, unlike americium and plutonium, as presented in the previous chapter. The different initial bound fractions potentially result in the radionuclides being transported by different processes in the two experiments, which this modelling aims to investigate and identify.

Geochemical modelling of radionuclide speciation and saturation indices provided insight to the relevant transport processes possible for the radionuclides in the two experiments, finding that uranium or neptunium self-colloids could have formed in the injection cocktails of the migration experiments.

These radionuclides were previously modelled during the CRR experiment (Smith et al., 2006; Kosakowski and Smith, 2004). However, only limited modelling of these radionuclides has been carried out previously for the CFM project (Reimus, 2016).

## 7.2. Caesium model calibration

This section discusses the calibration of the transport model described in Chapter 4 for the transport and resulting breakthrough of caesium in CFM Run 13-05 and CRR Run 32. Caesium-137 was injected in both experiments at the mass and concentrations given in Table 6.1, as measured by off-site  $\gamma$ -spectroscopy. The concentration of caesium removed by centrifugation (or initial bound fraction) was measured at the beginning of both experiments. Caesium showed significantly different initial bound fractions between the two experiments, 63.9% in CFM Run 13-05, but only 8% in CRR Run 32. The cause of the different values is discussed further in the following sections.

	<b>CFM Run 13-05:</b> <sup>137</sup> Cs	<b>CRR Run 32:</b> <sup>137</sup> Cs
Mass (M <sub>0</sub> )	0.271 µg	0.19 µg
Concentration (C <sub>0</sub> )	0.084 µg/l <sup>1</sup>	1.9 µg/l
Initial 'colloid-bound' fraction/ Mass removed by centrifugation	63.9%/ 0.17 µg	8%/ 0.015 µg
Cocktail equilibration time	35 days <sup>2</sup>	5 days
Colloid mass	Total: 224.3 mg	2.01 mg

1: Peak concentration in re-circulation circuit

2: Value measured after 401 days due to equipment problems

**Table 7.1 Mass and concentration of caesium used in CFM Run 13-05 and CRR Run 32**

### 7.2.1. Conceptual Model

Geochemical modelling using PHREEQC (Appendix A) of the injection cocktail was carried out by Dr Janice Kenney to provide information on caesium speciation, redox state and potential precipitates (although caesium was redox insensitive). This modelling used the SIT/ ANDRA Thermodynamic database. Figure 7.1 and Figure 7.2 show the predicted caesium speciation for CFM Run 13-05 and CRR Run 32 respectively. This modelling showed that caesium is expected to be present solely as Cs<sup>+</sup> at the average pH of Grimsel groundwater

(pH 9.6). Cs sorption to clay minerals and rock surfaces is controlled by cation exchange processes. Surface complexation of caesium is unlikely to occur because caesium sorption to FEBEX bentonite has been observed to be pH independent (Missana et al., 2004), unlike surface complexation which is pH dependent. Modelled saturation indices in the injection cocktails showed negative saturation indexes, and therefore no caesium precipitates are predicted to form in either migration experiment.

Since no precipitates are predicted to form, the 'initial bound' fraction of caesium removed from solution in the initial cocktail can only be caused by sorption to the colloids. Despite this relatively simple aqueous geochemistry, there is a large difference in the measured 'initial bound' fraction between the two experiments.

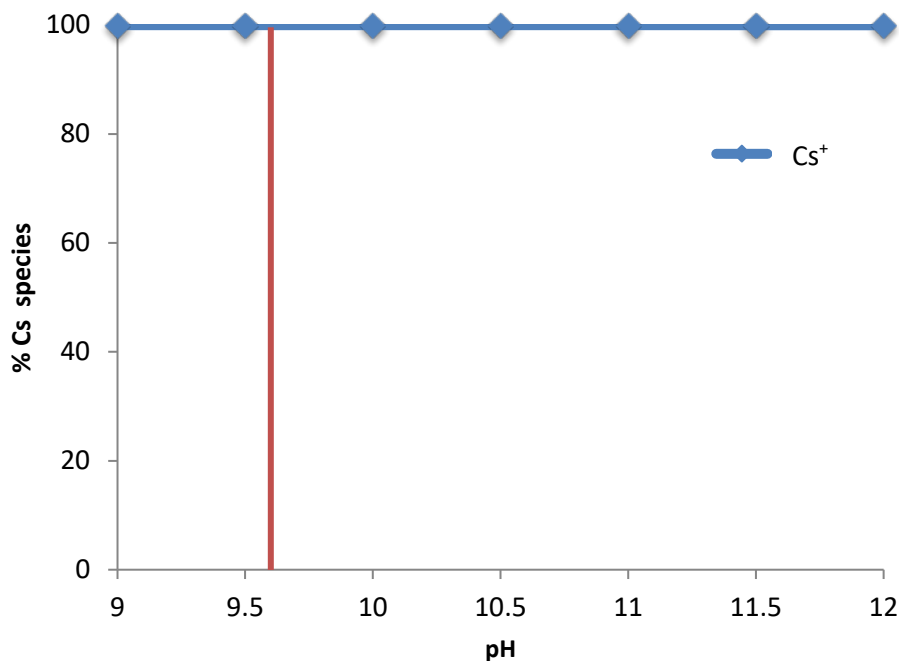


Figure 7.1 Predicted caesium speciation in CFM Run 13-05 from PHREEQC. Red line = Grimsel groundwater average pH (9.6)

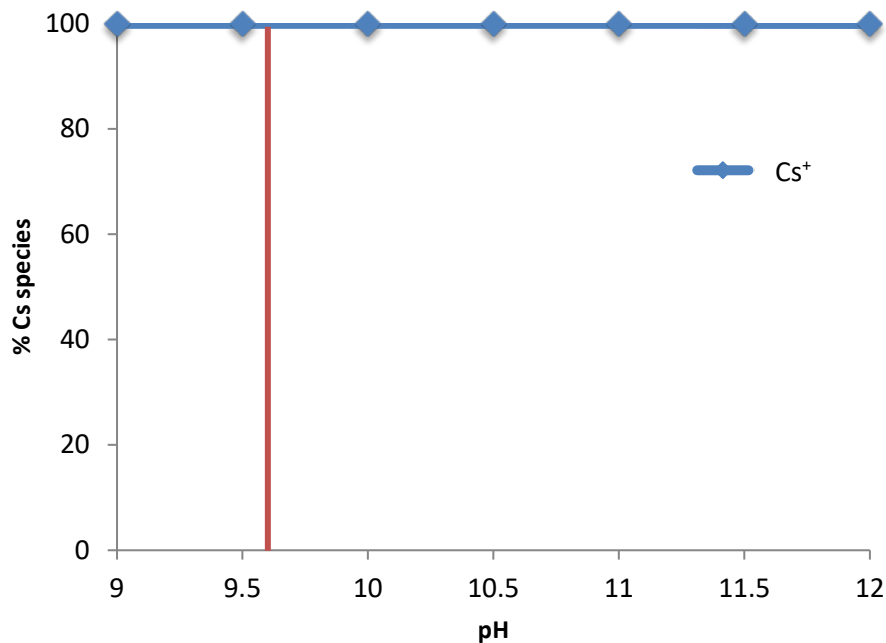


Figure 7.2 Predicted caesium speciation in CRR Run 32 from PHREEQC. Red line = Grimsel groundwater average pH (9.6)

A potential cause of the different initial bound fractions could be the different cocktail equilibration times (5 days for CRR Run 32, 35 days for CFM Run 13-05), which could have allowed more time for sorption to occur in the CFM Run 13-05 cocktail. Laboratory experiments testing caesium sorption to FEBEX bentonite colloids observed that sorption was complete within a time period of a week (Missana et al., 2004), making the increased sorption in CFM Run 13-05 unlikely to be related to equilibration time. The same experiments showed a non-linear sorption isotherm for caesium to FEBEX bentonite, as shown in Figure 7.3 (Missana et al., 2004; Missana and Geckeis, 2006). Bentonite is mainly composed of smectite clay, a sheet silicate mineral, and cations such as caesium can sorb on the basal plane/ interlayer of the clay, or to the edges of the clay layers (Missana et al., 2004). The non-linear sorption isotherm is interpreted by the presence of a site with lower affinity but with a capacity of approximately  $5 \times 10^{-8}$  mol/g of clay (Site 1), situated on the basal plane of the clay and a high affinity site with a limited capacity of  $1 \times 10^{-12}$  mol/g of clay

(Site 2), situated on the edge of the clay layers (Missana et al., 2004). These edge sites are thought to arise due to the presence of illite-smectite mixed layers in FEBEX bentonite (Missana et al., 2004).

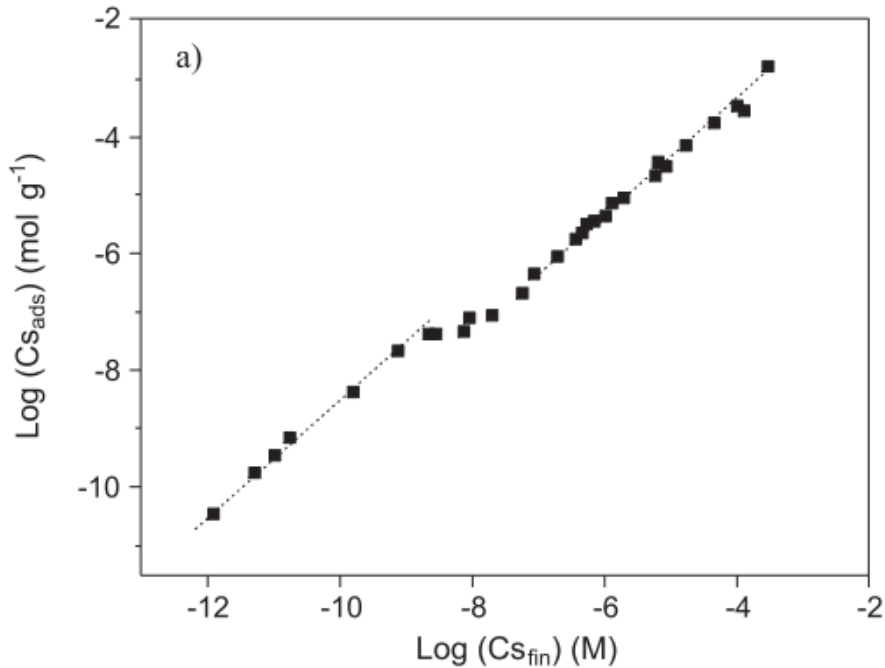


Figure 7.3 Caesium sorption isotherm to FEBEX bentonite colloids in Grimsel groundwater, contact time two weeks.  $C_{s_{ads}}$  represents sorbed concentration of Cs,  $C_{s_{fin}}$  represents final aqueous Cs concentration (From: Missana and Geckeis, 2006)

It is thought that different sorption mechanisms are present for the two sites, as it appears that caesium uptake is slower to the stronger edge site (Site 2) than to the planar site (Site 1) (Missana et al., 2004). This has been interpreted as cation exchange processes occurring on the planar site (Site 1), with a slower sorption or diffusion process onto the edge site (Site 2) (Missana et al., 2004). Desorption can occur from both sites, as sorption to the bentonite has been shown to be reversible (Missana et al., 2004). Figure 7.4 shows a conceptual diagram of the sorption processes to the different sites.

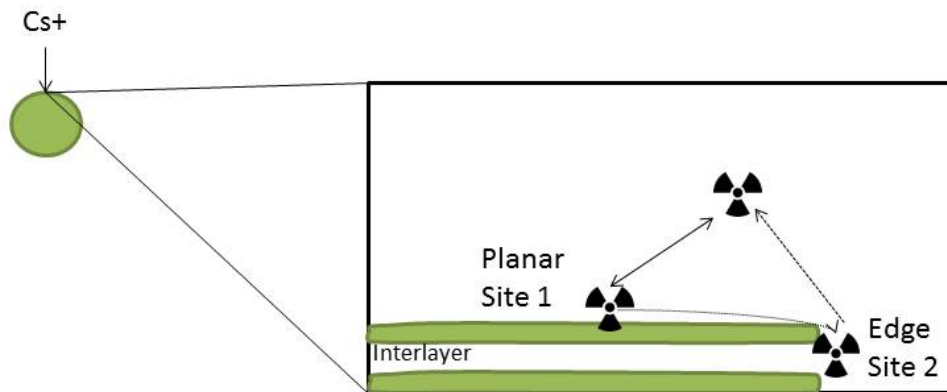


Figure 7.4 Conceptual diagram for the two sorption sites on FEBEX bentonite clay colloids (not to scale).

It is likely that the different initial bound fractions are caused by different caesium concentrations used in the injection cocktails of the experiments. Figure 7.5 shows the different concentrations of caesium (also given in Table 6.1) used in the two migration experiments with  $K_d$  values to FEBEX bentonite calculated from the laboratory experiments in Missana et al. (2004).

Figure 7.5 shows that the  $K_d$  is higher at the Cs concentration used in CFM Run 13-05 than in CRR Run 32. The lower caesium concentration in CFM Run 13-05 ( $8.8 \times 10^{-10}$  mol/l) means that the stronger edge site (Site 2) controls sorption, resulting in the higher  $K_d$  and higher percentage of caesium sorbed to the colloids in CFM Run 13-05. The concentration of caesium used in CRR Run 32 ( $1.38 \times 10^{-8}$  mol/l) means that the edge site has reached capacity, and so the weaker planar site (Site 1) controls sorption in the experiment, resulting in the lower  $K_d$  and lower initial bound fraction.

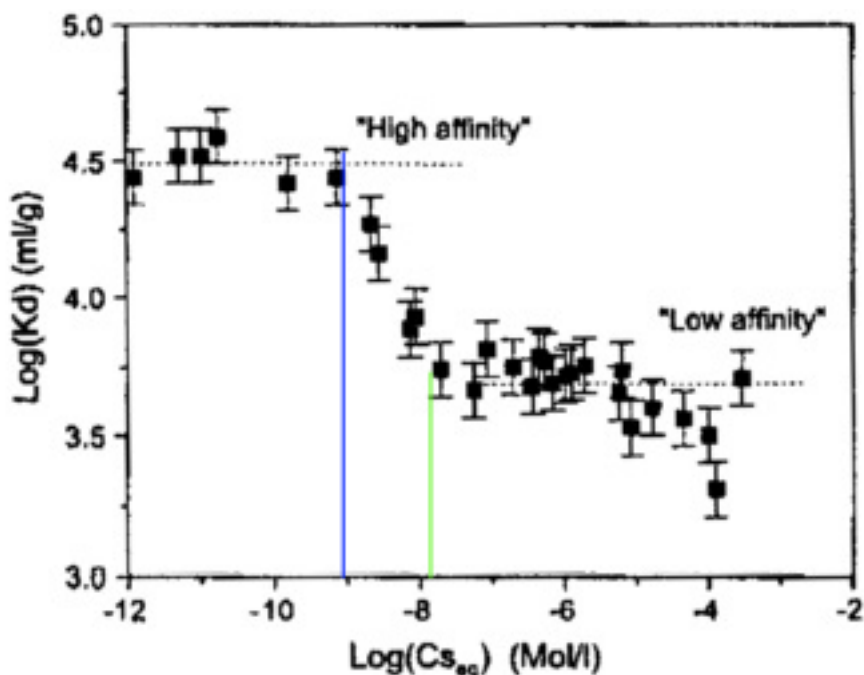


Figure 7.5 Caesium  $K_d$  values to FEBEX bentonite colloids with varying Cs concentration. Blue = CFM Run 13-05 Cs concentration ( $8.8 \times 10^{-10}$  mol/l), Green = CRR Run 32 Cs Concentration ( $1.38 \times 10^{-8}$  mol/l). Altered from Missana et al. (2004)

Multiple sorption sites for caesium have been modelled on other clays, for instance caesium sorption to illite was modelled with a 'frayed edge' and 'type 2' site in Poinsot et al. (1999), with a third planar site added by Bradbury and Baeyens (2000). Caesium sorption to montmorillonite has been described by both single site (Durrant et al., 2018) and multiple site models (Kasar et al., 2017). This is likely to be due to differences in the structure of the clays used in the different experiments, as there are fewer edge sites in pure smectite found in some montmorillonite clays than the illite-smectite mixed layers found in the bentonite and some montmorillonite (Missana et al., 2004).

Experiments investigating caesium sorption to Grimsel granodiorite and fracture fill material (FFM) noted lower  $K_d$  values to the granodiorite/ FFM than for bentonite colloids (Missana and Geckeis, 2006).  $K_d$  values were higher for the fracture fill material than the Grimsel granodiorite, which is probably due to the higher percentage of sheet silicates and

clay found in the FFM (Missana and Geckeis, 2006). In these experiments, slower sorption was observed for sorption to the fracture fill material over a period of several weeks but not for the granodiorite (Missana and Geckeis, 2006).

Dittrich and Reimus (2015b) used batch and column experiments to investigate caesium transport in the presence of FEBEX bentonite colloids and Grimsel fracture fill material, using a two-sorption site model to describe sorption to both colloids and fracture fill material. The additional sorption site on the FFM improved the model fit of the experiments in relation to modelling observed sorption-desorption hysteresis between different stages of the column experiments (Dittrich and Reimus, 2015b).

### **7.2.2. Transport Model setup**

During the calibration of this model, it was first attempted to model the transport of caesium with one type of sorption site on both colloids and FFM, adding additional sites if it was necessary to model these experiments using consistent parameter values.

#### ***One sorption site model***

Initial modelling used the same one-site model as used for americium and plutonium (Chapter 6), with the addition of an equation that describes kinetic sorption of aqueous caesium to fracture fill material/ granodiorite (Equation 4.11), instead of using a retardation factor, which couples to the aqueous caesium transport equation (Equation 4.6). This was added due to kinetic effects for caesium sorption to Grimsel FFM observed by Missana and Geckeis (2006). This model used the non-calibration parameters given in Table 6.6.

Parameter	Symbol	CFM Run 13-05	CRR Run 32	Justification
Radioactive decay constant	$\lambda_d$	7.28x10 <sup>-10</sup> (1/s)		Based on isotope values
Bound fraction		63.9%	8%	Experimentally measured
Unbound fraction		36.1%	92%	Experimentally measured

**Table 7.2 Non-calibration parameters for one-site caesium model**

The calibration parameters for the one-site model were the sorption and desorption rates from mobile colloids ( $k_{amc}$  and  $k_{mca}$ ), desorption rates from immobile colloids ( $k_{ica}$  and  $k_{icai}$ ), sorption and desorption rates to fracture fill material ( $k_{ai}$  and  $k_{ia}$ ), and limits to the sorption capacity of the colloid ( $S_{mcmax}$ ) and fracture fill material ( $N_{imax}$ ) (which were initially set so there was no capacity limit).

***Two sorption site model***

The two site model is based on the conceptual diagram described above (Figure 7.4), and adds equations describing the additional sorption sites on the colloid and fracture fill material to the one-site model. Equation 7.1 describes the transport of colloid-bound caesium sorbed to the second site on the colloid:

$$\begin{aligned} \theta b R_c \frac{\partial S_{mc2}}{\partial t} + \nabla \cdot (\theta b \mathbf{v} S_{mc2} - \theta b \mathbf{D} \nabla S_{mc2}) \\ = -\theta b \lambda_d S_{mc2} + k_{trans} \theta b \left( 1 - \frac{S_{mc2}}{S_{mc2max}} \right) S_{mc} - k_{mca2} \theta b S_{mc2} \\ - k_{att} \theta b \left( 1 - \frac{F}{F_{max}} \right) S_{mc2} + k_{det} (1 - \theta) b \rho_f S_{ic2} - k_{iat} \theta b \left( 1 - \frac{F_i}{F_{imax}} \right) S_{mc2} \end{aligned}$$

**Equation 7.1 Transport of colloid-bound caesium sorbed to the second edge site.**

where  $S_{mc2}$  is the concentration of radionuclide sorbed to the second site of a mobile colloid [ $ML^{-3}$ ],  $k_{trans}$  is the transfer rate from the first sorption site to the second site [ $T^{-1}$ ];  $S_{mc2max}$  is the capacity of the second site [ $ML^{-3}$ ],  $k_{mca2}$  is the desorption rate from Site 2 [ $T^{-1}$ ],

$S_{ic2}$  is the concentration of radionuclide sorbed to the second site of an attached colloid [-], and  $S_{ici2}$  is the concentration of radionuclide sorbed to the second site of an irreversibly attached colloid [-].

Equation 7.1 is coupled to Equation 4.7, (radionuclides sorbed to mobile colloids on the first site), and to the aqueous radionuclide transport equation (Equation 4.6). In addition, equations describing radionuclides sorbed to the second site of immobile colloids were added (which are based on Equation 4.8 and Equation 4.9). Finally, an additional equation describing radionuclide sorption to a second site on the fracture fill material was added (Equation 4.11):

$$(1 - \theta)b\rho_f \frac{\partial N_{i2}}{\partial t} = k_{ai2}\theta b \left(1 - \frac{N_{i2}}{N_{i2max}}\right) N - k_{ia2}(1 - \theta)b\rho_f N_{i2} - (1 - \theta)b\lambda_d N_{i2}$$

**Equation 7.2 Second radionuclide sorption site on FFM**

where  $N_{i2}$  is the concentration of radionuclide sorbed to the second site on fracture fill material, per mass of FFM (-),  $k_{ai2}$  and  $k_{ia2}$  are the sorption and desorption rates for the second site [ $T^{-1}$ ] and  $N_{i2max}$  is the capacity of this second site [-]. This equation was coupled to the aqueous radionuclide transport equation (Equation 4.6). All other model settings remained the same, apart from when the aqueous caesium breakthrough was modelled in CRR Run 32, which required the model to run for 6000 hours (instead of 1000 minutes), as samples were collected over a longer time period than other radionuclides.

The two-site model used the non-calibration parameter values in Table 6.6, with the calibration parameters listed in Table 7.3, which includes information about the methodology used to set initial values. It is important to note how the concentration of

caesium sorbed to the individual sites at the beginning of each experiment is calculated. The model assumes that sorption occurs to both sites on the colloid during the cocktail equilibration period. However, with the available experimental data, it is not possible to distinguish the concentration sorbed to the individual sites.

This model assumes that the majority of colloid-bound caesium observed in breakthrough curves is sorbed to the strong edge site on the colloid (Site 2). Thermodynamic sorption modelling of laboratory experiments investigating caesium sorption to illite showed that at the concentration of colloid bound caesium in the migration experiments, the caesium is expected to be sorbed to the edge site (Poinsot et al., 1999; Bradbury and Baeyens, 2000; Missana et al., 2014a, 2014b; Cherif et al., 2017; Siroux et al., 2017). This strong edge site (Site 2) is assumed to be full at the beginning of the experiment, due to the relatively long cocktail equilibration time and the fact that laboratory experiments show that sorption equilibrium is expected to have been reached in this time (Missana et al., 2004; Missana and Geckeis, 2006).

Using these two assumptions, back calculations determined the required capacity of Site 2 (and therefore the initial concentration of caesium sorbed in Site 2) that results in the same experimental recovery measured in the two migration experiments. This calculation took into account colloid recovery, and also assumes that there is limited desorption from Site 2 during the migration experiments as Missana et al. (2004) show that caesium sorption is not completely reversible, which is thought to be caused by caesium sorbed to Site 2. Any remaining colloid-bound caesium not sorbed to Site 2 is then assumed to be sorbed to Site 1.

The results of these calculations, as well as the values of the other calibration parameters, are discussed further below.

Parameter	Symbol	Methodology
Sorption rate to mobile colloids, Site 1	$k_{amc}$	Based on $K_d$ value (calculated by $K_d = k_{amc}/k_{mca}$ ), from experimental values in Missana et al. (2004)
Desorption rate from mobile colloids, Site 1	$k_{mca}$	
Desorption rate from immobile colloids, Site 1	$k_{ica}/k_{icai}$	Same value as $k_{mca}$
Site capacity on colloids, Site 1	$N_{mcm_{max}}$	Using experimental data Missana et al. (2004); sorption not expected to be limited
Sorption rate to FFM, Site 1	$k_{ai}$	From models of laboratory experiments Dittrich and Reimus (2015b) to Grimsel FFM
Desorption rate from FFM, Site 1	$k_{ia}$	
Site capacity on FFM, Site 1	$N_{imax}$	Same capacity as $N_{mcm_{max}}$ ; sorption not expected to be limited
Transfer rate between mobile colloid Site 1 and 2	$k_{trans}$	Based on $K_d$ value (calculated by $k_{trans}/k_{mca2}$ ), from experimental values in Missana et al. (2004)
Desorption rate from mobile colloids, Site 2	$k_{mca2}$	
Desorption rate from immobile colloids, Site 2	$k_{ica2}/k_{icai2}$	Same as $k_{mca2}$
Site capacity on colloids, Site 2	$S_{mc2max}$	Based on calculations on experimental recovery (see discussion in text)
Sorption rate to FFM, Site 2	$k_{ai2}$	From models of laboratory experiments Dittrich and Reimus (2015b) to Grimsel FFM
Desorption rate from FFM, Site 2	$k_{ia2}$	
Site capacity on FFM, Site 2	$N_{i2max}$	Same capacity as found on colloids ( $S_{mc2max}$ )
Cs sorbed to colloids at beginning of experiment, Site 1	N/A	Colloid-bound caesium concentration not sorbed to Site 2 (see discussion in text)
Cs sorbed to colloids at beginning of experiment, Site 2	N/A	Capacity of Site 2, site assumed to be fully filled (see discussion in text)

Table 7.3 Calibration parameters for two-site caesium model, with methodology of setting initial parameter values

### 7.2.3. Model Results

#### *One sorption site model*

The results of the one sorption site model for caesium breakthrough in CFM Run 13-05 and CRR Run 32 are shown in Figure 7.6, which used the parameters in Table 7.4. Although the model was able to replicate the breakthrough of caesium in CFM Run 13-05, the model struggled to produce a good match with the caesium breakthrough in CRR Run 32,

especially after 10 hours, when the breakthrough is dominantly aqueous caesium (Möri et al., 2004). In addition, Table 7.4 shows that consistent parameters describing colloid desorption were not found, and so the two sorption site model was used to attempt to find consistent parameter values that described both experiments.

Parameter	Symbol	CFM Run 13-05	CRR Run 32
Sorption rate to mobile colloids	$k_{amc}$	$1 \times 10^{-8} \text{ m}^3/\text{kg}\cdot\text{s}$ ( $3.6 \times 10^{-5} \text{ m}^3/\text{kg}\cdot\text{hr}$ )	
Desorption rate from mobile colloids	$k_{mca}$	$8 \times 10^{-6} \text{ 1/s}$ (0.0288 1/h)	$7 \times 10^{-4} \text{ 1/s}$ (2.52 1/h)
Desorption rate from immobile colloids	$k_{ica}/k_{icai}$		
Sorption rate to FFM	$k_{ai}$	$3 \times 10^{-3} \text{ 1/s}$ (10.8 1/h)	
Desorption rate from FFM	$k_{ia}$	$1 \times 10^{-5} \text{ 1/s}$ (0.036 1/h)	

Table 7.4 Calibrated parameter values for one-site caesium model

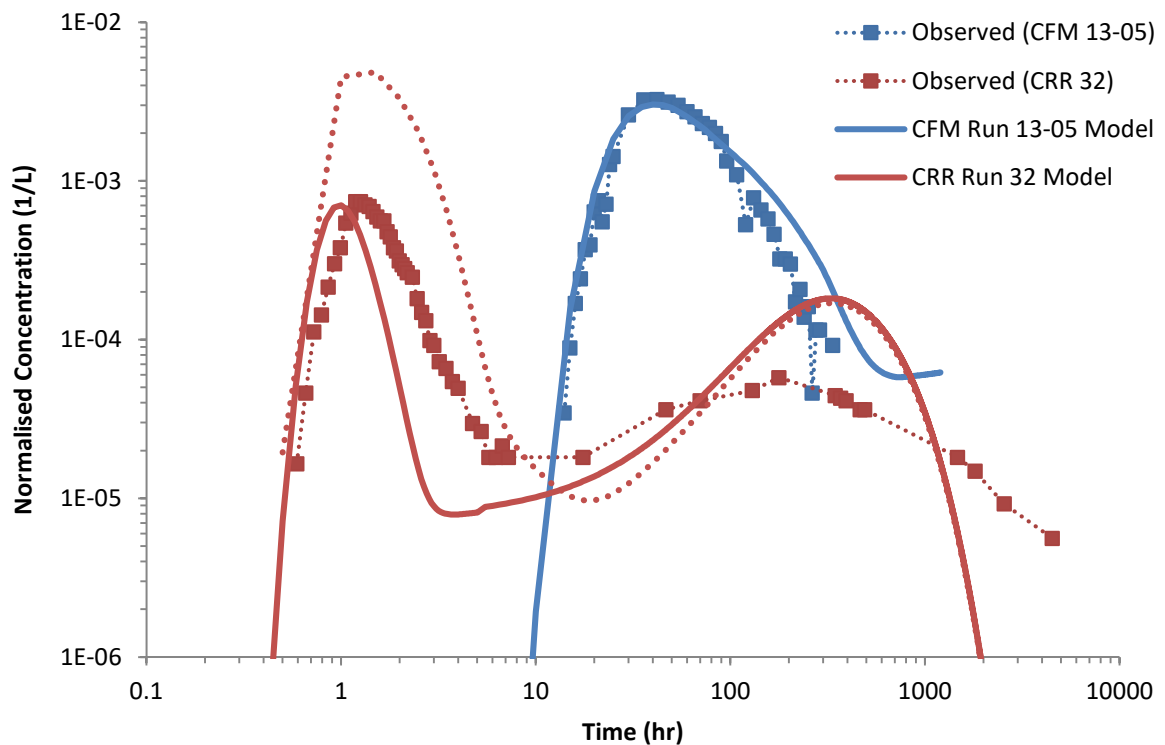


Figure 7.6 Calibrated breakthrough curve for one-site caesium model in CFM Run 13-05 and CRR Run 32. The dotted red line represents a modelled breakthrough for Cs in CRR Run 32 which used the parameters obtained from the CFM Run 13-05 one-site calibrated model.

**Two sorption site model**

The results of the two-site model for caesium breakthrough in CFM Run 13-05 and CRR Run 32 are shown in Figure 7.7, which used the calibrated parameters in Table 7.5.

Table 7.5 shows that unlike the one-site model, consistent parameters were found to describe caesium sorption and desorption from the two colloid sorption sites. Two sorption sites were also included on the fracture fill material, as this was found to improve model fit to the aqueous caesium breakthrough in CRR Run 32.

Parameter	Symbol	CFM Run 13-05	CRR Run 32
Sorption rate to mobile colloids, Site 1	$k_{amc}$	$8 \times 10^{-3} \text{ m}^3/\text{kg}\cdot\text{s}$ (28.8 $\text{m}^3/\text{kg}\cdot\text{hr}$ )	
Desorption rate from mobile colloids, Site 1	$k_{mca}$	$2 \times 10^{-3} \text{ 1/s}$ (7.2 $\text{h}^{-1}$ )	
Desorption rate from immobile colloids, Site 1	$k_{ica}/k_{icai}$		
Site capacity on colloids, Site 1	$N_{mcm\max}$	10000 $\mu\text{g/l}$	
Sorption rate to FFM, Site 1	$k_{ai}$	$2.25 \times 10^{-3} \text{ 1/s}$ (8.1 $\text{h}^{-1}$ )	
Desorption rate from FFM, Site 1	$k_{ia}$	$1.25 \times 10^{-5} \text{ 1/s}$ (0.045 $\text{h}^{-1}$ )	
Site capacity on FFM, Site 1	$N_{imax}$	10000	
Transfer rate between mobile colloid Site 1 and 2	$k_{trans}$	$1 \times 10^{-5} \text{ 1/s}$ (0.036 $\text{h}^{-1}$ )	
Desorption rate from mobile colloids, Site 2	$k_{mca2}$	$5 \times 10^{-7} \text{ 1/s}$ (0.0018 $\text{h}^{-1}$ )	
Desorption rate from immobile colloids, Site 2	$k_{ica2}/k_{icai2}$		
Site capacity on colloids, Site 2	$S_{mc2\max}$	0.02205 $\mu\text{g/l}$	
Sorption rate to FFM, Site 2	$k_{ai2}$	$6.5 \times 10^{-4} \text{ 1/s}$ (2.34 $\text{h}^{-1}$ )	
Desorption rate from FFM, Site 2	$k_{ia2}$	$5 \times 10^{-7} \text{ 1/s}$ (0.0018 $\text{h}^{-1}$ )	
Site capacity on FFM, Site 2	$N_{i2\max}$	0.02205	
Cs sorbed to colloids at beginning of experiment, Site 1	N/A	0.056 $\mu\text{g/l}$	0.131 $\mu\text{g/l}$
Cs sorbed to colloids at beginning of experiment, Site 2	N/A	0.02205 $\mu\text{g/l}$	

Table 7.5 Calibrated parameter values for two-site caesium model

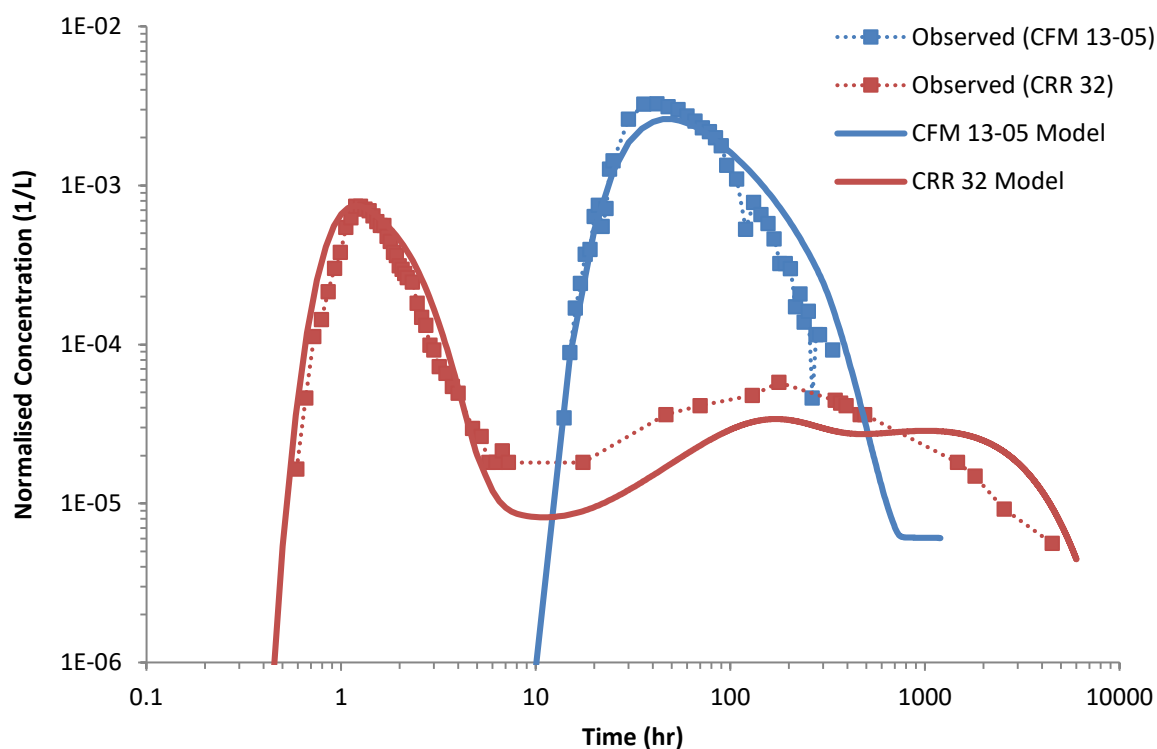


Figure 7.7 Calibrated breakthrough curve for two-site caesium model for CFM Run 13-05 and CRR Run 32

#### CFM Run 13-05

Figure 7.8 shows in detail the calibrated breakthrough curve for the two-site caesium model in CFM Run 13-05 on a linear scale, with a comparison of the observed and modelled recovery in Figure 7.9. The model gives a good match to the experimental data; however, the modelled breakthrough is slightly lower than the peak breakthrough, and is slightly higher than the experimental concentration on the falling limb of the breakthrough curve. This is similar to the Am and Pu model results for this experiment described in the previous chapter, and is most likely caused by errors carried forward from the colloid breakthrough model calibration. Despite this, the modelled recovery (9.5%) compares well to the experimental recovery (8%). It is likely that reduction in the error from the colloid breakthrough calibration would improve the model fit for caesium breakthrough in this experiment.

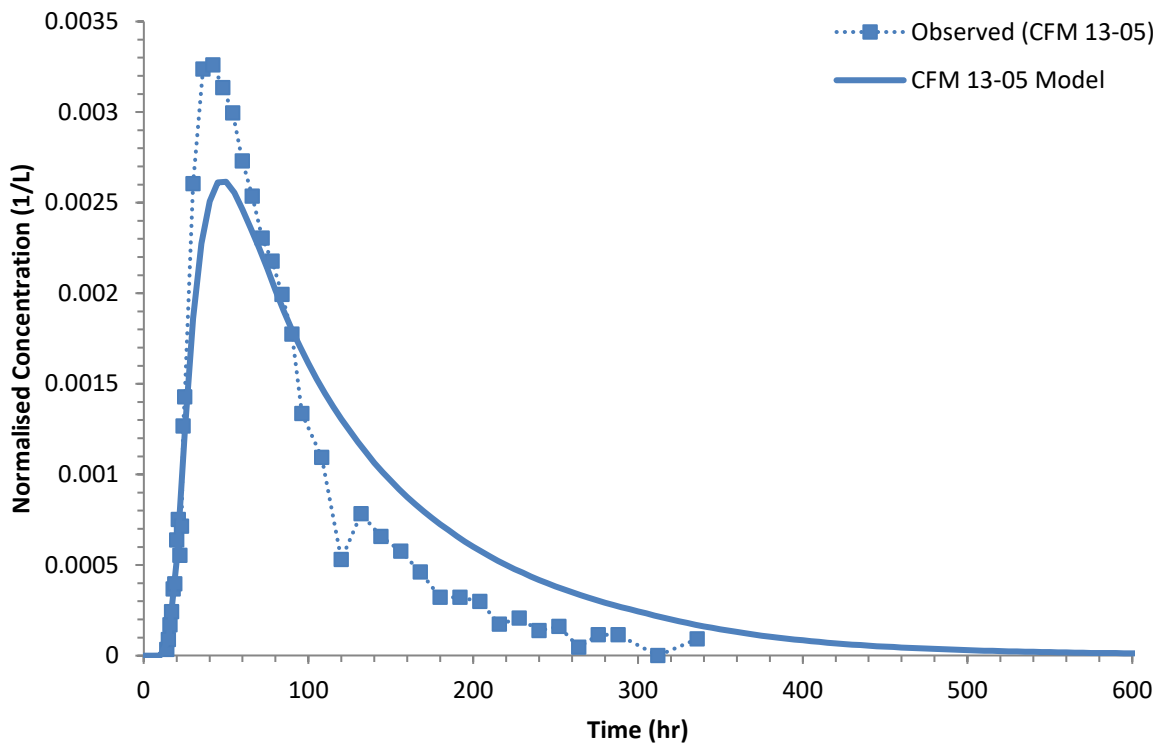


Figure 7.8 Calibrated breakthrough curve for two-site caesium model in CFM Run 13-05

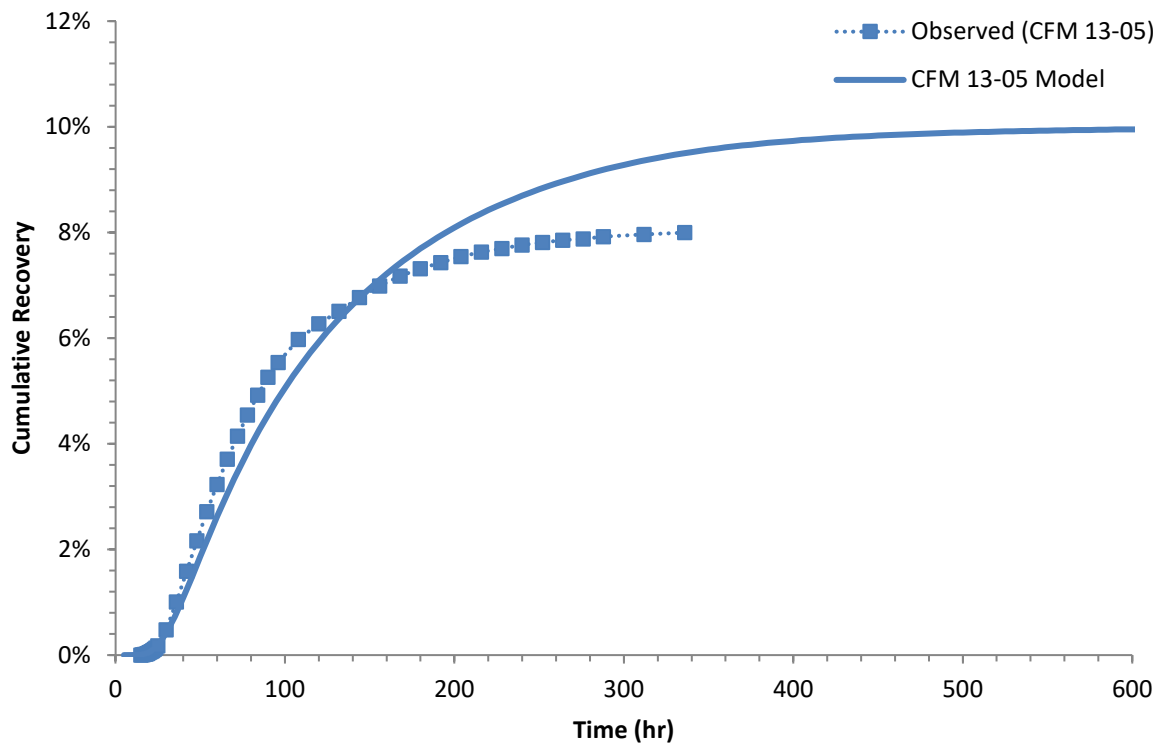


Figure 7.9 Comparison of cumulative recovery for observed and modelled data for <sup>137</sup>Cs in CFM Run 13-05 (two site model)

### CRR Run 32

Figure 7.10 shows the calibrated breakthrough curve for CRR Run 32 using the two-site model on a semi-log scale, with a comparison of the observed and modelled cumulative recovery shown in Figure 7.11. The breakthrough curves show two peaks, the first is caused by colloid-bound caesium, to which the model gives a good match to the experimental data. The second peak is caused by the breakthrough of retarded aqueous caesium. The modelled breakthrough gives a good match to the experimental data, although the model result is slightly lower than the experimental data for the second peak and is higher than the experimental data on the falling limb of the second peak on the breakthrough curve. The calculated model recovery (88%) is higher than the experimental recovery (70%) due to the discrepancies with the aqueous caesium on the second peak of the breakthrough curve.

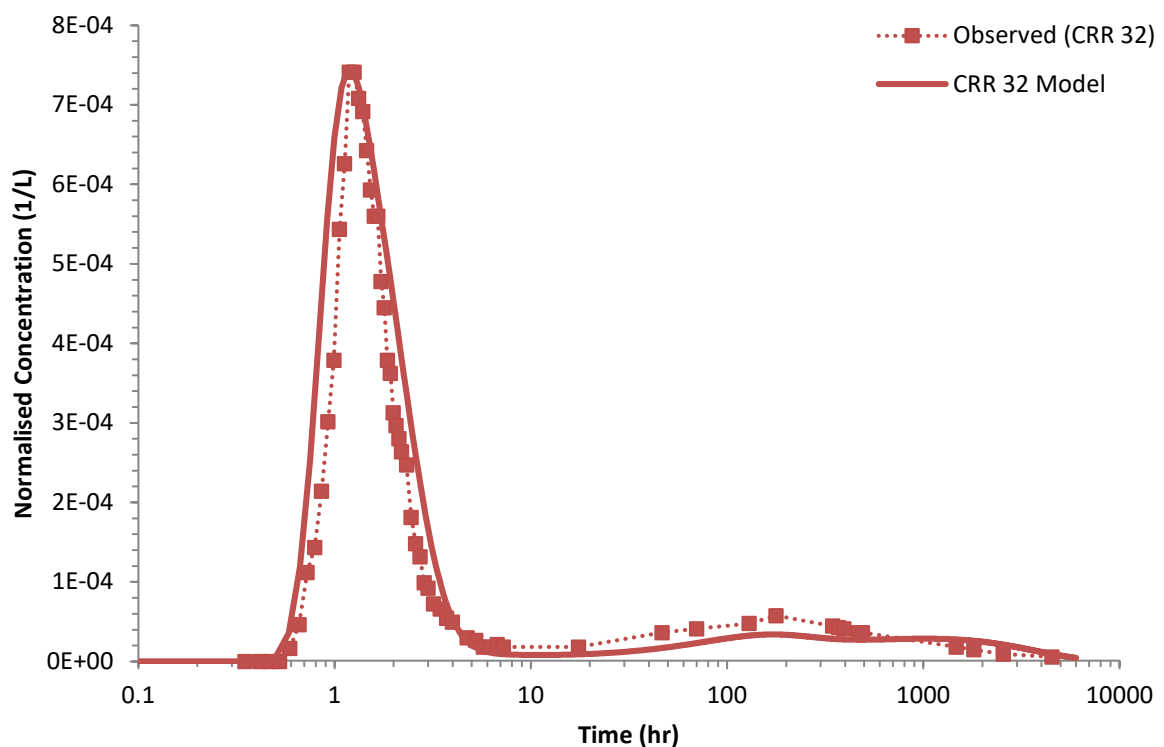


Figure 7.10 Calibrated breakthrough curve for two-site caesium model for CRR Run 32

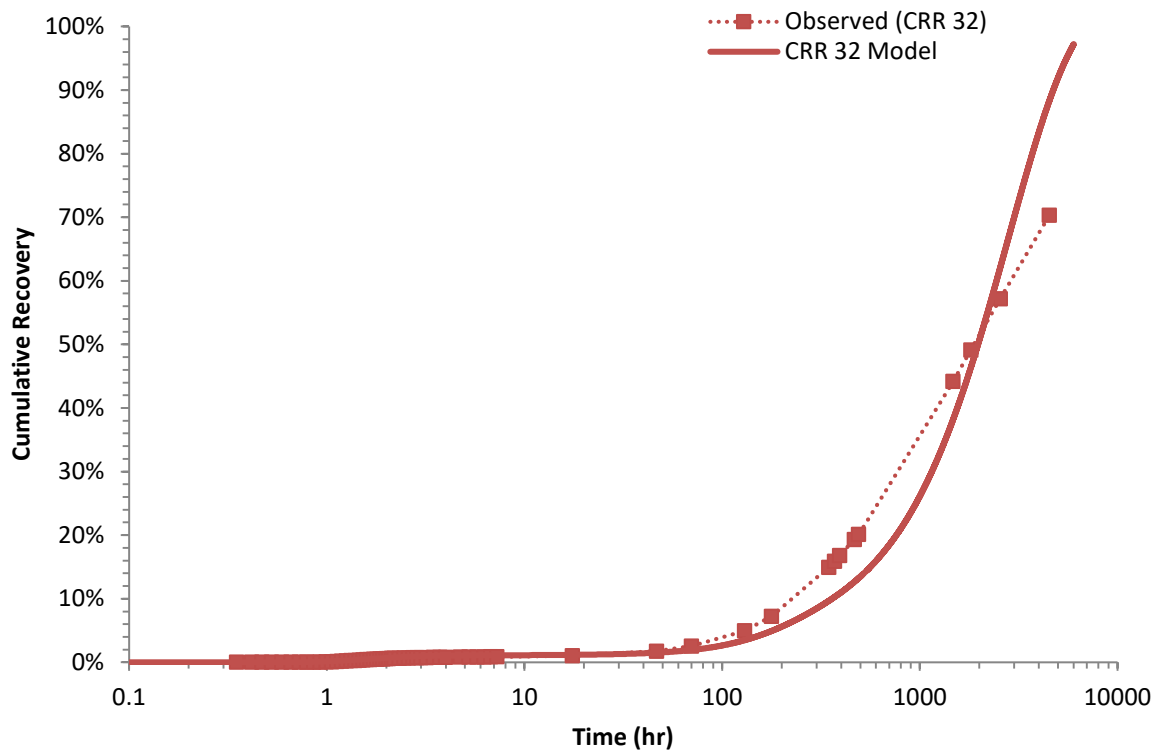


Figure 7.11 Comparison of cumulative recovery for observed and modelled data for  $^{137}\text{Cs}$  in CRR Run 32 (two-site model)

#### 7.2.4. Discussion and Conclusions

Caesium transport is partly facilitated by bentonite colloids in both CFM Run 13-05 and CRR Run 32, and therefore colloid processes are important controls on caesium transport, although to less of an extent than was observed for americium or plutonium. Aqueous caesium is also observed in the breakthrough curve for CRR Run 32, but is heavily retarded compared to the colloid-bound peak. A corresponding aqueous caesium peak is not observed in the CFM Run 13-05 dataset, as these data have not been collected (a corresponding peak would occur ~6 months after the experiment, and may be at concentrations below the detection limit of the  $\gamma$ -spectroscopy used to measure caesium concentration).

Initial attempts to model caesium breakthrough in the two experiments included one type of sorption site on the bentonite colloids. Using this model, it was not possible to find consistent desorption rates for the two experiments. However, desorption rates used in the model reflect the caesium sorption isotherm described in the conceptual model. In CFM Run 13-05 a slower desorption rate was used than in CRR Run 32. This reflects the fact that the caesium sorbs to the strong edge site (Site 2), where stronger sorption is expected (Missana et al., 2004). Whereas, at the caesium concentration used in CRR Run 32, more of the caesium is sorbed to the weaker lower affinity planar site, reflected by the use of a higher desorption rate.

The two-site model gave good matches to caesium breakthrough, using the same parameter values to model the different experiments. The model assumes that the key site in the model for caesium migration in the two experiments is the edge site on the colloid (Site 2) as shown in Figure 7.12. This assumption is based on the results of thermodynamic sorption models applied to model caesium sorption, albeit to other clays (Poinssot et al., 1999; Bradbury and Baeyens, 2000; Missana et al., 2014a, 2014b; Cherif et al., 2017; Siroux et al., 2017), which all show that at the concentration of colloid-bound caesium in the migration experiments, the edge site is expected to be the dominant site for transport.

As detailed in Section 7.2.2, the capacity of the colloid edge site (Site 2) was a calibration parameter as there was no experimental data that would determine the concentration of caesium fixed to the individual sites. Table 7.6 shows the concentration of caesium sorbed to the two colloid sites, and shows that almost a fifth (17%) of caesium injected in CFM Run 13-05 was sorbed to Site 2 in the experiment (this corresponds to a

quarter of the colloid-bound caesium). In CRR Run 32, only 1% of caesium was sorbed to Site 2 (13% of the colloid bound caesium).

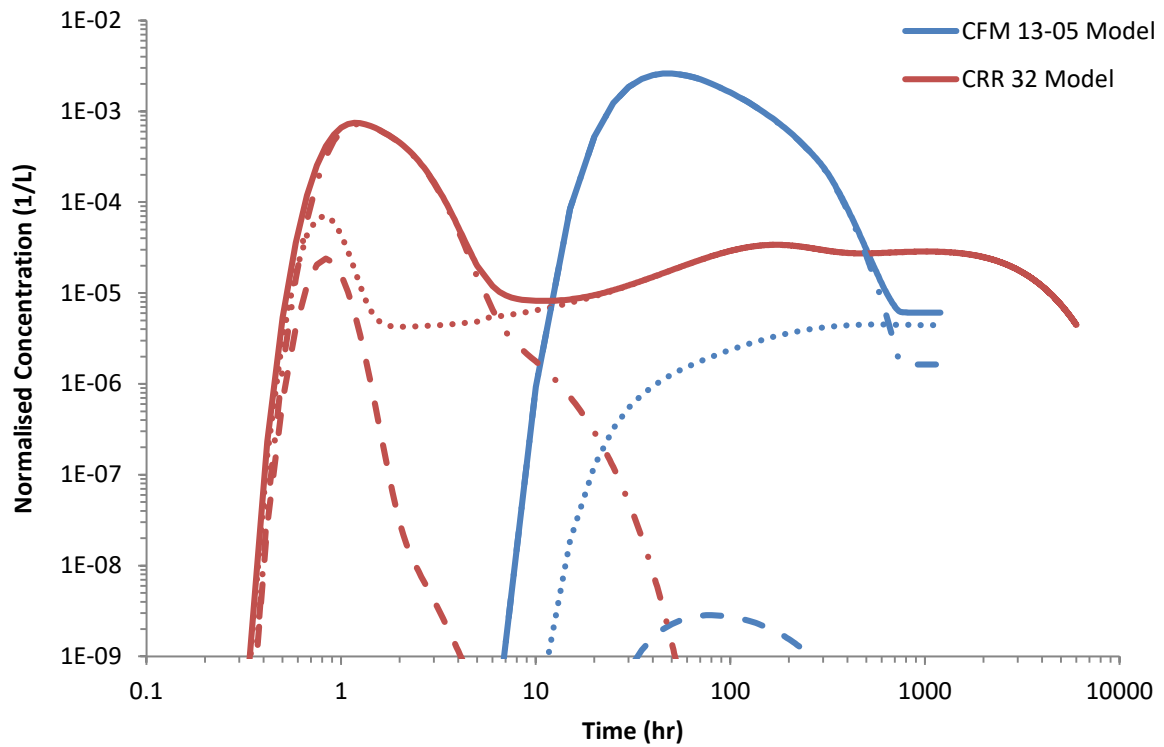


Figure 7.12 Contribution of different caesium phases to modelled breakthrough curves. (Solid = total concentration, dotted = aqueous caesium, dashed = colloid Site 1, dash/dot = colloid Site 2, red lines represents CRR Run 32 components, blue lines represent CFM Run 13-05).

	CFM Run 13-05	CRR Run 32
Colloid-bound caesium recovery	8.00%	0.76%
Total caesium recovery	8.00%	70%
Initial Bound Fraction	63.90%	8.00%
Sorbed Cs Concentration	0.077 µg/l	0.151 µg/l
Aqueous Cs Concentration	0.0435 µg/l	1.74 µg/l
Site 1 Concentration	0.056 µg/l	0.131 µg/l
Site 2 Concentration/ capacity	0.0205 µg/l	
% of sorbed Cs on Site 1	73.32%	86.41%
% of sorbed Cs on Site 2	26.68%	13.59%
% of total Cs sorbed to Site 1	46.85%	6.91%
% of total Cs sorbed to Site 2	17.05%	1.09%

Table 7.6 Concentrations and percentages of caesium sorbed to different sites on colloids

Figure 7.13 compares  $K_d$  values from this model to those obtained by Missana et al. (2004), using the parameters in Table 7.5, and the assumption that  $K_d = \text{sorption rate} / \text{desorption rate}$  (as used in Wold (2010) to estimate desorption rates).

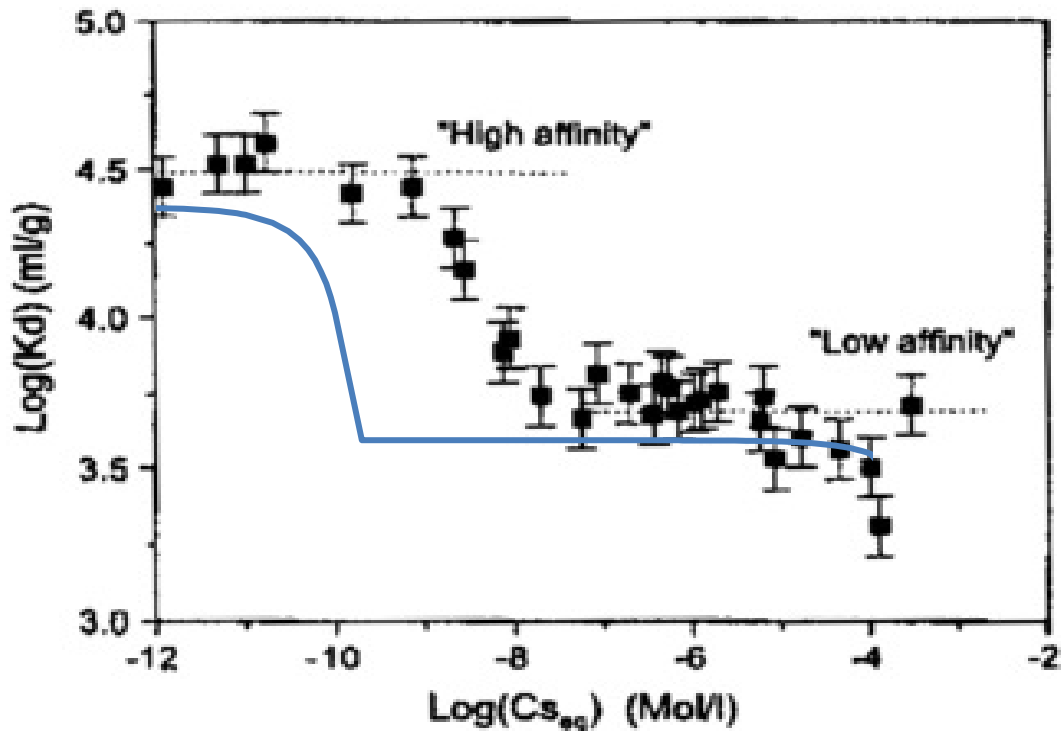


Figure 7.13 Calculated caesium  $K_d$  values to colloids (blue line) with changes in caesium concentration using sorption rates in Table 7.5, compared to results from Missana et al. (2004)

Figure 7.13 shows that the  $K_d$  values from this modelling are similar to  $K_d$  values measured in the experimental data (Missana et al., 2004). However, the capacity of the edge site (Site 2) used in this model ( $0.0205 \mu\text{g/l}$  or  $1.5 \times 10^{-10} \text{ mol/l}$ ) is roughly two orders of magnitude lower than the capacity of the site in the experimental data ( $\sim 6 \times 10^{-8} \text{ mol/l}$ ) (Missana et al., 2004). This does not take into account that in Missana et al. (2004) much higher clay concentrations were used ( $1\text{-}2 \text{ g/l}$ ) than the migration experiments ( $0.02\text{-}0.06 \text{ g/l}$ ). Normalising the site capacity from Missana et al. (2004) to the clay concentration used in the migration experiments the capacity of the site is still approximately an order of

magnitude larger than used in the model ( $6 \times 10^{-10}$  mol/l in the model,  $2 \times 10^{-9}$  mol/l in the experiment). Higher site capacities were also found in other laboratory experiments and modelling of laboratory experiments investigating caesium sorption to clays ( $\sim 7 \times 10^{-9}$  mol/l for montmorillonite Kasar et al., (2017);  $\sim 1 \times 10^{-9}$  mol/l for Na-smectite Missana et al. (2014)).

When the higher site capacity for the edge site (Site 2) from Missana et al. (2004) was used in this model the calculated recovery of caesium was higher than the experimental data in both experiments (using the same sorption rates in Table 7.5). The calculations in this model assumed that the full capacity of the edge site (Site 2) is filled at the beginning of the experiments as there was still some aqueous caesium present in the injection cocktail. If the second site was under capacity at the beginning of the experiment, much higher initial bound fractions would be expected. As the model assumed limited desorption from this site, the increased concentrations of caesium sorbed to the edge site resulted in higher recovery values in this model.

The likely reason for the discrepancy in site capacity is due to differences in the field and laboratory experiments. In the laboratory experiments only caesium is present. However, in the field experiments caesium plus several other radionuclides are present. These other radionuclides are likely to undergo competitive sorption, potentially filling the edge site (Site 2), resulting in a capacity for caesium that appears lower in the field experiments. One way to test this hypothesis is developing a thermodynamic sorption model of the bentonite colloids and radionuclides in PHREEQC; however, these models are intensive, requiring a large amount of data, and further experimental work is needed to fully understand the sorption of caesium in these field migration experiments.

It is possible to compare the sorption rates in this model with those used in laboratory experiments and other models of the CFM and CRR migration experiments. Reimus (2016) used a one-site model for caesium transport in both CRR Run 32 and CFM Run 13-05. The high desorption rate used for CRR Run 32 by Reimus (2016) ( $1.6 \text{ h}^{-1}$ ) is slightly lower than the rate used for Site 1 in this model ( $7.2 \text{ h}^{-1}$ ), but is close to the value used in the one sorption site model ( $2.52 \text{ h}^{-1}$ ), indicating that this difference is probably due to the additional site in the two-site model. The rates in Reimus (2016) used for CFM Run 13-05 ( $0.04\text{-}0.075 \text{ h}^{-1}$ ) are slightly higher than the desorption rate used for Site 2 in the two sorption site model ( $0.0018 \text{ h}^{-1}$ ), but again similar to the value used in the one sorption site model ( $0.0288 \text{ h}^{-1}$ ).

The interpretation of column experiments involving Grimsel FFM, bentonite colloids and caesium by Dittrich and Reimus, (2015b) was based on a two-site colloid and FFM sorption model. The desorption rate used for Site 1 on the colloids ( $8 \text{ h}^{-1}$ ) is very similar to that used here ( $7.2 \text{ h}^{-1}$ ). However, the desorption rate for Site 2 was far higher ( $0.4 \text{ h}^{-1}$ ) (compared with  $0.0018 \text{ h}^{-1}$  in this model). The sorption rates in this work are based on the laboratory data in Missana et al. (2004). The resulting sorption isotherm used by Dittrich and Reimus (2015b) results in higher  $K_d$  values for sorption to the edge site than the isotherm measured in Missana et al. (2004), despite efforts to keep these consistent. This is potentially caused by the lower concentration of clay used in Dittrich and Reimus (2015b) ( $100 \text{ mg/l}$ ) than Missana et al. (2004) ( $1\text{-}2 \text{ g/l}$ ).

Although included in Table 7.5 as a calibration parameter, the sorption rate to the first site on mobile colloids ( $k_{amc}$ ) was found to have little impact on the resulting

breakthrough curve in both experiments, as the majority of sorption to the colloids occurred in the injection cocktail before the migration experiments took place. The final value of  $k_{amc}$  was therefore chosen to best match the sorption isotherm from Missana et al. (2004). The transfer (or sorption rate) from the first site to the second site on the colloids ( $k_{trans}$ ) was found to be a slightly more sensitive parameter during the calibration process; however, it was not the most sensitive parameter as again the majority of sorption had occurred in the injection cocktail before the experiments were run.

During the modelling of CRR Run 32 it was found that the addition of the second sorption site on the FFM improved model fit, as was also found in the modelling of column experiments described in Dittrich and Reimus (2015b). Figure 7.14 and Figure 7.15 show the model results when using one sorption site on the FFM, with two sorption sites on the bentonite colloid for CFM Run 13-05 and CRR Run 32 respectively. This shows a poor model fit for the aqueous breakthrough in CRR Run 32, however in CFM Run 13-05 there was little improvement to the model fit with the addition of the second FFM sorption site, as mostly colloid-bound caesium is included in the breakthrough curve data.

The FFM sorption rates used in the current study were much higher ( $8.1 \text{ h}^{-1}$  and  $2.34 \text{ h}^{-1}$  for Site 1 and 2) than those used in the modelling of the laboratory column experiments by Dittrich and Reimus, (2015b) ( $0.05 \text{ h}^{-1}$  for Site 1, and  $0.001 \text{ h}^{-1}$  for Site 2 in the experimental work). The desorption rates used in the current work, however, were lower ( $0.045 \text{ h}^{-1}$  and  $0.0018 \text{ h}^{-1}$  for Sites 1 and 2 respectively) than those used in the model of laboratory column data ( $0.6\text{-}0.8 \text{ h}^{-1}$  for Site 1 and  $0.008$  to  $0.011 \text{ h}^{-1}$  for Site 2). A potential reason for the differences is the higher concentration of caesium used in the column

experiments, and so weaker sorption would be expected to the clay materials in the FFM (if the same non-linear behaviour is assumed). Another potential reason is that the column experiments use different particle sizes of fracture fill material. Caesium sorption on FFM has been shown to be size dependent, lower  $K_d$  values being observed for larger size fractions (Missana and Geckeis, 2006). The laboratory experiments used crushed FFM increasing the surface area available for sorption, and is therefore not representative of the migration experiments which used intact FFM.

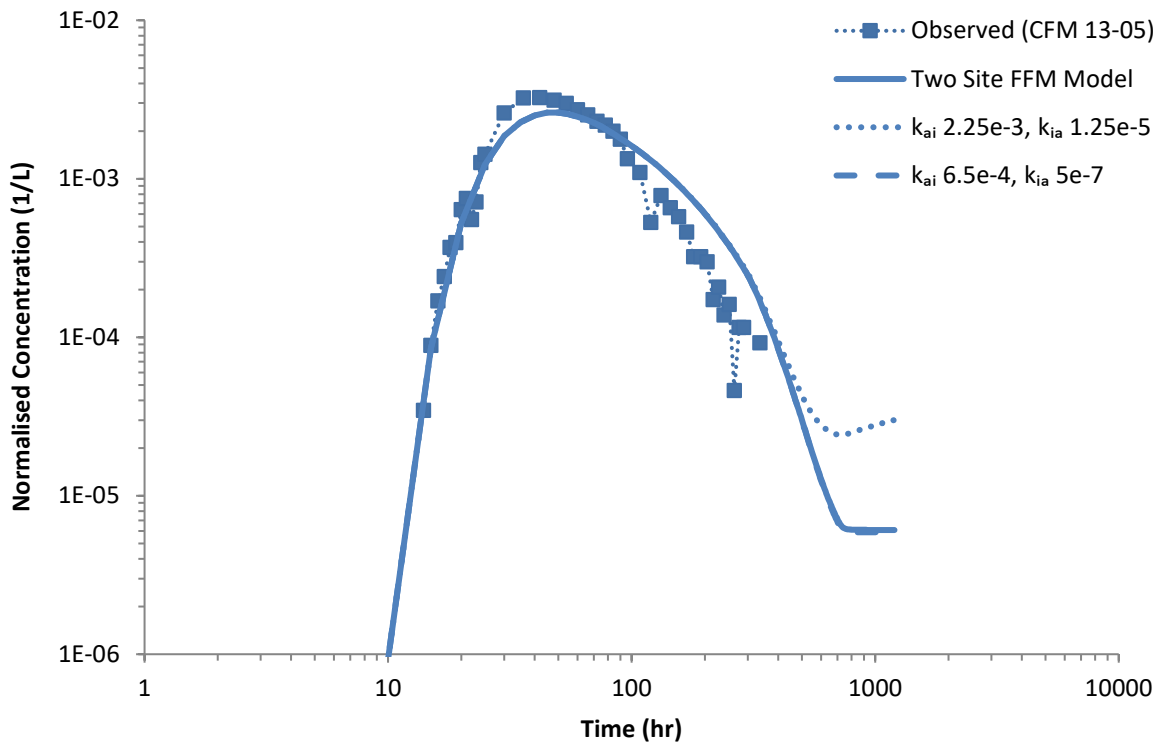


Figure 7.14 Results of one-site FFM model for CFM Run 13-05. Dashed and dotted lines are model results with two sorption sites on colloid and one sorption site on FFM.

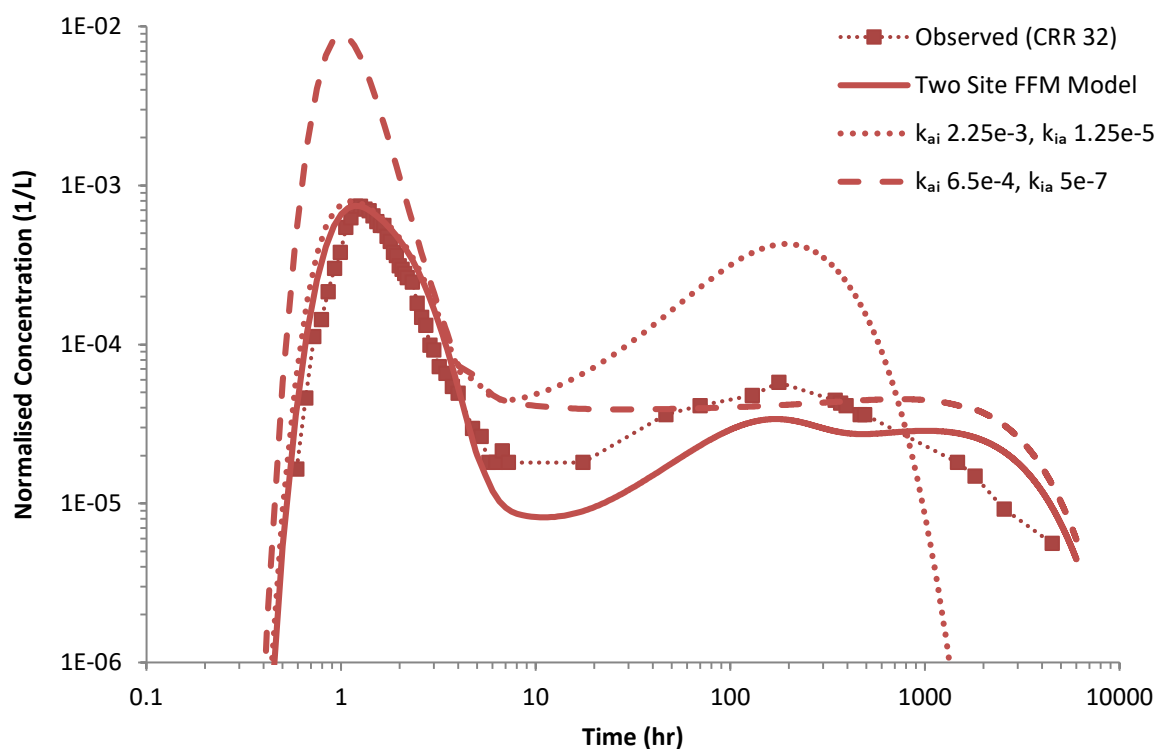


Figure 7.15 Results of one-site FFM model for CRR Run 32. Dashed and dotted lines are model results with two sorption sites on colloid and one sorption site on FFM.

In summary, it has been possible to model the transport of caesium in CFM Run 13-05 and CRR Run 32 successfully, by including two different sorption sites on the colloid surfaces. The aqueous caesium breakthrough in CRR Run 32 was modelled with two sorption sites on the Grimsel FFM as this improved the model fit. The second site could be due to the presence of clay minerals in the FFM (Gaus and Smith, 2008). This was also included in CFM Run 13-05, but as limited aqueous caesium was observed in the breakthrough data, this had limited effect on the fit to data collected during the experiment. However, some discrepancies remain with the capacity of the edge site on the colloids (Site 2) in comparison with the laboratory sorption experiments, the capacity used in this study being at least an order of magnitude lower when normalised to the amount of clay used in the laboratory and field experiments. It is possible that the other radionuclides in the injection cocktail are competing with caesium to sorb on the selective edge site (Site 2). Missana et al. (2014b)

showed that competitive sorption of other cations (particularly K<sup>+</sup>) reduced K<sub>d</sub> values of caesium sorption to smectite-rich clays, and this was identified as an area of required research for other radionuclides in Bradbury and Baeyens (2005). Competitive sorption could result in a lower apparent capacity for caesium sorption to the strong edge sites in the field migration experiments compared with what was detected in the laboratory experiments. However, this requires further investigation.

### 7.3. Uranium model calibration

Uranium-233 was injected in both CFM Run 13-05 and CRR Run 32, at the mass and concentrations in Table 7.7, as measured using ICP-MS. Uranium showed different colloid-bound fractions in the injection cocktails of the two experiments, with a value of 83.5% in CFM Run 13-05 and 6% in CRR Run 32. The cause of this difference is discussed in the following sections.

	CFM Run 13-05: <sup>233</sup> U	CRR Run 32: <sup>233</sup> U
Mass (M <sub>0</sub> )	0.225 µg	20.2 µg
Concentration (C <sub>0</sub> )	0.07 µg/l <sup>1</sup>	202 µg/l
Initial 'Colloid-bound' fraction/ Mass removed by centrifugation	83.5%/ 0.18 µg	6%/ 1.2 µg
Cocktail equilibration time	35 days <sup>2</sup>	5 days
Colloid mass	Total: 224.3 mg	2.01 mg

1: Peak concentration in re-circulation circuit

2: Value measured after 401 days due to equipment problems

**Table 7.7 Mass and concentration of uranium used in CFM Run 13-05 and CRR Run 32**

#### 7.3.1. Geochemical conceptual model

Geochemical modelling was carried out by Dr Janice Kenney using PHREEQC (as detailed in Appendix A), modelling the injection cocktails, using the SIT database collated by Andra. This provided information on the potential precipitates and uranium aqueous

speciation in both experiments. Figure 7.16 and Figure 7.17 show the predicted speciation of uranium in CFM Run 13-05 and CRR Run 32 respectively, and Figure 7.18 and Figure 7.19 show the predicted saturation indices for uranium precipitates in CFM Run 13-05 and CRR Run 32 respectively.

PHREEQC predicts that at the Eh and pH values of reference Grimsel groundwater (pH 9.6, Eh -220mV, Bennett, (2014)), uranium will be mostly present as uranium (VI), with some low concentrations (<1%) of uranium (IV) additionally present. Additional modelling showed that as Eh values decrease to -260mV and -280mV, increasing amounts of uranium is found as uranium (IV), with as much as 10-20% uranium predicted to be uranium (IV). These Eh values are within the potential range of Eh values for the injection cocktail solutions (the measured experimental error is  $\pm 50$ mV (Schäfer, pers. Comm.)), meaning that more uranium (IV) could be present in the injection cocktail than suggested by the PHREEQC modelling. Uranium (VI) is expected to be more mobile than uranium (IV), as uranium (IV) undergoes more adsorption processes (Dittrich and Reimus, 2015a). In addition, it is important to note that the PHREEQC model does not include colloid surfaces, which means that processes such as surface-mediated reduction to uranium (V) or (IV) will not be included in the model. Surface-mediated reduction of uranium (VI) has been observed in the presence of montmorillonite containing Fe(II) (Tsarev et al., 2016).

The geochemical modelling predicts that the majority of uranium in the two experiments should be present as neutral or negatively charged ternary complexes ( $\text{CaUO}_2(\text{CO}_3)_3^{2-}$  and  $\text{Ca}_2\text{UO}_2(\text{CO}_3)_3$ ). These complexes make uranium highly mobile in the high

pH of Grimsel groundwater, as the likelihood of sorption of the neutral or negatively charged species to the negatively charged rock surfaces is reduced (Dittrich and Reimus, 2015a).

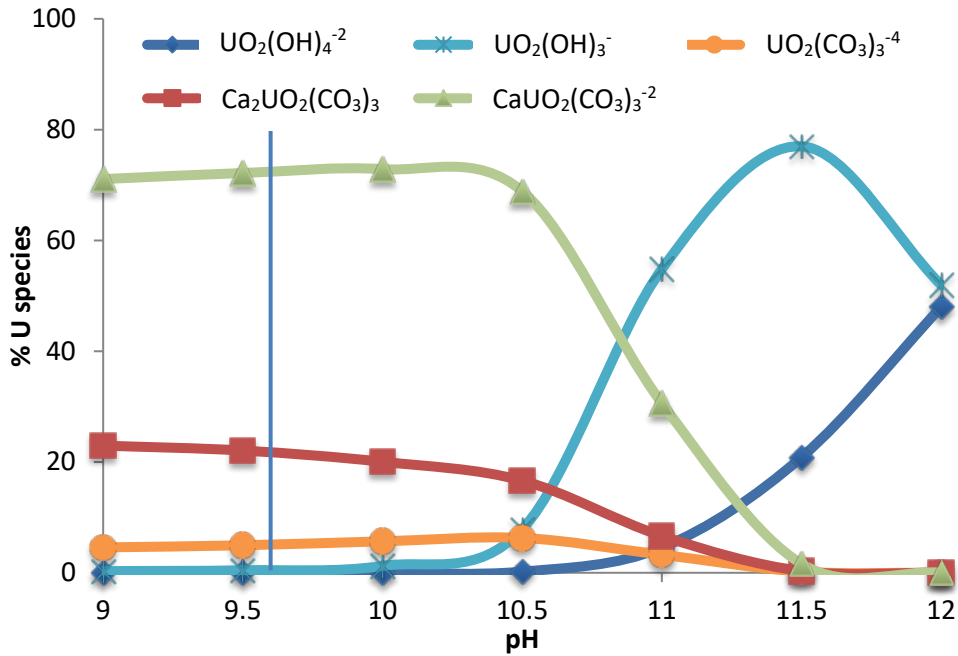


Figure 7.16 Predicted uranium speciation in CFM Run 13-05 from PHREEQC. Blue line = Grimsel groundwater pH (9.6). This modelling assumes an  $E_h(\text{SHE}) = -220\text{mV}$

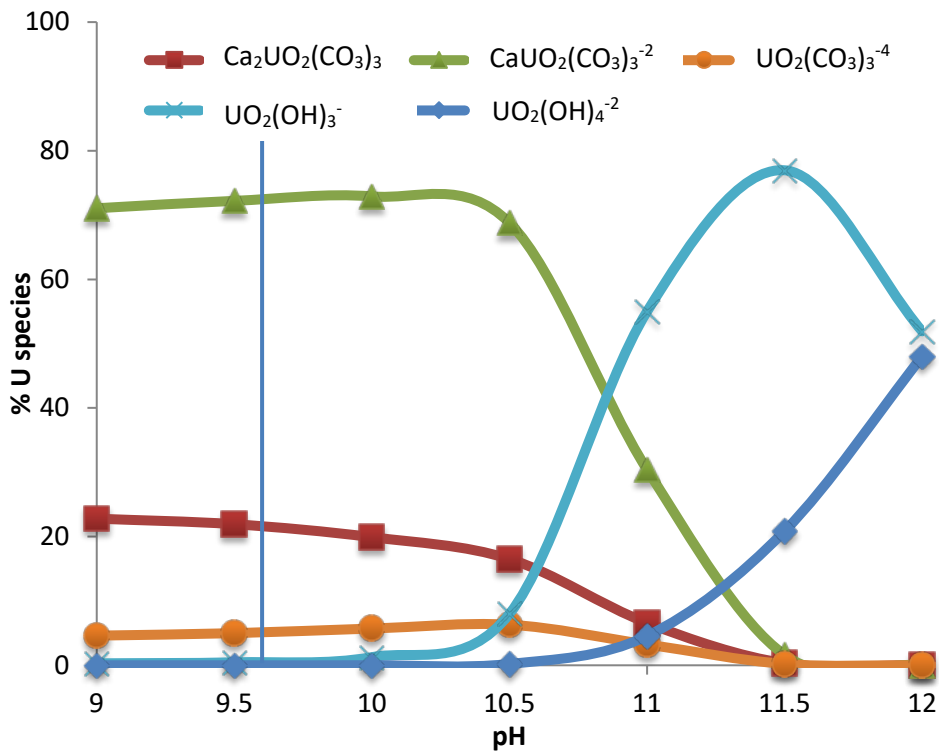


Figure 7.17 Predicted uranium speciation in CRR Run 32 from PHREEQC. Blue line = Grimsel groundwater pH (9.6). This modelling assumes an  $E_h(\text{SHE}) = -220\text{mV}$

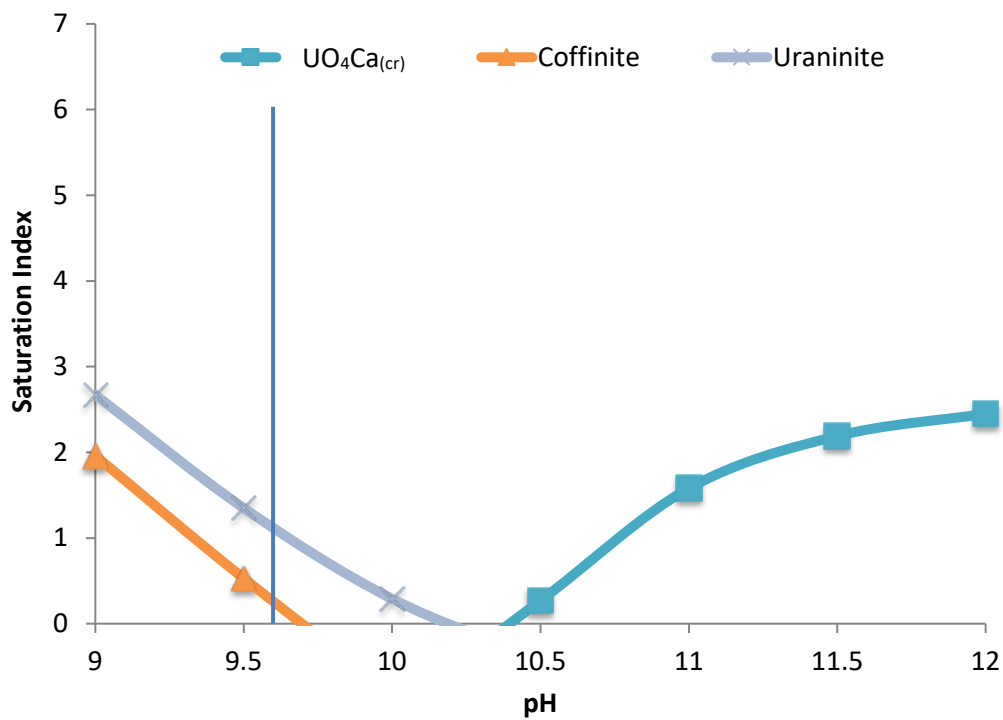


Figure 7.18 Predicted saturation indexes in CFM Run 13-05 for uranium precipitates. Blue line = Grimsel groundwater pH (9.6). This modelling assumes an  $E_h (SHE) = -220mV$

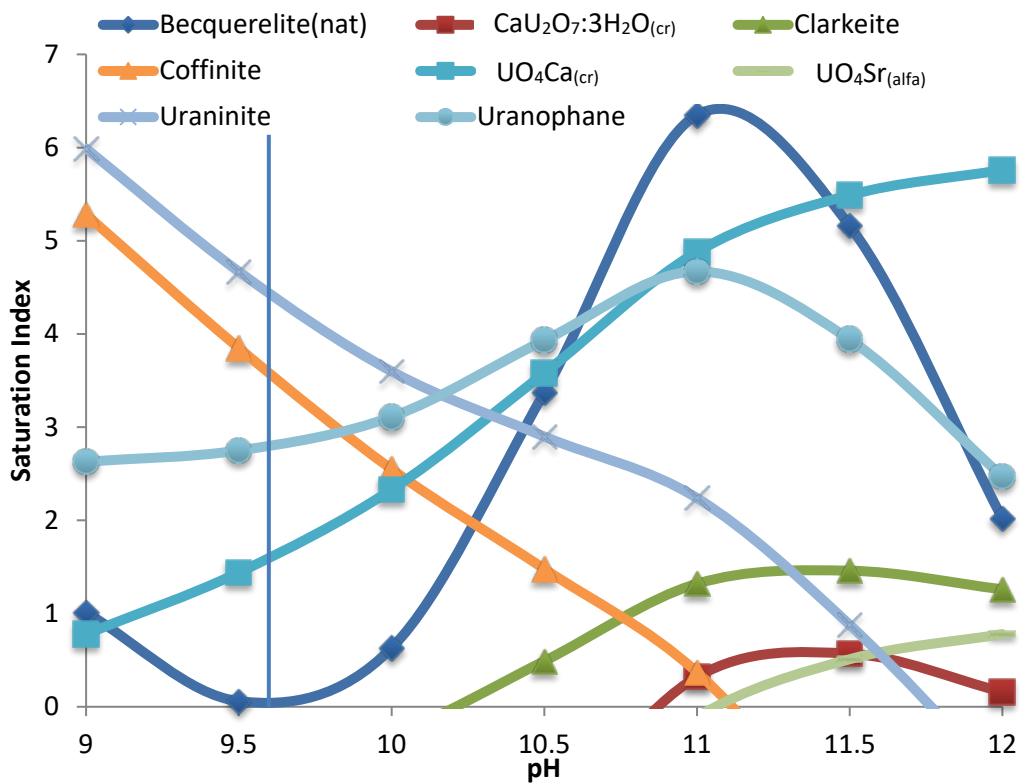


Figure 7.19 Predicted saturation indexes in CRR Run 32 for uranium precipitates. Blue line = Grimsel groundwater pH (9.6). This modelling assumes an  $E_h (SHE) = -220mV$

Laboratory experiments testing uranium (VI) sorption to Grimsel FFM observed no sorption in the presence of FEBEX bentonite colloids (Huber et al., 2011), but slow sorption in the presence of Zn-/ Ni- montmorillonite (Huber et al., 2015). This difference is believed to be caused by lower Eh in the montmorillonite experiment, causing reduction of uranium (VI) to uranium (IV) (Huber et al., 2015). Kinetic effects were observed for the sorption of uranium (VI) to Grimsel FFM and granodiorite by Missana and Geckeis (2006), which is also thought to be caused by the slow reduction of uranium (VI) to uranium (IV) during these experiments carried out over 18 weeks. In batch and column experiments detailed in Dittrich and Reimus (2015a), no sorption to Grimsel granodiorite was observed at pH 8.8. This is probably due to the fact that these experiments were carried out in oxidising conditions and were of limited duration (1000 minutes and 20 hours for the batch and column experiments respectively), which meant that no reduction to uranium (IV) and subsequent sorption could take place.

Laboratory experiments testing uranium (VI) sorption to FEBEX bentonite colloids did observe sorption to FEBEX colloids (Missana and Geckeis, 2006; Missana et al., 2004). Kinetic effects were observed, with full sorption equilibrium not being reached until ~18 weeks (Missana and Geckeis, 2006). This could be caused by a slow kinetic sorption process, or additionally by the slow reduction of uranium (VI) to uranium (IV) and subsequent sorption to the colloids (Missana and Geckeis, 2006). Other experiments observed no sorption of uranium (VI) to FEBEX bentonite colloids (Huber et al., 2011), and limited sorption to synthetic Ni- labelled montmorillonite colloids (Huber et al., 2015). Huber et al. (2011) undertook their experiments at a higher Eh than Missana and Geckeis (2006), Missana et al. (2004) and Huber et al., (2015) used, limiting the potential for uranium (VI) reduction to

uranium (IV) and subsequent sorption to, or precipitation on, the colloids. Lower Eh values used in Huber et al.'s (2015) experiments potentially allowed for some uranium reduction and limited sorption to the Ni- montmorillonite colloids. In addition, the sorption period of the experiments of the latter two studies lasted 24 hours, which meant that there was limited time for reduction to take place.

A higher initial bound fraction of uranium was measured in CFM Run 13-05 (83.5%) than in CRR Run 32 (6%), although due to the higher concentrations used in CRR Run 32, a larger mass of uranium is removed from solution (1.2  $\mu\text{g}$ ) than in CFM Run 13-05 (0.19  $\mu\text{g}$ ). It is normally assumed that the amount of uranium removed from solution by centrifugation (and therefore the initial bound fraction) is caused by radionuclide sorption to colloids. A potential cause of the different initial bound fractions could be the different injection cocktail equilibration times (5 days for CRR Run 32, 35 days for CFM Run 13-05). The longer equilibration time in CFM Run 13-05 could have allowed for more reduction from uranium (VI) to uranium (IV) and subsequent sorption to occur, causing the higher percentage of uranium removed from solution and therefore the higher initial bound fraction.

Another potential cause of the different bound fraction is the formation of precipitates in the injection cocktail. The PHREEQC model predicts positive saturation indices for several uranium solid phases for both experiments. Due to the higher uranium concentration in CRR Run 32, higher saturation indices are predicted for this experiment, but the low initial bound fraction suggests that limited precipitates formed in this experiment. This is even though several minerals in CRR Run 32 are several orders of magnitude (up to  $\sim 5$ ) oversaturated. It is important to note that the precipitates with the highest saturation

indices in CRR Run 32 (coffinite and uraninite) are both uranium (IV) mineral phases, whereas the precipitates with the lower saturation indices (uranophane,  $\text{UO}_4\text{Ca}$  and becquerelite) are all uranium (VI) mineral phases. The low initial bound fraction in CRR Run 32 could therefore be caused by the uranium remaining as uranium (VI) in the injection cocktail and therefore the uranium (IV) mineral phases with the highest saturation indices are not precipitating, maintaining oversaturation in the injection cocktail.

The higher initial bound fraction in CFM Run 13-05 suggests that precipitates potentially formed in the cocktail of this experiment. This could have been due to the longer cocktail equilibration time allowing for the reduction and subsequent precipitation of the oversaturated uranium (IV) precipitates (coffinite and uraninite). It has not been possible to confirm whether these self-colloids formed, as no imaging of the injection cocktail has been carried out. As it has not been possible to confirm whether the precipitates formed, the model assumes that any uranium precipitates migrate in the experiment like colloid-bound uranium.

Potential non-linear sorption has been observed for uranium sorption to FEBEX bentonite colloids (Missana and Geckeis, 2006), which could be caused by precipitation at higher concentrations, or partial reduction of uranium (VI). Additionally, it is possible that there are different sorption sites or mechanisms controlling sorption to the bentonite, as both ionic exchange and surface complexation could have occurred (Missana et al., 2004). Surface complexation is expected to be the most important mechanism for uranium interaction with bentonite colloids at the high pH of Grimsel groundwater (Missana and Geckeis, 2006; Missana et al., 2004). Although higher concentrations of uranium were used

in CRR Run 32 ( $8.6 \times 10^{-7}$  mol/l) compared with CFM Run 13-05 ( $4.3 \times 10^{-10}$  mol/l), the laboratory experiments do not show conclusively that a non-linear sorption isotherm will cause the different initial bound fractions (Missana et al., 2004; Missana and Geckeis, 2006).

Iron (II) mineral phases, such as magnetite can incorporate uranium (VI), effectively immobilising it (Marshall et al., 2015; Nico et al., 2009). In addition, magnetite can reduce and incorporate uranium (VI) to uranium (V) (Roberts et al., 2017). PHREEQC modelling of Grimsel groundwater shows that magnetite is oversaturated at pH and Eh of Grimsel groundwater (see Chapter 3). It is therefore possible that this process could have occurred in the injection cocktail of the two experiments if magnetite precipitates in the injection cocktail. The experiments and models detailed above consider uranium (V) to be a transition phase between uranium (VI) and uranium (IV). However, as there is very limited information about the migration behaviour of uranium (V) and there are no data as to whether magnetite did precipitate in the injection cocktail, this process needs further study before inclusion in the transport model.

An additional influence on uranium speciation, and therefore sorption, is carbonate concentration, especially at the high pH of Grimsel groundwater. Experiments found that uranium (IV) sorption is stronger at lower concentrations of atmospheric CO<sub>2</sub> and dissolved inorganic carbon (Tournassat et al., 2018). Potential differences in the injection cocktail preparation could have caused differences in carbonate concentrations and therefore the different initial bound fraction. In addition, uranium sorption shows pH dependence, typically with weaker sorption at higher pH values (pH > 7) (Tsarev et al., 2016; Tournassat et al., 2018). Differences in the way radionuclides are added to the injection cocktail (at acidic

pH and undergoing pH adjustment) could have caused the different initial bound fractions. However, as limited information exists about the preparation of the injection cocktail for CFM Run 13-05 (at the time of writing), it has not been possible to confirm whether differences in the injection preparation caused the differences in the initial bound fractions.

Uranium behaviour is also altered by the presence of bacteria and phosphate, as bacteria can cause the reduction of uranium (VI) to uranium (IV) (Renshaw et al., 2005), or cause the precipitation of uranium (IV) phosphate minerals (Kenney et al., 2018), which can in turn cause further uranium sorption to these phosphate minerals (Troyer et al., 2016). Additional modelling using PHREEQC, using a concentration of phosphate equivalent to the total phosphate available from the number of bacterial cells found in Grimsel groundwater shows no differences in uranium speciation or expected precipitation. Therefore, it is unlikely that differences in bacterial cell counts between the two experiments caused the different initial bound fractions of uranium.

In summary, the different uranium initial bound fractions are likely to be caused by the different cocktail equilibration time for the two experiments. Although added as uranium (VI) into both experimental injection cocktails, it is likely that the longer cocktail equilibration time in CFM Run 13-05 allowed for more reduction to uranium (IV). The uranium (IV) either then underwent stronger sorption to the colloids (than uranium (VI)), or formed uranium (IV) self-colloids, both options causing a higher initial bound fraction. For CRR Run 32, the low initial bound fraction suggests that the uranium remained as uranium (VI) in the injection cocktail. This is due to the fact that uranium (VI) is expected to only weakly sorb to the colloids, and despite the high saturation indices for several uranium (IV)

minerals, the low initial bound fraction suggests that no self colloids formed in the experiment, as uranium remained as uranium (VI).

### 7.3.2. Transport Model setup

The model for uranium transport is as described in the Chapter 6 for americium and plutonium transport, but with the addition of the matrix diffusion equation (Equation 4.10), which couples to the equation for aqueous uranium transport (Equation 4.6). This was added to the model primarily for CRR Run 32, in which the falling limb of the uranium breakthrough curve follows the  $t^{-3/2}$  pattern (as shown in Figure 7.20) that indicates matrix diffusion (Smith et al., 2006). The model used the values of the non-calibration parameters given in Table 7.8.

Parameter	Symbol	CFM Run 13-05	CRR Run 32	Justification
Radioactive decay constant	$\lambda_d$	1.38x10 <sup>-13</sup> (1/s)		Based on isotope values (not expected to be significant in experiment)
Initial bound fraction		83.5%	6%	Experimentally measured
Initial unbound/ aqueous fraction		16.5%	94%	Experimentally measured

Table 7.8 Non-calibration parameters for uranium model

The calibration parameters for uranium transport in the model were: the sorption and desorption rate to mobile colloids ( $k_{amc}$  and  $k_{mca}$ ), the desorption rate from immobile colloids ( $k_{ica}/k_{icai}$ ), the aqueous uranium retardation factor (R), the matrix diffusion transfer rate ( $k_{im}$ ) and the matrix porosity multiplied by the matrix extinction length (a distance where matrix diffusion is no longer expected to be significant) ( $\theta_{im}$ ).

### 7.3.3. Model Results

The results of the calibrated model for uranium breakthrough in CFM Run 13-05 and CRR Run 32 are shown in Figure 7.20, which used the values of the calibrated parameters in Table 7.9. As Table 7.9 shows, although consistent parameters were found to describe the interaction of uranium with colloids and matrix diffusion, a different retardation factor was used for aqueous uranium and potential reasons for this difference are discussed below.

Parameter	Symbol	CFM Run 13-05	CRR Run 32
Sorption rate to mobile colloids	$k_{amc}$	$1 \times 10^{-8} \text{ m}^3/\text{kg.s}$ ( $3.6 \times 10^{-5} \text{ m}^3/\text{kg.hr}$ )	
Desorption rate from mobile colloids	$k_{mca}$	$6 \times 10^{-6} \text{ 1/s}$ ( $0.0216 \text{ 1/h}$ )	
Desorption rate from immobile colloids	$k_{ica}/k_{icai}$		
Aqueous phase retardation factor	$R$	1000	1.3
Matrix diffusion transfer rate	$k_{im}$	$1.9 \times 10^{-4} \text{ (1/s)}$	
Matrix porosity/ extinction length	$\theta_{im}$	5	

Table 7.9 Calibrated parameter values for uranium model

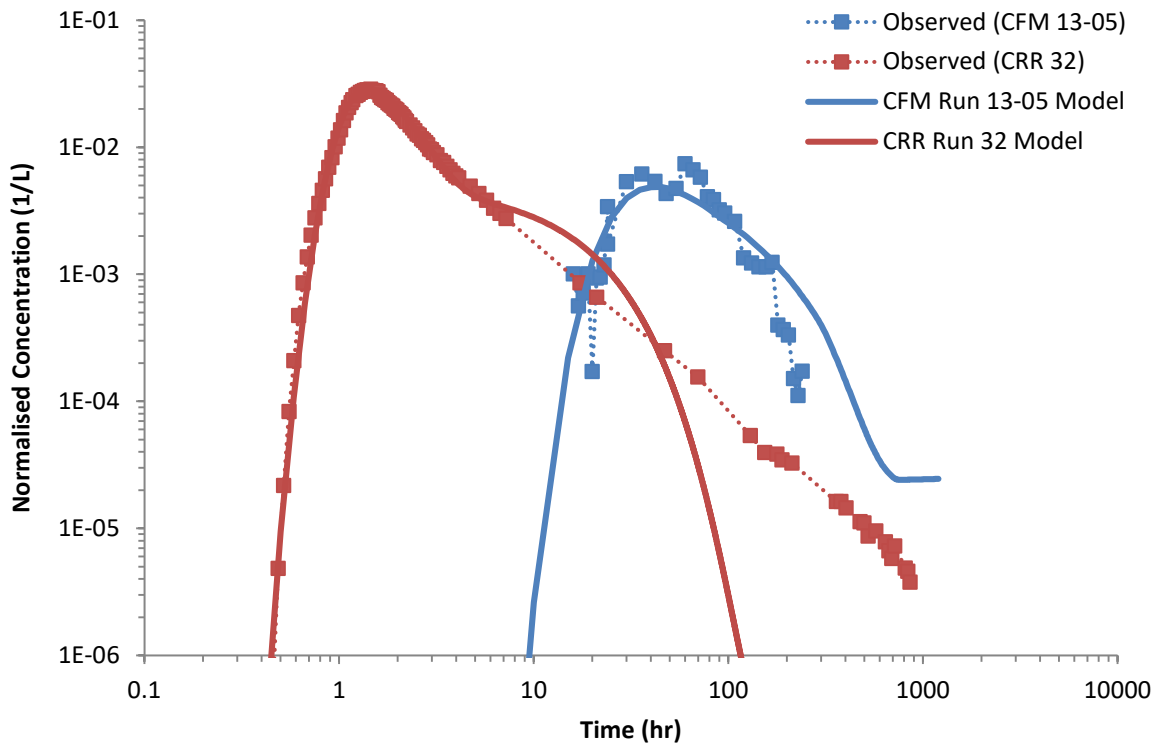


Figure 7.20 Calibrated model results for uranium breakthrough in CFM Run 13-05 and CRR Run 32

***CFM Run 13-05***

The modelled breakthrough of uranium-233 in CFM Run 13-05 is shown on a linear scale in Figure 7.21, with a comparison between the modelled and observed cumulative recovery shown in Figure 7.22. The model shows a good match to the rising limb and the peak of the breakthrough curve, but the model shows slightly higher concentrations on the falling limb of the breakthrough curve, as was found for other radionuclide models in CFM Run 13-05. Again, it is important to note that this calibration result has carried forward any error in the conservative tracer or colloid calibration, and it is likely that improvements to the fit of colloid breakthrough would improve the model results. Despite this, the modelled recovery (17%) compares extremely well to the experimental recovery (15%), as measured using ICP-MS.

The results of a model run using the parameters and processes used to model CRR Run 32 are also shown in Figure 7.21 (using the parameters in Table 7.9). This model run gives a poor model match to the experimental data due to the second peak, which is caused by the breakthrough of aqueous uranium that has undergone matrix diffusion.

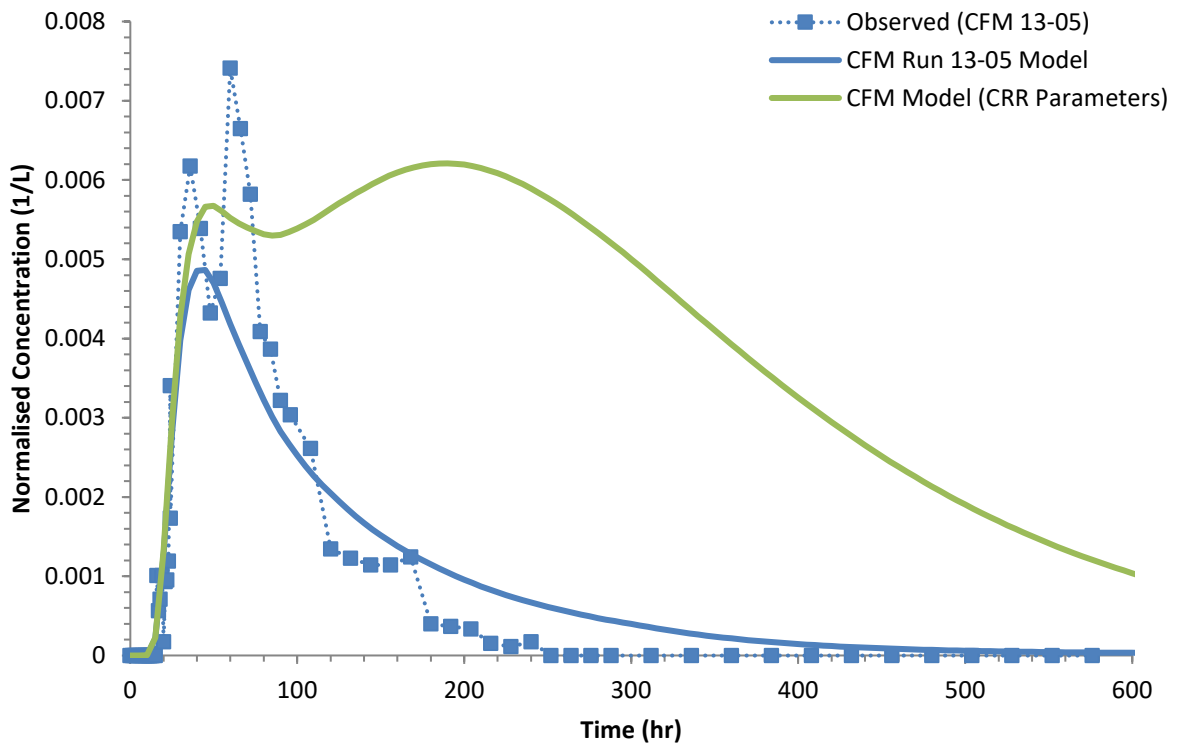


Figure 7.21 Calibrated model breakthrough for uranium-233 in CFM Run 13-05 (Blue line = CFM Run 13-05 model; Green line = Model run using CRR Run 32 parameter values)

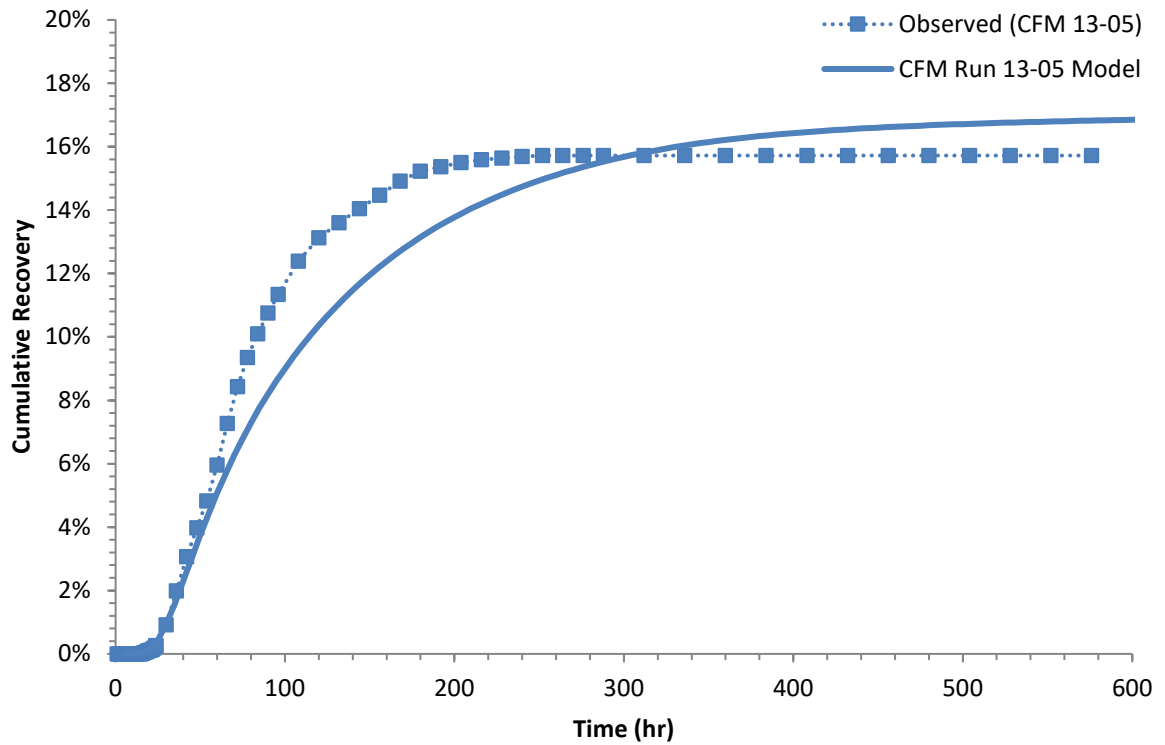


Figure 7.22 Comparison of cumulative recovery for observed and modelled data for <sup>233</sup>U in CFM Run 13-05

### ***CRR Run 32***

The modelled breakthrough of uranium-233 in CRR Run 32 is shown on a semi-log scale in Figure 7.23, with a comparison between the modelled and observed cumulative recovery in Figure 7.24. The model shows a good match on a semi-log scale, with an excellent match to the peak and rising limb of the breakthrough curve, but has difficulty replicating the  $t^{-3/2}$  tailing observed in the falling limb past 10 hours on the breakthrough (as shown in more detail in Figure 7.20). Changes to how matrix diffusion and sorption to matrix pores are represented in the model could improve this model fit. Despite this, the modelled recovery (98%) compares well to the experimental recovery measured by ICP-MS (103%  $\pm$ 5%), and is slightly higher than the recovery as measured by  $\alpha$ -spectroscopy (80%) (which was measured in a pair with  $^{237}\text{Np}$ , and assumes that these two radionuclides are expected to have a similar recovery).

Also shown in Figure 7.23 is a model run that used the model parameters used for CFM Run 13-05 (parameters given in Table 7.9), which shows a poor match to the experimental data as the model breakthrough of purely colloid-bound uranium is too low to match the experimental data.

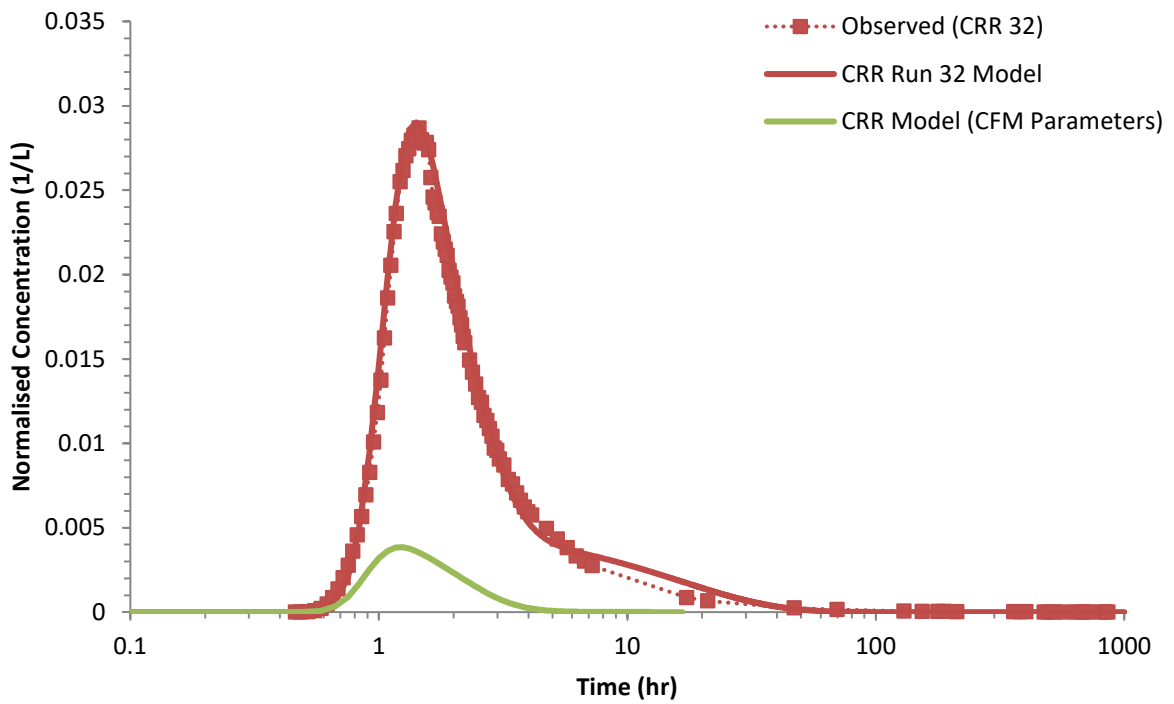


Figure 7.23 Calibrated model breakthrough for uranium-233 in CRR Run 32. Green line = CFM Run 13-05 model parameter values.

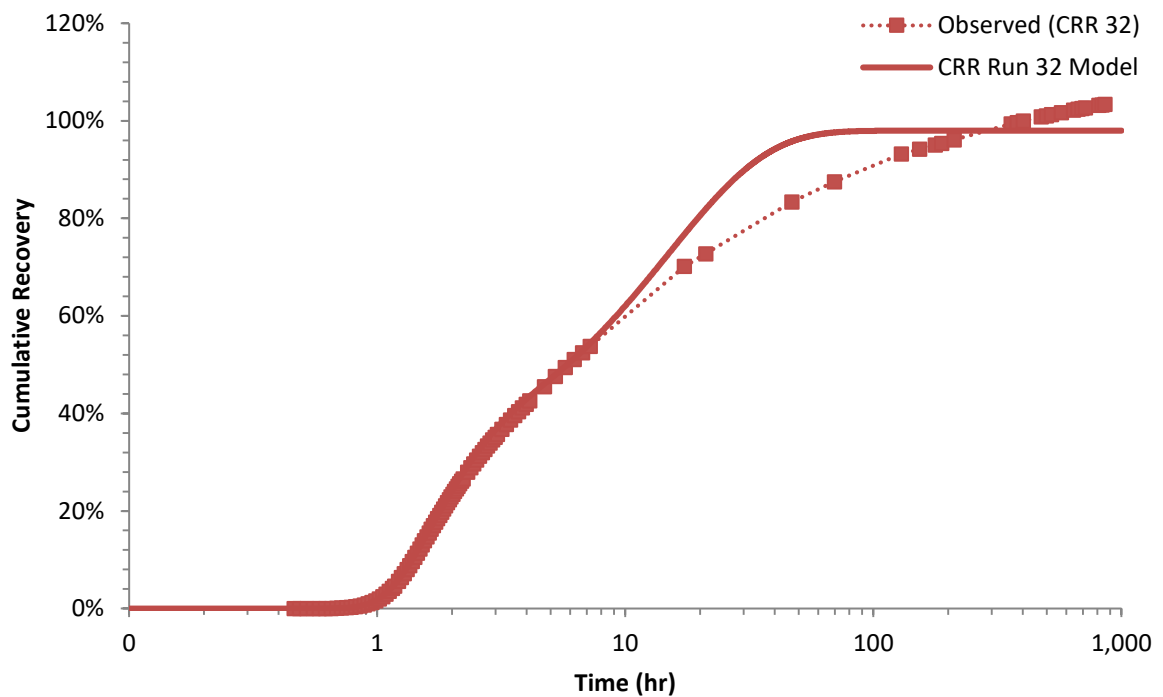


Figure 7.24 Comparison of cumulative recovery for observed and modelled data for <sup>233</sup>U in CRR Run 32

### 7.3.4. Discussion and Conclusions

Although good model matches were found to uranium breakthrough in the two migration experiments, different parameters were used to represent the different experiments. Figure 7.25 shows the contribution of the different phases to modelled breakthrough curves. In CFM Run 13-05, colloid-bound uranium contributes the most to breakthrough; however, in CRR Run 32 aqueous uranium is important to breakthrough. Therefore, the transport of uranium is only facilitated by colloids in CFM Run 13-05.

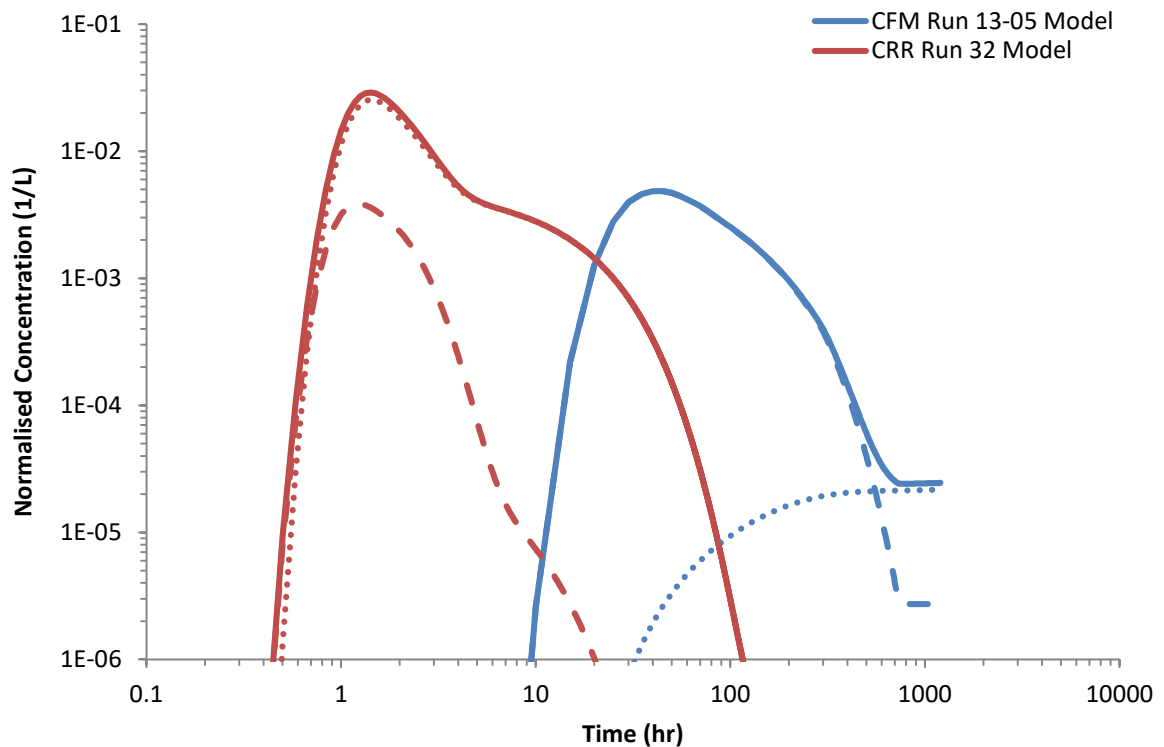


Figure 7.25 Contribution of different uranium phases to modelled breakthrough curves in CFM Run 13-05 and CRR Run 32. Total = Solid line; Colloid-bound = Dashed line; Aqueous = Dotted line.

As Table 7.9 shows, different retardation factors were used for aqueous uranium in the two experiments. This is the main difference in calibration parameters (with the other difference being the initial colloid-bound fractions). Although not the only potential cause, the conceptual model discussed in Section 7.3.1 identified the different equilibration times

as the main factor causing the different initial bound fractions in the injection cocktail. The longer time in CFM Run 13-05 allowed for more of the uranium (VI) to reduce to uranium (IV) and subsequently sorb to the colloids, or form uranium (IV) precipitates. Because of this, more uranium could be present as uranium (IV) in CFM Run 13-05 than CRR Run 32. As uranium (IV) undergoes stronger sorption processes to rock surfaces than uranium (VI) (Dittrich and Reimus, 2015a), a higher retardation factor in CFM Run 13-05 would be expected. In CRR Run 32, the lower retardation factor is consistent with the expectation that the majority of uranium is present as uranium (VI) during the experiment.

Although different retardation factors were required and independently calibrated to account for the expected differences in redox state, consistent sorption and desorption rates to the colloids were used for the two experiments, although these parameters had limited impact on uranium breakthrough in CRR Run 32. The sorption rate to colloids ( $k_{amc}$ ), although included as a calibration parameter in Table 7.9, was found to have a limited effect on the breakthrough curves in either experiment, and so was not changed from its initial value. The desorption rate used in the model ( $0.021 \text{ h}^{-1}$ ) compares well to the desorption rate used in the CFM Run 13-05 model in Reimus, (2016) ( $0.02 \text{ h}^{-1}$ ), although the rate is much lower than the rate used in the model of CRR Run 32 ( $10 \text{ h}^{-1}$ ) in the same report.

No laboratory data of desorption kinetics of uranium in Grimsel groundwater exist to compare with, as limited sorption to the colloids was observed in these experiments (Huber et al., 2011, 2015). Although not carried out in Grimsel groundwater, Sherriff et al. (2015) measured a desorption rate for uranium (VI) from bentonite colloids of  $0.002 \text{ h}^{-1}$ , which is

lower than the desorption rate used in this model, but it is difficult to compare these values directly due to the different groundwater chemistry used in this experiment.

Consistent matrix diffusion parameters were used for the two models. Due to colloid-bound uranium being more important to breakthrough in CFM Run 13-05, the breakthrough was insensitive to changes to matrix diffusion parameters as it is only applied to aqueous uranium (the model assumes that colloids do not undergo matrix diffusion). Therefore, these parameters were chosen to provide a better match to breakthrough in CRR Run 32. Due to the different formulations used to describe matrix diffusion, it is not possible to compare the parameter values here to those in Reimus (2016).

Long term breakthrough data of uranium were measured in CFM Run 13-05 using accelerator mass spectroscopy (AMS) (Quinto et al., 2017), but this data were not available for model calibration. If this data were available, it would be possible to further calibrate the breakthrough of aqueous uranium, potentially including kinetic sorption to granodiorite/fracture fill material, as was observed in some laboratory experiments (Missana and Geckeis, 2006).

To conclude, uranium breakthrough has been successfully modelled for the two experiments. Different aqueous uranium retardation factors were used, which reflects the different initial bound fractions. These were probably caused by a different cocktail equilibration time, thus allowing for more uranium (VI) reduction and subsequent sorption to the colloids, or the precipitation of uranium (IV) self colloids in CFM Run 13-05. As uranium (IV) undergoes stronger sorption processes, more sorption to the rock surfaces occurred in CFM Run 13-05, making colloid-bound uranium more important in the

breakthrough curve. In CRR Run 32, uranium migrates in the experiment largely as slightly retarded aqueous uranium (VI), undergoing matrix diffusion. Further investigation of these hypothesis' would be useful if a similar migration experiment is run in the future. This could include detailed investigation of the source term to confirm uranium speciation and redox state, determination of the type of colloid facilitating transport (whether bentonite or self colloid) and measurement of a 'final bound fraction', which will help to confirm the conceptual model used and further constrain the transport model.

#### 7.4. Neptunium model calibration

Neptunium-237 was injected in both CFM Run 13-05 and CRR Run 32, at the mass and concentrations in Table 7.10. ICP-MS was used to measure the concentration and recovery. Of the radionuclides modelled in this study, neptunium had the lowest initial 'colloid-bound' fraction (30.9% in CFM Run 13-05 and <1% CRR Run 32). The cause of this and the different initial colloid- bound fractions is discussed further below.

	<b>CFM Run 13-05:</b> <sup>237</sup> Np	<b>CRR Run 32:</b> <sup>237</sup> Np
Mass (M <sub>0</sub> )	4.59 µg	25.8 µg
Concentration (C <sub>0</sub> )	1.43 µg/l <sup>1</sup>	258 µg/L
Initial 'Colloid-bound' fraction/ Mass removed by centrifugation	30.9%/ 1.41 µg	0 - 1%/ <0.258 µg
Cocktail equilibration time	35 days <sup>2</sup>	5 days
Colloid mass	Total: 224.3 mg	2.01 mg

1: Peak concentration in re-circulation circuit

2: Value measured after 401 days due to equipment problems

**Table 7.10 Mass and concentration of neptunium used in CFM Run 13-05 and CRR Run 32**

##### 7.4.1. Geochemical conceptual model

PHREEQC modelling was carried out by Dr Janice Kenney to determine the speciation and saturation indices of solid neptunium phases in both CFM Run 13-05 and CRR Run 32

(see Appendix A for more details). Figure 7.26 and Figure 7.27 show the predicted speciation of neptunium in CFM Run 13-05 and CRR Run 32 respectively. Figure 7.28 and Figure 7.29 show, respectively, the predicted saturation indices of solid neptunium phases for the two experiments.

PHREEQC predicts that in both experiments neptunium will be present in the Np(IV) redox state at the Eh value used (-220mV, the average value for Grimsel groundwater (Bennett, 2014)). In both experiments and at the pH of Grimsel groundwater (pH 9.6), the vast majority of neptunium is predicted to be present as neutrally charged  $\text{Np(OH)}_4$ , with a small percentage additionally present as  $\text{Np(CO}_3\text{)(OH)}_3^-$ . In both experiments  $\text{NpO}_{2(s)}$  and an amorphous hydrated  $\text{NpO}_2$  species are both predicted to have positive saturation indices, with higher saturation indices in CRR Run 32 due to the higher concentration of neptunium used.

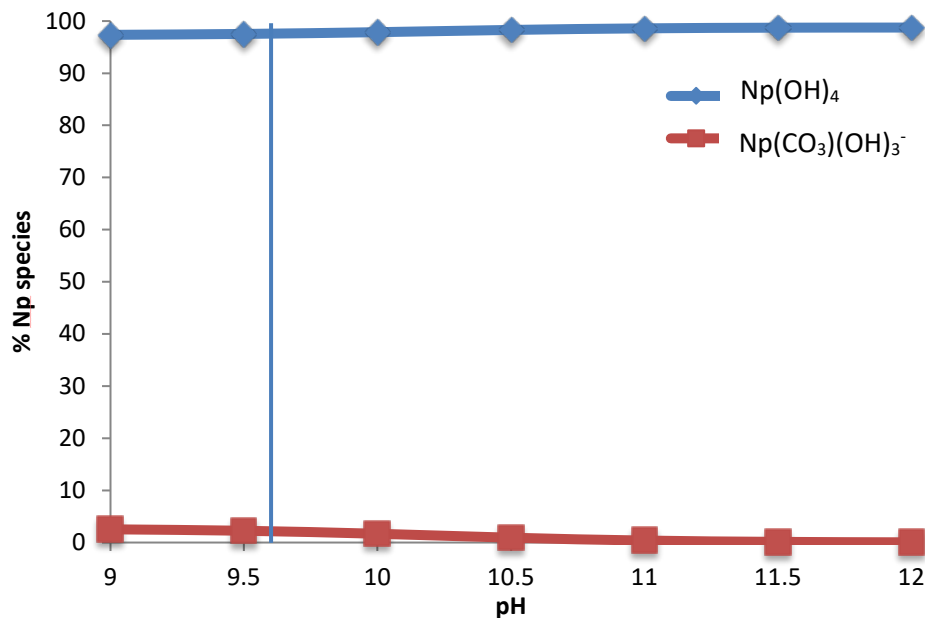


Figure 7.26 Predicted neptunium speciation in CFM Run 13-05 from PHREEQC. Blue line = Grimsel groundwater pH (9.6)

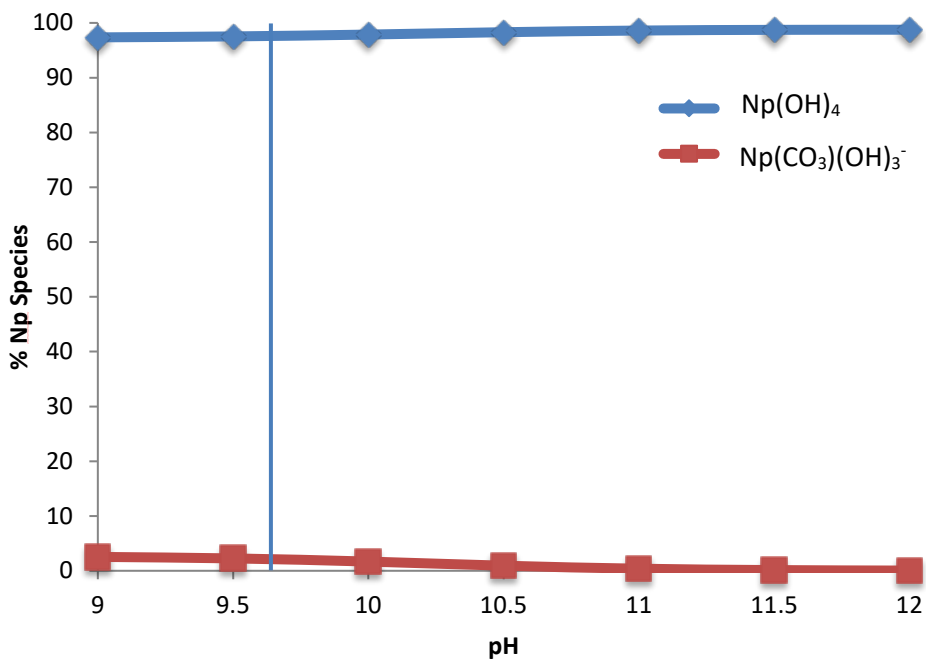


Figure 7.27 Predicted neptunium speciation in CRR Run 32 from PHREEQC. Blue line = Grimsel groundwater pH (9.6)

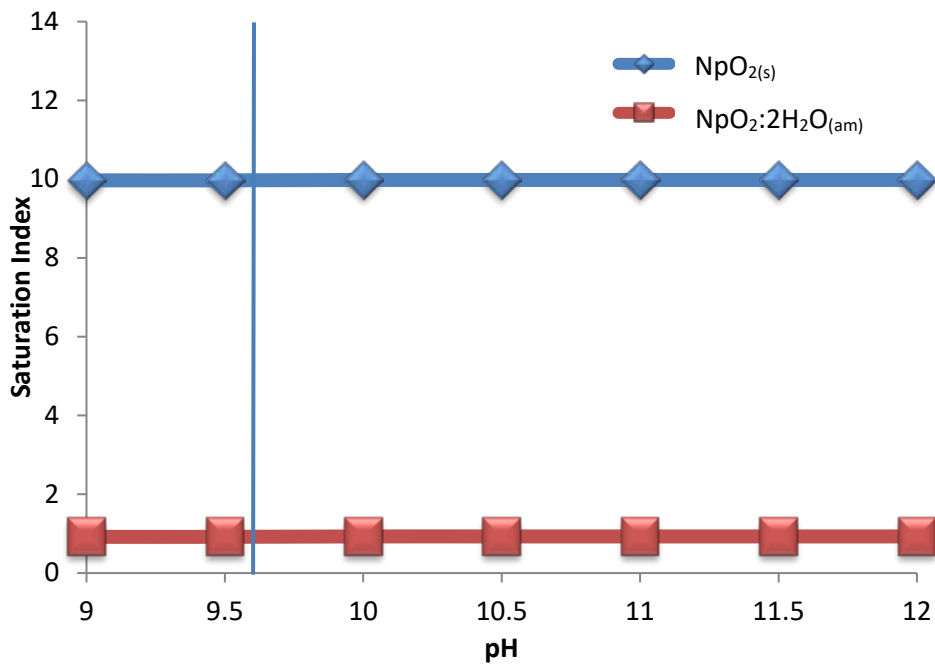


Figure 7.28 Predicted saturation indexes in CFM Run 13-05 for neptunium precipitates. Blue line = Grimsel groundwater pH (9.6)

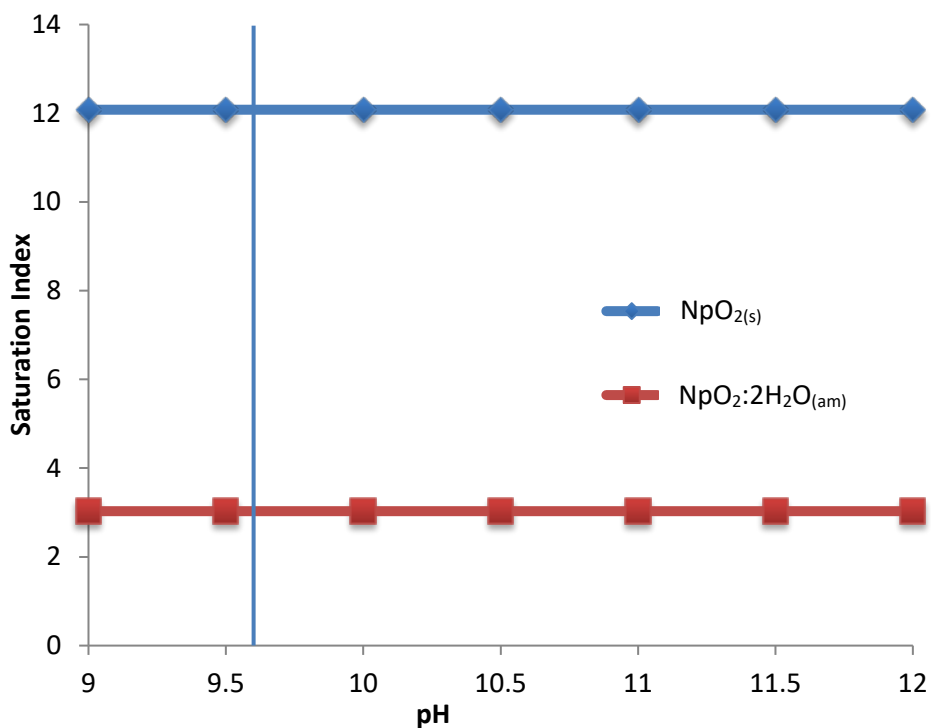


Figure 7.29 Predicted saturation indexes in CRR Run 32 for neptunium precipitates. Blue line = Grimsel groundwater pH (9.6)

Neptunium can be present in redox states between neptunium (III) and neptunium (VI), but is more likely to exist as neptunium (IV) or neptunium (V) in natural waters (Duro et al., 2000). At the average Eh of Grimsel groundwater (-220mV (Bennett, 2014)), PHREEQC predicts that neptunium is expected to be present in Grimsel groundwater as neptunium (IV), which was also found in earlier geochemical modelling carried out during the CRR project (Missana and Geckeis, 2006; Duro et al., 2000). However, laboratory experiments carried out during CRR found that neptunium was stable as oxidised neptunium (V) in reducing Grimsel groundwater (Eh ~ -220mV) (Missana and Geckeis, 2006). Because of this, in CRR Run 32 neptunium was added to the injection cocktail as neptunium (V) (Möri et al., 2004), which differs from the results of the geochemical modelling. This was also the case for the injection cocktail of CFM Run 13-05 (Schäfer, pers. Comm.). It is important to consider the redox state of neptunium, as neptunium (IV) is less soluble and is considered to

undergo sorption to rock surfaces, whereas neptunium (V) is thought to be relatively mobile as its speciation ( $\text{NpO}_2^+$ ) is thought to undergo weak sorption to rock surfaces (Reimus, 2016; Schmeide and Bernhard, 2010; Zavarin et al., 2012; Marsac et al., 2015; Müller et al., 2015). Neptunium (IV) has been observed to undergo colloid-facilitated transport by bentonite in laboratory columns, although these experiments were not carried out in Grimsel groundwater (Nagasaki et al., 1999).

One drawback to the PHREEQC modelling is that it does not include the presence of the colloid surfaces in the injection cocktail, and so processes such as surface-mediated reduction of neptunium (V) to neptunium (IV) will not be included. Partial surface-mediated reduction of neptunium (V) to neptunium (IV) has been observed on illite surfaces (Marsac et al., 2015), especially at pH values where neptunium (V) sorption is weak. These experiments also noted increased neptunium sorption with decreasing Eh due to this reduction process. In oxic conditions, Zavarin et al. (2012) did not observe surface mediated reduction of neptunium (V) on the surface of montmorillonite. As the migration experiments were carried out in reducing conditions, it is possible that colloid surfaces in the injection cocktail could have facilitated some reduction of neptunium (V) to neptunium (IV) during the cocktail equilibration time before the experiments.

Sorption experiments investigating neptunium (V) sorption onto FEBEX bentonite colloids observed no sorption to the colloids (Missana and Geckeis, 2006), which is thought to be caused by neptunium remaining as neptunium (V). However, limited sorption of neptunium (V) to FEBEX bentonite colloids was observed by Huber et al. (2011), and in experiments with Zn-/ Ni- montmorillonite colloids (Huber et al., 2015). These experiments

were carried out in the presence of Grimsel FFM and showed a slow removal of neptunium from solution. This is attributed to either the slow reduction of neptunium (V) to neptunium (IV) and/or kinetic sorption to the FFM (Huber et al., 2011). In the latter experiment, sorption to montmorillonite colloids did not occur initially, but occurred after 100 hours where neptunium (IV) sorbed to the montmorillonite colloids, and then to the FFM (Huber et al., 2015). Alternatively, neptunium (IV) self-colloids could have formed (Huber et al., 2015). The different behaviour observed is probably due to lower Eh values measured in Huber et al. (2015) thereby promoting more reduction processes. An additional reason is that montmorillonite colloids have a higher surface area than bentonite colloids, which could promote more sorption to the montmorillonite colloids but not the bentonite.

Elo et al. (2017) did show weak pH dependent sorption of neptunium (V) to montmorillonite, which has also been demonstrated for bentonite (Li et al., 2015; Verma et al., 2017), with increased sorption in these experiments above pH 7. These experiments show that the limited sorption reached equilibrium relatively quickly (within 24 hours) (Verma et al., 2017). Neptunium (V) desorption from montmorillonite is also pH-dependent, with less desorption occurring at higher pH (Elo et al., 2017), indicating the formation of stronger surface complexes at higher pH.

The presence of iron-oxides is also an important control on sorption, with the presence of hematite retarding neptunium (V) migration (Müller et al., 2015; Verma et al., 2017). Neptunium (V) sorption is also affected by ionic strength, as experiments demonstrated that increasing ionic strength (from 0.05 M to 0.3 M) resulted in less sorption

to bentonite (Li et al., 2015), although the concentration of Grimsel groundwater ( $I = 0.001$  M) is lower than used in these experiments.

A non-linear sorption isotherm has been observed for neptunium (V) sorption to Na-illite, which is probably caused by different sorption mechanisms (Marsac et al., 2015). Surface complexation is thought to be the main mechanism for sorption at high pH (such as found in Grimsel groundwater) to both bentonite (Verma et al., 2017) and montmorillonite (Zavarin et al., 2012), whereas, at lower pH, ion exchange is the predominant sorption mechanism (Elo et al., 2017).

Different initial bound fractions were measured for the two experiments, with a higher colloid bound fraction measured in CFM Run 13-05 (30.9%) than in CRR Run 32 (<1%). The injection cocktail had a longer equilibration time in CFM Run 13-05 (35 days), than in CRR Run 32 (5 days). Sorption of neptunium (V) to bentonite and montmorillonite (discussed above) occurs quickly, and so sorption kinetics can be discounted as causing the different bound fractions. However, the longer equilibration time in CFM Run 13-05 could have allowed for the reduction of neptunium (V) to neptunium (IV), and subsequent sorption to the colloids. The low initial bound fraction for CRR Run 32 indicates that neptunium remained as neptunium (V) in the injection cocktail.

Other potential causes for the different initial bound fractions include differences in the cocktail preparation. More colloids are present in the CFM Run 13-05 cocktail, providing more surfaces for sorption and therefore resulting in the higher initial bound fraction. Radionuclides were added to the colloid suspension at acidic pH, then pH was raised to  $\sim 9.6$  using NaOH (Möri et al., (2004); Schafer, pers. Comm.). Differences in this process could

have led to more sorption in the cocktail for CFM Run 13-05. The colloids in the two experiments were also different, and the addition of montmorillonite colloids in CFM Run 13-05 could have facilitated more sorption due to the montmorillonite colloids having a greater surface area than FEBEX bentonite colloids (Huber et al., 2015). Due to the lack of information about the preparation of the injection cocktail for CFM Run 13-05, it is not possible at the time of writing to exclude any of the potential causes of the different initial bound fractions described and therefore requires further investigation.

The PHREEQC modelling above predicts positive saturation indices for  $\text{NpO}_2$  and hydrated  $\text{NpO}_2$  phases in both experiments. Formation of  $\text{NpO}_2$  nanoparticles has been observed in experiments where siderite reduced neptunium (V) to neptunium (IV) (Scheinost et al., 2016). It has not been possible to confirm whether any precipitates formed in the injection cocktail of the two migration experiments, as imaging of the injection cocktails has not been conducted. However, it is unlikely that any precipitates formed in CRR Run 32 due to the extremely low initial bound fraction, even with the higher neptunium concentration and predicted saturation indices for this experiment. This indicates that the shorter equilibration time (5 days) is too short to allow for neptunium reduction and subsequent precipitate formation. The formation of precipitates cannot be discounted as causing the higher initial bound fraction in CFM Run 13-05; however, this needs further investigation. For the purposes of modelling the experiments, any precipitates will be assumed to migrate through the system as colloid-bound neptunium as it has not been confirmed whether precipitates formed in the experiment.

Sorption experiments investigating neptunium (V) sorption to Grimsel granodiorite and Grimsel FFM observed very limited (almost no) sorption to either material (Missana and Geckeis, 2006), although slightly higher  $K_d$  values were calculated for the FFM ( $K_d \sim 3$  L/kg compared to 0.2 L/kg for the granodiorite). Limited sorption indicates that aqueous neptunium (V) will be mobile in the migration experiments. As neptunium (V) is expected in the injection cocktail for CRR Run 32, the aqueous neptunium will be mobile in the experiment.

In summary, the different initial bound fractions are likely to be caused by the different cocktail equilibration time for the two experiments. Although added as neptunium (V) in both experimental cocktails, the longer cocktail equilibration time in CFM Run 13-05 could have allowed for more reduction to neptunium (IV). Neptunium (IV) undergoes stronger sorption to the bentonite colloids, or neptunium (IV) self-colloids could have formed, causing the higher initial bound fraction. For CRR Run 32, the low initial bound fraction suggests that neptunium remained in the pentavalent oxidation state which is expected to migrate through the migration experiments as aqueous neptunium with limited retardation.

#### **7.4.2. Transport Model setup**

The model for neptunium transport is the same as described for uranium transport in Section 7.3.2. The matrix diffusion equation (Equation 4.10) was used due as the falling limb of the breakthrough curve in CRR Run 32 follows a  $t^{-3/2}$  pattern that is indicative of matrix diffusion (Smith et al., 2006). The model used the non-calibration parameters given in Table 7.11.

Parameter	Symbol	CFM Run 13-05	CRR Run 32	Justification
Radioactive decay constant	$\lambda_d$	1.03x10 <sup>-14</sup> (1/s)		Based on isotope values
Bound Fraction		30.9 %	1%	Experimentally measured
Unbound Fraction		69.1%	99%	Experimentally measured

Table 7.11 Non-calibration parameters for neptunium model

The calibration parameters for neptunium were the same as for uranium transport, namely: the sorption and desorption rate for mobile colloids ( $k_{amc}$  and  $k_{mca}$ ), the desorption rate from immobile colloids ( $k_{ica}/k_{icai}$ ), the aqueous neptunium retardation factor (R), the matrix diffusion transfer rate ( $k_{im}$ ) and the matrix porosity multiplied by the matrix extinction length ( $\theta_{im}$ ).

#### 7.4.3. Model Results

The calibrated model results for neptunium transport in CFM Run 13-05 and CRR Run 32 are shown in Figure 7.30, which used the values of the calibration parameters shown in Table 7.12. Table 7.12 shows that although consistent parameters were used to describe the interaction of the interaction of neptunium to the colloids, a different retardation factor was used, the cause of which is discussed further below.

Parameter	Symbol	CFM Run 13-05	CRR Run 32
Sorption rate to mobile colloids	$k_{amc}$	8.1x10 <sup>-6</sup> m <sup>3</sup> /kg.s (0.029 m <sup>3</sup> /kg.hr)	
Desorption rate from mobile colloids	$k_{mca}$	7x10 <sup>-6</sup> 1/s (0.025 1/h)	
Desorption rate from immobile colloids	$k_{ica}/k_{icai}$		
Aqueous neptunium retardation factor	R	1000	1.35
Matrix diffusion transfer rate	$k_{im}$	2.3x10 <sup>-4</sup> 1/s	
Matrix porosity/ extinction length	$\theta_{im}$	7	

Table 7.12 Calibrated parameter values for neptunium model

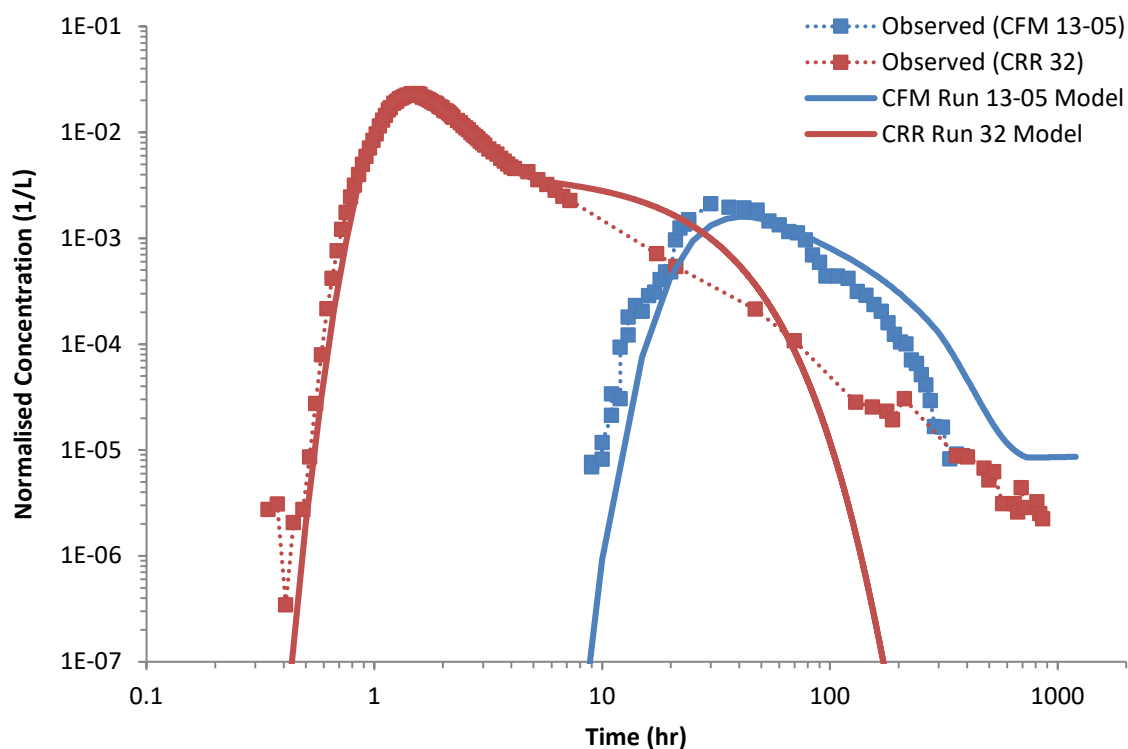


Figure 7.30 Calibrated model results for neptunium transport in CFM Run 13-05 and CRR Run 32

#### ***CFM Run 13-05***

Figure 7.31 shows the modelled breakthrough of neptunium-237 on a linear scale in CFM Run 13-05, with a comparison between the modelled and observed cumulative recovery in Figure 7.32. The modelled recovery (5.4%) compares extremely well to the experimental recovery (4%).

The breakthrough curve shows a good match to the rising limb of the breakthrough curve. However, the model peak is slightly lower and the falling limb slightly higher than the experimental data. This is similar to other radionuclides modelled in CFM Run 13-05, and it is important to note that any error from the conservative tracer or colloid calibration from the previous chapter is carried forward to this calibration.

Figure 7.31 also shows a model run that used the calibrated parameters for CRR Run 32. The model shows an extremely poor match to the experiment, mainly due to a second peak caused by the breakthrough of aqueous neptunium that has undergone matrix diffusion.

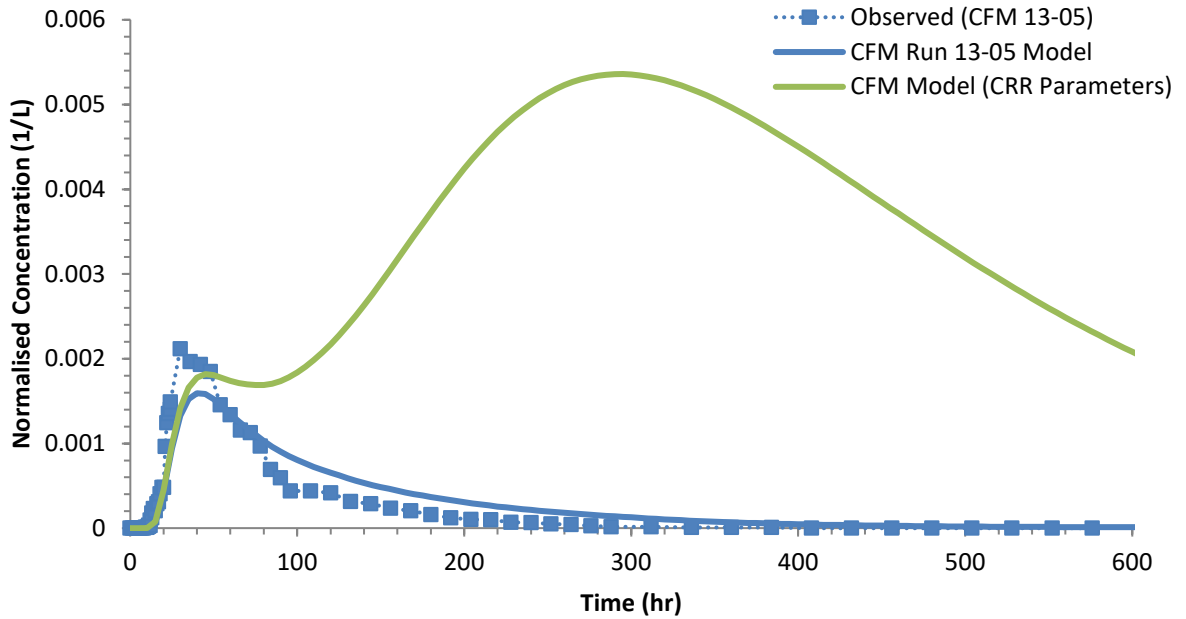


Figure 7.31 Calibrated model breakthrough for neptunium-237 in CFM Run 13-05. Blue line = CFM model, Green line = CRR model parameter values.

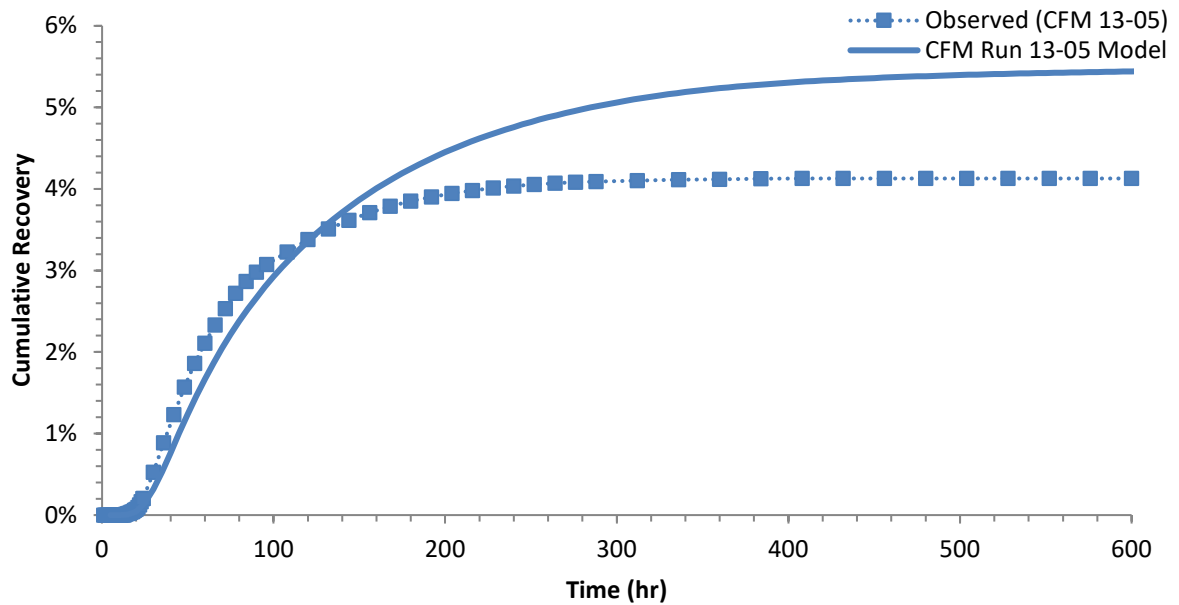


Figure 7.32 Comparison of cumulative recovery for observed and modelled data for <sup>237</sup>Np in CFM Run 13-05

### **CRR Run 32**

Figure 7.33 shows the modelled breakthrough for neptunium-237 on a semi-log scale in CRR Run 32, with a comparison between the observed and modelled cumulative recovery shown in Figure 7.34. The model shows an excellent match to the rising limb and peak of the breakthrough curve. However, it struggles to replicate some of the tailing observed past 10 hours (as seen more clearly in Figure 7.30). This tailing is most likely caused by matrix diffusion, and changes to the how matrix diffusion and sorption to matrix pores are represented in the model may improve the model fit here. Because of this, the modelled recovery (98%) is higher than the experimental recovery (82% measured by ICP-MS, 80% measured by  $\alpha$ -spectroscopy, as a pair with  $^{233}\text{U}$ , which assumes that they have the same recovery). Also shown in Figure 7.33 is a model run which used the parameters from the CFM Run 13-05 model. This shows an extremely poor match to the experiment indicating that representing the transport as dominated by colloid-facilitated neptunium is not appropriate for this experiment.

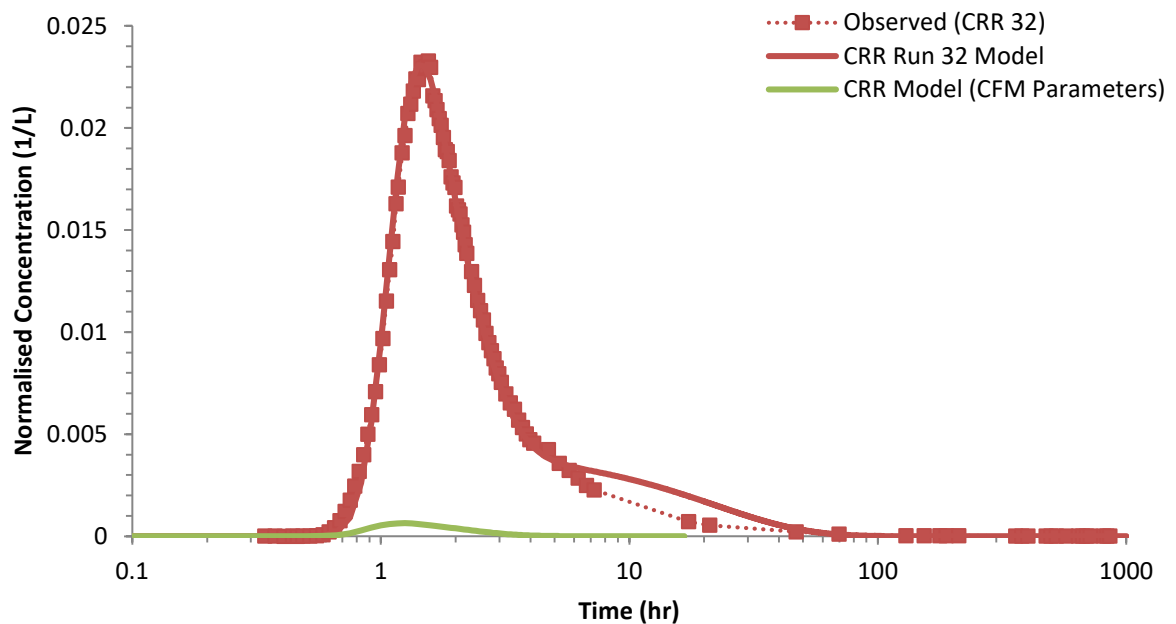


Figure 7.33 Calibrated model breakthrough for neptunium-237 in CRR Run 32. Green line = model run with CFM Run 13-05 parameter values.

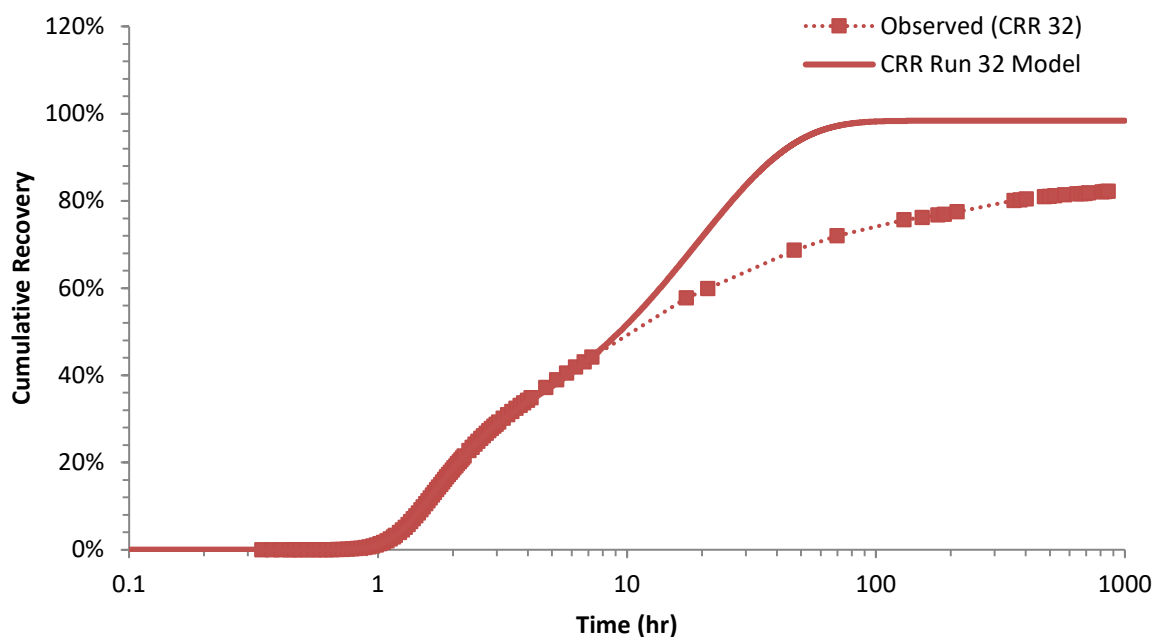


Figure 7.34 Comparison of cumulative recovery for observed and modelled data for  $^{237}\text{Np}$  in CRR Run 32

#### 7.4.4. Discussion and Conclusions

Good model matches were obtained for neptunium transport in the two experiments. However, different retardation factors for aqueous neptunium were included for the two experiments, as was also found for uranium transport. Figure 7.35 shows the different phases that contribute to the modelled breakthrough. In CRR Run 32, neptunium was best represented as being transported as an aqueous species, whereas in CFM Run 13-05 a better representation involved partial colloid-facilitated transport of neptunium.

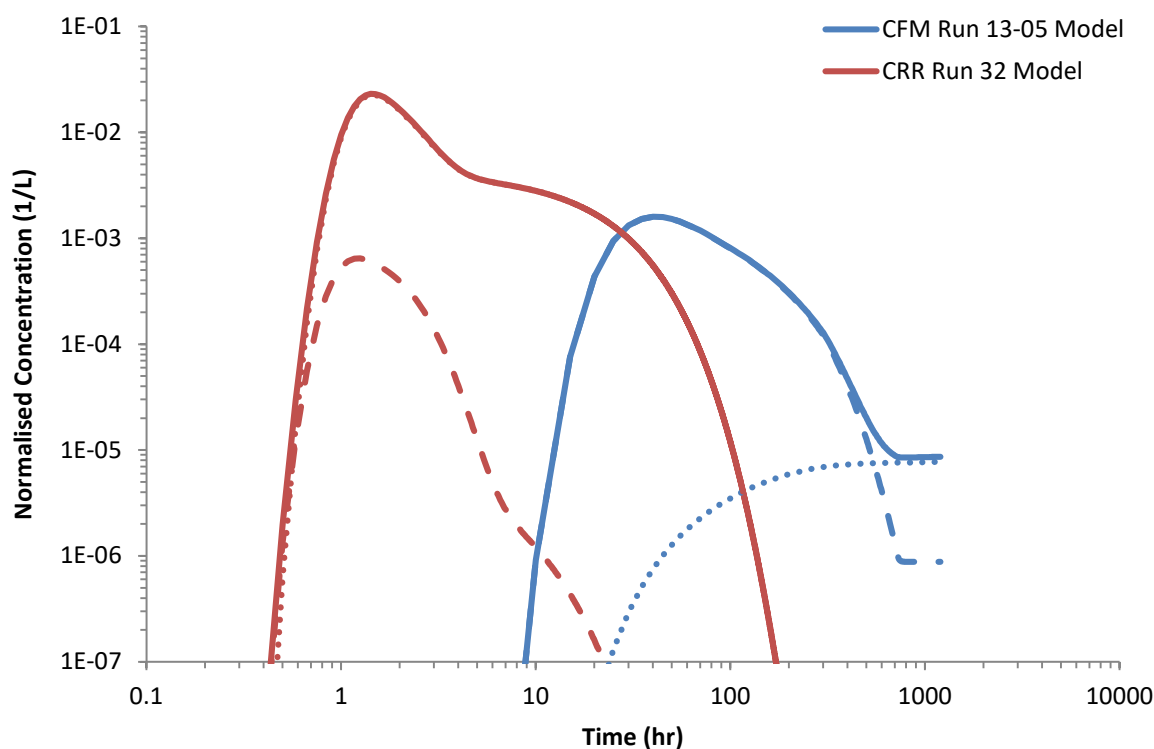


Figure 7.35 Contribution of different neptunium phases to modelled breakthroughs (Dashed = colloid bound; Dotted = aqueous)

The breakthrough of aqueous neptunium in CRR Run 32 occurred with limited retardation (retardation factor = 1.35), which is consistent with the majority of neptunium remaining as neptunium (V), the same oxidation state that was added in the injection cocktail (Möri et al., 2004). Colloid-facilitated transport of neptunium did not occur in the experiment, which is expected due to the limited propensity of neptunium (V) to sorb and the very low initial colloid-bound fraction in the injection cocktail, the latter potentially resulting (at least in part) from the short cocktail equilibration time.

In CFM Run 13-05, neptunium was modelled assuming that only colloid-bound neptunium was observed in the breakthrough curve. This led to the use of the large retardation factor ( $R = 1000$ ). As discussed in Section 7.4.1, one potential cause of the different initial bound fractions is that the injection cocktail of CFM Run 13-05 had a longer

cocktail equilibration time, which allowed for the added neptunium (V) to reduce to neptunium (IV). The neptunium (IV) could then sorb to the colloids, or form neptunium (IV) precipitates, causing the higher initial bound fraction. The higher retardation factor used in CFM Run 13-05 is consistent with neptunium being present as neptunium (IV) in the source term of the experiment. However, there are no experimental data to confirm whether full or partial reduction of neptunium (V) occurred. Further investigation is required to determine whether the kinetics of neptunium reduction in Grimsel groundwater in the presence of bentonite and montmorillonite colloids would allow for the reduction of neptunium (V) in the injection cocktail of CFM Run 13-05.

Limited laboratory investigations have investigated neptunium (IV) sorption, with no published data available to quantify neptunium (IV) sorption to bentonite colloids, FFM or granodiorite in the Grimsel system. Nagasaki et al. (2017) investigated neptunium (IV) sorption to shale, illite and MX-80 bentonite, although in solutions with an ionic strength ( $I = 0.1 - 6M$ ) orders of magnitude higher than Grimsel groundwater ( $I = 0.001M$ , (Bennett, 2014)).  $K_d$  values for neptunium (IV) sorption in these experiments were in the same order of magnitude ( $K_d \sim 130 \text{ m}^3/\text{kg}$ ) as values for plutonium (IV) sorption to FEBEX bentonite colloids in Missana and Geckeis (2006). These  $K_d$  values are approximately  $\sim 30$  times higher than the  $K_d$  measured for neptunium (V) to FEBEX bentonite colloids in the same experiments as reported by Missana and Geckeis (2006).

As  $K_d$  values measured for Np (IV) to MX-80 bentonite were similar to those measured for Pu (IV) to FEBEX bentonite, it is possible that neptunium (IV)  $K_d$  values are similar to plutonium (IV) sorption to Grimsel granodiorite and fracture fill material. If these

$K_d$  values are roughly comparable, it is possible that the corresponding high retardation factor ( $>1000$ ) used for Pu (IV) in this study (Chapter 6) could be used for Np (IV). The fact that neptunium in CFM Run 13-05 could be modelled as only colloid-bound neptunium implies that all of the neptunium in the experiment has been reduced to neptunium (IV), either in the injection cocktail or during the migration experiment itself, as neptunium (V) would be expected to migrate in the experiments as aqueous neptunium with little retardation (as was found for CRR Run 32). This process however needs further investigation, as no experimental data exist to confirm that these assumptions are valid.

Accelerator mass spectroscopy (AMS) data has been collected for the long term breakthrough in CFM Run 13-05 (Quinto et al., 2017). This data was not available at time of model calibration, but it would have been possible to further calibrate the breakthrough of aqueous neptunium with this data, potentially including sorption kinetics of the aqueous neptunium to the granodiorite/ FFM as necessary.

Although included as a calibration parameter in Table 7.12, changes to the sorption rate to the colloids ( $k_{amc}$ ) were found to have little effect on the breakthrough in either experiment. Therefore, the sorption rate was not changed from the initial value (which was based on the parameter used in the COLFRAC/ JNC model of CRR Run 32 (Smith et al., 2006)).

Consistent desorption rates were used to model both experiments, although the desorption rate was not a sensitive parameter in CRR Run 32. The desorption rate used in this model ( $0.025 \text{ h}^{-1}$ ) compares reasonably well to modelling of CFM Run 13-05 in Reimus (2016), which used desorption rates between  $0.028- 0.15 \text{ h}^{-1}$  and  $0.035 \text{ h}^{-1}$  (depending on

the injection function used), although is much lower than the rate used to model CRR Run 32 in the same report ( $10 \text{ h}^{-1}$ ).

Consistent matrix diffusion parameters were also used between the experiments, although changes to these parameters had little impact on the breakthrough of CFM Run 13-05. Therefore, the matrix diffusion parameters were chosen to provide the best breakthrough in CRR Run 32. Due to the different formulations of matrix diffusion, it is not possible to compare them directly with the parameters used by Reimus (2016).

To conclude, neptunium transport was successfully modelled in both experiments. In CRR Run 32, neptunium migrated as aqueous neptunium (V) with limited retardation, showing very limited sorption to the bentonite colloids or the Grimsel FFM/ granodiorite, as shown in laboratory experiments (Missana and Geckeis, 2006). However, in CFM Run 13-05, colloid-facilitated transport of neptunium occurred. This was potentially caused by the (full or partial) reduction of neptunium (V) to neptunium (IV) in the injection cocktail, causing a higher initial bound fraction. However, this process cannot be confirmed without further investigation. In addition, in CFM Run 13-05 it appears that aqueous neptunium underwent stronger sorption to the Grimsel FFM/ granodiorite, as neptunium was able to be modelled assuming limited aqueous neptunium breakthrough. If neptunium (IV) was present in the injection cocktail, it therefore underwent more sorption to the geological media, although this again needs further investigation in laboratory experiments as there are no data testing neptunium (IV) sorption in the Grimsel system.

## 7.5. Summary

This chapter detailed the model calibration for caesium, uranium and neptunium transport in CFM Run 13-05 and CRR Run 32. Differences in experimental preparation led to the radionuclides exhibiting different behaviour between the two experiments, which led to different processes and calibration parameters required to be used in the model. Typically, more colloid facilitated transport occurred in CFM Run 13-05, whereas in CRR Run 32 aqueous radionuclide transport was more important.

For caesium, the different concentrations used and the presence of a non-linear sorption isotherm to bentonite colloids caused different initial bound fractions. The non-linear sorption is thought to be caused by the presence of two sorption sites on the bentonite, a limited capacity, high affinity site on the edge of the clay and a high capacity, low affinity, site on the plane of the clay. The lower concentration of caesium used in CFM Run 13-05 meant that caesium sorption was controlled by the high affinity edge site, whereas in CRR Run 32 the higher concentration used filled this site and therefore the lower affinity planar site controlled sorption. A second sorption site on the colloids was added to the model, and consistent parameters were found to describe sorption and desorption rates to the two sites for both experiments. However, when comparisons of the resulting sorption isotherm were made to laboratory data produced by Missana et al. (2004), the capacity of the high affinity edge site used in the model was lower than the experimental data. This was thought to be caused by the competitive sorption of other radionuclides in the injection cocktail of the migration experiments that resulted in the capacity of the edge site not being reached. However, this needs further investigation, potentially through the creation of a

thermodynamic sorption model which would also require the collection of further experimental data.

For uranium and neptunium, it is hypothesised that the different cocktail equilibration time (longer for CFM Run 13-05 - 35 days, than for CRR Run 32 – 5 days) caused the different initial bound fractions. The longer equilibration time in CFM Run 13-05 allowed for the reduction of the radionuclides, which were added as oxidised uranium (VI) and neptunium (V), to uranium (IV) and neptunium (IV). The reduced radionuclides then underwent stronger sorption or formed self colloids, causing the higher initial bound fractions. However, this process needs further investigation as current laboratory data cannot confirm whether this occurred and there are other potential causes for the different behaviour (e.g. different pH values used in the preparation of the injection cocktail). The different initial bound fractions lead to predominantly aqueous radionuclide transport in CRR Run 32, but colloid-facilitated transport in CFM Run 13-05. Despite the different processes, the transport of the two radionuclides was modelled successfully.

From the modelling of these three radionuclides, important processes that control radionuclide migration have been identified, as well as areas that require further investigation through studies in laboratories, or through the running of further migration experiments, as detailed further in the next chapter.

## **7.6. List of References**

Bennett, D.G. (2014) **2014:11 Radionuclide Solubility Limits in SKB's Safety Case**. Stockholm, Sweden.

Bradbury, M.H. and Baeyens, B. (2000) A generalised sorption model for the concentration dependent uptake of caesium by argillaceous rocks. **Journal of Contaminant Hydrology**, 42 (2–4): 141–163 DOI: 10.1016/S0169-7722(99)00094-7

Bradbury, M.H. and Baeyens, B. (2005) Modelling the sorption of Mn(II), Co(II), Ni(II), Zn(II), Cd(II), Eu(III), Am(III), Sn(IV), Th(IV), Np(V) and U(VI) on montmorillonite: Linear free energy relationships and estimates of surface binding constants for some selected heavy metals and actinide. **Geochimica et Cosmochimica Acta** [online], 69 (4): 875–892 DOI: 10.1016/j.gca.2004.07.020. Available from: <http://linkinghub.elsevier.com/retrieve/pii/S0016703704005757>

Cherif, M.A., Martin-Garin, A., Gérard, F. and Bildstein, O. (2017) A robust and parsimonious model for caesium sorption on clay minerals and natural clay materials. **Applied Geochemistry**, 87 DOI: 10.1016/j.apgeochem.2017.10.017

Dittrich, T.M. and Reimus, P. (2015a) Uranium transport in a crushed granodiorite: Experiments and reactive transport modeling. **Journal of Contaminant Hydrology** [online], 175–176: 44–59 DOI: 10.1016/j.jconhyd.2015.02.004. Available from: <http://dx.doi.org/10.1016/j.jconhyd.2015.02.004>

Dittrich, T.M. and Reimus, P.W. (2015b) **Arbeitsbericht NAB 15-09: Laboratory investigation of colloid-facilitated transport of caesium by bentonite colloids in a crystalline rock system.** Wettingen, Switzerland

Duro, L., Bruno, J., Rollin, C. and Guimera, J. (2000) **AN 99-218: Prediction of the solubility and speciation of Radionuclides in Febex and Grimsel waters.** Wettingen, Switzerland

Durrant, C.B., Begg, J.D., Kersting, A.B. and Zavarin, M. (2018) Cesium sorption reversibility and kinetics on illite, montmorillonite, and kaolinite. **Science of the Total Environment** [online], 610–611: 511–520 DOI: 10.1016/j.scitotenv.2017.08.122. Available from: <https://doi.org/10.1016/j.scitotenv.2017.08.122>

Elo, O., Muller, K., Ikeda-Ohno, A., Bok, F., Scheinost, A.C., Holtta, P. and Huittinen, N. (2017) Batch sorption and spectroscopic speciation studies of neptunium uptake by montmorillonite and corundum. **Geochimica et Cosmochimica Acta**, 198: 168–181 DOI: 10.1016/j.gca.2016.10.040

Gaus, I. and Smith, P.A. (2008) **Nagra Arbeitsbericht NAB 08-27: Modellers dataset for the Colloid Formation and Migration Project Status: End of CFM Phase 1.** Wettingen, Switzerland

Huber, F., Heck, S., Truche, L., Bouby, M., Brendle, J., Hoess, P. and Schäfer, T. (2015) Radionuclide desorption kinetics on synthetic Zn / Ni-labeled montmorillonite nanoparticles. **Geochimica et Cosmochimica Acta**, 148: 426–441 DOI: 10.1016/j.gca.2014.10.010

Huber, F., Kunze, P., Geckeis, H. and Schäfer, T. (2011) Sorption reversibility kinetics in the ternary system radionuclide-bentonite colloids/nanoparticles-granite fracture filling material. **Applied Geochemistry** [online], 26 (12): 2226–2237 DOI: 10.1016/j.apgeochem.2011.08.005. Available from: <http://dx.doi.org/10.1016/j.apgeochem.2011.08.005>

Kasar, S., Kumar, S., Saha, A., Tomar, B.S. and Bajpai, R.K. (2017) Mechanistic and thermodynamic aspects of Cs(I) and Sr(II) interactions with smectite-rich natural clay. **Environmental Earth Sciences**, 76 (7): 1–9 DOI: 10.1007/s12665-017-6595-8

Kenney, J.P.L., Ellis, T., Nicol, F.S., Porter, A.E. and Weiss, D.J. (2018) The effect of bacterial growth phase and culture concentration on U(VI) removal from aqueous solution. **Chemical Geology** [online], 482 (December 2017): 61–71 DOI: 10.1016/j.chemgeo.2018.01.025. Available from: <https://doi.org/10.1016/j.chemgeo.2018.01.025>

Kosakowski, G. and Smith, P. (2004) **Nagra Technical Bulletin NTB 04-01: Grimsel Test Site Investigation Phase V Modelling the transport of Solutes and Colloids in a Water Conducting Shear**

**Zone at the Grimsel Test Site** [online]. Wettingen, Switzerland. Available from: <http://www.nagra.ch/en/cat/publikationen/technicalreports-ntbs/ntbs-2001-2012/downloadcentre.htm>

Li, P., Liu, Z., Ma, F., Shi, Q., Guo, Z. and Wu, W. (2015) Effects of pH, ionic strength and humic acid on the sorption of neptunium(V) to Na-bentonite. **Journal of Molecular Liquids** [online], 206: 285–292 DOI: 10.1016/j.molliq.2015.02.014. Available from: <http://linkinghub.elsevier.com/retrieve/pii/S016773221500104X>

Marsac, R., Banik, N. Ial, Lützenkirchen, J., Marquardt, C.M., Dardenne, K., Schild, D., Rothe, J., Diascorn, A., Kupcik, T., Schäfer, T. and Geckeis, H. (2015) Neptunium redox speciation at the illite surface. **Geochimica et Cosmochimica Acta**, 152: 39–51 DOI: 10.1016/j.gca.2014.12.021

Marshall, T.A., Morris, K., Law, G.T.W., W. Mosselmans, J.F., Bots, P., Roberts, H. and Shaw, S. (2015) Uranium fate during crystallization of magnetite from ferrihydrite in conditions relevant to the disposal of radioactive waste. **Mineralogical Magazine** [online], 79 (6): 1265–1274 DOI: 10.1180/minmag.2015.079.6.02. Available from: <http://openurl.ingenta.com/content/xref?genre=article&issn=0026-461X&volume=79&issue=6&spage=1265>

Missana, T., Benedicto, A., García-Gutiérrez, M., Alonso, U., García-Gutiérrez, M. and Alonso, U. (2014a) Modeling cesium retention onto Na-, K- and Ca-smectite: Effects of ionic strength, exchange and competing cations on the determination of selectivity coefficients. **Geochimica et Cosmochimica Acta** [online], 128: 266–277 DOI: 10.1016/j.gca.2013.10.007. Available from: <http://dx.doi.org/10.1016/j.gca.2013.10.007>

Missana, T., García-Gutiérrez, M. and Alonso, U. (2004) Kinetics and irreversibility of cesium and uranium sorption onto bentonite colloids in a deep granitic environment. **Applied Clay Science**, 26 (1–4 SPEC. ISS.): 137–150 DOI: 10.1016/j.clay.2003.09.008

Missana, T., García-Gutiérrez, M., Benedicto, A., Ayora, C. and De-Pourcq, K. (2014b) Modelling of Cs sorption in natural mixed-clays and the effects of ion competition. **Applied Geochemistry** [online], 49: 95–102 DOI: 10.1016/j.apgeochem.2014.06.011. Available from: <http://dx.doi.org/10.1016/j.apgeochem.2014.06.011>

Missana, T. and Geckeis, H. (2006) **Nagra Technical Bulletin NTB 03-02: CRR Final Project Report 2 - Supporting Laboratory Experiments with Radionuclides and Bentonite Colloids**. Wettingen, Switzerland

Möri, A., Alexander, W.R., Degueldre, C., Eikenberg, J., Fierz, T., Geckeis, H., Geier, F., Hauser, W., Schäfer, T. and Smith, P.A. (2004) **Nagra Technical Bulletin NTB 03-01: The CRR Final Project Report series 1 - Description of the Field Phase - Methodologies and Raw Data** [online]. Wettingen, Switzerland. Available from: <http://www.nagra.ch/en/cat/publikationen/technicalreports-ntbs/ntbs-2001-2012/downloadcentre.htm>

Müller, K., Gröschel, A., Rossberg, A., Bok, F., Franzen, C., Brendler, V. and Foerstendorf, H. (2015) In situ spectroscopic identification of neptunium(V) inner-sphere complexes on the hematite-water interface. **Environmental Science and Technology**, 49 (4): 2560–2567 DOI: 10.1021/es5051925

Nagasaki, S., Riddoch, J., Saito, T., Goguen, J., Walker, A. and Yang, T.T. (2017) Sorption behaviour of Np(IV) on illite, shale and MX-80 in high ionic strength solutions. **Journal of Radioanalytical and Nuclear Chemistry**, 313 (1): 1–11 DOI: 10.1007/s10967-017-5290-2

- Nagasaki, S., Tanaka, S. and Suzuki, A. (1999) Sorption of neptunium on bentonite and its migration in geosphere. **Colloids and Surfaces A: Physicochemical and Engineering Aspects**, 155 (2–3): 137–143 DOI: 10.1016/S0927-7757(99)00046-1
- Nico, P.S., Stewart, B.D. and Fendorf, S. (2009) Incorporation of oxidized uranium into Fe (Hydr)oxides during Fe(II) catalyzed remineralization. **Environmental Science and Technology**, 43 (19): 7391–7396 DOI: 10.1021/es900515q
- Poinsot, C., Baeyens, B. and Bradbury, M.H. (1999) Experimental and modelling studies of caesium sorption on illite. **Geochimica et Cosmochimica Acta**, 63 (19–20): 3217–3227 DOI: 10.1016/S0016-7037(99)00246-X
- Quinto, F., Blechschmidt, I., Garcia Perez, C., Geckeis, H., Geyer, F., Golser, R., Huber, F.M., Lagos, M., Lanyon, B., Plaschke, M., Steier, P., Schäfer, T., Perez, C.G., Geckeis, H., Geyer, F., Golser, R., Huber, F.M., Lagos, M., Lanyon, B., et al. (2017) Multi-actinide analysis with AMS for ultra-trace determination in small samples : application to an in situ radionuclide tracer test within the Colloid Formation and Migration (CFM) experiment at the Grimsel Test Site (GTS, Switzerland). **Analytical Chemistry**, 89 (13): 7182–7189 DOI: 10.1021/acs.analchem.7b01359
- Reimus, P.W. (2016) **Nagra NAB 16-61: GTS Phase VI- CFM Phase 3: Interpretation of colloid-facilitated radionuclide transport experiments from the CRR and CFM projects**. Wettingen, Switzerland
- Renshaw, J.C., Butchins, L.J.C., Livens, F.R., May, I., Charnock, J.M. and Lloyd, J.R. (2005) Bioreduction of uranium: Environmental implications of a pentavalent intermediate. **Environmental Science and Technology**, 39 (15): 5657–5660 DOI: 10.1021/es048232b
- Roberts, H.E., Morris, K., Law, G.T.W., Mosselmans, J.F.W., Bots, P., Kvashnina, K. and Shaw, S. (2017) Uranium(V) Incorporation Mechanisms and Stability in Fe(II)/Fe(III) (oxyhydr)Oxides. **Environmental Science & Technology Letters** [online], p. acs.estlett.7b00348 DOI: 10.1021/acs.estlett.7b00348. Available from: <http://pubs.acs.org/doi/abs/10.1021/acs.estlett.7b00348>
- Scheinost, A.C., Steudtner, R., Hübner, R., Weiss, S. and Bok, F. (2016) Neptunium<sup>V</sup> Retention by Siderite under Anoxic Conditions: Precipitation of NpO<sub>2</sub>-Like Nanoparticles and of Np<sup>IV</sup> Pentacarbonate. **Environmental Science & Technology** [online], 50 (19): 10413–10420 DOI: 10.1021/acs.est.6b02399. Available from: <http://pubs.acs.org/doi/10.1021/acs.est.6b02399>
- Schmeide, K. and Bernhard, G. (2010) Sorption of Np(V) and Np(IV) onto kaolinite: Effects of pH, ionic strength, carbonate and humic acid. **Applied Geochemistry** [online], 25 (8): 1238–1247 DOI: 10.1016/j.apgeochem.2010.05.008. Available from: <http://dx.doi.org/10.1016/j.apgeochem.2010.05.008>
- Sherriff, N., Livens, F., Bryan, N., Elo, O., Huittinen, N., Muller, K., Holtta, P., Alonso, Ú., Missana, T., Quinto, F., Lagos, M., Plaschke, M., Schäfer, T., Geckeis, H. and Steier, P. (2015) **BELBaR D3.09: Understanding of Radionuclide Colloid Interaction**. European Commission: Brussels.
- Siroux, B., Beaucaire, C., Tabarant, M., Benedetti, M.F. and Reiller, P.E. (2017) Adsorption of strontium and caesium onto an Na-MX80 bentonite: Experiments and building of a coherent thermodynamic modelling. **Applied Geochemistry**, 87 DOI: 10.1016/j.apgeochem.2017.10.022
- Smith, P.A., Guimera, J., Kosakowski, G., Pudewills, A. and Ibaraki, M. (2006) **Nagra Technical Bulletin NTB 03-03: Grimsel Test Site Investigation Phase V - The CRR Final Project Report series 3: Results**

**of the Supporting Modelling Programme.** Wettingen, Switzerland

Tournassat, C., Tinnacher, R.M., Grangeon, S. and Davis, J.A. (2018) Modeling uranium(VI) adsorption onto montmorillonite under varying carbonate concentrations: A surface complexation model accounting for the spillover effect on surface potential. **Geochimica et Cosmochimica Acta** [online], 220: 291–308 DOI: 10.1016/j.gca.2017.09.049. Available from: <https://doi.org/10.1016/j.gca.2017.09.049>

Troyer, L.D., Maillot, F., Wang, Z., Wang, Z., Mehta, V.S., Giammar, D.E. and Catalano, J.G. (2016) Effect of phosphate on U(VI) sorption to montmorillonite: Ternary complexation and precipitation barriers. **Geochimica et Cosmochimica Acta** [online], 175: 86–99 DOI: 10.1016/j.gca.2015.11.029. Available from: <http://dx.doi.org/10.1016/j.gca.2015.11.029>

Tsarev, S., Waite, T.D. and Collins, R.N. (2016) Uranium Reduction by Fe(II) in the Presence of Montmorillonite and Nontronite. **Environmental Science and Technology**, 50 (15): 8223–8230 DOI: 10.1021/acs.est.6b02000

Verma, P.K., Romanchuk, A.Y., Vlasova, I.E., Krupskaya, V. V., Zakusin, S. V., Sobolev, A. V., Egorov, A. V., Mohapatra, P.K. and Kalmykov, S.N. (2017) Np(V) uptake by bentonite clay: Effect of accessory Fe oxides/hydroxides on sorption and speciation. **Applied Geochemistry** [online], 78: 74–82 DOI: 10.1016/j.apgeochem.2016.12.009. Available from: <http://dx.doi.org/10.1016/j.apgeochem.2016.12.009>

Wold, S. (2010) **TR-10-20 Sorption of prioritized elements on montmorillonite colloids and their potential to transport radionuclides potential to transport radionuclides** [online]. Stockholm. Available from: <http://www.skb.se/upload/publications/pdf/TR-10-20.pdf>

Zavarin, M., Powell, B.A., Bourbin, M., Zhao, P. and Kersting, A.B. (2012) Np(V) and Pu(V) ion exchange and surface-mediated reduction mechanisms on montmorillonite. **Environmental Science and Technology**, 46 (5): 2692–2698 DOI: 10.1021/es203505g

## 8. CONCLUSIONS

### 8.1. Introduction

Colloid-facilitated radionuclide transport is one process that could affect radionuclide behaviour in the post-closure phase of a geological disposal facility (GDF). There has been a need to improve process understanding of colloid-facilitated radionuclide transport, and so it has been investigated in experiments that have been carried out at the Grimsel Test Site in Switzerland: the Colloid Formation and Migration (CFM) project, and the earlier Colloid and Radionuclide Retardation (CRR) project.

In addition to the extensive field and laboratory investigation programme carried out during both projects, a detailed modelling programme has been carried out during both CRR (Smith et al., 2006; Kosakowski and Smith, 2004) and CFM (Noseck et al., 2016) projects. This study fits into this context as one of the modelling teams working as part of the CFM project.

In this study, two migration experiments that investigated the migration of radionuclides in the presence of bentonite colloids have been modelled. The two experiments (CFM Run 13-05 and CRR Run 32) were carried out between the same boreholes but under different flow conditions and were prepared differently. The aim of this research was to develop a new model for colloid-facilitated radionuclide transport that could be applied to the two experiments, with the aim of replicating the transport of conservative tracers, bentonite colloids and radionuclides, using physically based parameters and processes, and the same parameter values for both experiments in the model. From this modelling, the dominant transport processes controlling radionuclide migration in the two migration experiments were to be identified.

Previous models of the experiments (detailed in Chapter 3) needed different parameter values to describe the same processes, in order to model the same species in different experiments and used either 1D or homogeneous 2D representations of the complex geological structure of the MI shear zone where the experiments take place. A key advance incorporated in the present modelling was to account for the heterogeneous 2D flow field within the shear zone. The models developed in the present study included a 2D transmissivity distribution generated by inverse modelling. This provided more information on flow geometry and the different flow paths contained within the shear zone than previous models. The transport model was created in COMSOL Multiphysics, a flexible finite-element coupled equation solver, which allowed for different processes to be removed and added into the model with relative ease.

The following subsections first deal with the different objectives used to meet the aim of the project, as detailed in Chapter 1, before describing the implications from the modelling and finally suggesting future lines of research.

## **8.2. Objectives 1 and 2: Development of the model for Colloid-Facilitated Radionuclide Transport**

Objective 1 of the study was concerned with the development of a 2D groundwater flow and solute transport model. Objective 2 was to extend this model to simulate colloid-facilitated transport.

Details of the relevant background are found in Chapter 3, with the transport model development described in Chapter 4. The model, created in COMSOL Multiphysics, included

a transmissivity distribution generated by Inverse Modelling. Groundwater flow was solved within the COMSOL model, using a subset of the model domain used by the inverse model.

The model developed here is the first used in the migration experiments at Grimsel that uses a heterogeneous 2D transmissivity model domain, solving for the flow field of the different migration experiments. The model uses this flow field as a basis to represent conservative tracer, colloid, radionuclide and colloid-facilitated radionuclide transport, using a series of coupled equations to describe the different transport phases.

The model included similar processes to those included in other models of the CFM project: irreversible and reversible colloid attachment; reversible radionuclide kinetic sorption to mobile colloids; desorption from immobile colloids; and aqueous radionuclide equilibrium sorption to rock surfaces. Both colloid attachment and radionuclide sorption to colloids could be limited by a Langmuir type sorption isotherm, and one sorption site was included on the bentonite colloids. Additional processes, such as radionuclide matrix diffusion, aqueous radionuclide kinetic sorption to rock surfaces or additional sorption sites were added as necessary. The model was applied to the two field migration experiments using a staged approach, i.e. conservative tracer breakthrough was calibrated first, then colloid breakthrough, and finally radionuclide breakthrough.

### **8.3. Objective 3: Application of the transport model to two in-situ field experiments**

The model developed in COMSOL Multiphysics was applied to two colloid/ radionuclide migration experiments, CFM Run 13-05 and CRR Run 32. These experiments were both carried out in 'CRR Dipole 1', between the same boreholes ~2.25m apart. A key difference

between the experiments was that CFM Run 13-05 was run at much lower flow rates than the earlier experiment CRR Run 32, due to the installation of a novel mega-packer system. The model was applied to the breakthrough of: conservative tracers and bentonite colloids (Chapter 5); americium and plutonium (Chapter 6); and caesium, uranium and neptunium (Chapter 7).

The modelled breakthrough curves are shown in Figure 8.1 for conservative tracer and bentonite colloid breakthrough, Figure 8.2 for americium and plutonium breakthrough, and Figure 8.3 for caesium (using the two sorption site model), uranium and neptunium breakthrough. More detail on the model calibration can be found in the respective chapters, but these figures show that a good match was obtained for the different species in both experiments. Table 8.1 shows that the modelled recovery was close to the measured recovery. Where differences exist, the model mostly predicts higher recovery than measured in the experiment, giving a conservative prediction of recovery. An exception to this was the conservative tracer model in CFM Run 13-05, where the lower recovery is due to the model not replicating additional dispersion of the tracer on the falling limb of the breakthrough curve.

<b>Recovery</b>	<i>CFM Run 13-05</i>	<i>CRR Run 32</i>
Conservative Tracer	92.6% (76%)	92% (98%)
Colloids	36% (43%)	85-100% (95%)
Americium	25% (24%)	70% (87%)
Plutonium	28% (38%)	86% (78%)
Caesium	8% (9.5%)	70% (88%)
Uranium	15% (17%)	80-103% (98%)
Neptunium	4% (5.4%)	80-83% (98%)

**Table 8.1** Experimental recovery values for the different species modelled in both experiments. Values in brackets represent modelled recovery values.

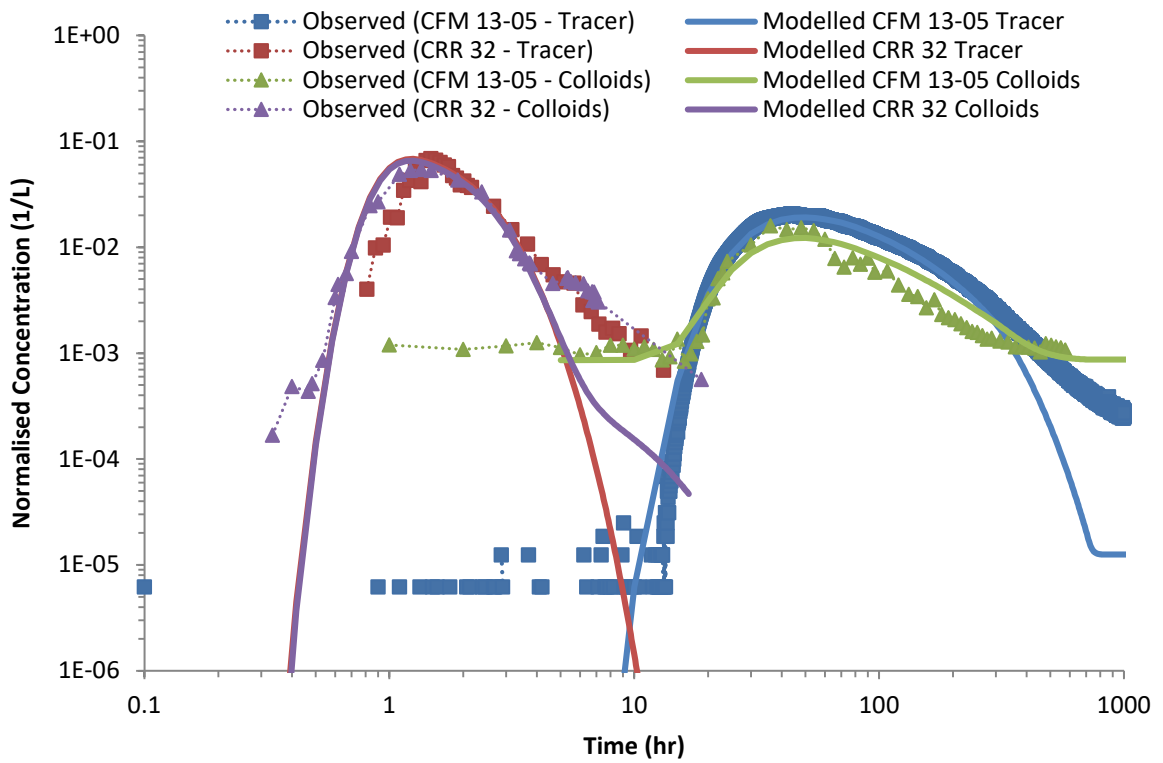


Figure 8.1 Calibrated model results for breakthrough of conservative tracer and bentonite colloids in CFM Run 13-05 and CRR Run 32.

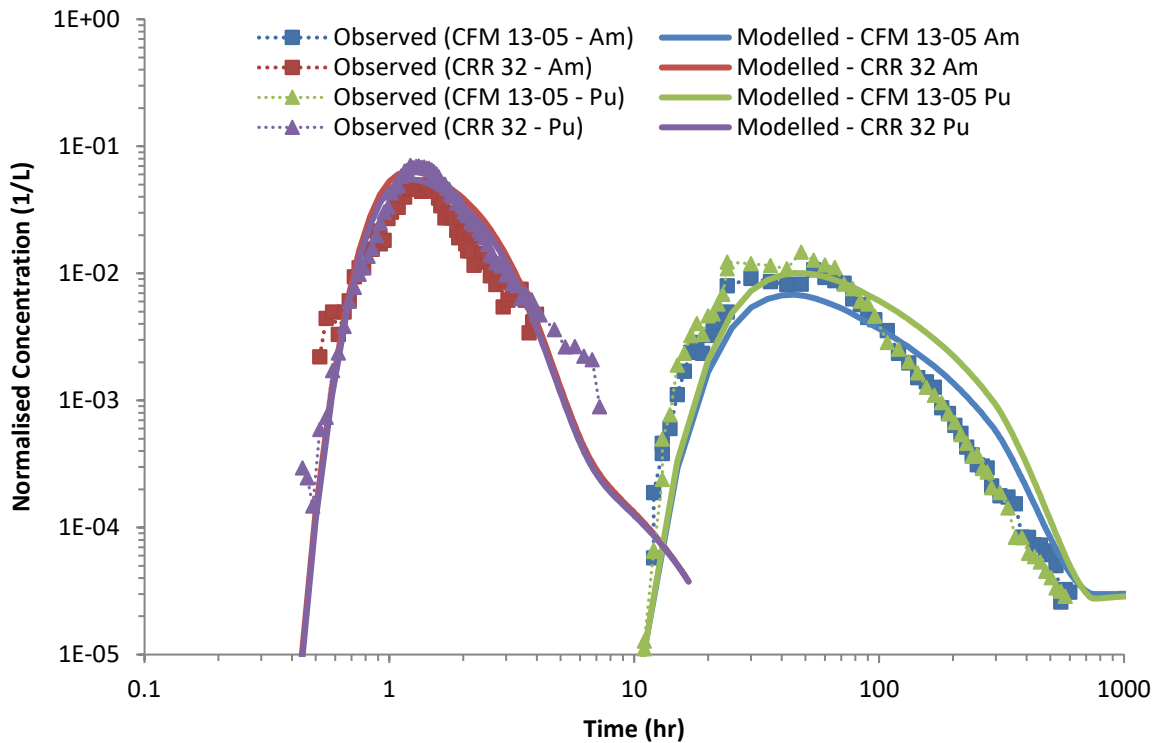


Figure 8.2 Calibrated model results for breakthrough of americium and plutonium in CFM Run 13-05 and CRR Run 32.

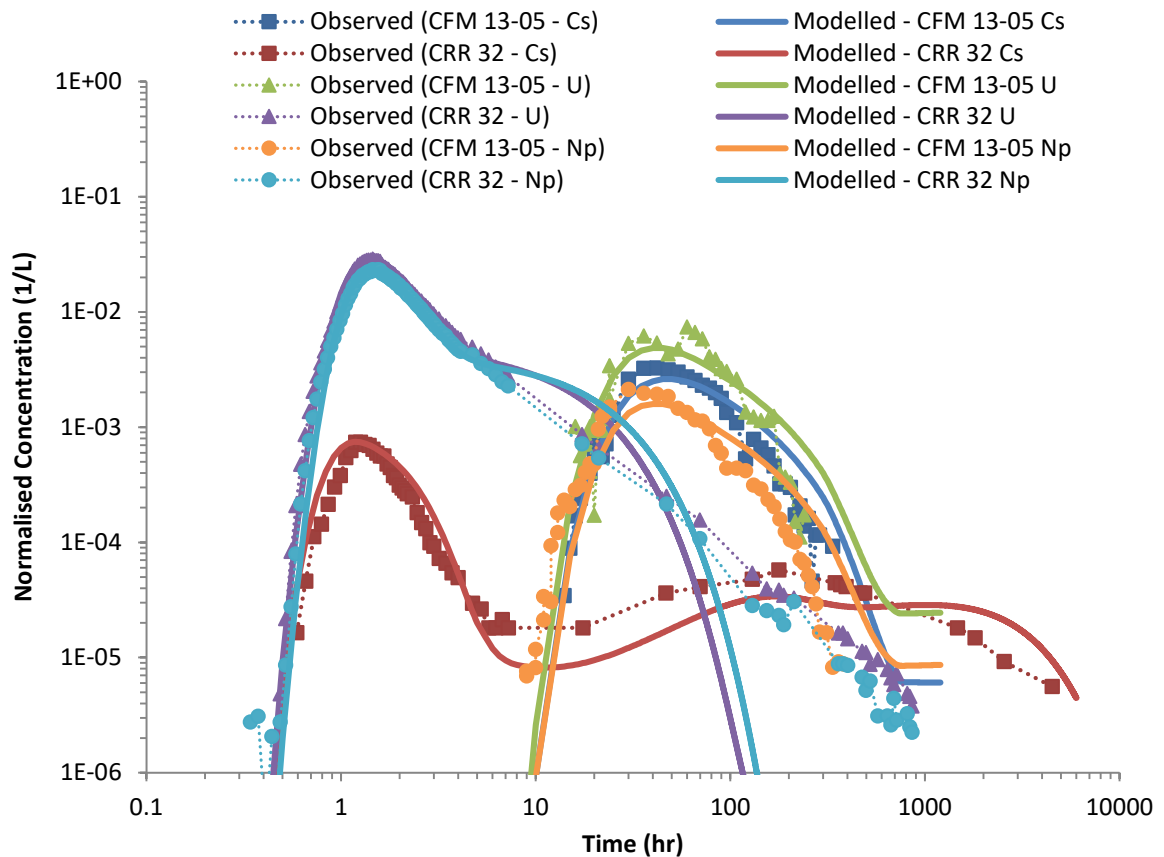


Figure 8.3 Calibrated model results for breakthrough of caesium (two-site model), uranium and neptunium in CFM Run 13-05 and CRR Run 32.

The calibration parameters used in the model are shown in Table 8.2 for conservative tracers, Table 8.3 for the breakthrough of bentonite colloids and Table 8.4 for radionuclide breakthrough. More information on these can be found in the respective chapters. These tables show that consistent parameter values were used in this model for conservative tracer and colloid breakthrough, and for certain radionuclides. Consistent parameter values could not be found for every radionuclide, due to different radionuclide chemistry or different experimental conditions, as discussed further in the relevant chapters and in the next section.

These consistent parameters were found using the full 2D transport model, which included the transmissivity distribution generated by an inverse model. It was attempted to

model the experiments using a 1D ‘channel model’, using a similar approach to other models of the CFM project (e.g. Noseck et al. (2016) and Reimus, (2016)). This 1D model was unsuccessful in finding consistent parameters, as different hydraulic conductivity values were used, and an unrealistic dilution factor was used to model the two experiments. This is due to the highly heterogeneous nature of the MI shear zone, which is not accurately represented by the effective parameters used in the 1D model for the two different experimental flow systems.

<b>Conservative Tracers</b>	Longitudinal dispersivity	Parallel plate scaling factor
	$\alpha_l$ (m)	f (-)
CFM Run 13-05	0.1	7
CRR Run 32	0.1	7

**Table 8.2 Summary of the calibrated parameter values for conservative tracer breakthrough in both experiments. Red = sensitive parameter.**

<b>Colloids</b>	Reversible attachment $k_{att}$ ( $s^{-1}$ )	Detachment rate $k_{det}$ ( $s^{-1}$ )	Irreversible attachment $k_{iat}$ ( $s^{-1}$ )	Colloid retardation $R_c$ (-)	Colloid blocking $F_{max}$ (-)
CFM Run 13-05	$5 \times 10^{-6}$	$5 \times 10^{-5}$	$4 \times 10^{-6}$	1	5
CRR Run 32	$5 \times 10^{-6}$	$5 \times 10^{-5}$	$4 \times 10^{-6}$	1	5

**Table 8.3 Summary of the calibrated parameter values for bentonite colloid breakthrough in both experiments. Red = sensitive parameter.**

<b>Radionuclides</b>	Sorption rate to colloids $k_{amc}$ ( $m^3kg.s^{-1}$ )	Desorption rate $k_{mca}/k_{ica}/k_{cai}$ ( $s^{-1}$ )	Aqueous retardation R (-)	Sorption rate to FFM $k_{ai}$ ( $s^{-1}$ )	Desorption from FFM $k_{ia}$ ( $s^{-1}$ )
CFM 13-05/ Am	$5.89 \times 10^{-5}$	$4.53 \times 10^{-6}$	>1000	-	-
CRR 32/ Am	$5.89 \times 10^{-5}$	$4.53 \times 10^{-6}$	>1000	-	-
CFM 13-05/ Pu	$1 \times 10^{-8}$	$1 \times 10^{-6}$	>1000	-	-
CRR 32/ Pu	$1 \times 10^{-8}$	$1 \times 10^{-6}$	>1000	-	-
CFM 13-05/ Cs	$8 \times 10^{-3}$ ( $1 \times 10^{-5}$ )*	$2 \times 10^{-3}$ ( $5 \times 10^{-7}$ )*	1	$2.25 \times 10^{-3}$ ( $6.5 \times 10^{-4}$ )*	$1.25 \times 10^{-5}$ ( $5 \times 10^{-7}$ )*
CRR 32/ Cs	$8 \times 10^{-3}$ ( $1 \times 10^{-5}$ )*	$2 \times 10^{-3}$ ( $5 \times 10^{-7}$ )*	1	$2.25 \times 10^{-3}$ ( $6.5 \times 10^{-4}$ )*	$1.25 \times 10^{-5}$ ( $5 \times 10^{-7}$ )*
CFM 13-05/ U	$1 \times 10^{-8}$	$6 \times 10^{-6}$	>1000	-	-
CRR 32/ U	$1 \times 10^{-8}$	$6 \times 10^{-6}$	1.3	-	-
CFM 13-05/ Np	$8.1 \times 10^{-6}$	$7 \times 10^{-6}$	>1000	-	-
CRR 32/ Np	$8.1 \times 10^{-6}$	$7 \times 10^{-6}$	1.35	-	-
<b>Radionuclides</b>	Matrix diffusion transfer rate $k_{im}$ ( $s^{-1}$ )	Matrix diffusion porosity $\theta_{im}$ (-)			
CFM 13-05/ U	$1.9 \times 10^{-4}$	5			
CRR 32/ U	$1.9 \times 10^{-4}$	5			
CFM 13-05/ Np	$2.3 \times 10^{-4}$	7			
CRR 32/ Np	$2.3 \times 10^{-4}$	7			

Table 8.4 Summary of the calibrated parameter values for radionuclide breakthrough in both experiments. Red = sensitive parameter. \*Indicates parameters for the second sorption site on either the colloid or FFM as used in the caesium model (see Chapter 7). In addition, the capacity of the individual sites on the colloids are not shown for Cs model.

The highly heterogeneous nature of the shear zone also led to issues concerning the resulting factor used to scale between the hydraulic (or cubic law) aperture used in the inverse model and the transport (or mass balance) aperture required in the transport model. This model represents the shear zone as a series of parallel plates, and used a high scaling factor ( $f = 7$ ), which corresponds to approximately 18 parallel equal sized fractures, far more than present in the MI shear zone (Gaus and Smith, 2008). Modelling in Forbes (2016) showed that the number of parallel plates required to scale between the two apertures increases with transmissivity variance. According to the transmissivity distribution from the inverse model, transmissivity within 'CRR Dipole 1' varies by over four orders of magnitude,

and includes a very low transmissivity 'pinch point' zone in the middle of the dipole, resulting in the requirement of including a large number of parallel fractures to scale between the hydraulic and transport fracture apertures.

When available, parameters used in the model have been compared with those used in previous models of the experiments (for instance Noseck et al. (2016) or Reimus (2016) for modelling from CFM), or from laboratory experiments (for instance the desorption batch experiments detailed in Huber et al. (2011, 2015)). Where comparisons have been made, the rates used in this model are in general agreement with those found using other models and from laboratory experiments. As the parameter values were typically close to laboratory experiments and previous models and were typically the same value for the different experiments, this increases confidence that the model is using an accurate representation of different processes and in the ability of the model to make predictions in the future.

#### **8.4. Objective 4: Identifying important radionuclide transport processes**

Table 8.4 highlights the sensitive calibration parameters for each radionuclide modelled in this study. By identifying these sensitive parameters, and using the geochemical conceptual model of each radionuclide, it is possible to suggest which radionuclide transport processes might be important for radionuclide migration in the two field experiments.

It is important to describe the conservative tracer and colloid transport mechanisms as these may also control radionuclide transport. Different conservative tracers were used for the two experiments, amino-G acid (AGA) in CFM Run 13-05 and iodine-131 in CRR Run 32, and these showed different transport mechanisms. The AGA tracer used in CFM Run 13-05 underwent no retardation processes as expected; however, the model does not replicate all

of the dispersion on the falling limb of the breakthrough curve, which was potentially caused by diffusion of the tracer into slower flow paths or the adjacent rock matrix.

The iodine-131 used in CRR Run 32 arrived later than the colloids in the experiment, and this was attributed to colloid size-exclusion processes by Kosakowski (2004) and Geckeis et al. (2004). However, the breakthrough of colloids in CRR Run 32 (and colloid-facilitated radionuclides) occurred at the same time as uranine in an earlier migration experiment (CRR Run 29) carried out under a similar flow field. Uranine breakthrough in CRR Run 29 was modelled with no retardation factor and a good model match was obtained. This suggests that although iodine-131 would not be expected to undergo sorption and retardation processes, its delayed arrival in CRR Run 32 is caused by retardation of the iodine tracer and not due to the early arrival of size-excluded colloids, contrary to earlier work (Möri et al., 2004; Geckeis et al., 2004).

For colloid transport, colloid attachment controls the breakthrough and recovery in the experiment. Both irreversible and reversible colloid attachment processes were included in the transport model to replicate colloid breakthrough. Colloid recovery was lower in the longer residence time experiment CFM Run 13-05, which was expected as the colloids undergo more interaction with the rock/ attachment surfaces with increasing residence time. This conclusion was also reached in column experiments carried out with similar bentonite colloids within Grimsel granodiorite (Schäfer et al., 2004).

#### **8.4.1. Americium and plutonium**

Americium and plutonium had the highest initial bound fractions of the radionuclides modelled here (americium >99%, plutonium 84-99%), and underwent similar transport

processes in the two experiments. Geochemical modelling suggests that favourable conditions (positive saturation indices) existed for precipitation of self colloids in both experimental injection cocktails. It is thought that in CRR Run 31 (a similar migration experiment to CRR Run 32, but without bentonite colloids), both americium and plutonium self colloids could have formed in the injection cocktail (Möri et al., 2004), as recovery of these species was higher than expected (although this could have also been caused by sorption to background colloids).

The initial bound fraction does not give an indication of whether the radionuclide has sorbed to the bentonite colloids or has precipitated as self colloids. No experimental data exist to confirm whether any self colloids had formed in the injection cocktail. Because of this, the model assumed that any self colloids that formed underwent similar transport processes as bentonite colloids and that sorption of the radionuclides to the colloids was the predominant cause of the initial bound fractions, which is an avenue for further investigation.

In both experiments americium and plutonium migration is colloid-facilitated, and therefore colloid attachment is a key control on their migration. In addition, the sorption of americium and plutonium to the colloids is not irreversible, with the rate of desorption forming another key control on migration. Dissolved americium and plutonium did not breakthrough in the current data from either experiment, the aqueous species showing strong sorption to rock surfaces. However, long term data measured using Accelerator Mass Spectroscopy (AMS) does show delayed aqueous breakthrough of both radionuclides in CFM

Run 13-05 (Quinto et al., 2017). However, these data were not available for model calibration.

#### **8.4.2. Caesium**

Unlike americium and plutonium, caesium showed very different initial bound fractions in the experiments (63% in CFM Run 13-05 and 8% in CRR Run 32). Caesium is expected to be present as Cs (I)<sup>+</sup> in Grimsel groundwater, showing a relatively simple geochemistry in the geochemical model. Unlike the other radionuclides, no caesium precipitates or self colloids were predicted to form in the injection cocktail of either experiment as unfavourable environments (negative saturation indices) for precipitation were expected, suggesting that the initial bound fraction is caused solely by caesium sorbing to the bentonite colloids.

The cause of the different initial bound fractions appears to be the different caesium concentration used in the experiments, and the fact that caesium has a non-linear sorption isotherm to the FEBEX bentonite colloids (Missana et al., 2004). The non-linear behaviour is caused by the presence of two different types of sorption site on the FEBEX bentonite: one high-affinity site on the edge of the clay sheets, which has a limited capacity; and one site situated on the plane of the clay sheets, which has a higher capacity, but shows a lower affinity. The lower caesium concentration used in CFM Run 13-05 meant that the stronger edge site had not reached capacity and that a higher percentage of caesium sorbed to the colloids. In CRR Run 32, the higher concentration used meant that the edge site had reached capacity, and that the low affinity planar site controlled caesium sorption. Because of this, a lower percentage of caesium sorbed to the colloids resulting in the lower bound fraction.

Initial attempts at modelling caesium using one sorption site on the colloids were unsuccessful in finding a consistent set of parameters to describe caesium-colloid sorption and desorption rates for the two experiments. Once the two-site model was developed, it was possible to describe the sorption of caesium to colloids and rock surfaces using a consistent set of parameter values for both experiments. Compared to laboratory data, the capacity of the edge site used in this model was lower than the laboratory data. The exact cause of this difference requires further investigation, but a potential cause was that the other radionuclides present in the injection cocktail compete with caesium, filling the edge site, resulting in a lower available capacity in the field experiment, whereas in the laboratory experiments only caesium is included, so less competitive sorption occurs.

Caesium transport was partially facilitated by colloids in both experiments; the transport of both colloid-bound and dissolved caesium was observed in CRR Run 32. As was found for americium and plutonium, caesium sorption to the colloids was reversible, with the rate of desorption forming a key control on the migration of colloid bound caesium. Kinetic sorption to two sites was used to describe caesium sorption to rock surfaces, although this was only important for calibrating the breakthrough in CRR Run 32 as in CFM Run 13-05 only colloid-bound caesium was observed (the data for aqueous caesium breakthrough was not collected).

### **8.4.3. Uranium and neptunium**

Uranium and neptunium also showed different initial bound fractions between the experiments. Uranium had initial bound fractions of 6% in CRR Run 32 and 83% in CFM Run 13-05, and neptunium had the lowest initial bound fractions of all the radionuclides

modelled (30% in CFM Run 13-05 and <1% in CRR Run 32). The cause of the different initial bound fractions is thought to be similar for the two radionuclides. However, due to the complex chemistry that these radionuclides exhibit this needs further investigation.

In CRR Run 32, it is thought that the shorter time between injection cocktail preparation and the experiment (5 days) meant that the radionuclides remained in the oxidised redox state in which they were added into the injection cocktail, i.e. uranium (VI) and neptunium (V). This contradicts the geochemical modelling, which used the average Eh of Grimsel groundwater, which expected neptunium (IV) to be present in the reducing Grimsel groundwater. In addition, geochemical modelling predicted favourable conditions for precipitation of self colloids in the injection cocktail, but the low initial bound fraction suggests that precipitation had not occurred, potentially as the cocktail equilibration time was not long enough to allow reduction and precipitation to occur. As the radionuclides remained in their oxidised redox state, they weakly sorbed to both the colloids in the injection cocktail (resulting in the low colloid-bound fractions), and rock surfaces in the migration experiment. The result of this is that the two radionuclides migrated in this experiment mainly as aqueous dissolved species, undergoing limited retardation and some matrix diffusion.

For CFM Run 13-05, however, the longer cocktail equilibration time (35 days) meant that the two radionuclides could have reduced to uranium (IV) and neptunium (IV). These reduced radionuclides are expected to undergo stronger sorption to the colloids (Missana and Geckeis, 2006), leading to the higher initial bound fractions observed in this experiment. In addition, the geochemical model predicted favourable chemical conditions for the

formation of self colloids, and the longer cocktail equilibration time could have allowed for their formation in this experiment, which would be included in the measurement of the high initial bound fraction. However, self colloid formation could not be confirmed with the available laboratory data, and so requires further investigation. There are also other potential causes for the differing initial bound fractions which cannot be discounted with current data, such as different pH, carbonate or iron oxide concentrations in the Grimsel groundwater used to prepare the two injection cocktails, all of which again need further investigation and should be taken into account when designing future migration experiments.

The consequence of the higher initial bound fraction is that the transport of uranium and neptunium in CFM Run 13-05 was colloid-facilitated (whether caused by sorption to the bentonite colloids, or the formation of self colloids). Limited breakthrough of aqueous species was modelled, which could be related to the reduced radionuclides in the source term undergoing stronger sorption to the rock surface (Missana and Geckeis, 2006), and a retarded breakthrough. As was observed for the other radionuclides, both uranium and neptunium sorption to the colloids was reversible, with the rate of desorption again forming a key rate control on their migration.

Once these different transport mechanisms were incorporated into the model, the transport of the two radionuclides was modelled successfully in both experiments.

## **8.5. Modelling implications**

From the modelling carried out in this study several transport processes have been identified for tracers, bentonite colloids and several radionuclides (as described in the

previous section). It is important to note that any understanding that has been gained from this modelling will be relatively specific to the geochemical conditions found at the Grimsel test site (i.e. pH ~9.6, low ionic strength glacial meltwater). This is because the behaviour and stability of the bentonite colloids used in the migration experiments and the behaviour of the radionuclides in the experiment (i.e. how they interact with the bentonite colloids and Grimsel FFM) is mainly controlled by the geochemistry of the Grimsel groundwater and the migration experiments. Therefore, caution needs to be applied if using the results of this modelling on other sites in different geological and geochemical settings as different behaviour may occur. This is also important considering the value of certain parameters (for instance the desorption rate from colloids  $k_{mca}$ ) is dependent on the assumptions made in this model (for instance the retardation factor, and the parallel plate model) and likely to be specific to the chemical conditions (pH, ionic strength, RN concentrations) found in the two migration experiments.

The modelling carried out in this study has improved understanding of the behaviour of radionuclide and colloid-facilitated radionuclide transport in the two migration experiments carried out at the Grimsel Test Site. Previous models, although providing good matches to the model data, required the use of different parameter values to model the same species in different experiments. For the majority of radionuclides modelled in this study, the same consistent set of parameter values were used to describe their transport, as was also achieved for tracer and bentonite colloid transport.

This model is the first model of the migration experiments that combines a transmissivity distribution generated by inverse modelling with a colloid-facilitated radionuclide transport

model. This provided more information on flow path geometry and directly solved for groundwater flow during the experiment (some of the previous models were descriptive for groundwater flow). Chapter 5 details the use of a 1D 'channel' model to also model the experiments. The 1D model was not able to find the same parameter values to describe groundwater flow and solute transport between experiments, and the 2D model provided a better representation of the macrodispersion present in the different flow paths within the MI shear zone and the mass loss that occurred during the migration experiments.

Colloid attachment processes are clearly occurring during the experiments, as colloid recovery is lower than conservative tracers in both experiments. In addition, colloid recovery was lower in CFM Run 13-05 (as the experiment had a longer residence time) than in CRR Run 32. This finding is the same as similar laboratory column experiments (Schäfer et al., 2004). Colloid filtration theory predicts that colloids will be most stable and limited colloid attachment would occur in the low ionic strength, high pH groundwater, such as that found at Grimsel. The fact that colloid attachment did occur in the migration experiments indicates that the bentonite colloids used in the experiment could be less mobile in other geochemical (and hydrogeological) settings with lower pH and higher ionic strength groundwater, potentially limiting colloid-facilitated radionuclide transport in other geochemical environments.

The sorption of all the radionuclides to the bentonite colloids in this study has been shown to be reversible during the migration experiments. For americium, plutonium and caesium, the same parameter set was used to describe the interaction between these radionuclides and the bentonite colloids. The transport and recovery of these radionuclides

was controlled by the rate of desorption from the bentonite colloids, which was particularly the case for americium and plutonium as the model assumed that only colloid-bound radionuclides were observed in the available breakthrough data. Caesium required the use of a two-sorption site model to find the same parameter values, due to the non-linear sorption behaviour it exhibits with the colloids. This is the first time that a two-site model has been applied to the transport of caesium in the migration experiments, which was successful in using the same parameter values to describe caesium sorption to the different sites.

Uranium and neptunium were not able to be modelled using consistent parameter values. Geochemical modelling of the injection cocktails has again, for the first time, been applied as part of a geochemical conceptual model for the transport of these two radionuclides. It is likely that differing geochemical conditions in the experiments (a different injection cocktail equilibration time) caused differences in the transport behaviour observed for these two radionuclides. This led to different transport behaviour, as it is thought that in CRR Run 32 these radionuclides remained in the oxidised state that they were added, being transported as an aqueous species. In CFM Run 13-05 it is thought that these radionuclides reduced and therefore showed stronger sorption to the colloids and rock surfaces in the experiment, as mostly colloid-bound radionuclide was observed in the experiment. In addition, self-colloids of these two radionuclides could have formed in CFM Run 13-05, although this could not be confirmed with available experimental data.

All of the radionuclides modelled in this study showed reversible sorption to the colloids. Under the 'colloid ladder' described previously (Figure 2.1), this would show that

colloid-facilitated radionuclide transport would be insignificant in the conditions of the Grimsel Test Site and in similar settings (Möri et al., 2004). However, Schäfer et al. (2016) describe a more appropriate 'colloid ladder', where an assessment of desorption rate compared to the residence time is made, as this could still cause colloid-facilitated radionuclide transport.

An assessment of whether colloid-facilitated radionuclide transport would be significant for a GDF setting is outside the scope of this study, as there are likely to be differences between the experimental conditions in this study and the conditions found in a GDF setting, which include the concentration of colloids, the time scales involved and the method of release of the radionuclides and colloids. Some discussion is present in Noseck et al. (2016) based on the implications of previous modelling carried out in the CFM project to which the reader is referred.

## **8.6. Areas for future work**

Throughout the course of this work, areas for potential future research have been identified. Firstly, this model raises several areas for future work on the behaviour of certain radionuclides that need further investigation, including:

- Improve understanding of the formation of self-colloids in the Grimsel groundwater environment. This will improve understanding on the migration behaviour of several radionuclides modelled in this study and could involve study of precipitation rates in the presence of the bentonite colloids and inclusion of self colloids in this transport model.

- For caesium, improving understanding of the sorption process to clay colloids, including the non-linear sorption isotherm, the multiple sorption sites and capacity of these sorption sites in the presence of competing radionuclides.
- For uranium and neptunium, improving the understanding of the geochemistry of these radionuclides in the Grimsel groundwater environment and in migration experiments, with a focus on the complex redox chemistry that these radionuclides show in colloidal suspensions.

If an additional migration experiment is to be run during the remainder of the CFM project, this needs to represent the preparation of previous experiments closely. In addition, measurements of the colloidal fraction of recovered radionuclides and analysis of colloid type (to determine whether carrier colloids or self colloids were transporting radionuclides) would be useful data to collect to help constrain future modelling efforts.

The calibrations generated by this model could potentially be improved by carrying out a detailed sensitivity analysis on the transmissivity distribution and investigating further the use of the parallel plate model in the highly heterogeneous MI shear zone. In addition, changes to the colloid model could reduce some of the error seen in the radionuclide breakthrough calibrations, as could changes to the matrix diffusion representation for some of the radionuclides. Another improvement in the model could be explicitly modelling the injection cocktails of each experiment, and potential competition between the radionuclides.

The model developed in this study is very flexible and could very easily be applied to the other radionuclides injected in the two migration experiments (such as thorium, strontium

and technetium), as well as to a wide range of other migration experiments. If more complex processes between colloids and radionuclides are shown to be important in future migration experiments, then this model can be easily extended to represent them. An example of this could be the long-term breakthrough curve data measured by Accelerator Mass Spectroscopy (AMS) in CFM Run 13-05, which is thought to represent the breakthrough of aqueous radionuclides.

Finally, the methods developed here to model colloid-facilitated radionuclide transport in the two migration experiments can be applied to assess: colloid-facilitated radionuclide transport at other sites, such as a future GDF site; colloid-facilitated transport of other species (e.g. heavy metals); or colloid-facilitated radionuclide transport caused by other colloids.

## 8.7. List of References

Bryan, N. and Sherriff, N. (2016) **BELBaR D3.10 Mechanistic model of radionuclide colloid interaction**. European Commission, Brussels.

Dittrich, T.M., Boukhalfa, H., Ware, S.D. and Reimus, P.W. (2015) Laboratory investigation of the role of desorption kinetics on americium transport associated with bentonite colloids. **Journal of Environmental Radioactivity** [online], 148: 170–182 DOI: 10.1016/j.jenvrad.2015.07.001. Available from: <http://dx.doi.org/10.1016/j.jenvrad.2015.07.001>

Forbes, A. (2016) **Examining the Effects of Small Scale Heterogeneity on the Effective Apertures Calculated from Flow and Transport Data**. MSc Nuclear Decommissioning and Waste Management Project, University of Birmingham

Gaus, I. and Smith, P.A. (2008) **Nagra Arbeitsbericht NAB 08-27: Modellers dataset for the Colloid Formation and Migration Project Status: End of CFM Phase 1**. Wettingen, Switzerland

Geckeis, H., Schafer, T., Hauser, W., Rabung, T., Missana, T., Degueldre, C., Möri, A., Eikenberg, J., Fierz, T. and Alexander, W.R. (2004) Results of the colloid and radionuclide retention experiment (CRR) at the Grimsel Test Site (GTS), Switzerland - Impact of reaction kinetics and speciation on radionuclide migration. **Radiochimica Acta**, 92 (9–11): 765–774 DOI: 10.1524/ract.92.9.765.54973

Huber, F., Heck, S., Truche, L., Bouby, M., Brendle, J., Hoess, P. and Schäfer, T. (2015) Radionuclide desorption kinetics on synthetic Zn / Ni-labeled montmorillonite nanoparticles. **Geochimica et Cosmochimica Acta**, 148: 426–441 DOI: 10.1016/j.gca.2014.10.010

Huber, F., Kunze, P., Geckeis, H. and Schäfer, T. (2011) Sorption reversibility kinetics in the ternary system radionuclide-bentonite colloids/nanoparticles-granite fracture filling material. **Applied Geochemistry** [online], 26 (12): 2226–2237 DOI: 10.1016/j.apgeochem.2011.08.005. Available from: <http://dx.doi.org/10.1016/j.apgeochem.2011.08.005>

Jennings, A. and Kirkner, D. (1984) Instantaneous equilibrium approximation analysis. **Journal of Hydraulic Engineering** [online], 110 (12): 1700–1717 DOI: doi:10.1061/(ASCE)0733-9429(1984)110:12(1700). Available from: [http://ascelibrary.org/doi/abs/10.1061/\(ASCE\)0733-9429\(1984\)110:12\(1700\)](http://ascelibrary.org/doi/abs/10.1061/(ASCE)0733-9429(1984)110:12(1700))

Kosakowski, G. (2004) Anomalous transport of colloids and solutes in a shear zone. **Journal of Contaminant Hydrology**, 72: 23–46 DOI: 10.1016/j.jconhyd.2003.10.005

Kosakowski, G. and Smith, P. (2004) **Nagra Technical Bulletin NTB 04-01: Grimsel Test Site Investigation Phase V Modelling the transport of Solutes and Colloids in a Water Conducting Shear Zone at the Grimsel Test Site** [online]. Wettingen, Switzerland. Available from: <http://www.nagra.ch/en/cat/publikationen/technicalreports-ntbs/ntbs-2001-2012/downloadcentre.htm>

Missana, T., García-Gutiérrez, M. and Alonso, Ú. (2004) Kinetics and irreversibility of cesium and uranium sorption onto bentonite colloids in a deep granitic environment. **Applied Clay Science**, 26 (1–4 SPEC. ISS.): 137–150 DOI: 10.1016/j.clay.2003.09.008

Missana, T. and Geckeis, H. (2006) **Nagra Technical Bulletin NTB 03-02: CRR Final Project Report 2 - Supporting Laboratory Experiments with Radionuclides and Bentonite Colloids**. Wettingen, Switzerland

Möri, A., Alexander, W.R., Degueldre, C., Eikenberg, J., Fierz, T., Geckeis, H., Geier, F., Hauser, W., Schäfer, T. and Smith, P.A. (2004) **Nagra Technical Bulletin NTB 03-01: The CRR Final Project Report series 1 - Description of the Field Phase - Methodologies and Raw Data** [online]. Wettingen, Switzerland. Available from: <http://www.nagra.ch/en/cat/publikationen/technicalreports-ntbs/ntbs-2001-2012/downloadcentre.htm>

Noseck, U., Flügge, J., Reimus, P., Cvetkovic, V., Lanyon, B., Schäfer, T. and Blechschmidt, I. (2016) **Nagra Technical Report NTB 16-06: Colloid Formation and Migration Project: Modelling of tracer, colloid and radionuclide/homologue transport for dipole CFM 06.002- Pinkel surface packer**. Wettingen, Switzerland

Quinto, F., Blechschmidt, I., Garcia Perez, C., Geckeis, H., Geyer, F., Golser, R., Huber, F.M., Lagos, M., Lanyon, B., Plaschke, M., Steier, P., Schäfer, T., Perez, C.G., Geckeis, H., Geyer, F., Golser, R., Huber, F.M., Lagos, M., Lanyon, B., et al. (2017) Multi-actinide analysis with AMS for ultra-trace determination in small samples : application to an in situ radionuclide tracer test within the Colloid Formation and Migration (CFM) experiment at the Grimsel Test Site (GTS , Switzerland). **Analytical Chemistry**, 89 (13): 7182–7189 DOI: 10.1021/acs.analchem.7b01359

Reimus, P.W. (2016) **Nagra NAB 16-61: GTS Phase VI- CFM Phase 3: Interpretation of colloid-facilitated radionuclide transport experiments from the CRR and CFM projects**. Wettingen, Switzerland

Schäfer, T., Geckeis, H., Bouby, M. and Fanghänel, T. (2004) U, Th, Eu and colloid mobility in a granite fracture under near-natural flow conditions. **Radiochimica Acta**, 92 (9–11): 731–737 DOI: 10.1524/ract.92.9.731.54975

Schäfer, T., Sherriff, N., Bryan, N., Livens, F., Bouby, M., Darbha, G., Stoll, M., Huber, F., Schafer, T., Holtta, P., Elo, O., Suorsa, V., Honkaniemi, E., Niemiaho, S., Missana, T., Alonso, Ú., Mayordomo, N., Koloma, K., Cervinka, R., et al. (2016) **BELBaR D3.11: WP3 partners final report on experimental results on micro to macroscale colloid rock interaction and colloid radionuclide interaction.**

Brussels

Sherriff, N., Issa, R., Morris, K., Livens, F., Heath, S. and Bryan, N. (2015a) Reversibility in radionuclide/bentonite bulk and colloidal ternary systems. **Mineralogical Magazine** [online], 79 (6): 1307–1315 DOI: 10.1180/minmag.2015.079.06. Available from: <http://openurl.ingenta.com/content/xref?genre=article&issn=0026-461X&volume=79&issue=6&spage=1307>

Sherriff, N., Livens, F., Bryan, N., Elo, O., Huittinen, N., Muller, K., Holtta, P., Alonso, Ú., Missana, T., Quinto, F., Lagos, M., Plaschke, M., Schäfer, T., Geckeis, H. and Steier, P. (2015b) **BELBaR D3.09: Understanding of Radionuclide Colloid Interaction**

Smith, P.A., Guimera, J., Kosakowski, G., Pudewills, A. and Ibaraki, M. (2006) **Nagra Technical Bulletin NTB 03-03: Grimsel Test Site Investigation Phase V - The CRR Final Project Report series 3: Results of the Supporting Modelling Programme.** Wettingen, Switzerland

# APPENDICES

## List of Appendices

<b>APPENDICES</b> .....	289
Appendix A. GEOCHEMICAL MODEL.....	291
A.1. Model Setup.....	291
A.2. Example PHREEQC Input Files.....	292
CFM Run 13-05 Cocktail, Eh -220mV, pH 9.6.....	292
CRR Run 32 Cocktail, Eh -220mV, pH 9.6.....	293
A.3. List of References.....	294
Appendix B. CODE USED IN TRANSPORT MODEL.....	295
B.1. R Script to generate model Geometry files.....	295
B.2. C Function to read .hds/ .dat file into COMSOL.....	296
B.3. C Function to read K field into COMSOL.....	301
B.4. List of References.....	305
Appendix C. COLLOID TRANSPORT MODEL VERIFICATION.....	306
C.1. Background.....	306
C.2. Methods.....	306
Model Setup.....	307
Model Calibration.....	308
C.3. Results.....	309
Variable Permeability.....	309
Model Calibration.....	312
C.4. Discussion.....	315
C.5. List of References.....	316
Appendix D. COLLOID RECOVERY PLOTS.....	317
D.1. Background.....	317
D.2. Methods.....	317
D.3. List of References.....	322
D.4. Code Used.....	322
Appendix E. DATA AND MODEL FILES.....	326
E.1. List of Digital Files.....	326
E.2. List of References.....	327

## List of Figures

Figure C.1 Pictures from visual fluorescein migration test. Images taken at (from left to right): Top - 1, 5 and 10 minutes; Middle - 15, 20 and 25 minutes; Bottom - 30, 32 and 50 minutes .....	310
Figure C.2 Zones of lower permeability (highlighted in blue) .....	311
Figure C.3 Colour Plots of Concentration ( $\text{kg/m}^3$ ), with experimental results to the right. Images taken at 15 and 20 minutes after tracer injection .....	311
Figure C.4 Calibrated Breakthrough for Experiment B (blue line), with conservative breakthrough (yellow line) .....	314
Figure D.1 Colloid recovery plot with no irreversible colloid attachment .....	319
Figure D.2 Colloid recovery with an irreversible attachment rate $k_{iat} = 1e-7 \text{ 1/s}$ .....	319
Figure D.3 Colloid recovery with an irreversible attachment rate $k_{iat} = 1e-6 \text{ 1/s}$ .....	320
Figure D.4 Colloid recovery with an irreversible attachment rate $k_{iat} = 3e-6 \text{ 1/s}$ .....	320
Figure D.5 Colloid recovery with an irreversible attachment rate $k_{iat} = 5e-6 \text{ 1/s}$ . Red points indicate areas where parameters gave good match to CRR 32 breakthrough .....	321
Figure D.6 Colloid recovery with an irreversible attachment rate $k_{iat} = 6e-6 \text{ 1/s}$ . Red points indicate areas where parameters gave good match to CRR 32 breakthrough .....	321

## List of Tables

Table C.1 Non-calibration parameter values used in model .....	308
Table C.2 Typical parameters for broad sensitivity analysis .....	309
Table C.3 Calibrated model parameters .....	313

## List of Equations

Equation C.1 Colloid Filtration Equation .....	307
--	-----

## Appendix A. **GEOCHEMICAL MODEL**

This appendix details the geochemical modelling in PHREEQC that has been developed by Dr Janice Kenney and has been used to provide information on radionuclide speciation in the injection cocktail of the two migration experiments, and on the potential for precipitates or self colloids to have formed in the injection cocktail prior to the experiments being carried out.

### **A.1. Model Setup**

PHREEQC (Parkhurst and Appelo, 2013) was used to calculate the speciation and saturation indices of components of Grimsel groundwater (Chapter 4), and the radionuclides included in the injection cocktail of both CFM Run 13-05 and CRR Run 32 (Chapters 6 and 7). For this model, the solution keyword in PHREEQC was used, detailing the concentration of the different species measured in reference Grimsel groundwater (Bennett, 2014), and the concentration of the different radionuclides as measured in both experiments (Möri et al., 2004; Schäfer et al., n.d.). The values of pH and Eh were initially either based on the values of reference Grimsel groundwater or measured in CRR Run 32 (no measurements could be found for CFM Run 13-05), although a detailed sensitivity analysis of changes in both pH (between pH 9 and pH 12) and Eh (between -140 mV and -280 mV) was carried out to determine the controls on chemistry in the Grimsel system.

Initial modelling used the PSI-Nagra thermodynamic database (Thoenen et al., 2014) that was imported into PHREEQC, and also considered the LLNL.dat database built into PHREEQC, as well as the SIT.dat/ Andra Thermochemie database (Giffaut et al., 2014). Comparing the available species or the calculation of both radionuclide speciation and saturation indices,

the SIT/ Thermochemie database was chosen for detailed modelling due to the larger number of radionuclide species available in the database.

One drawback of the PHREEQC model is that bentonite colloid surfaces are not included in the model due to the large dataset required to include the various ion exchange and surface complexation reactions involved with radionuclides sorbing to the bentonite colloids. This means that processes such as surface-mediated reduction which could alter the redox state of the different radionuclides will not be reflected in the results of the geochemical model. This may be important for some of the redox sensitive radionuclides which could be transported differently in different redox states (e.g. Np, U).

An additional drawback is that the model assumes thermodynamic equilibrium, which may not be an appropriate assumption (although the cocktail equilibration times are relatively long; 5 days for CRR Run 32, and 35 days in CFM Run 13-05). If equilibrium for sorption or precipitation was not reached in the cocktails before the experiments, differences may exist between predictions from the model and what occurred in the injection cocktail.

Example PHREEQC input model files are shown in the next section for both CFM Run 13-05 and CRR Run 32. These inputs formed the basis of the different sensitivity analyses carried out, the results of which are shown in Chapters 4, 6 and 7.

## **A.2. Example PHREEQC Input Files**

### **CFM Run 13-05 Cocktail, Eh -220mV, pH 9.6**

SOLUTION 1 CFM COCKTAIL - -220mV

```
temp 12
pH 9.6
pe -3.73
```

redox pe  
 units mol/l  
 density 0.999  
 Al 2.63e-006  
 Am 4.3e-010  
 Ba 3.41e-009  
 Br 3.8e-007  
 C(4) 0.00045  
 Ca 0.00014  
 Cl 0.00016  
 Cs 8.8e-010  
 F 0.00036  
 Fe 3e-009  
 K 5e-006  
 Mg 6.2e-007  
 Mn 5e-009  
 Na 0.00069  
 Np 8.6e-009  
 Pu 2e-009  
 S 6.1e-005  
 Si 0.00025  
 Sr 2e-006  
 Th 4.5e-009  
 U 4.3e-010  
 -water 2.25 # l

**CRR Run 32 Cocktail, Eh -220mV, pH 9.6**

SOLUTION 1 CRR COCKTAIL - -220mV

temp 12  
 pH 9.6  
 pe -3.73  
 redox pe  
 units mol/l  
 density 0.999  
 Al 2.63e-006  
 Am 6.66e-10  
 Br 3.8e-007  
 C(4) 0.00045  
 Ca 0.00014  
 Cl 0.00016  
 Cs 1.38e-08  
 F 0.00036  
 Fe 3e-009  
 I 9.23e-013  
 K 5e-006  
 Mg 6.2e-007  
 Mn 5e-009  
 Na 0.00069  
 Np 1.09e-06

Pu 6.7477e-09  
S 6.1e-005  
Si 0.00025  
Sr 2e-006  
Tc 1.04e-08  
Th 1.10e-08  
U 8.69e-07  
-isotope 87Sr 1.11e-011  
-water 0.1 # L

### A.3. List of References

Bennett, D.G. (2014) **2014:11 Radionuclide Solubility Limits in SKB's Safety Case**. Stockholm, Sweden.

Giffaut, E., Grivé, M., Blanc, P., Vieillard, P., Colàs, E., Gailhanou, H., Gaboreau, S., Marty, N., Madé, B. and Duro, L. (2014) **Andra thermodynamic database for performance assessment: ThermoChimie**. Applied Geochemistry, 49: 225–236 DOI: 10.1016/j.apgeochem.2014.05.007

Möri, A., Alexander, W.R., Degueldre, C., Eikenberg, J., Fierz, T., Geckeis, H., Geier, F., Hauser, W., Schäfer, T. and Smith, P.A. (2004) **Nagra Technical Bulletin NTB 03-01: The CRR Final Project Report series 1 - Description of the Field Phase - Methodologies and Raw Data**. Wettingen, Switzerland

Parkhurst, D.L. and Appelo, C.A.J. (2013) **Description of input and examples for PHREEQC version 3-- A computer program for speciation, batch- reaction, one-dimensional transport, and inverse geochemical calculations**. Book 6, chap. A43, 497 p., available only at <http://pubs.usgs.gov/tm/06/a43>.

Schäfer, T., Lanyon, B. and Blechschmidt, I. (n.d.) **CFM 13-05 Data Set**. Unpublished dataset, personal communication.

Toenen, T., Hummel, W., Berner, U. and Curti, E. (2014) **The PSI / Nagra Chemical Thermodynamic Database 12 / 07**. Villigen, Switzerland

## Appendix B. CODE USED IN TRANSPORT MODEL

This appendix details the various codes used in the course of this study, for instance to set up the transport model, or to help produce statistics of the model output.

### B.1. R Script to generate model Geometry files

Summary of Code: The R code reads the rows and columns file of the different K-zones used by the PEST model to create .dxf files that can be imported into the COMSOL model.

```
### Generate COMSOL DXF Geometry Import File ###  
  
setwd("C:/Data/Inverse Modelling/HydroFrame/RFiles/ExampleFilesNeededForCOMSOL/")  
  
library("adehabitat")  
  
cols<-unlist(read.table(file = "Col_Dis.txt"))  
  
rows<-unlist(read.table(file = "Row_Dis.txt"))  
  
Offset<-unlist(read.table(file="Offset.txt",skip=1,header=FALSE))  
  
totw<-cols[1]  
  
toth<-rows[1]  
  
xoff<-Offset[1]  
  
yoff<-Offset[2]  
  
rows<-rows[-c(1:2)]  
  
cols<-cols[-c(1:2)]  
  
rows_out<-toth-rows[1]  
  
for (r in 1:length(rows)){  
  
  rows_out<-c(rows_out,rows_out[r-1]-rows[r])  }  
  
cols_out<-cols[1]  
  
for (c in 1:length(cols)){  
  
  cols_out<-c(cols_out,cols_out[c-1]+cols[c])      }  
  
## Reverse rows toth-  
  
K.r<-0
```

```

myKzones<-data.frame(t(rep(NA,3)))[-1,]
colnames(myKzones)<-c("Zone","x","y")
rows<-rows_out
cols<-cols_out
for(c in 1:length(cols)){
  K.l<-K.r
  K.r<-cols[c]
  K.b<-toth
  for(r in 1:length(rows)){
    K.t<-K.b
    K.b<-rows[r]
    temp<-data.frame(rep(paste("K",(c-1)*length(rows)+r,sep=""),4),c(K.l,K.l,K.r,K.r),c(K.b,K.t,K.t,K.b))
    colnames(temp)<-c("Zone","x","y")
    myKzones<-rbind(myKzones,temp)  }
  }

myKzones$x<-myKzones$x+xoff
myKzones$y<-myKzones$y+yoff

ar <- as.area(myKzones)
##area.plot(ar, values=1)
area2dxr(ar, file = "KZones")

```

## B.2. C Function to read .hds/ .dat file into COMSOL

Summary of Code: The purpose of this C code is to allow COMSOL to read the necessary hydraulic head values from a .hds file generated by a MODFLOW model of the full shear zone that can be used on the boundary of the transport model. The code follows the template specified by the COMSOL API for External Functions (COMSOL, 2013).

```
#include <stdio.h>
```

```

#include <math.h>

#include <stdlib.h>

#include <string.h>

#ifdef _MSC_VER
#define EXPORT __declspec(dllexport)
#else
#define EXPORT
#endif

static const char *error = NULL;

EXPORT int init(const char *str) {
return 1;    }

EXPORT const char * getLastError() {
return error; }

double* readdisc (char *myfile,int *arr_len,double *tot_len)
{
    // read in Row/Column array - Rows.txt/Cols.txt need to be in KField folder
    FILE *fp;
    char str [80];
    int i;
    double *myarr,prev;
    fp = fopen(myfile,"r"); // read mode
    if( fp == NULL )
    {
        error="Error while opening row/col file.\n";
        return NULL;    }
    fscanf (fp, "%s", &str);
    *tot_len=atof(str);
    fscanf (fp, "%i", arr_len);
    myarr = (double*) malloc (*arr_len * sizeof(double));
    prev=0;
    for (i = 0;i<*arr_len;i++){
        fscanf (fp, "%s", &str);
        myarr[i]=prev+atof(str);
        prev=myarr[i];    }
}

```

```

fclose(fp);

return myarr;          }

double** readHarr (char *myfile,int nc,int nr)
    // read in K array - KField.dat needs to be in KField folder
{
    FILE *fp;

    char str [80];

    int r,c;

    double **myarr;

    fp = fopen(myfile,"r"); // read mode

    if( fp == NULL )

    {
        error="Error while opening H file.\n";

        return NULL;          }

    /* Allocate array */

    myarr = (double**) malloc (nr * sizeof(double));

    /* Read in H values */

    for (r = 0;r<nr;r++){

        myarr[r] = (double*) malloc (nc * sizeof(double));

        for (c = 0;c<nc;c++){

            fscanf (fp, "%s", &str);

            myarr[r][c]=atof(str);          }}

    fclose(fp);

    return myarr;          }

void readOffset(double *xoff, double *yoff){

    FILE *fp;

    char str [80];

    char *myfile = "C:\\Data\\GetK\\KField\\Offset.txt";

    fp = fopen(myfile,"r"); // read mode

    if( fp == NULL )

    { // failed to open file

        error="Error while opening the offset file.\n";

        *xoff=999;

```

```

        *yoff=999;        }
else {        fgets(str, 80, fp);

        fscanf (fp, "%s", &str);

        *xoff=atof(str);

        fscanf (fp, "%s", &str);

        *yoff=atof(str);

        fclose(fp);}        }

int searcharr(double *myarr, int arr_max,int arr_min,double mycoord){

    // binary search to find row/column of coordinate

    while(arr_min<arr_max)

    {    int middle = (arr_min+arr_max)/2;

        if(myarr[middle] == mycoord)

            return middle;

        else if (myarr[middle] > mycoord)

            arr_max = middle;

        else

            arr_min = middle + 1;        }

    return arr_min;        }

EXPORT int eval(const char *func,

int nArgs,

const double **inReal,

const double **inImag,

int blockSize,

double *outReal,

double *outimag) {

    int i;

    double totw,toth;

    double xoff,yoff;

    int nc,nr,np,r,c;

    double *rows, *cols;

    double **Hs;

```

```

if (strcmp("getH", func) == 0) {
    if (nArgs != 2) {
        error = "Two argument expected";
        return 0;    }
    /* Read in row and column details */
    readOffset(&xoff,&yoff);
        if (xoff==999 | yoff==999) {
            return 0;}
        cols=readdisc("C:\\Data\\GetK\\KField\\Col_Dis.txt",&nc,&totw);
            if (cols==NULL) {return 0;}
        rows=readdisc("C:\\Data\\GetK\\KField\\Row_Dis.txt",&nr,&toth);
            if (rows==NULL) {return 0;}
        Hs=readHarr("C:\\Data\\GetK\\KField\\HField.dat",nc,nr);
            if (Hs==NULL) {return 0;}
        for (i=0;i<blockSize;i++){ // for each coordinate
            double x = inReal[0][i]-xoff;
            double y = toth-(inReal[1][i]-yoff);
            if (x<0 | y<0 | | y>toth | | x>totw) {
                // if x/y coordinate is outside bounds of K field
                outReal[i]=0; // return 0 for K
                r = -2;
                c = -2;    }
        else{
            r = searcharr(rows,nr-1,0,y);
            c = searcharr(cols,nc-1,0,x);
            outReal[i]=Hs[r][c];    }
        free(rows);
        free(cols);
        free(Hs);
        return 1;    }
    else {
        error = "Unknown function";
        return 0;    }    }

```

### B.3. C Function to read K field into COMSOL

Summary of Code: The purpose of this C code is to allow COMSOL to read the necessary transmissivity values from the inverse model. The code follows the template specified by the COMSOL API for External Functions (COMSOL, 2013).

```
#include <stdio.h>

#include <math.h>

#include <stdlib.h>

#include <string.h>

#ifdef _MSC_VER

#define EXPORT __declspec(dllexport)

#else

#define EXPORT

#endif

static const char *error = NULL;

EXPORT int init(const char *str) {

return 1; }

EXPORT const char * getLastError() {

return error;    }

double* readdisc (char *myfile,int *arr_len,double *tot_len)    {

    // read in Row/Column array - Rows.txt/Cols.txt need to be in KField folder

    FILE *fp;

    char str [80];

    int i;

    double *myarr,prev;

    fp = fopen(myfile,"r"); // read mode

    if( fp == NULL )

    {

        error="Error while opening row/col file.\n";

        return NULL;    }

    fscanf (fp, "%s", &str);
```

```

*tot_len=atof(str);

fscanf (fp, "%i", arr_len);

myarr = (double*) malloc (*arr_len * sizeof(double));

prev=0;

for (i = 0;i<*arr_len;i++){

    fscanf (fp, "%s", &str);

    myarr[i]=prev+atof(str);

    prev=myarr[i];    }

fclose(fp);

return myarr;    }

double** readKarr (char *myfile,int nc,int nr)

    // read in K array - KField.dat needs to be in KField folder

{
    FILE *fp;

    char str [80];

    int r,c;

    double **myarr;

    fp = fopen(myfile,"r"); // read mode

if( fp == NULL )

{
    error="Error while opening K file.\n";

    return NULL;    }

/* Allocate array */

myarr = (double**) malloc (nr * sizeof(double));

/* Read in K values */

for (r = 0;r<nr;r++){

    myarr[r] = (double*) malloc (nc * sizeof(double));

    for (c = 0;c<nc;c++){

        fscanf (fp, "%s", &str);

        myarr[r][c]=atof(str);    }}

fclose(fp);

return myarr;    }

```

```

void readOffset(double *xoff, double *yoff){

    FILE *fp;

    char str [80];

    char *myfile = "C:\\Data\\GetK\\KField\\Offset.txt";

    fp = fopen(myfile,"r"); // read mode

    if( fp == NULL )

    { // failed to open file

        error="Error while opening the offset file.\n";

        *xoff=999;

        *yoff=999;

    } else {

        fgets(str, 80, fp);

        fscanf (fp, "%s", &str);

        *xoff=atof(str);

        fscanf (fp, "%s", &str);

        *yoff=atof(str);

        fclose(fp);}    }

int searcharr(double *myarr, int arr_max,int arr_min,double mycoord){

    // binary search to find row/column of coordinate

    while(arr_min<arr_max)

    {    int middle = (arr_min+arr_max)/2;

        if(myarr[middle] == mycoord)

            return middle;

        else if (myarr[middle] > mycoord)

            arr_max = middle;

        else

            arr_min = middle + 1;    }

    return arr_min; }

EXPORT int eval(const char *func,

```

```

int nArgs,

const double **inReal,

const double **inImag,

int blockSize,

double *outReal,

double *outImag) {

    int i;

    double totw,toth;

    double xoff,yoff;

    int nc,nr,np,r,c;

    double *rows, *cols;

    double **Ks;

    if (strcmp("getperm", func) == 0) {

        if (nArgs != 2) {

            error = "Two argument expected";

            return 0; }

        /* Read in row and column details */

        readOffset(&xoff,&yoff);

        if (xoff==999 || yoff==999) {

            return 0;}

        cols=readdisc("C:\\Data\\GetK\\KField\\Col_Dis.txt",&nc,&totw);

        if (cols==NULL) {return 0;}

        rows=readdisc("C:\\Data\\GetK\\KField\\Row_Dis.txt",&nr,&toth);

        if (rows==NULL) {return 0;}

        Ks=readKarr("C:\\Data\\GetK\\KField\\KField.dat",nc,nr);

        if (Ks==NULL) {return 0;}

    for (i=0;i<blockSize;i++){ // for each coordinate

        double x = inReal[0][i]-xoff;

        double y = toth-(inReal[1][i]-yoff);

        if (x<0 || y<0 || y>toth || x>totw) {

```

```

        // if x/y coordinate is outside bounds of K field
        outReal[i]=0; // return 0 for K

        r = -2;

        c = -2;

    } else{

        r = searcharr(rows,nr-1,0,y);

        c = searcharr(cols,nc-1,0,x);

        outReal[i]=Ks[r][c];}

free(rows);

free(cols);

free(Ks);

return 1;    }

else {

error = "Unknown function";

return 0; }    }

```

## B.4. List of References

COMSOL (2013) **COMSOL Multiphysics**. v4.4. COMSOL

## Appendix C. **COLLOID TRANSPORT MODEL VERIFICATION**

This appendix discusses the modelling used to verify that the colloid transport and attachment equations added into the COMSOL model were set up correctly and that the model produced accurate results. This was done through the modelling of laboratory column migration experiments.

### **C.1. Background**

Validation of the colloid attachment equations was possible by modelling experiments carried out by Walkden (2014), in which the migration of Na-bentonite colloids over an artificial granite fracture was investigated. The reader is directed to the report which contains the experimental setup and protocol, but in summary a granite surface 30cm x 14.9 cm was sealed under Perspex, with an inlet and outlet drilled into the Perspex located halfway across the fracture and inset from either edge. Depending on the experiment, fluorescein tracer or a bentonite colloid suspension was pumped through the fracture whilst in a fridge, with the concentration measured by fluorimeter or nephelometer.

### **C.2. Methods**

The colloid migration experiment modelled is described as Experiment B in Walkden (2014), which used a 9.09mg/l suspension of Na-bentonite colloids which were injected into the fracture at a flow rate of 0.35 ml/min, before the line was switched to equilibrated water for the remainder of the experiment. The visual fluorescein tracer experiment referred to as Experiment A in the report was also used to calibrate the variable permeability zones that were included in the model to represent the granite fracture.

## Model Setup

COMSOL Multiphysics (v4.4) (COMSOL, 2013) was used to model the experiments, representing the fracture as an equivalent porous medium. The model domain of 30 x 14.9cm was used as this was the size of the fracture. Inlets were 3cm in size and rectangles were included in the model to allow the regular rectangular ‘mapped’ grid to be used across the majority of the model. The colloid transport and attachment equations as described in Chapter 4 were used, with the addition of an equation to describe straining of colloids (Equation C.1):

$$\frac{\partial(\rho_B F_s)}{\partial t} = \lambda \theta |\mathbf{u}| C$$

### Equation C.1 Colloid Filtration Equation

Where  $F_s$  = mass of filtered colloids per unit mass of rock [1],  $\lambda$  = filter factor [ $L^{-1}$ ],  $C$  = aqueous colloid concentration [ $ML^{-3}$ ],  $u$  = advective velocity [ $LT^{-1}$ ]. This equation was used in Burns (2013) to model the transport of Na colloids within sandstone cores, but was not used for the main transport modelling in this study as the effect on the breakthrough for reasons described in Chapter 4. The following boundary conditions were used with the model:

- Specified Pressure condition (0 Pa) on one face of the outlet, with a specified water flux over the outlet (0.35 ml/min, divided by the perimeter of the outlet).
- A Dirichlet specified concentration condition on the inlet that represents the initial concentration of colloids within the injected suspension (9.09 mg/l)
- An advective flux only condition (zero dispersive flux) on the outlet.

The grid used was a combination of the regular ‘mapped’ grid and the ‘free quad’ option around the inlets, with a maximum element size of 0.003m. The COMSOL stationary solver was used for solving steady state groundwater flow, with this result being used in the time dependent solver for the different colloid transport equations, with a maximum time step of 3.3 seconds for 750 minutes. Results were outputted every 5 minutes. Table C.1 shows the non-calibration parameters that were used in all model runs.

Parameter	Value
$\rho_b$ (granite bulk density)	2120 kg/m <sup>3</sup>
$\theta$ (porosity)	0.2
b (fracture aperture)	1 mm
k (intrinsic permeability)	1e-11 m <sup>2</sup>
$\mu$ (fluid viscosity)	0.001 Pa*s
$\rho$ (fluid density)	1000 kg/m <sup>3</sup>
$D_d^*$ (molecular diffusion co-efficient)	1e-8 m <sup>2</sup> /s
$g_x$ (acceleration due to gravity along strike)	0
$g_y$ (acceleration due to gravity down dip)	$-\sin(15^\circ)*9.82 \text{ m/s}^2$

Table C.1 Non-calibration parameter values used in model

### Model Calibration

Model calibration was carried out by first adding zones with different intrinsic permeability to visually match the tracer patterns observed during Experiment A, as shown in Figure C.1. Once this was carried out, broad and detailed sensitivity analyses for reversible colloid attachment and detachment rate constants, irreversible colloid attachment and straining of colloids were carried out. The calibration process was carried out visually against a breakthrough curve provided in the report, but the parametric sweep feature of COMSOL

was used to automate the sensitivity analyses. For the sensitivity analyses, typical values were chosen for the different rate constants from Burns (2013) and from CFM modelling in Huber et al. (2014), as given in Table C.2.

Parameter	Typical Value	Parameter Purpose	Source(s) of Typical Value
$k_{att}$	$1 \times 10^{-6} \text{ (s}^{-1}\text{)}$	Reversible attachment rate	Huber et al. (2014); Burns (2013)
$k_{det}$	$2 \times 10^{-4} \text{ (s}^{-1}\text{)}$	Reversible detachment rate	Burns (2013)
$F_{max}$	$5 \times 10^{-5} \text{ (-)}$	Maximum reversibly attached mass per unit mass of rock	Burns (2013)
$k_{ia}$	$1 \times 10^{-5} \text{ (s}^{-1}\text{)}$	Irreversible attachment rate	Burns (2013)
$F_{imax}$	$7.5 \times 10^{-5} \text{ (-)}$	Maximum irreversibly attached mass per unit mass of rock	Burns (2013)
$\lambda$	$20 \text{ (m}^{-1}\text{)}$	Filtration rate	Huber et al., (2014); Burns, (2013)
$\alpha_l$	$0.01 \text{ (m)}$	Longitudinal dispersivity	~Tenth of travel distance
$\alpha_t$	$0.001 \text{ (m)}$	Transverse dispersivity	Tenth of longitudinal dispersivity

Table C.2 Typical parameters for broad sensitivity analysis

### C.3. Results

#### Variable Permeability

Figure C.1 shows several pictures taken during the fluorescein tracer experiment (Experiment A). From these pictures, two slower flow paths were identified and two zones with an intrinsic permeability of  $0.5 \times 10^{-11} \text{ m}^2$  were added (half of the original value), of 5cm x 2.5cm and 5cm x 5.9cm, as shown in Figure C.2. Figure C.3 shows the resulting concentration contour plots in comparison to the images on the experiment. It was possible for more zones to be added, however the resulting match to the experimental images were in good agreement to the model.

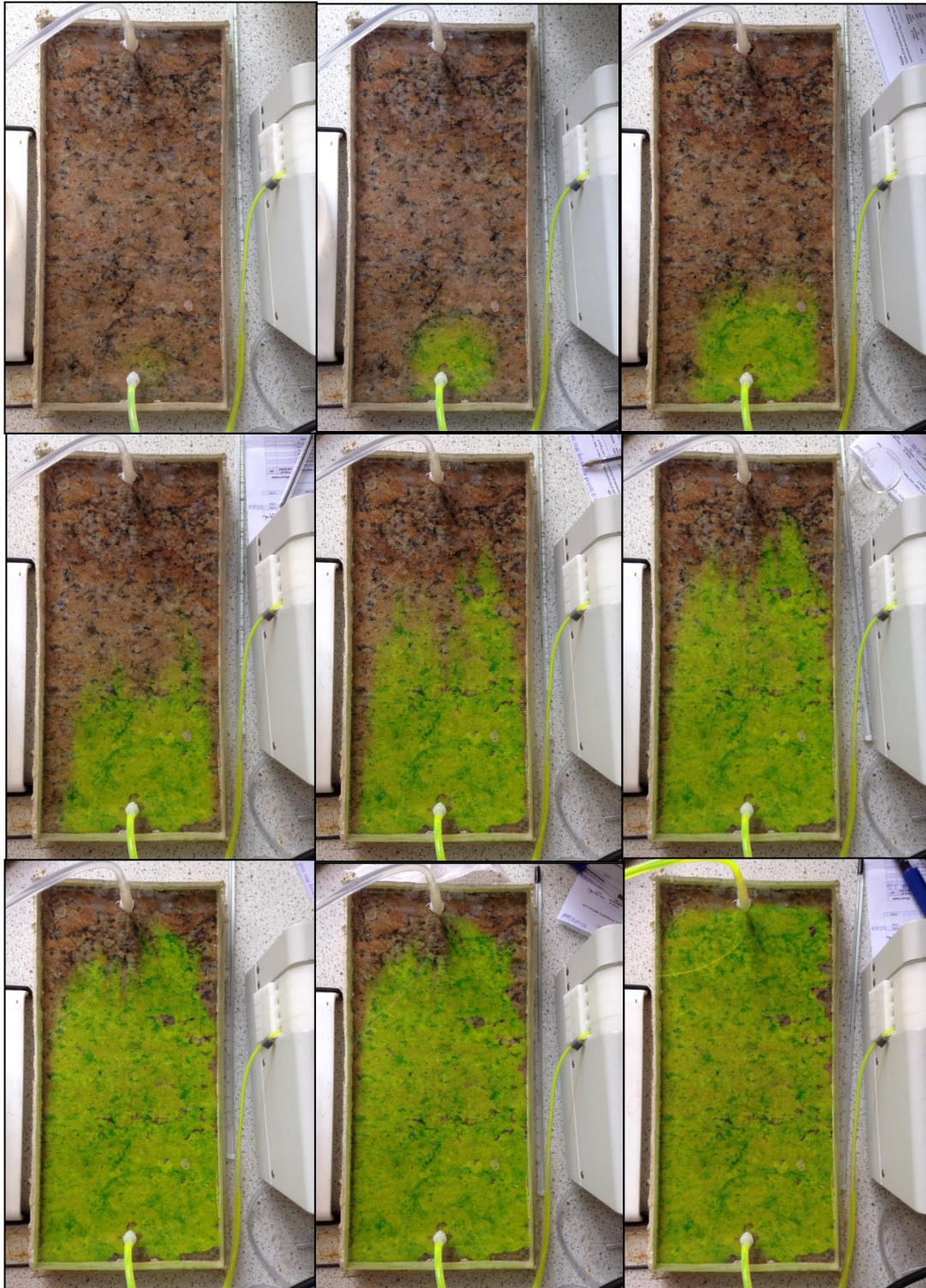
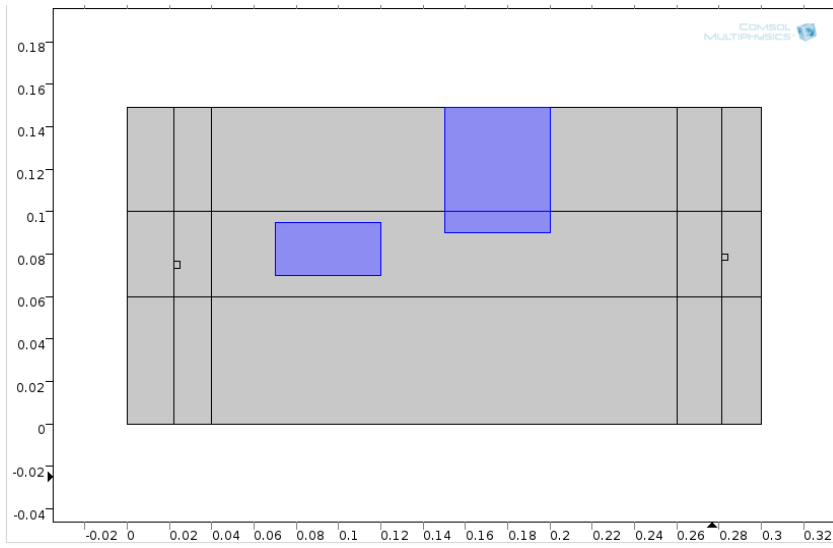
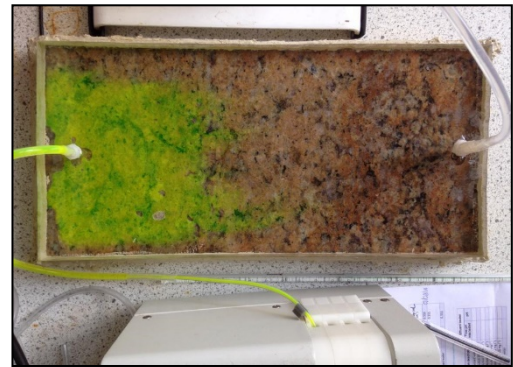
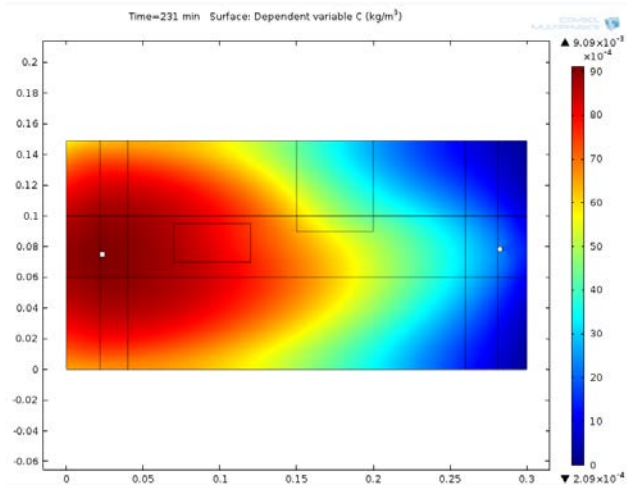


Figure C.1 Pictures from visual fluorescein migration test. Images taken at (from left to right): Top - 1, 5 and 10 minutes; Middle - 15, 20 and 25 minutes; Bottom - 30, 32 and 50 minutes



**Figure C.2 Zones of lower permeability (highlighted in blue)  
15 minutes**



**20 minutes**

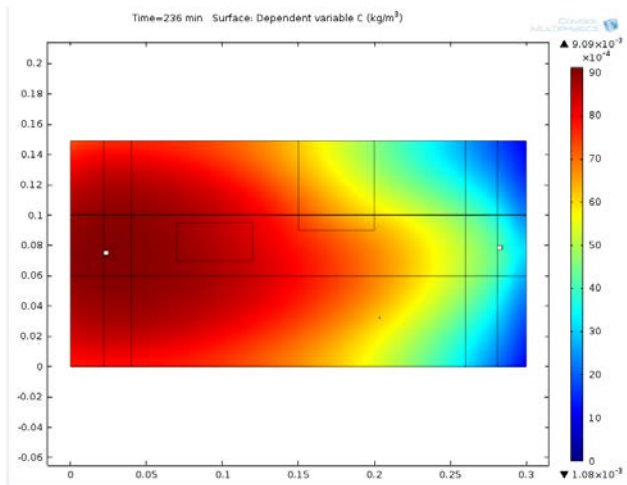


**Figure C.3 Colour Plots of Concentration ( $\text{kg}/\text{m}^3$ ), with experimental results to the right. Images taken at 15 and 20 minutes after tracer injection**

## Model Calibration

Initial sensitivity analyses were run to determine which parameters were important calibration parameters, by varying the different parameters by several orders of magnitude. It was determined that the attachment and detachment rates ( $k_{att}$ ,  $k_{det}$  and  $k_{ia}$ ) and the filtration factor ( $\lambda$ ) for the colloid straining are the most sensitive parameters and were parameters used in the fine sensitivity analysis. The factors that limit colloid attachment ( $F_{max}$  and  $F_{imax}$ ) were not sensitive at the attachment rates and were not deemed calibration parameters to investigate in detail in the fine sensitivity analyses.

The broad sensitivity analysis showed that the reversible attachment and detachment processes were sensitive at larger values, and so fine sensitivity analysis was carried out at large reversible attachment and detachment rate constants. Large reversible attachment and detachment rate constants produced a retarded breakthrough when compared to slower attachment rates. Once calibration of the colloid attachment parameters was completed, the dispersivity (both longitudinal and transverse) were altered. Table C.3 shows the calibrated parameters that produced the breakthrough curve as shown in Figure C.4.

Parameter	Typical Value	Parameter Purpose
$k_{att}$	0.01 ( $s^{-1}$ )	Reversible attachment rate
$k_{det}$	0.04 ( $s^{-1}$ )	Reversible detachment rate
$F_{max}$	5 (-)	Maximum reversibly attached mass per unit mass of rock
$k_{ia}$	$4.2 \times 10^{-5}$ ( $s^{-1}$ )	Irreversible attachment rate
$F_{imax}$	0.01 (-)	Maximum irreversibly attached mass per unit mass of rock
$\lambda$	750 ( $m^{-1}$ )	Filtration rate
$\alpha_l$	0.01 (m)	Longitudinal dispersivity
$\alpha_t$	0.001 (m)	Transverse dispersivity

**Table C.3** Calibrated model parameters

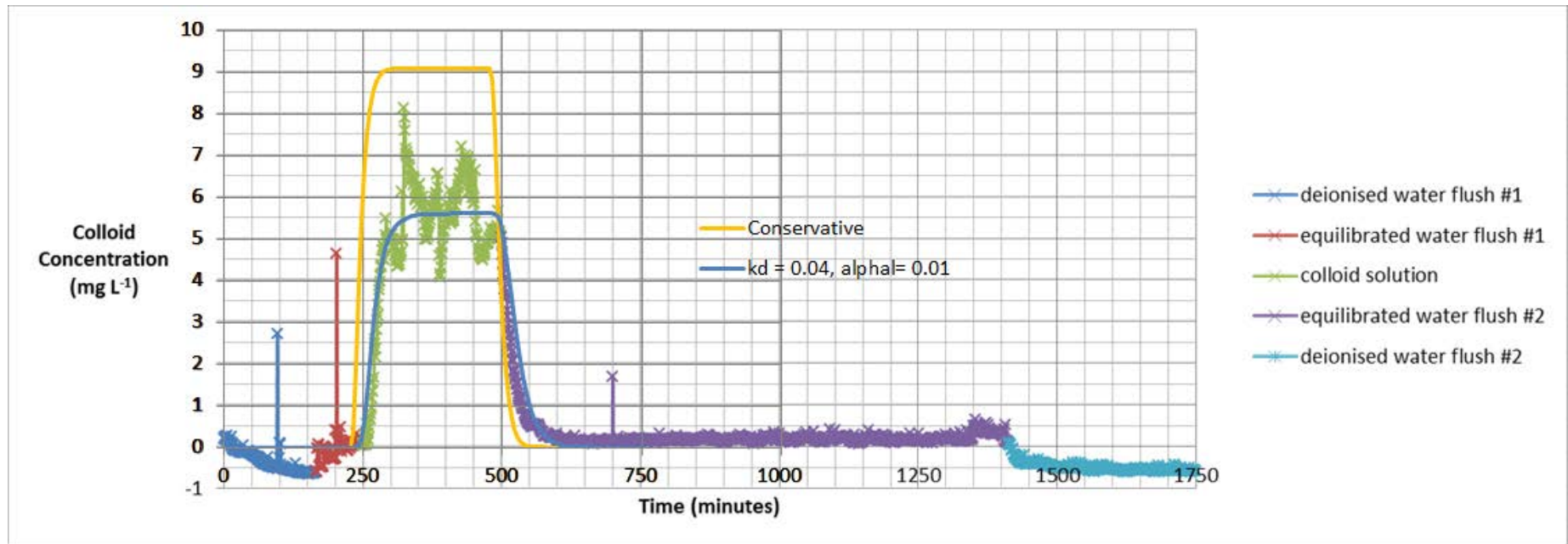


Figure C.4 Calibrated Breakthrough for Experiment B (blue line), with conservative breakthrough (yellow line)

#### **C.4. Discussion**

Figure C.4 shows the resulting breakthrough curve from the model calibration, and shows a good match to the experimental data, validating the colloid attachment equations. The figure also shows the corresponding breakthrough for when the colloid attachment processes are not included (i.e. a conservative tracer).

The reversible colloid attachment values derived from the calibration are higher than typical values to provide the retardation factor needed to match colloid breakthrough ( $R \sim 1.1$ ) which also indicates the colloid exclusion chromatography is not occurring in this experiment. This is likely to be due to the large aperture of the artificial fracture used in the experiment.

The irreversible colloid attachment and straining values are also higher than the typical values in Table C.1, indicating that colloid filtration is resulting in less mass observed at breakthrough. Comparing the colloid breakthrough (blue) curve which a conservative breakthrough (yellow line) in Figure C.4 shows that there is less area underneath the curve (around 63% recovery) indicating that colloid filtration processes are more important in this experiment than in Burns (2013). The colloid straining and irreversible attachment work have the same impact on the breakthrough curve, and for future modelling of the CFM experiments it was decided that only the irreversible colloid attachment process be included to reduce the number of free calibration parameters.

## C.5. List of References

Burns, D. (2013) **Modelling of experimental breakthrough curves of colloid injection**. NERC Research Report, University of Birmingham

COMSOL (2013) **COMSOL Multiphysics**. v4.4. COMSOL

Huber, F., Noseck, U. and Schäfer, T. (2014) **Colloid / nanoparticle formation and mobility in the context of deep geological nuclear waste disposal**. Karlsruhe, Germany

Walkden, S. (2014) **Bentonite Colloid Investigations on a granite fracture**. MSc Nuclear Decommissioning and Waste Management Project, University of Birmingham

## Appendix D. **COLLOID RECOVERY PLOTS**

This appendix details some of the plots used to help constrain the calibration parameters for colloid attachment used in the early stages of modelling the breakthrough of bentonite colloids for the migration experiments.

### **D.1. Background**

There is a lack of physical parameters that can be used to derive and predict the colloid attachment and detachment rate constants to model colloid breakthrough. To provide a better constraint on parameter values in the model, plots were generated to show the colloid recovery for varied colloid attachment and detachment rates for the CFM Run 13-05 experiment. Dr Lindsay McMillan wrote a large portion of the R code used to generate the contour plots.

### **D.2. Methods**

Initial attempts at calibrating bentonite colloid breakthrough for CFM Run 13-05 were run where the full experimental dataset was not available for calibration. The CFM Run 13-05 model was run within COMSOL Multiphysics and the colloid recovery was noted for a variety of attachment and detachment rate constants. Here, the model assumed unlimited reversible and irreversible (where applicable) colloid attachment. This data was then used to make an interpolated colour plot showing the colloid recovery for CFM Run 13-05 for different reversible attachment and detachment rates. This process was repeated for different irreversible attachment rates. Finally, attachment and detachment rates that produced good matches to the colloid breakthrough in CRR Run 32 were also plotted on certain plots to give constraints on the values of the attachment rates that could be used in the CFM Run 13-05 model.

To produce the interpolated colour plots of colloid recovery, the statistical programming language R was used, using the “sp”, “gstat”, “gridExtra”, “lattice”, “mapproj” and “rgeos” packages. The full code used is located at the end of this Appendix, but essentially the code reads in the colloid recovery values from different model runs, interpolating these values across a larger range of values. The final plots are given in Figure D.1 to Figure D.6 for different irreversible colloid attachment rates, with a modelled recovery between 0 and 85%. Similar patterns emerge from the different contour plots, in that a thin band of parameters controls the transition between low and high colloid recoveries, and this band ends on the ratio between attachment and detachment rate above a certain threshold. Varying the irreversible attachment rate has little impact on the shape of the contour plots, but alters the maximum recovery that can be obtained (for instance an irreversible attachment rate of  $5 \times 10^{-6}$  1/s gives a maximum recovery of 46%). These plots helped to constrain colloid attachment and detachment rates that would provide good matches for CFM Run 13-05 and CRR Run 32 with consistent parameters, but became less important when the experimental breakthrough data became available to calibrate against.

### CFM 13-05 Colloid Behaviour - Reversible Attachment

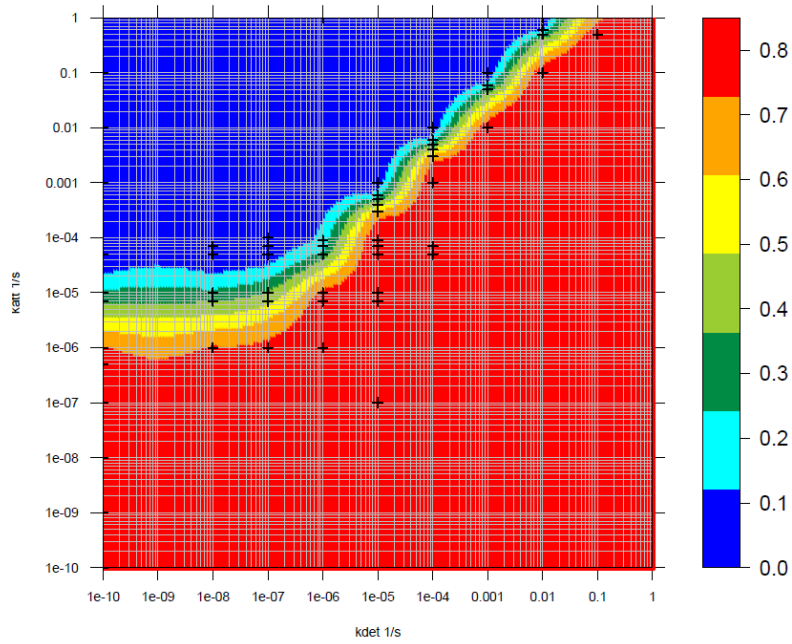


Figure D.1 Colloid recovery plot with no irreversible colloid attachment

### CFM 13-05 Colloid Behaviour - $k_{iat} 10^{-7}$ 1/s

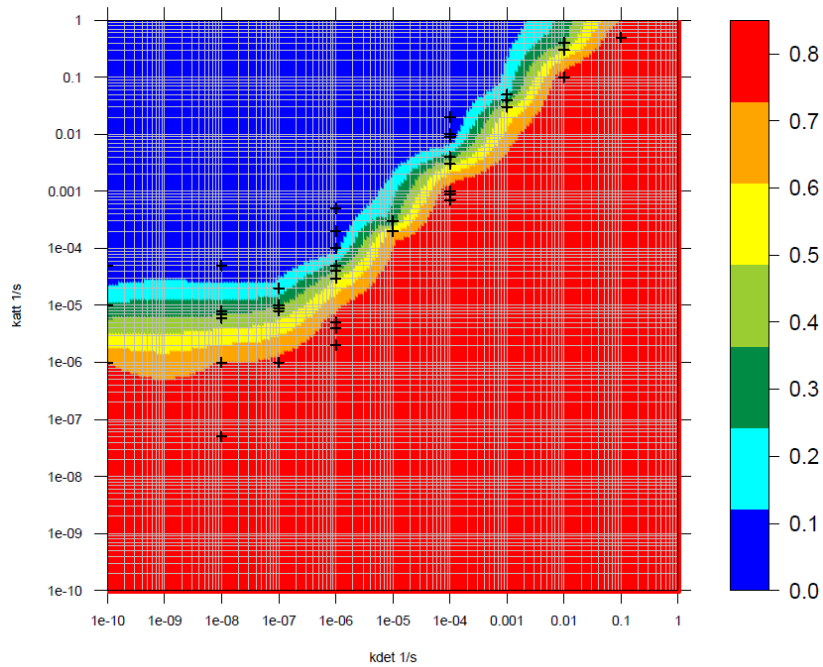


Figure D.2 Colloid recovery plot with an irreversible attachment rate  $k_{iat} = 1 \times 10^{-7}$  1/s

CFM 13-05 Colloid Behaviour -  $k_{iat} 1e-6 1/s$

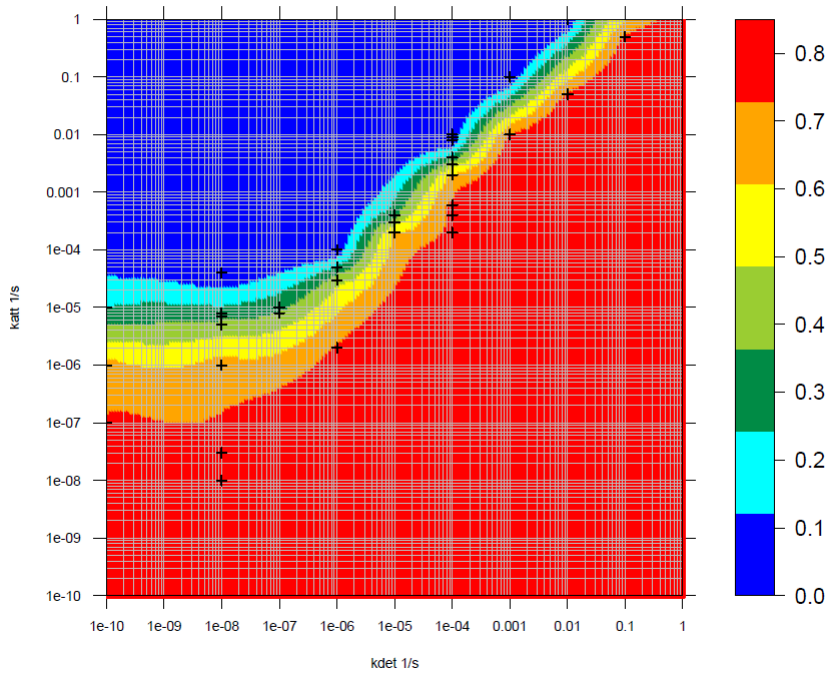


Figure D.3 Colloid recovery plot with an irreversible attachment rate  $k_{iat} = 1z10^{-6} 1/s$

CFM 13-05 Colloid Behaviour -  $k_{iat} 3e-6 1/s$

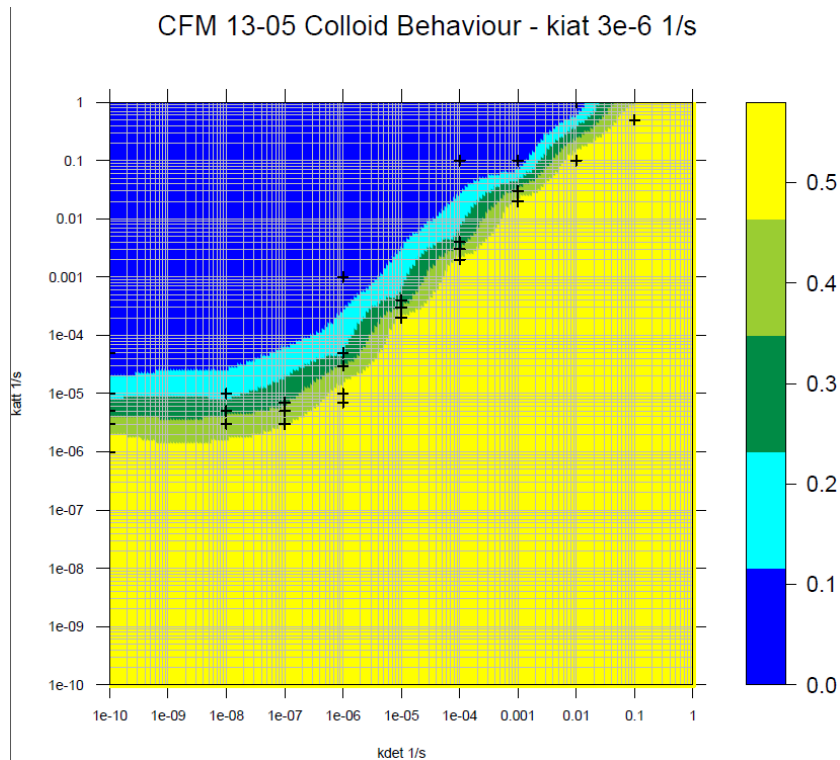


Figure D.4 Colloid recovery plot with an irreversible attachment rate  $k_{iat} = 3x10^{-6} 1/s$

CFM 13-05 Colloid Behaviour -  $k_{iat} 5e-6$  1/s

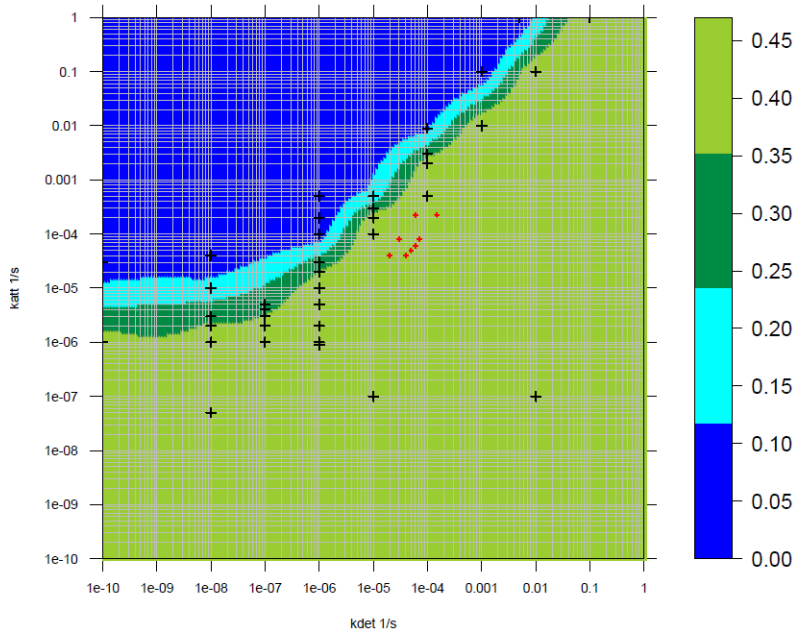


Figure D.5 Colloid recovery with an irreversible attachment rate  $k_{iat} = 5 \times 10^{-6}$  1/s. Red points indicate areas where parameters gave good match to CRR 32 breakthrough.

CFM 13-05 Colloid Behaviour -  $k_{iat} 6e-6$  1/s

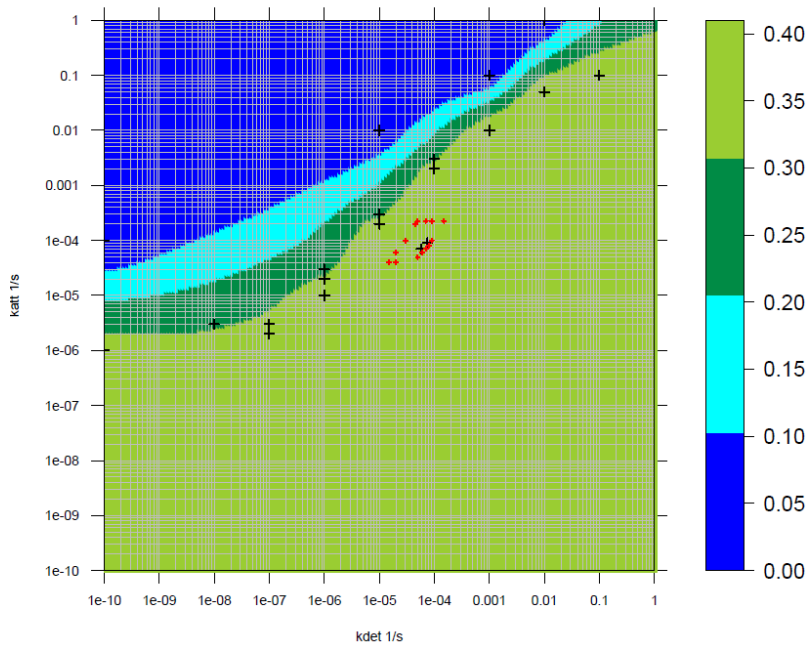


Figure D.6 Colloid recovery with an irreversible attachment rate  $k_{iat} = 6 \times 10^{-6}$  1/s. Red points indicate areas where parameters gave good match to CRR 32 breakthrough.

### D.3. List of References

Augie, B. (2015) **gridExtra: Miscellaneous Functions for “Grid” Graphics**. R Package

Bivand, R.S. and Lewin-Koh, N. (2016) **maptools: Tools for Reading and Handling Spatial Objects** R Package

Bivand, R.S. and Rundel, C. (2017) **rgeos: Interface to Geometry Engine - Open Source (GEOS)** R Package

Deepayan, S. (2008) **Lattice: Multivariate Data Visualization with R**. New York: Springer. R Package

Pebesma, E.J. (2004) Multivariable geostatistics in S: the gstat package. **Computers and Geosciences**, 30: 683–691

Pebesma, E.J. and Bivand, R.S. (2005) Classes and methods for spatial data in R. **R News**, 5 (2)

R Core Team (2015) **R: A language and environment for statistical computing**.

### D.4. Code Used

```
##### colour functions #####  
  
krige.colors<-function(maxstep) {  
  mycols<-c(1:maxstep)  
  
  for (i in 1:maxstep) {  
    mycols[i]<-getKrigecolor(i,maxstep) }  
  
  mycols }  
  
getKrigecolor<-function(mystep, maxstep) {  
  
  #Find colour of graph line  
  
  TotSteps<-1020  
  
  if (maxstep>1){  
    mystep<-mystep-1  
  
    maxstep<-maxstep-1  
  
    Mypos<-round(mystep*TotSteps/maxstep,digits=0)  
  
  } else {Mypos<-0}  
  
  R<-0  
  
  G<-0  
  
  B<-0  
  
  if (Mypos<=255) {  
  
    R<-255  
  
    G<-Mypos  
  
  } else if (Mypos<=510) {
```

```

R<-510-Mypos
G<-255
}else if (Mypos<=765) {
  G<-255
  B<-Mypos-510
}else if (Mypos<=1020) {
  G<-1020-Mypos
  B<-255
}
rgb(R, G, B, maxColorValue=255)
}

##### end colour functions #####

# Read in all data
Recovery<-read.table("3e-6.csv",header=TRUE,sep = ",")
Recovery$recovery[Recovery$recovery==0]<-0.001
Recovery$katt<-log(Recovery$katt,10)
Recovery$kdet<-log(Recovery$kdet,10)
coordinates(Recovery) <- ~ kdets+katts

#Read in CRR
#CRR<-read.table("CRR5e-6.csv",header=TRUE,sep = ",")
#CRR$katt<-log(CRR$katt,10)
#CRR$kdet<-log(CRR$kdet,10)
#coordinates(CRR) <- ~ kdets+katts

## create a grid onto which we will interpolate:
## now expand to a grid with 500 meter spacing:
Colgrid <- expand.grid(katt=seq(log(1e-10,10),log(1,10),0.05), kdets=seq(log(1e-10,10),log(1,10),0.05))

## convert to SpatialPixel class
coordinates(Colgrid) <- ~ kdets+katts

#gridded(T2aKgrd) <- TRUE
#gridded(T3aKgrd) <- TRUE

## test it out:
#plot(grd, cex=0.5)

#points(e, pch=1, col='red', cex=0.7)

#title("Interpolation Grid and Sample Points")

```

```

## make gstat object:

Recoveryg <- gstat(id="recovery", formula=recovery~1, data=Recovery)

### Approach 1 (ignore trends in data and plot using Exponential model)

plot(variogram(Recoveryg, cutoff=3, width=0.1), threshold=10) # data has a trend as does not level off at end but keeps rising

### Fit data

Recoveryv<-variogram(Recoveryg, cutoff=4, width=0.1)

Recoveryv.fit <- fit.variogram(Recoveryv, model=vgm(model="Lin"))

plot(Recoveryv,model=Recoveryv.fit,as.table=TRUE)

## update the gstat object:

Recoveryg <- gstat(Recoveryg, id="recovery", model=Recoveryv.fit )

## perform ordinary kriging prediction:

Recoveryp <- predict(Recoveryg, model=Recoveryv.fit, newdata=Colgrid)

NoCols<-5

# totcollist<-rev(krige.colors(NoCols))

#totcollist<-col2rgb(c("blue", "cyan", "springgreen4", "yellowgreen", "yellow", "orange", "red"),alpha = 0)

totcollist<-col2rgb(c("blue", "cyan", "springgreen4", "yellowgreen", "yellow"),alpha = 0)

  totcollist<-rgb(red = totcollist[1,],green = totcollist[2,],blue = totcollist[3,],maxColorValue = 255)

  mylist<-seq(1e-10,9e-10,1e-10)

mylist2<-1e-10

mylist3<-1e-10

for (i in 1:9){

  mylist<-c(mylist,mylist*10)

  mylist3<-c(mylist3,mylist2*10^i)

}

  mylist3<-c(mylist3,1)

  Recoveryp$recovery.pred[Recoveryp$recovery.pred>0.58]<-0.58

Recoveryp$recovery.pred[Recoveryp$recovery.pred<0]<-0

  Upperrecovery<-0.41

Lowerrecovery<-0.33

# Plot Contour

myplot<-spplot(Recoveryp, zcol="recovery.pred", col.regions=totcollist, cuts=NoCols,

  colorkey=TRUE,xlim=c(-10,0),ylim=c(-10,0),cex=0.5,

  #colorkey=list(width=2,labels=list(at=labelat, labels=labeltext),space="top"),

```

```

#key.space=list(x=0.1,y=.95,corner=c(0,1)), auto.key =list(title = "test"),

contour=FALSE, labels=TRUE, pretty=TRUE, col='black',

main=list(label="CFM 13-05 Colloid Behaviour - kiat 3e-6 1/s",cex=1,font=0.5),ylab=list("katt 1/s",cex=0.5),

xlab=list("kdet 1/s",cex=0.5),scales=list(x=list(at=seq(-10,0,1),lab=mylist3),

          y=list(at=seq(-10,0,1),lab=mylist3),cex=0.5),

par.settings = list(axis.line = list(lwd = 0.5),fontsize=list(text=12,points=8),

          layout.widths=list(right.padding=0.5,left.padding=0),

          layout.heights=list(bottom.padding=0,top.padding=0)),

panel = function(...) {

# plot coloured dots

panel.pointsplot(...)

# plotting grid lines

panel.abline(h=log(mylist,10),col="grey",lty=1,lwd=0.5)

panel.abline(v=log(mylist,10),col="grey",lty=1,lwd=0.5)

# plotting data points

sp.points(Recovery,col="black",cex=0.5)

#plotting CRR

#sp.points(CRR,col="red",cex=0.2)

cairo_pdf(file="test.pdf",width=5,height=5)

grid.arrange(myplot)

dev.off()

```

## Appendix E. DATA AND MODEL FILES

### E.1. List of Digital Files

Harvey (2019) contains the following datasets that make up this digital appendix:

- Blank COMSOL Model containing model geometry, boundary conditions and coded equations without any couplings between colloid bound and aqueous radionuclide transport.
- Spreadsheet containing the model output for the breakthrough of conservative tracer and colloids from the full 2D COMSOL model for CFM Run 13-05 and CRR Run 32; the source term used in the analytical model for CFM Run 13-05, output from the analytical spreadsheet model for conservative tracer in CFM Run 13-05 and CRR Run 32; model output for breakthrough of conservative tracer and colloids from the 1D COMSOL Channel Model, and model output for the predictions of the REMO-2 Experiment (see Chapter 5 for more information).
- Spreadsheet containing the model output for the breakthrough of americium and plutonium from the COMSOL model for CFM Run 13-05 and CRR Run 32 (see Chapter 6 for more information).
- Spreadsheet containing the model output for the breakthrough of caesium, uranium and neptunium from the COMSOL 2D model. For caesium this contains the model results for the one sorption site model, two-site colloid/ one-site FFM model and the full two site colloid and FFM model (see Chapter 7 for more information).

- PHREEQC Input model file containing the input for Grimsel groundwater (pH 9.6, Eh - 220mV); the CFM Run 13-05 cocktail (without colloids) at pH 9.6, Eh -220 mV and the CRR Run 32 Cocktail (without colloids) at pH 9.6, Eh -220mV.

These files are available from the National Geoscience Data Centre run by the BGS.

## E.2. List of References

Harvey, B. E. (2019): Collection of data supporting PhD Thesis "Development of coupled processes numerical models of tracer, colloid and radionuclide transport in field migration experiments' by B Harvey, HydroFrame WP5. **British Geological Survey**. (Dataset). Available from: <https://dx.doi.org/10.5285/c93488f9-9ebf-4240-87a4-1277baaeb91f>